Multiscale modelling of granular soils : from the grain to the structure scale

Chaofa Zhao

UNIVERSITE BRETAGNE LOIRE

CENTRALE NANTES

Thèse de Doctorat

Chaofa ZHAO

Mémoire présenté en vue de l'obtention
du grade de Docteur de l'Ecole Centrale de Nantes
Sous le label de l'UNIVERSITÉ BRETAGNE LOIRE

École doctorale : Sciences pour l'Ingénieur, Géosciences, Architecture

Discipline : Génie Civil
Unité de recherche : Institut de recherche en génie civil et mécanique

Soutenue le 13 décembre 2017

Modélisation multi-échelle des sols granulaires : de l'échelle des grains aux structures géotechniques

JURY

Président :	**Ali DAOUADJI**, Professeur des Universités, INSA Lyon
Rapporteurs :	**François NICOT**, Directeur de Recherche, IRSTEA Grenoble
	Farid LAOUAFA, Ingénieur (HDR), INERIS France
Examinateurs :	**Niels KRUYT**, Professeur, Université de Twente, Pays-Bas
	Xianfeng LIU, Professeur, Université Jiaotong du Sud-Ouest, Chine
Directeur de thèse :	**Zhen-Yu YIN,** Maître de conférences (HDR), Ecole Centrale de Nantes
Co-directeur de thèse :	**Pierre-Yves HICHER**, Professeur émérite, Ecole Centrale de Nantes

ACKNOWLEDGMENTS

I would like to express my sincerest gratitude to Professors Pierre-Yves Hicher and Zhen-Yu Yin for their dedication in guiding me during my three-year study at the Ecole Centrale de Nantes. The rigorous training that I received from them in a professional environment conducive to inquiry and exploration established a communication platform that steadily strengthened my work. Invaluable to me was the give-and-take of our discussions, always interwoven with their constructive feedback. Following their example, I have been inspired not only to pursue ideas from my own curiosity but also to create a solid foundation for the future.

I am also very grateful to Professors François Nicot, Farid Laouafa, Ali Daouadji, Xianfeng Liu and Niels Kruyt for their helpful suggestions throughout my research work. As my scientific committee, they have helped me greatly improve my thesis and they have significantly facilitated the whole process of my research.

Likewise, I extend my gratitude to Professors Anil Misra and Olivier Millet for their valuable advice in improving my understanding of micromechanics of granular materials. I am equally indebted to Professor Zhongxuan Yang for his continuous encouragement and support over these years. I am also grateful for the insights I derived through discussions with Professors Panagiotis Kotronis, Giulio Sciarra, Mahdia Hattab, Christophe Dano and Yvon Riou during my PhD study.

I would also like to thank Shimu, Ms. Pearl-Angelika Lee. Her instruction greatly shaped my view on research life while also improving my language skills significantly in both French and English. I also extend my gratitude to Mr. Roth Edwards for his generous help with my English.

Equally, I am indebted to Ms. Françoise Hulaud and Mr. Jean-Jacques Hulaud for their parental love. Over the course of three years, they treated me as one of their own family members as we shared many unforgettable moments. Their generous help and absolute support guided me through the inevitable difficulties of life. Without their infinite trust and

affectionate care, I simply would not have had the freedom to focus so completely on my research.

Thanks also to my friends in the GeM lab: Zheng Li, Jian Li, Fan Yu, Qian Zhao, Yinfu Jin, Younes Salami, Menghuan Guo, Ibrahim Bitar, Zexiang Wu, Jiangxin Liu, Andreea Roxana Vasilescu, Sanae Ahayan, Jie Yang, Zhuang Jin, Ran Zhu, Huan Wang and Borana Kullolli, for accompanying me in this interesting, enjoyable and unforgettable experience.

Finally, a big thanks to everyone in my family for their continuous encouragement and unyielding support. Their unwavering love over these years supported and inspired me in my daily work, without which this thesis would not exist.

ABSTRACT

The mechanical behaviour of granular soils is an important aspect in geotechnical engineering. Current modelling approaches for the behaviour of granular soils employ phenomenological constitutive relations based upon classical continuum mechanics. This problem can be circumvented by using multiscale constitutive relations based on thermodynamic principles with internal variables. Using a multiscale approach, this thesis attempts to construct multiscale constitutive relations that account for the microstructure of granular soils and to demonstrate their capabilities in solving geotechnical problems at both small and large deformations. The thesis aims to: 1) construct a multiscale constitutive relation for dry granular soils based on a thermodynamic framework which requires fewer *ad hoc* assumptions; 2) extend the multiscale thermomechanical formulations for partially saturated granular soils for which a micromechanical model is formulated; 3) implement the model using an implicit integration algorithm in a finite element code; 4) apply the model to analyse the instability of granular soils for both localised and diffuse failures; and 5) demonstrate the capability of the multiscale approach in solving some typical geotechnical problems by implementing the model in an explicit finite element code. The proposed multiscale approach offers a simulation tool that provides valuable insights into engineering problems from the grain to the structure scale.

Key words: granular soils, multiscale modelling, thermodynamic principles, integration algorithm, instability, geotechnical structures

RÉSUMÉ

Le comportement mécanique des sols granulaires est un élément important à prendre en compte dans l'ingénierie géotechnique. Les approches de modélisation actuelles pour le comportement des sols granulaires utilisent des relations constitutives phénoménologiques basées sur la mécanique classique du continuum. Ce problème peut être contourné en utilisant des relations constitutives multi-échelles basées sur les principes thermodynamiques avec variables internes. En utilisant une approche multi-échelle, cette thèse tente de construire des relations constitutives multi-échelles qui tiennent compte de la microstructure des sols granulaires et les mettre en œuvre pour résoudre des problèmes géotechniques à la fois en petites et grandes déformations. La thèse vise à: 1) construire une relation constitutive multi-échelle pour les sols granulaires secs à partir d'un cadre thermodynamique qui nécessite moins d'hypothèses ad hoc; 2) étendre les formulations thermomécaniques multi-échelles aux sols granulaires partiellement saturés pour lesquels un modèle micromécanique est formulé; 3) implémenter le modèle en utilisant un algorithme d'intégration implicite dans un code aux éléments finis; 4) appliquer le modèle pour analyser l'instabilité des sols granulaires dans les cas de ruptures localisées et diffuses; et 5) démontrer la capacité de l'approche multi-échelle à résoudre certains problèmes géotechniques typiques en mettant en œuvre le modèle dans un code aux éléments finis explicite. L'approche multi-échelle proposée aboutit à un outil de simulation qui fournit des informations précieuses sur les problèmes d'ingénierie depuis l'échelle des grains jusqu'à l'échelle de la structure.

Mots clés : sols granulaires, modélisation multi-échelle, principes thermodynamiques, algorithme d'intégration, instabilité, structures géotechniques

TABLE OF CONTENTS

LIST OF FIGURES

LIST OF TABLES

LIST OF NOTATIONS AND ABBREVIATIONS

LATIN SYMBOLS

$\mathbf{A}$	Second-order fabric tensor
$\mathbf{a}^T$	First partial derivative of the yield function at inter-particle contacts
$\mathbf{b}^T$	First partial derivative of the potential function at inter-particle contacts
$\mathbf{C}$	Consistent tangential moduli for CPPM
c	cth inter-particle contact
D	Dilatancy parameter at inter-particle contact
d_{50}	Grain size correspond to 50% pass by mass on the size distribution curve
$\mathbf{E}$	Constraint matrices of strain under mixed control
E_c	Kinetic energy
e	Void ratio
e_0	Initial void ratio
e_c	Void ratio at critical state
e_{ref}	Reference void ration in critical state line
e_w	Void ratio of water
$\mathbf{F}$	Deformation tensor in Lagrangian description
F	Yield function at inter-particle contact
$\mathbf{f}^c$	Force at inter-particle contact
f_{ref}	Reference normal force
G	Potential function at inter-particle contact
H	Hardening variable used in the implementation of CPA
k_{ij}^c	Stiffness matrix at the microscale
k_{rR}	Ratio of tangential stiffness over normal stiffness at inter-particle contact

k_{pR} Ratio of plastic stiffness over normal stiffness at inter-particle contact

l_i Branch vector between two contacting particles

M The slope of critical state line in p'-q plane

N Number of inter-particle contacts

NP Number of integration points over a unit sphere

p' Mean effective stress

p_{ref} Reference mean effective stress

q Deviatoric stress

r Radius of particles

$\mathbf{S}$ Constraint matrices of stress under mixed control

s Matric suction

$\dot{s}_{ij}$ Nominal stress tensor

S_r Degree of saturation

T Absolute temperature

u Internal energy per unit volume

V Volume of granular assembly

W Work input per unit volume

W_2 Global second-order work

W_2^c Particle scale second-order work

W_2^{el} Elementary scale second-order work

W_r^p Plastic work at inter-particle contact induced by tangential force

w Water content

GREEK SYMBOLS

α α th integration point on a unit sphere

$\boldsymbol{\alpha}^c$ Back force at cth inter-particle contact

β	Angle in local coordinate (n, s, t)
γ	Angle in local coordinate (n, s, t)
$\boldsymbol{\delta}^c$	Inter-particle displacement at cth contact
$\Delta\lambda$	Plastic multiplier for both CPPM and CPA
$\Delta^2\lambda$	Increment of plastic multiplier for CPPM
$\Delta\mathbf{X}$	Loading vector
κ	Hardening function in the CH model
λ	Compression index in critical state line
λ^c	Non-negative plastic multiplier
μ	Standard deviation in Gauss distribution
$\boldsymbol{\varepsilon}$	Euler strain tensor
ε_q	Deviatoric strain
$\xi(\gamma, \beta)$	Directional density function of homogenization
$\boldsymbol{\Pi}$	First Piola-Kirchhoff stress tensor
ϖ	Dissipation energy increment per unit volume
ρ	Density of granular soils
$\boldsymbol{\sigma}$	Cauchy stress tensor
ϕ	Gibbs free energy per unit volume
ϕ_μ^c	Inter-particle contact friction angle
ϕ_d^c	Dilatancy angle at inter-particle contact
ϕ_p^c	Peak friction angle at inter-particle contact
$\boldsymbol{\chi}^c$	Dissipative force at cth inter-particle contact
Ψ	Helmholtz free energy per unit volume
$w(\alpha)$	Weight coefficient in αth direction
Ω	Integration domain in a unit sphere

ABBREVIATIONS

BBM	Barcelona Basic Model
BXD	Drained biaxial compression test
BXU	Undrained biaxial compression test
CPA	Cutting plane algorithm
CPPPM	Closest point projection method
DEM	Discrete Element Method
FEM	Finite element method
REV	Representative element volume
RTOL	Tolerance for mixed control, set to be 10^{-3}
TOL_1	Tolerance of yield criterion at inter-particle contacts, set as 10^{-7}
TOL_2	Tolerance of residual plastic displacement for CPPM, set as 10^{-2}
TXD	Drained triaxial compression test
TXU	Undrained triaxial compression test
UFTOL	Tolerance of out-of-balance force for micro-macro iteration, set as 10^{-3}-10^{-6}

GENERAL INTRODUCTION

1. Motivation

Granular materials consist of solid particles with interparticle voids that can be fully or partially filled with fluids. The mechanical behaviour of granular materials is important in many branches of engineering and science, such as in pharmaceutical industry, agriculture, energy, and geotechnical and geophysical applications. Granular soils from clay to rockfill materials (with increasing of grain size) are very typical granular materials and construction fills in engineering practice. Although many efforts have been made to improve our understanding of the behaviour of granular soils, developing more physical and practical methods of geotechnical design is still an open issue.

Based upon continuum mechanics, the finite element method (FEM) has been widely used to solve geotechnical problems, in which constitutive models are required to represent the behaviour of granular soils. Generally, these models are developed based upon classical continuum mechanics using the concept of representative element volume (REV) and some assumptions, such as the critical state theory and/or the dilatancy theory (Rowe, 1962; Schofield and Wroth, 1968). Due to the complexities of granular soils including pressure dependent modulus, loading path dependency, and induced fabric anisotropy *etc*., many *ad hoc* parameters are required to reproduce the behaviour of granular soils by constitutive models at the macro scale. In this phenomenological modelling, constitutive equations are proposed rather for mathematical fitting than with physics insight.

To circumvent the shortcomings of constitutive models based on continuum mechanics, the discrete element method (DEM) has been used and, in some cases, combined with FEM to solve boundary value problems. In this approach, DEM samples were used to serve as the Gauss integration points in FEM. The applicability of the FEM×DEM approach was well demonstrated by Zhao and Guo (2014), Nguyen *et al.* (2017), *etc*. However, the experimental data on particle properties and on their contacts are difficult to obtain precisely. Hence, this method can be only qualitatively used for engineering problems. In addition, the demand of

computational cost is still an unsolved problem; consequently, the number of particles in one Gauss integration point is very limited even though parallel computing techniques have been used.

Given the limitations of the phenomenological models and the huge computational cost of DEM, constitutive models based on micromechanics have been developed. In this approach, the stress-strain relations are obtained by defining interparticle contact laws and averaging the local variables to obtain the global ones with homogenization techniques. Micromechanical models have proved their efficiency in describing the behaviour of granular soils under various loading conditions with few parameters with physical meanings (Chang and Hicher, 2005; Yin and Chang, 2009; Nicot and Darve, 2005, 2011; Xiong *et al*., 2017).

From an energy perspective, the thermodynamic principles lead to a generally accepted framework. However, many heuristic models, including the original Cam-Clay model (Schofield and Wroth, 1968), do not satisfy this theory, so one may raise the question: do the micromechanical models satisfy the first and the second laws of the thermodynamic principles? If not, how to construct a thermodynamically consistent micromechanical model? For practical purposes, the micromechanical models should be accurately integrated into a finite element code to analyse boundary value problems. In particular, it is of interest to demonstrate that this numerical method can be widely used in geotechnical engineering practice.

2. Objectives

The overall objective of this thesis is to develop a multiscale approach to describe the behaviour of granular soils in order to solve geotechnical problems. For this purpose, the thesis will focus on the following specific objectives:

First, since the thermodynamic principles represent the general physical laws, it is important to develop the techniques of thermodynamics with internal variables (Houlsby and Puzrin, 2007) for constructing micromechanical models. In doing so, the micromechanical models for granular soils are natural outcomes of both physical and energy conservation models.

Thermomechanical formulations for constructing micromechanical models for dry and partially saturated granular soils can then be derived and serve as theoretical bases for constructing thermodynamically constrained micromechanical models.

Additionally, numerical techniques for integrating the developed micromechanical models to solve boundary value problems will be discussed and demonstrated. Numerical integration schemes will be proposed to accurately integrate micromechanical models. As an example, the CH model (Chang and Hicher, 2005) will be implemented into a finite element code to fulfil multiscale modelling of geotechnical problems. With this approach, the extent of grain scale instability to granular assembly failure will be investigated. Furthermore, this method will be used to solve some classical geotechnical problems at small and large deformations.

3. Outline of the thesis

This thesis elaborates the objectives presented above in the following chapters:

Chapter 1 reviews the basic theories of micromechanics of granular materials, the developed micromechanical models, and the development of multiscale approaches in geotechnical engineering.

Chapter 2 answers the question: how to construct a thermodynamically consistent micromechanical model for dry granular materials. Thermodynamics with internal variables has been extended to the multiscale approach, based on which a micromechanical model for dry granular soils has been constructed.

Chapter 3 develops the thermomechanical multiscale modelling approach to partially saturated granular soils. A micromechanical model for unsaturated granular soils based on the proposed framework has been constructed.

Chapter 4 focuses on the implicit integration of the micromechanical models based on the static hypothesis through three levels of integration algorithms. The CH model has been selected as an example to be accurately integrated and has been implemented into an implicit finite element code for multiscale modelling of boundary value problems.

Chapter 5 introduces the capability of the CH model in describing the instability of granular assemblies. Consistent relations for the second-order work at the micro scale, the material point scale and the engineering scale have been obtained. With this method, localised and diffuse failures of granular assemblies have been analysed.

Chapter 6 presents the applications of the CH model in solving geotechnical problems at small and large deformations. Four examples, including a square footing, the excavation of a tunnel, a retaining wall and the installation of a closed-ended displacement pile, have been analysed with an explicit finite element method to demonstrate that micromechanical models can be applied successfully to geotechnical engineering.

Finally, a general conclusion summarizes the work presented in this thesis and discusses potential directions for future development.

CHAPTER 1 MULTISCALE MODELLING OF GRANULAR MATERIALS

1.1 Introduction

Granular materials are composed of a large number of grains and voids. To describe the behaviour of granular materials, heuristic models have been constructed based upon classical continuum mechanics (Kolymbas, 2012). In this kind of phenomenological modelling approach, many *ad hoc* parameters need to be calibrated in order to simulate the complex behaviour of granular materials under a wide range of loading conditions. In comparison, the multiscale modelling approach regards granular materials as assemblies of discrete grains and voids (Chang and Hicher, 2005; Yin and Chang, 2009; Nicot and Darve, 2005, 2011; Radjai *et al*., 2017), and thus accounts for more physics. Correspondingly, inter-particle contact laws have to be defined and localization and averaging operators need to be given, as shown in Figure 1.1 (Cambou *et al*., 2009, 2016). This chapter begins with recent developments of micromechanics in granular materials, in which the elastic and plastic contact laws, relations between micro-macro variables and the techniques used to construct multiscale models will be discussed. After that, attention is paid to constitutive relations developed on the basis of micromechanics of granular materials. Finally, the multiscale modelling approaches that have been used in solving geotechnical problems will be discussed.

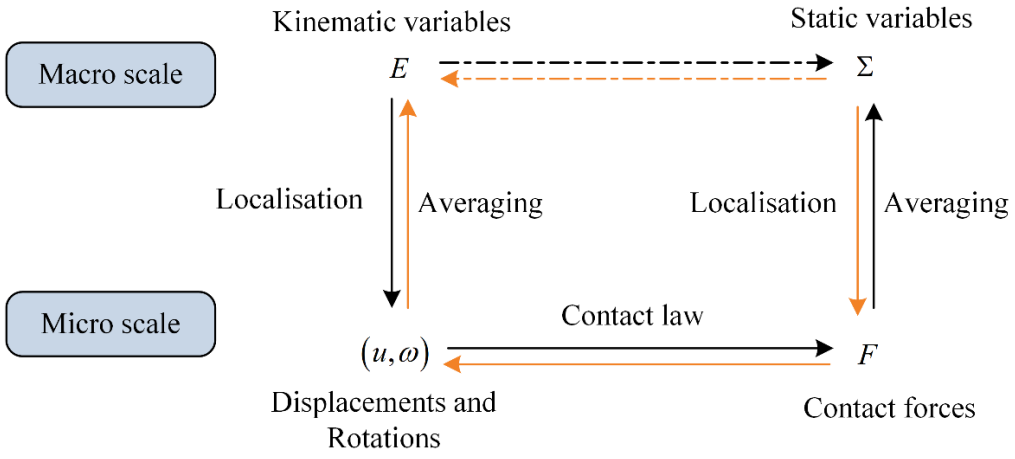

Figure 1.1 General framework of multiscale approach in granular materials (figure from Cambou *et al*., 2009)

1.2 Micromechanics of granular materials

1.2.1 Interparticle contact laws

The relations between two contacting particles depend on the characteristics of grains, such as stiffness and geometry. In terms of the grain stiffness, hard grains are such that deformation of the grain itself can be negligible, while soft grains can be deformed with or without time dependency. The geometry of the grain greatly affects the frictional behaviour between particle contacts. Therefore, different interparticle contact laws should be defined for different kinds of granular materials. Among these relations, elastic and plastic local relations for spherical grains have been widely adopted.

1) Elasticity

The expression of the stiffness between two contacting particles due to normal and shear forces can be dated back to Hertz and Mindlin (Mindlin and Deresiewicz, 1953), who considered two contacting elastic bodies as two rigid bodies connected by deformable springs. These springs are distributed in the normal direction to represent normal forces and in the tangential direction to describe shearing forces. For simplicity, the two springs are generally considered as uncoupled from each other. The normal stiffness depends on the normal force and the properties of grains, given as

$$k_n^c = C_1 \left(f_n^c \right)^{\alpha} \tag{1.1}$$

where C_1 and α are material parameters, f_n^c is the interparticle contact normal force. A general expression for shear stiffness was suggested as

$$k_r^c = C_2 k_n^c \left(1 - \frac{f_r^c}{f_n^c \tan \phi_\mu^c} \right)^{\beta} \tag{1.2}$$

where C_2 and β are material constants, f_r^c is the interparticle contact shear force and ϕ_μ^c is the friction angle between grains.

Revised forms of Eqs. (1.1) and (1.2) have been widely adopted in literature. In DEM simulations as well as in the micromechanical models constructed by Nicot and Darve (2005,

2011), the normal and tangential stiffness are material constants. In comparison, Chang and Hicher (2005) adopted spherical particles to describe granular soils, in which the revised stiffness was adopted

$$k_n^c = k_{n0}^c \left(\frac{f_n^c}{G_g l^2} \right)^\alpha , \; k_r^c = k_{r0}^c \left(\frac{f_n^c}{G_g l^2} \right)^\alpha \tag{1.3}$$

where G_g is the elastic modulus of particles and l is the branch length of two contacting particles, while the reference normal stiffness k_{n0}^c is given by

$$k_{n0}^c = G_g \frac{d}{2} \left(\frac{\sqrt{12}}{1-v_g} \right)^{2/3} \tag{1.4}$$

in which d is the particle diameter and v_g being the Poisson's ratio of the grains.

2) Plasticity

A Coulomb type plastic criterion has been extensively adopted to represent the frictional behaviour of granular materials. A general formulation of this type of criterion can be expressed as

$$F\left(f_i^c, \kappa \right) = \sqrt{\left(f_s^c \right)^2 + \left(f_t^c \right)^2} - f_n^c \kappa \left(\delta_i^c \right) \tag{1.5}$$

in which κ is a function of the interparticle displacement δ_i^c. If κ is a constant then Eq. (1.5) reduces to be a pure plastic function, which has been generally applied in DEM simulations (Cundall and Strack, 1979), in the μ-D model (Nicot and Darve, 2005) and in the H-model (Nicot and Darve, 2011), see also section 1.3. By comparison, the CH model (Chang and Hicher, 2005) and its developing models consider displacement hardening yield criteria for sand, clay and other cohesive granular materials, which will be addressed in detail in section 1.3. Note that for clay, a second compression type plastic criterion is needed (Yin and Chang, 2009; Yin *et al*., 2009, 2010, 2011, 2013, 2014).

1.2.2 Strain tensors

In classical continuum mechanics, many definitions of a strain tensor can be found in the literature, such as the left or right Cauchy-Green strain tensor, Piola deformation tensor,

Green-Lagrange strain tensor, Euler-Almansi strain tensor *etc*. (Bagi, 2006; Cambou *et al*., 2009, 2016). These tensors are expressed in terms of the translation gradient tensor. In micromechanics of granular materials, strain tensors are defined based on the granular assemblies which can be viewed as a REV. The global deformation of the assembly originates from displacements and rotations of particles. With these micromechanics-based strain tensors, discrete element simulation results can be explained and micromechanical models can be constructed. There are many ways to define strain tensors in terms of the interparticle displacements. Among them, most of the strain tensors were defined based on an equivalent continuum and a best-fit method (Bagi, 2006).

1) Strains based on an equivalent continuum

In these approaches, the granular assembly is replaced by a continuous field through a suitable translation field, which assigns the displacements of particle centres to the equivalent continuum. Strain tensors defined along this line can be found in the work of Bagi (1993, 1996), Kruyt and Rothenburg (1996), Kuhn (1997, 1999), Cambou *et al*. (2000) and Kruyt (2003).

2) Strains defined from the best-fit methods

In these methods, the deviations between the theoretical displacement field and the actual displacement field should be minimum, hence the obtained displacement field is the best-fit of the actual displacement field. The difference between the strain tensors lies in the consideration of the local displacement field (Bagi, 2006; Cambou *et al*., 2016). For instance, the displacement of the centres of neighbouring grains was adopted in Cundall and Strack (1979). In contrast the relative displacement at the interparticle contacts was used in Liao *et al*. (1997), whereas the relative displacement of the centres of neighbouring particles was calculated in Cambou (2000).

In this thesis, only the strain tensor conforming to the best-fit type proposed by Liao *et al.* (1997) will be presented, since it will be used as an assumption in the following chapters. In micromechanics of granular materials, if each particle would move exactly according to a

uniform translation gradient ε_{ij}, then the deformation at contact c would be

$$d\delta_i^c = \varepsilon_{ji} l_j^c \tag{1.6}$$

Since the displacement fields of granular materials are strongly heterogeneous, for a general ε_{ij} we would find that

$$d\delta_i^c - \varepsilon_{ji} l_j^c \neq 0 \tag{1.7}$$

To find a strain tensor ε_{ij} which is closer to the actual displacement field, the square sum of the deviations in Eq. (1.7) should be the smallest, that is to say

$$Z = \sum_{c=1}^{N} \left(d\delta_i^c - \varepsilon_{ji} l_j^c \right) \left(d\delta_i^c - \varepsilon_{ji} l_j^c \right) \to \min \tag{1.8}$$

The condition for minimum of Z can be obtained when

$$\frac{\partial Z}{\partial \varepsilon_{kl}} = 0 \tag{1.9}$$

Solving Eq.(1.9) leads to

$$\left(\sum_{c=1}^{N} l_n^c l_m^c \right) \varepsilon_{ni} = \sum_{c=1}^{N} d\delta_i^c l_m^c \tag{1.10}$$

in which n, m and i can be 1, 2 or 3. Defining a fabric tensor as

$$A_{nm} = \left(\frac{1}{V} \sum_{c=1}^{N} l_n^c l_m^c \right)^{-1} \tag{1.11}$$

and combining Eqs. (1.10) and (1.11), the strain tensor proposed by Liao *et al*. (1997) can be obtained

$$\varepsilon_{ni} = \left(\frac{1}{V} \sum_{c=1}^{N} d\delta_i^c l_m^c \right) A_{nm} \tag{1.12}$$

which states that the strain of a granular assembly is the volumetric summation of interparticle displacements with branch vectors and connection with fabric tensor.

1.2.3 Effective stress tensors

Instead of the total stress tensor, effective stress tensors have been widely used in granular

materials, in particularly in soil mechanics. For dry and fully saturated granular materials, the relation between total stress σ_{ij}^{total} and effective stress σ_{ij}' can be generally written as

$$\sigma_{ij}^{total} = \sigma_{ij}' + \chi p_w \tag{1.13}$$

where p_w is the fluid pressure in fully saturated condition; $\chi = 0$ for dry state and $\chi = 1$ for the saturated condition. In both cases, the effective stress σ_{ij}' has been well established in micromechanics of granular materials, which is equal to the so-called contact stress tensor σ_{ij} given by interparticle contact force and branch vector connecting two contact particles. This formulation is also termed as the Love-Weber formula (Love, 1927; Weber, 1966), given as

$$\sigma_{ij} = \frac{1}{V}\sum_{c=1}^{N} f_i^c l_j^c \tag{1.14}$$

in which f_i^c is the force at interparticle contacts.

For partially saturated granular materials, the difficulty in using Eq.(1.13) lies in quantifying the coefficient χ. On one hand, it has been found that the parameter χ could not be generally expressed via a function of the degree of saturation, particularly under drying-wetting cyclic loadings (Gens *et al*., 2006). On the other hand, efforts also have been made to give the definition of the effective stress σ_{ij}'. From recent results obtained by discrete element simulations, it seems that the Love-Weber formula could not be generally used as an effective stress tensor for unsaturated granular materials. This issue is a focal topic for researchers with interests in partially saturated granular materials (Duriez and Wan, 2016; Chalak *et al*., 2017).

1.2.4 Fabric tensors

To describe the internal structure of granular materials, fabric tensors have been introduced. Generally, the geometrical information on granular particles and their spatial arrangement can be described by a second-rank tensor. Various definitions of the fabric tensor have been proposed (Satake, 1982; Oda e*t al*., 1985; Santamarina and Cascante, 1996; Kuganenthira *et al*., 1996; Pan and Dong, 1999; Li and Li, 2009; Fu and Dafalias, 2015). These tensors can be

classified as contact normal-based, particle orientation-based and void-based tensors (Wang *et al*., 2017). The former two types of tensors can be generally expressed as

$$\mathbf{F} = \frac{1}{2N}\sum_{k=1}^{N} \mathbf{v}^k \otimes \mathbf{v}^k \tag{1.15}$$

where N is the number of the entities being quantified; the superscript k is the kth entity; $\mathbf{v}^k$ is the directional entity which could be the unit contact normal or the unit particle orientation vector. The void-based fabric tensor was initially proposed by Li and Li (2009) and then developed by Fu and Dafalias (2015) for two-dimensional assemblies. The fabric tensor based on void cell system suggested by Li and Li (2009) can be written as

$$\mathbf{F}_v = \frac{E_0}{N_v}\sum_{k=1}^{N_v} v^k \mathbf{n}^k \otimes \mathbf{n}^k \Big/ E_v\left(\mathbf{n}^k\right) \tag{1.16}$$

where v^k is the length of the kth void vector whose direction is $\mathbf{n}^k$; $E_v\left(\mathbf{n}^k\right)$ is the directional distribution of the void vector density; N_v is the total number of void vectors; E_0 is a normalization factor which can be derived from the statistics theory (Kanatani, 1984; Li and Yu, 2011) and is equal to 2π in 2D space and 4π in 3D space. From these definitions, we can see that the fabric tensor defined in Eq.(1.11) is a revised form of the contact-based fabric tensor and satisfies the unit volume requirement of the thermodynamically consistent fabric tensor (Li and Dafalias, 2015).

Fabric tensors can be decomposed into an isotropic part and a deviatoric part. An isotropic material indicates that the same material response can be obtained if the loading direction is rotated. The deviatoric part, also termed as fabric anisotropy, includes inherent anisotropy and induced anisotropy. The former one refers to an initial anisotropy that is caused by previous loadings, such as the inherent anisotropy of granular soils caused by the gravity, while the latter one is induced by the subsequent loadings.

It has been recognized that the non-coaxial behaviour of granular materials under proportional loading and continuous rotational shearing originates from their fabric anisotropy. Therefore, well considering the evolution of fabric anisotropy is crucial for describing the non-coaxial

deformation of granular materials. Discrete element simulations have found that the fabric anisotropy tends to reach a steady state even when the inherent anisotropy is different (Fu and Dafalias, 2011; Kruyt, 2012; Zhao and Guo, 2013; Kruyt and Rothenburg, 2014, 2016; Yang and Wu, 2016). According to these findings, Li and Dafalias (2012) extended the classical critical state theory (Schofield and Wroth, 1968) by involving a fabric item, which also reaches a critical value at the classical critical state. In this framework, constitutive models were constructed to simulate the non-coaxial deformation of granular soils (Li and Dafalias, 2012; Gao *et al*., 2014; Gao and Zhao, 2017).

1.2.5 Averaging and localisation operators

The Love-Weber formula described by Eq. (1.14) has been proved to be a general expression for dry granular materials, it is therefore adopted as an averaging operator for micromechanical models (Chang and Hicher, 2005; Yin and Chang, 2009; Yin *et al*., 2009, 2010, 2011, 2013, 2014; Nicot and Darve, 2005, 2011; Xiong *et al*., 2017).

Two types of localisation operators: the kinematic method and the static hypothesis can be generally found in literature (Chang and Hicher, 2005; Nicot and Darve, 2005, 2011; Yin *et al*., 2009; Misra and Singh, 2014; Misra and Poorsolhjouy, 2015a; Xiong *et al*., 2017). The former one bridges global strains and inter-particle displacements, such as the widely-used expression in Eq.(1.6), based on which micromechanical models were constructed by Nicot and Darve (2005, 2011), Misra and Singh (2014), Xiong *et al*. (2017). The latter one gives inter-particle incremental forces from incremental global stresses, for instance the one adopted by Chang and Hicher (2005), rewritten as

$$\dot{f}_i^c = \dot{\sigma}_{ij} l_n^c A_{jn}, \quad f_i^c = \sigma_{ij} l_n^c A_{jn} \tag{1.17}$$

where A_{jn} is given in Eq. (1.11). Based on Eq. (1.17), a family of micromechanical models has been constructed (Chang and Hicher, 2005; Yin and Chang, 2009; Yin *et al*., 2011, 2013, 2014; Zhao *et al*., 2017).

1.2.6 Homogenisation integration

The summation of local quantities over all interparticle contacts can be approximated by directional statistics theory. This theory was first proposed by Kanatani (1984) for directional orientations represented by unit vectors, and then was extended by Li and Yu (2011) for directional vectors in which both magnitude and direction are of significance. The distribution of both orientations and vectors along all directions can be approximated by a probability density function $f(\mathbf{n})$. The approximation of the function $f(\mathbf{n})$ can be obtained by a smooth function $F(\mathbf{n})$, which can be expressed as a polynomial

$$F(\mathbf{n}) = C + C_i n_i + C_{ij} n_i n_j + C_{ijk} n_i n_j n_k + C_{ijkl} n_i n_j n_k n_l + \cdots \tag{1.18}$$

where $\mathbf{n}$ is a unit vector. The integration of the function $F(\mathbf{n})$ should satisfy

$$\oint_{\Omega} F(\mathbf{n}) d\Omega = 1 \text{ with } F(\mathbf{n}) \geq 0 \tag{1.19}$$

where $d\Omega$ is an elementary solid angle (Figure 1.2) and Ω represents the unit circle in 2D case and the unit sphere in 3D case. Let $\mathbf{n}^{(1)}$, $\mathbf{n}^{(2)}, \cdots$ and $\mathbf{n}^{(N)}$ be unit vectors representing an observed number of N local directional data. An empirical distribution of the contact probability density $f(\mathbf{n})$ is

$$f(\mathbf{n}) = \frac{1}{N} \sum_{c=1}^{N} \delta\left(\mathbf{n} - \mathbf{n}^{(c)}\right) \tag{1.20}$$

where $\delta(*)$ is the Dirac delta function defined as $\delta(*) = \begin{cases} +\infty, & \text{x=0} \\ 0, & \text{x} \neq 0 \end{cases}$, which also satisfies the identity $\int_{-\infty}^{+\infty} \delta(*) d* = 1$. $f(\mathbf{n})$ is nonnegative and automatically satisfies $\oint_{\Omega} f(\mathbf{n}) d\Omega = 1$.

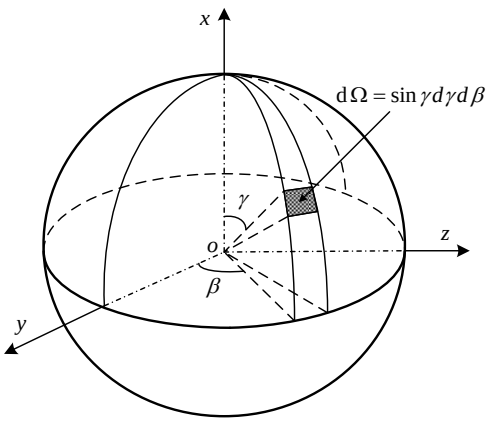

Figure 1.2 Integration domain in a unit sphere

Eq.(1.18) can be approximated using the polynomial function as

$$F(\mathbf{n}) = \frac{1}{E_0} F_{i_1 i_2 \cdots i_n} n_{i_1} n_{i_2} \cdots n_{i_n} = \frac{1}{E_0} \left[1 + D_{i_1 i_2} n_{i_1} n_{i_2} + \cdots + D_{i_1 i_2 \cdots i_n} n_{i_1} n_{i_2} \cdots n_{i_n} + \cdots \right] \tag{1.21}$$

where $E_0 = \oint_{\Omega} d\Omega$, which is equal to 2π in 2D space and 4π in 3D space; the tensor coefficients $F_{i_1 i_2 \cdots i_n}$ and $D_{i_1 i_2 \cdots i_n}$ can be determined by minimizing the least square error

$$E = \oint_{\Omega} \left[F(\mathbf{n}) - f(\mathbf{n}) \right]^2 d\mathbf{n} \to \min \tag{1.22}$$

The most fundamental quantities of these directional data are their average values. The average of the *n*th order tensor product, also termed as the moment tensor of order *n* is given as

$$N_{i_1 i_2 \cdots i_n} = \left\langle n_{i_1} n_{i_2} \cdots n_{i_n} \right\rangle = \frac{1}{N} \sum_{c=1}^{N} n_{i_1}^c n_{i_2}^c \cdots n_{i_n}^c = \oint_{\Omega} F(\mathbf{n}) n_{i_1} n_{i_2} \cdots n_{i_n} d\mathbf{n} \tag{1.23}$$

The directional tensor $F_{i_1 i_2 \cdots i_n}$ in Eq. (1.21) can be determined by minimizing the least square error criteria

$$\frac{\partial E}{\partial F_{i_1 i_2 \cdots i_n}} = 0 \quad \Rightarrow \oint_{\Omega} F(\mathbf{n}) n_{i_1} n_{i_2} \cdots n_{i_n} d\mathbf{n} = F_{j_1 j_2 \cdots j_n} \overline{n_{j_1} n_{j_2} \cdots n_{j_n} n_{i_1} n_{i_2} \cdots n_{i_n}} = N_{i_1 i_2 \cdots i_n} \tag{1.24}$$

where the identity $\overline{n_{i_1} n_{i_2} \cdots n_{i_n}} = \frac{1}{E_0} \oint_{\Omega} n_{i_1} n_{i_2} \cdots n_{i_n} d\Omega$, which can be explicitly integrated, as expressed by Li and Yu (2011). By substituting the obtained direction tensor $F_{i_1 i_2 \cdots i_n}$ from Eq. (1.24) to Eq. (1.21), we obtain

$$\left(F_{i_1 i_2 \cdots i_n} - D_{i_1 i_2 \cdots i_n} \right) n_{i_1} n_{i_2} \cdots n_{i_n} = F_{i_1 i_2 \cdots i_{n-2}} n_{i_1} n_{i_2} \cdots n_{i_{n-2}} \tag{1.25}$$

The coefficient tensor $D_{i_1 i_2 \cdots i_n}$ can be finally expressed as

$$D_{i_1 i_2 \cdots i_n} = \frac{1}{\alpha_{2n}} \frac{(2n)!}{2^n (n!)^2} \left(N_{i_1 i_2 \cdots i_n} - F_{j_1 j_2 \cdots j_{n-2}} \overline{n_{j_1} n_{j_2} \cdots n_{j_n} n_{i_1} n_{i_2} \cdots n_{i_n}} \right) \tag{1.26}$$

where the coefficient

$$\alpha_{2n}=\begin{cases}\dfrac{{}^{2n}C_n}{2^{2n}}, D=2\\ \dfrac{1}{2n+1}, D=3\end{cases} \tag{1.27}$$

in which ${}^nC_k$ stands for the number of k-combinations of a n-element set. In view of the symmetry in $F_{i_1i_2\cdots i_n}$ and $D_{i_1i_2\cdots i_n}$, their relation can be expressed as

$$F_{i_1i_2\cdots i_n}=D_{i_1i_2\cdots i_n}+F_{i_1i_2\cdots i_{n-2}}\delta_{i_{n-1}i_n} \tag{1.28}$$

For direction-dependent vectors with different magnitudes, Li and Yu (2011) gave the form of approximating the directional representative values as

$$\mathbf{M}(\mathbf{n})=m_0H_{ji_1\cdots i_n}n_{i_1}n_{i_2}\cdots n_{i_n}=m_0\left(G_0n_j+G_{ji_1}n_{i_1}+\cdots+G_{ji_1\cdots i_n}n_{i_1}n_{i_2}\cdots n_{i_n}+\cdots\right) \tag{1.29}$$

in which the direction tensors $H_{ji_1\cdots i_n}$ and $G_{ji_1\cdots i_n}$ can be determined by minimizing the least square error

$$E=\oint_{\Omega}\left[\mathbf{M}(\mathbf{n})-\overline{\mathbf{m}}(\mathbf{n})\right]\cdot\left[\mathbf{M}(\mathbf{n})-\overline{\mathbf{m}}(\mathbf{n})\right]d\Omega\ \rightarrow\min \tag{1.30}$$

where $\overline{\mathbf{m}}(\mathbf{n})$ is the directional distribution of a representative vector. The procedure for solving Eq.(1.30) is the same as for solving Eq.(1.22).

The described directional statistics theory has been widely applied in deriving the stress-force-fabric relations (Rothenburg and Bathurst, 1989; Li and Yu, 2013; He *et al*., 2017; Wang *et al*., 2017), in analysing results of discrete element simulations (Li and Yu, 2011; Li *et al*., 2013; Li, 2016), in experimental and numerical quantification of fabric tensors (Yang *et al*., 2007, 2008; Yang and Wu, 2016; Xie *et al.*, 2017), as well as in constructing micromechanical models (Chang and Hicher, 2005; Yin and Chang, 2009; Nicot and Darve, 2005, 2011; Misra and Singh, 2014, 2015; Misra and Poorsolhjouy, 2015a; Xiong *et al*., 2017; Zhao *et al*., 2017).

1.3 Micromechanical models

A variety of multiscale constitutive relations, also termed as micromechanical models, have been proposed based on micromechanics of granular materials. In this section, several typical micromechanical models will be reviewed. Specific attentions will be paid on the CH model

(Chang and Hicher, 2005) due to its good performance in describing the behaviour of granular soils and it will be a sound basis for the following chapters.

1.3.1 CH model

The CH micromechanical model (Chang and Hicher, 2005) was initially proposed for sand. Further developments by Yin and Chang (2009a, 2009b) and Yin *et al*. (2009, 2010, 2011, 2013, 2014), demonstrated its good performance in modelling the mechanical behaviour of sand and clay.

1.3.1.1 Inter-particle contact law

The local law is defined in the local coordinates (*n, s, t*), in which *n* is the normal to the contact plane, and *s* and *t* are orientations within the contact plane. The relationship between the local and global coordinates can be defined by the angles β and γ, as shown in Figure 1.3, and any local quantity can be expressed globally through the transition matrix, expressed as

$$P=\begin{bmatrix} \cos\gamma & \sin\gamma\cos\beta & \sin\gamma\sin\beta \\ -\sin\gamma & \cos\gamma\cos\beta & \cos\gamma\sin\beta \\ 0 & -\sin\beta & \cos\beta \end{bmatrix}=\begin{bmatrix} n_1 & n_2 & n_3 \\ s_1 & s_2 & s_3 \\ t_1 & t_2 & t_3 \end{bmatrix} \tag{1.31}$$

Soil specimens exhibit elastic and plastic behaviours which originate from the slip and rotation of the grains. Given that these elementary mechanisms control the global mechanical response, elasticity and plasticity are defined at the inter-particle contact.

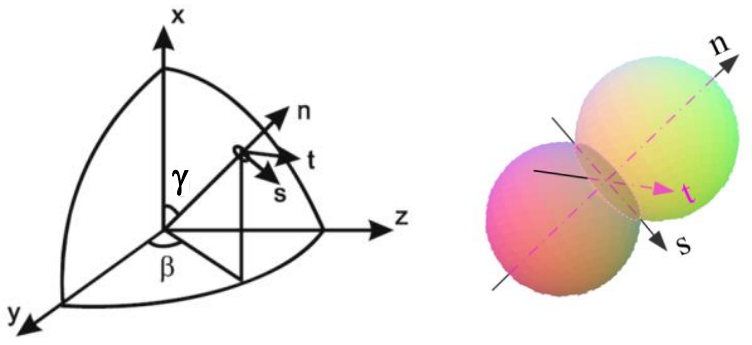

Figure 1.3 Local coordinate (n,s,t) and global coordinate (x,y,z)

1) Elasticity

A non-linear elastic force-displacement relationship has been suggested, with the same

stiffness in directions *s* and *t*, which can be written as

$$\dot{f}_i^c = k_{ij}^c \dot{\delta}_j^c \tag{1.32}$$

The stiffness matrix is given as

$$k_{ij}^c = \begin{bmatrix} k_n^c & 0 & 0 \\ 0 & k_r^c & 0 \\ 0 & 0 & k_r^c \end{bmatrix} \tag{1.33}$$

where the normal stiffness k_n^c depends on the normal force with an initial value k_{n0}^c which can be evaluated by Eq.(1.4), and the tangential stiffness k_r^c is proportional to k_n^c with a ratio k_{rR}, expressed as

$$k_n^c = k_{n0}^c \left(\frac{f_n^c}{f_{ref}} \right)^{1/2}, \; k_r^c = k_{rR} k_n^c \tag{1.34}$$

where f_{ref} is a reference force.

2) *Yield criterion and plastic flow*

To consider irrecoverable displacements between grains during loading, plasticity has been introduced in the local law. A Coulomb-type yield criterion has been adopted, expressed as

$$F\left(f_i^c, \kappa \right) = \sqrt{\left(f_s^c \right)^2 + \left(f_t^c \right)^2} - f_n^c \kappa\left(\delta_r^{cp} \right) \tag{1.35}$$

where the hardening parameter $\kappa\left(\delta_r^{cp} \right)$ is dependent on the tangential plastic displacement δ_r^{cp}, written as

$$\kappa\left(\delta_r^{cp} \right) = \frac{k_p^c \tan\phi_p^c \delta_r^{cp}}{f_n^c \tan\phi_p^c + k_p^c \delta_r^{cp}} \text{ with } \dot{\delta}_r^{cp} = \sqrt{\left(\dot{\delta}_s^{cp} \right)^2 + \left(\dot{\delta}_t^{cp} \right)^2} \tag{1.36}$$

where k_p^c is a function of the normal contact stiffness k_n^c with the ratio k_{pR} as a material constant

$$k_p^c = k_{pR} k_n^c \tag{1.37}$$

ϕ_p^c is the mobilized peak friction angle between particles in contact, function of the inter-particle friction angle ϕ_μ^c and the state variable e_c/e representative of the mesoscale, concordantly with the macro scale relation proposed by Biarez and Hicher (1994)

$$\tan\phi_p^c = \left(\frac{e_c}{e}\right)\tan\phi_\mu^c \tag{1.38}$$

in which e_c is the void ratio at the critical state:

$$e_c = e_{ref} - \lambda \log\left(\frac{p'}{p_{ref}}\right) \tag{1.39}$$

where e_{ref} and p_{ref} are values corresponding to a reference point on the critical state line; λ is the compression index; p' is the mean effective stress.

A local dilatancy law has been defined by the ratio between the normal plastic displacement increment and the tangential plastic displacement increment, which is a function of the dilatancy angle at inter-particle contacts:

$$D = \frac{\dot{\delta}_n^{cp}}{\dot{\delta}_r^{cp}} = \tan\phi_d^c - \frac{\sqrt{\left(f_s^c\right)^2 + \left(f_t^c\right)^2}}{f_n^c} \tag{1.40}$$

where ϕ_d^c depends on the state variable e/e_c and on the inter-particle friction angle

$$\tan\phi_d^c = \left(\frac{e}{e_c}\right)\tan\phi_\mu^c \tag{1.41}$$

1.3.1.2 Micro-macro relationship

Stress and strain can be obtained by volumetrically averaging the inter-particle force and displacement. The CH model has adopted the kinematic relation based on the best-fit hypothesis suggested by Liao *et al*. (1997), expressed by Eq.(1.12). For the relation between force and stress, the Love-Weber formula in Eq.(1.14) has been adopted. The micro-macro relations in Eqs.(1.12) and (1.14) are averaging operators. To integrate the local force-displacement relation, we need to define a localization operator. Based on energy conservation, the relationship between force and stress increments is given by Eq.(1.17). This

expression is denoted as a static hypothesis since the force increment is calculated from the stress increment. This is different from the kinematic hypothesis in which the local displacement is derived from the global strain.

1.3.1.3 Stress-strain relationship

Using the definition of the best-fit hypothesis (Eq.(1.12)) and combining the local law with the static hypothesis (Eq.(1.17)), one can write the incremental stress-strain relationship based on elasticity as

$$\dot{\varepsilon}_{ij} = \frac{1}{V}\sum_{c=1}^{N} \dot{\delta}_i^c l_n^c A_{jn} = \frac{1}{V}\sum_{c=1}^{N} \dot{\sigma}_{ij} l_m^c A_{im} \left(k_{ij}^c\right)^{-1} l_n^c A_{jn} = \dot{\sigma}_{ij}\left(\frac{1}{V}\sum_{c=1}^{N}\left(k_{ij}^c\right)^{-1} l_m^c l_n^c A_{im} A_{jn}\right) \tag{1.42}$$

from which the elastic compliance matrix S_{ijkl} can be expressed as

$$S_{ijkl} = \frac{1}{V}\sum_{c=1}^{N}\left(k_{ij}^c\right)^{-1} l_m^c l_n^c A_{km} A_{ln} \tag{1.43}$$

It should be mentioned that Eq.(1.43) is expressed in the local coordinates (*n, s, t*). The global stiffness matrix can be obtained by using Eq.(1.31). If plastic displacement occurs, the local elastic stiffness has to be replaced by a local elastoplastic stiffness. A predictor-corrector procedure is then needed to integrate the non-linear stress-strain relationship, which will be discussed in chapter 4.

1.3.1.4 Homogenisation integration

To obtain the stress-strain relation, it is necessary to sum up the local variables over all particle contacts. Based on the aforementioned statistics theory proposed by Kanatani (1984), Chang and Misra (1990) applied the statistical theory for calculating the summation of $\sum_{c}^{N} F^c$, based on the Eqs.(1.19) and (1.23), the integration can be calculated by

$$\frac{1}{N}\sum_{c=1}^{N} F^c = \int_0^{2\pi}\int_0^{\pi} F(\gamma,\beta)\xi(\gamma,\beta)\sin\gamma d\gamma d\beta \tag{1.44}$$

where F^c is the quantity defined between interparticle contact; N is the total number of inter-particle contacts. The directional distribution density function $\xi(\gamma, \beta)$ satisfies

$$1=\int_0^{2\pi}\int_0^{\pi}\xi(\gamma,\beta)\sin\gamma d\gamma d\beta \tag{1.45}$$

To integrate the random granular packing, we can write the directional distribution density function as a spherical harmonics expansion

$$\xi(\gamma,\beta)=\frac{1}{4\pi}\left\{1+\sum_{k=2}^{\infty}\left[a_{k0}P_k(\cos\gamma)+\sum_{m=1}^{k}P_k^m\left(\cos\gamma\left(a_{km}\cos m\beta+b_{km}\sin m\beta\right)\right)\right]\right\} \tag{1.46}$$

where $P_k(\cos\gamma)$ is the kth Legendre polynomial; $P_k^m(\cos\gamma)$ is the associated Legendre function; a_{k0}, a_{km} and b_{km} are fabric parameters. For an isotropic packing, these fabric parameters are equal to zero, therefore the density function can be written as

$$\xi(\gamma,\beta)=\frac{1}{4\pi} \tag{1.47}$$

To calculate the integration of the right-hand side of Eq.(1.44), we can adopt the Gauss integration method proposed by Bažant and Oh (1986), in which the integration of the function $u(x,y,z)$ over a unit sphere can be calculated as

$$\frac{1}{4\pi}\int_{S^2}u(x,y,z)ds=\frac{1}{4\pi}\int_0^{2\pi}\int_0^{\pi}u(x,y,z)\sin\gamma d\gamma d\beta=\sum_{\alpha=1}^{NP}u(x,y,z)w(\alpha) \tag{1.48}$$

where *NP* is the number of integration points, as shown in Figure 1.4. By combining Eqs.(1.44) and (1.48), and by considering an isotropic fabric packing, we obtain

$$\frac{1}{N}\sum_{c=1}^{N}F^c=\frac{1}{4\pi}\int_0^{2\pi}\int_0^{\pi}F(\gamma,\beta)\sin\gamma d\gamma d\beta=\sum_{\alpha=1}^{NP}F(\alpha)w(\alpha) \tag{1.49}$$

The volumetric average of the micro variables can be calculated by

$$\frac{1}{V}\sum_{c=1}^{N}F^c=\frac{N}{V}\sum_{\alpha=1}^{NP}F(\alpha)w(\alpha) \tag{1.50}$$

in which *V* is the volume of the assembly and *N* is the number of inter-particle contacts. The number of contacts per unit volume *N*/*V* for a packing of spheres can be estimated from the void ratio, the coordination number and the particle size (Chang *et al.*, 1990)

$$\frac{N}{V}=\frac{3C_n}{4\pi r^3(1+e)} \tag{1.51}$$

Based on the experimental data, the relationship between the void ratio e and the

coordination number C_n can be approximated by

$$C_n = 13.28 - 8e \tag{1.52}$$

where e is the void ratio of granular assembly.

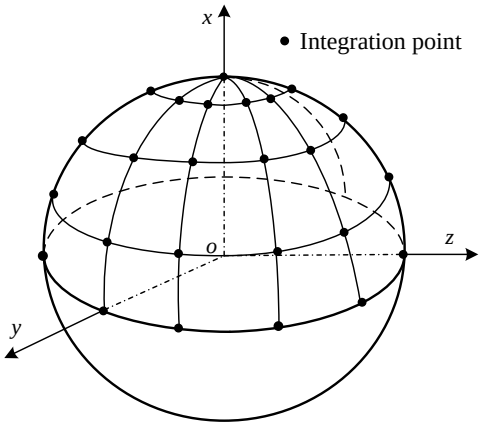

Figure 1.4 A distribution of integration points in half space of a unit sphere

Chang and Hicher (2005) investigated the influences of the number of integration points on the stress-strain relations and found that 74 integration points, as proposed by Bažant and Oh (1986), were sufficient to obtain accurate results. As shown in Figure 1.5, the CH model can well describe the behaviour of Toyoura sand with different initial void ratios under a wide range of confining pressures.

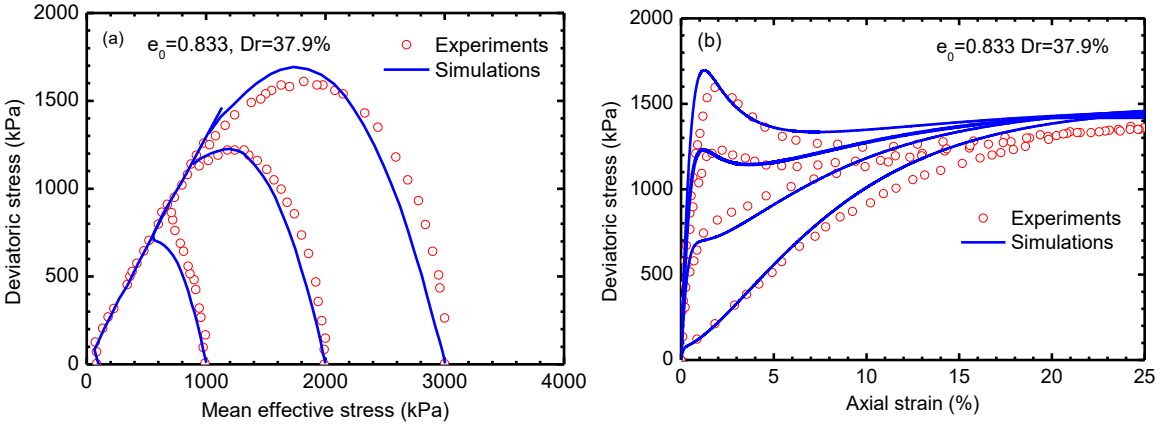

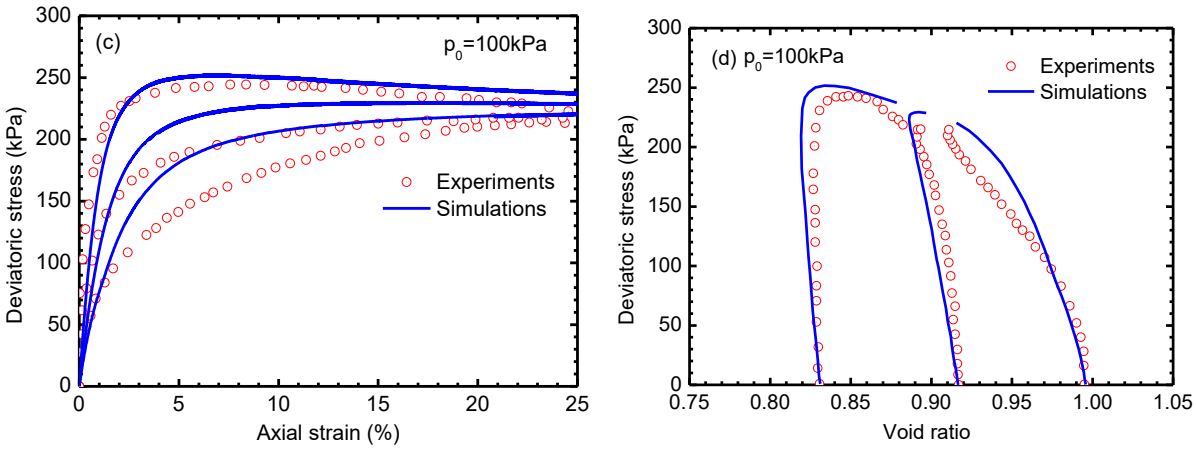

Figure 1.5 Experimental data and simulations of triaxial tests on Toyoura sand: (a) deviatoric stress versus mean effective stress for loose sand under undrained condition; (b) deviatoric stress versus axial strain for loose sand under undrained condition; (c) deviatoric stress versus axial strain for dense sand under drained condition; (d) deviatoric stress versus void ratio for dense sand under drained condition (figure from Chang *et al*., 2011)

1.3.2 Models developed based on the CH model

The CH micromechanical model has been further developed to describe the behaviour of unsaturated granular soils (Hicher and Chang, 2007), the behaviour of clays (Chang *et al*., 2009; Chang and Yin, 2010, 2011) and the effect of inherent anisotropy of sands and clays (Yin and Chang, 2009, 2010, 2011, 2013; Chang and Bennett, 2015). Generally, four kinds of contact laws that depend on the properties of particle contacts have been suggested. For saturated sand and clay, only mechanical forces were considered between the inter-particle contacts (Chang and Hicher, 2005; Chang and Hicher, 2009; Chang and Yin, 2009a, 2009b; Yin and Chang, 2009, 2010, 2011, 2013; Chang and Bennett, 2015); for unsaturated soils, both capillary forces and mechanical forces were considered (Hicher and Chang, 2007; Hicher and Chang, 2008); for cohesive soils, the chemical forces and mechanical forces are the main forces (Hicher *et al*., 2008a, 2008b; Hattab and Chang, 2015), while for lunar soils, the surface energy forces that include van der Waals forces, as well as the mechanical forces, were taken into account (Chang and Hicher, 2009).

1) Mechanical force in clayey materials

The same nonlinear elasticity that has been used for sand is adopted, while for plasticity two yield criteria are used: one for shear loading and another one for compression, as shown in Figure 1.6. The form of shearing yield criterion $F_1(f_i, \kappa_1)$ is the same with sand, as shown by the following equations

$$F_1(f_i^c, \kappa_1) = \sqrt{\left(f_s^c\right)^2 + \left(f_t^c\right)^2} - f_n^c \kappa_1(\delta_r^{cp}) \tag{1.53}$$

$$\kappa_1(\delta_r^{cp}) = \frac{k_p^c \tan\phi_p^c \delta_r^{cp}}{f_n^c \tan\phi_p^c + k_p^c \delta_r^{cp}} \tag{1.54}$$

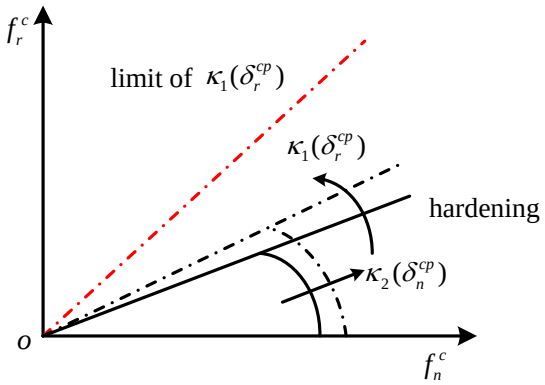

Figure 1.6 Hardening rule for clay in the CH model

A local dilatancy D_1 is defined by normal plastic displacement increment divided by tangential plastic displacement increment, which is a function of friction angle, state variable e_c/e and current force ratio $\tan\phi_m^c$, written as

$$D_1 = \frac{\dot{\delta}_n^{cp}}{\dot{\delta}_r^{cp}} = b\left(\frac{\tan\phi_m^c}{\tan\phi_\mu^c} - 1\right)\left(\frac{\tan\phi_m^c}{\tan\phi_\mu^c}\right)^a \left(1 - \frac{e}{e_c}\right) \tag{1.55}$$

$$\tan\phi_m^c = \frac{\sqrt{\left(f_s^c\right)^2 + \left(f_t^c\right)^2}}{f_n^c} \tag{1.56}$$

in which, *a* and *b* are material constants, state variable e_c/e is defined as previous Eq.(1.39).

Given that clays exhibit distinct deformation under the compression with constant stress ratio, a cap yield criterion is introduced, which depends on normal force and normal displacement

$$F_2(f_i^c, \kappa_2) = f_n^c - \kappa_2(\delta_n^{cp}) \tag{1.57}$$

$$\kappa_2(\delta_n^{cp}) = f_{ref} \cdot 10^{\delta_n^{cp}/C_p} \tag{1.58}$$

in which C_p. is a material constant that can be calibrated from the compression curve plotted in $\delta_n^{cp} - \log\left(f_n^c\right)$ plane. For the case of f_n^c smaller than f_{ref}, only elasticity takes place.

2) Capillary force

To simulate the behaviour of partially saturated granular materials, capillary forces were introduced between interparticle contacts (Hicher and Chang, 2007), which can be expressed as

$$f_n^{cap} = f_{\max} \exp\left(-c\frac{d}{R}\right) \tag{1.59}$$

where c is a material constant, d is the distance between two grains that are not necessarily in contact, R is the mean grain radius, $f_{\max}$ is the value of the capillary force at contact, given by

$$\begin{cases} f_{\max} = f_0 \dfrac{S_r}{S_0} & \text{for } 0 < S_r < S_0 \\ f_{\max} = f_0 \dfrac{S_0(1-S_r)}{S_r(1-S_0)} & \text{for } S_0 < S_r < 1 \end{cases} \tag{1.60}$$

where S_r is the degree of saturation; f_0 and S_0 are material constants. f_0 can be evaluated from the particle size distribution curve. An empirical expression proposed by Wu *et al*. (1984) was adopted to obtain the value of S_0, given as

$$S_0 = \left(-0.62\log\left(d_{10}\right) + 1.5\right)/100 \tag{1.61}$$

where d_{10} is the effective grain size in mm.

3) Chemical force in grouted sand

Adhesive forces were added at interparticle contacts to consider the effect of cement grout in the pores of granular materials by Hicher *et al*. (2008). A damage law was introduced to consider the amplitude of chemical force, expressed as

$$f_{ad} = f_{ad}^0 \exp\left(-\eta_b\left(\rho - \delta_b\right)\right) \text{ for } \rho > \delta_b \tag{1.62}$$

where f_{ad}^{0} is the initial adhesive force, η_b is a parameter which controls the degree of damage, ρ is a function of displacements, given by

$$\rho = \sqrt{\left(\beta\delta_n^{ct}\right)^2 + \left(\delta_r^c\right)^2} \tag{1.63}$$

in which δ_n^{ct} represents the normal interparticle displacement in elongation, δ_r^c is the tangential displacement, and β is a material parameter.

4) Surface energy force

To investigate the behaviour of lunar soils, the van der Waals force was considered between two particles in contact by Chang and Hicher (2009), written as

$$f_{suf}^{c} = \frac{A}{6D^3}a^2 + \frac{AR}{12D^2} \tag{1.64}$$

where A is the Hamaker coefficient which was estimated to be 4.3×10^{-20}J for lunar soils and 1.5×10^{-20}J for terrestrial quartz sand. D represents the thickness of the molecules layer between two particles and R is the mean radius of the particles.

By using the above four kinds of interparticle contact forces and the procedure described in the CH model, the behaviour of various granular materials under specific environment has been well described.

1.3.3 μ-D model

Different from the aforementioned CH model, the *μ-D* model (Nicot and Darve, 2005) adopts the strain tensor, Eq.(1.6), as a localization operator. The scheme of the *μ-D* model is shown in Figure 1.7. In this approach, the strain-displacement in Eq.(1.6) has been used as the localization operator, while the Love-weber formula described in Eq.(1.14) has been taken as the averaging operator. An elastic purely plastic relation was given as the interparticle force-displacement relation, as shown in Eq.(1.5), which can be rewritten as

$$\dot{f}_n^c = k_n^c\dot{\delta}_n^c \tag{1.65}$$

$$\dot{f}_r^c = \min\left\{\left\| f_r^c + k_n^c\dot{\delta}_r^c\right\|, \tan\left(f_n^c + k_n^c\dot{\delta}_n^c\right)\right\}\frac{f_r^c + k_n^c\dot{\delta}_r^c}{\left\| f_r^c + k_n^c\dot{\delta}_r^c\right\|} - f_r^c \tag{1.66}$$

where k_n^c is the normal stiffness, k_r^c is the tangential stiffness. For the integration scheme, the density function is equal to 1/4π thus only an isotropic fabric condition was considered in this model. A total of three parameters, k_n^c, k_r^c and φ_g, with physical meanings need to be calibrated.

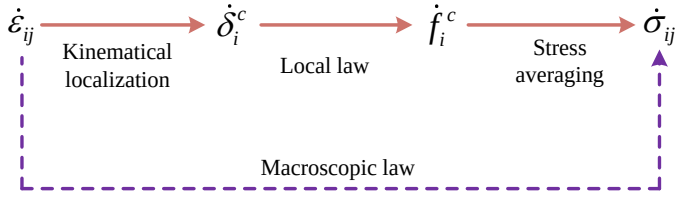

Figure 1.7 Scheme of the μ-D model based on a kinematic hypothesis

This model has demonstrated its efficiency in describing the behaviour of dry granular materials. However, as discussed by Nicot and Darve (2011), due to the choice of the kinematic assumption expressed in Eq.(1.6), the model could not correctly simulate the mechanical response of a granular specimen along a drained triaxial loading path (Figure 1.8). To improve the performance of this model, an adaptation was incorporated, by removing all contacts oriented along the directions within a cone, characterized by an *ad hoc* parameter θ_e. Alternatively, a meso-scale structure was introduced to enrich the relation between strain and inter-particle displacement (Nicot and Darve, 2011; Xiong *et al*., 2017).

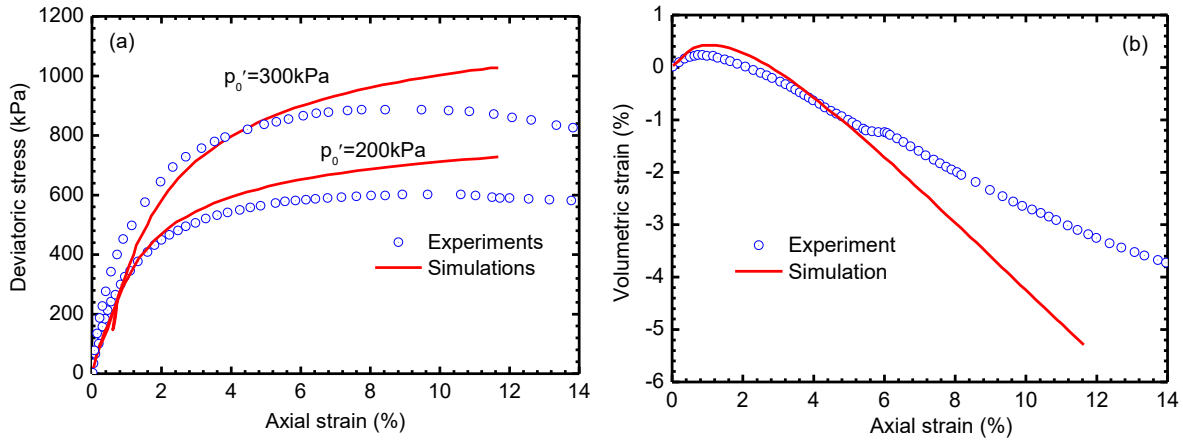

Figure 1.8 Validation stage along an axisymmetric drained triaxial loading path

1.3.4 H model

A hexagonal cluster was introduced to consider the mesoscale of granular material in the *μ-D* model, which was referred to as H model (Nicot and Darve, 2011). The H model shows a good performance in describing the typical behaviour of granular materials, as demonstrated by Nicot and Darve (2011) in a two-dimensional version and by Xiong *et al*. (2017) in a three-dimensional description, shown in Figure 1.9.

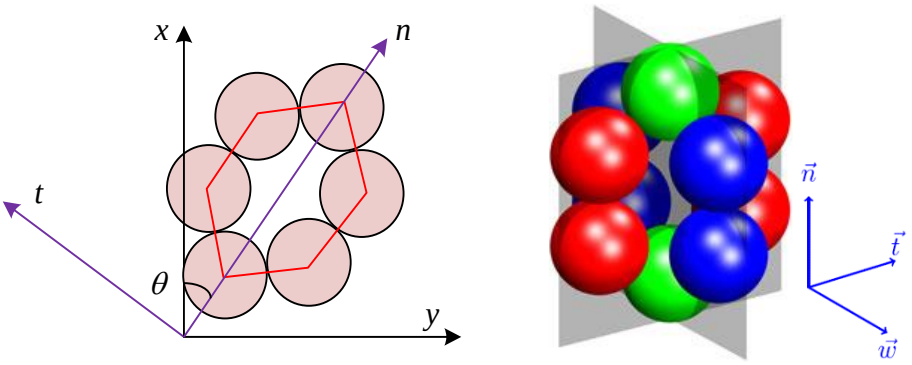

Figure 1.9 Hexagonal set of contacting particles (a) 2D; (b) 3D

To construct the H model, two levels of compatible equations should be considered. The deformation of each hexagon derived from global strain is given as

$$\delta l_n = -l_n \delta\varepsilon_{ij} n_i n_j \tag{1.67}$$

$$\delta l_t = -l_t \delta\varepsilon_{ij} t_i t_j \tag{1.68}$$

where l_n and l_t are dimensions of the hexagon along the direction n and t, as shown in Figure 1.9. To describe the relation between the meso-scale and the micro-scale, two kinds of interparticle contacts are considered. As shown in Figure 1.10, there are both normal and shear forces between particles 1 and 2, whereas only normal force exists between particles 2 and 3. The deformation of the hexagon can be calculated by

$$l_n = d_2 + 2d_1 \cos\alpha \tag{1.69}$$

$$l_t = 2d_1 \sin\alpha \tag{1.70}$$

where α is a parameter describing the degree of opening of the hexagon, d_1 and d_2 are distances between two neighboring particles. By using the elastic and pure plastic local law

expressed in Eqs.(1.65) and (1.66) and invoking the force equilibrium equation between particles, force increments can be computed. To integrate the forces in order to obtain the global stresses, the Love-Weber formula described in Eq.(1.14) has been adopted. Since the density function for isotropic fabric, i.e. 1/2π in 2D and 1/4π in 3D, has been adopted, this model in its present form cannot capture the non-coaxial deformation of granular materials under rotational shearing.

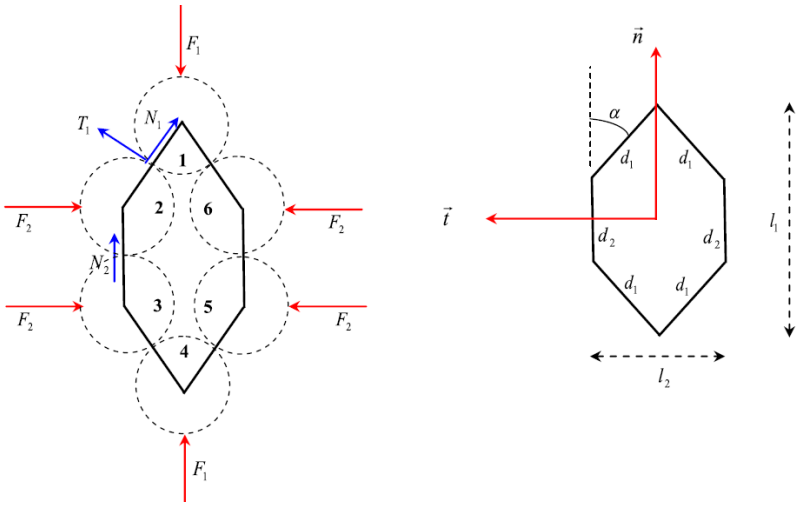

Figure 1.10 Geometrical description, external forces applied to each hexagon, and contact forces

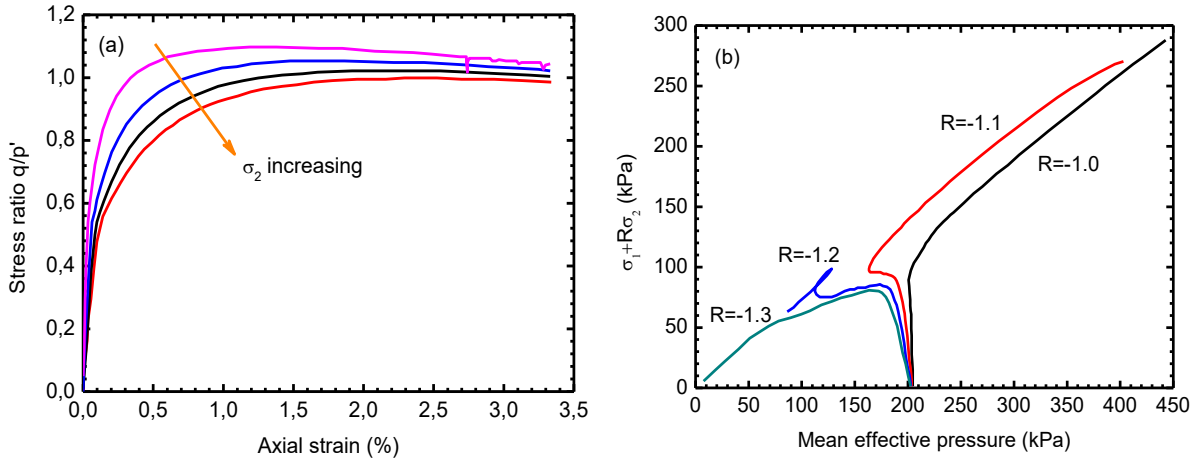

Figure 1.11 Evolution of the deviatoric ratio versus the axial strain at different initial confining pressures (Nicot and Darve, 2011)

The ability of the H model to reproduce the behaviour of granular materials has been demonstrated, in particular for the diffuse failure that cannot be well described by the *μ-D* model, as shown in Figure 1.11. Whereas the H model exhibits many interesting features, it

still has some limitations.

1.3.5 Other micromechanical models

Based upon the micromechanics of granular materials, many micromechanical models have been suggested for different purposes. To simulate the time-dependent behaviour of polymers, Misra and Singh (2015) suggested a viscous-elasto-plastic micromechanical model based on the kinematic assumption described in Eq.(1.6). Similarly, a higher-order micromechanical model has been constructed for capturing the strain localization of granular materials (Yang and Misra, 2012). From the scope of the meso-scale, a micromechanical model was suggested by Cambou *et al*. (2016) for granular materials by defining six phases which are sets of meso-domains with similar elongation degrees and orientations. In the light of Rowe's dilatancy theory (Rowe, 1962), Wan and Guo (2001) constructed a micromechanical model by extending the dilatancy function in order to consider fabric anisotropy. Based on energy conservation at various scales, Zhang and Buscarnera (2014, 2017) and Zhang *et al*. (2016) constructed micromechanical models for unsaturated granular materials by combining micromechanics and breakage mechanics.

1.4 Multiscale modelling of geotechnical problems

1.4.1 Discrete element method

DEM has been significantly developed since its first application to simulate the behaviour of granular materials by Cundall and Strack (1979). In this method, granular materials are regarded as the assembly of individual spherical particles. The relation between two contact particles is generally described by an elastic purely plastic contact law, as shown in Figure 1.12. An explicit displacement driven procedure has been implemented to solve the equilibrium equations of each particle (O'Sullivan, 2011).

This method has proved to be an efficient tool to investigate the microscopic and macroscopic behaviours of granular materials (O'Sullivan, 2011; Barreto *et al*., 2012; Belheine *et al.*, 2009; Scholtès *et al*., 2009; Zhu *et al*., 2016; Jiang *et al*., 2007; Yang *et al*., 2012; Zhao and Guo, 2013). With the rapid development of computational techniques, this approach has been

recently applied to solve boundary value problems (Jiang *et al*., 2006, 2008; Jiang and Yin, 2012, 2014; McDowell *et al*., 2012; Wang and Zhao, 2014). However, the parameters used in these calculations compared to realistic interparticle contacts are still questionable. In addition, the calculations require a lot of computational efforts, even if parallel computational techniques have been used.

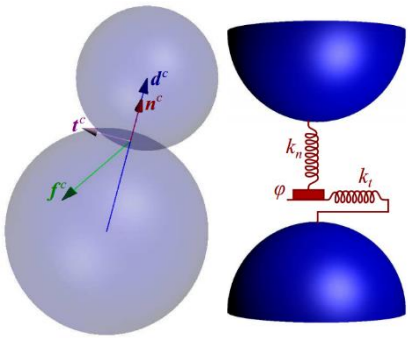

Figure 1.12 Interparticle contact in DEM

1.4.2 FEM×DEM coupling approaches

Given that FEM is an efficient technique for solving complex problems, whereas DEM gives more insight into the physics of particulate materials, they have been coupled to solve boundary value problems. Generally, two types of coupling methods can be found in the literature, i.e. contact coupling and Gauss integration point coupling.

1) *Contact coupling*

In this approach, the numerical model is composed of a FEM part and a DEM part, as shown in Figure 1.13. The granular materials with large deformations are replaced by DEM particles, whereas the domain that has small deformations is computed with FEM technique. The interface between FEM and DEM is a surface contact coupling for two-dimensional models and is volumetric contact coupling for three-dimensional models. The effectiveness of this approach has been proved by the work of Cai *et al.* (2007), Elmekati and El Shamy (2010), Li *et al*. (2015), *etc*.

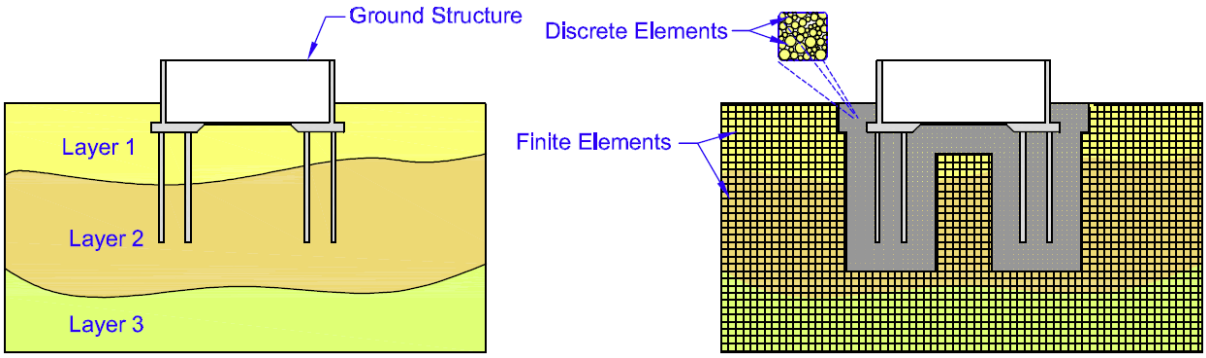

Figure 1.13 Physical and numerical models: (a) system layout; (b) FEM×DEM model

2) *Gauss integration point coupling*

This method takes the advantages of FEM for large-scale boundary conditions and the benefit of DEM to represent the material behaviour with only a few parameters with physical meaning instead of complicated constitutive models requiring a large set of constitutive parameters. This approach adopts the FEM to discretize the calculation domain into elements in which the Gauss integration points consist of DEM samples, as shown in Figure 1.14. For each Gauss point, strain increment and state variables are given to the attached DEM sample. After equilibrium iterations, DEM returns the updated stress and tangent operator to the Gauss point. The differential equations can be solved by a Newton-Raphson method in the implicit FEM. To reduce the time cost, parallel computational techniques have been used and the number of particles in the DEM simulations should be as small as possible.

This method has been successfully applied to geotechnical investigations, from elementary tests to classical geotechnical problems. The strain localization of granular materials has been investigated by Guo and Zhao (2014), Nitka *et al*. (2011) and Nguyen *et al*. (2017). With this approach, it has been found that the fabric anisotropy can be a method to break the symmetry of biaxial test with smooth boundaries and inside the shear band the material can reach a critical state. Additionally, the classical geotechnical problems including a retaining wall and a strip footing were analyzed. It was found that the solution was comparable with the analytical solutions (Guo and Zhao, 2016).

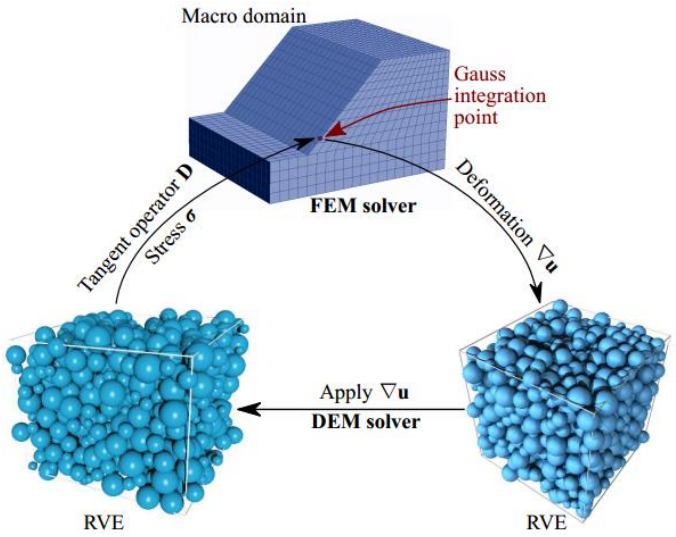

Figure 1.14 The procedure of hierarchical multiscale modelling (from Guo and Zhao, 2014)

1.4.3 FEM×micromechanical model

To overcome the shortcomings brought by DEM, implementing micromechanical models into FEM can be a good option to solve geotechnical problems more efficiently and accurately. The two-dimensional H model has been successfully implemented into FLAC by Veylon (2017). Its capability in describing the liquefaction of granular soils has been demonstrated. Given the good performance of the CH model in predicting granular soil behaviour, it will be implemented into FEM to investigate localized and diffuse failures of granular soils, and furtherly applied to solve geotechnical problems.

1.5 Concluding remarks

This chapter first briefly reviewed the basic theories of micromechanics of granular materials, including interparticle contact laws, strain, stress and fabric tensors as well as homogenization methods. Then, the constitutive relations constructed on the basis of micromechanics of granular materials were introduced and their performances in capturing the behaviour of granular soils were discussed. It was concluded that the CH model demonstrated its capacity in describing the mechanical behaviour of soils. Finally, the multiscale modelling approaches that can be applied to solve geotechnical problems were discussed. Since the computational cost as well as the difficulties in calibrating the parameters used in DEM simulations are still

significant, implementing micromechanical models into a finite element code could be an alternative direction in multiscale modelling of geotechnical problems.

CHAPTER 2 THERMOMECHANICAL FORMULATION FOR MICROMECHANICAL PLASTICITY IN GRANULAR SOILS

2.1 Introduction

Constitutive modelling is one of the most important research tasks in the field of the mechanics of materials. Based upon classical continuum mechanics, a variety of ways could be used to construct mathematical models for simulating the mechanical behaviour of soils. Among them many models were built based on various assumptions such as critical state soil mechanics (Li and Dafalias, 2011; Shen *et al*., 2012; Gao and Zhao, 2017), dilatancy functions (Fern *et al.*, 2016) and particle crushing (Yin *et al.*, 2016; Hyodo *et al*., 2017). Since thermodynamics is a basic law of physics, it has attracted much attention and was alternatively used to construct constitutive models. Ziegler and Wehrli (1987) pioneered the introduction of thermodynamics into constitutive modelling. Collins and Houlsby (1997) followed this path with a comprehensive analysis of the isothermal thermomechanics of geomaterials, while Collins and Hilder (2002) provided the framework for constructing elasto-plastic phenomenological models. Based upon the procedure of thermodynamics, Li (2007) and Coussy *et al*. (2010) extended the thermomechanical framework to unsaturated soils. Through this approach, once the free energy and the dissipative potential function are given, elasticity and plasticity (yield function, flow rule and hardening law) can be deduced correspondingly. Conversely, given an elastoplastic model, free and dissipative energies can be calculated to verify whether the laws of thermodynamics are respected. It can be found that this method has been successfully employed in elastoplastic constitutive models for describing soil behaviour (Collins *et al*.,2010; Coussy *et al.*, 2010; Lai *et al*., 2016; Li *et al.*, 2017; Zhang, 2017).

From yet another perspective, soils are composed of many individual grains and the evolution of the granular structure has a significant effect on the behaviour at the macro scale. The failure of a specimen is triggered by the slip and the rotation of grains in contact as well as the collapse of force-chains. To address these issues, micromechanics-based constitutive models

have been formulated to simulate soil behaviour (Chang and Hicher, 2005; Nicot and Darve, 2005, 2011; Xiong *et al*., 2017). In all these models, elastic and plastic relations between force and displacement are defined at inter-particle contacts and the overall stress-strain relations are obtained by integrating the local law onto all particle contacts. To formulate these micromechanical models, different assumptions are made between strain and displacement. The best fit hypothesis and the Voigt hypothesis are usually adopted for building relations between the macro strain and the local displacement (Cambou *et al*., 2009). Micromechanical models based on the best fit hypothesis proposed by Liao *et al*. (1997) can be found in Chang and Hicher (2005), Hicher and Chang (2005, 2007), Yin and Chang (2009a, 2009b) and Yin *et al*. (2009, 2011, 2013, 2014), in which the force increment is calculated from the stress increment. These models are also called static hypothesis based models. Other models, called kinematic hypothesis based models, in which displacement increment are calculated from strain increment, are based on the Voigt hypothesis (Nicot and Darve, 2005, 2011; Misra and Singh, 2014; Xiong *et al*., 2017).

Although the physical meanings of thermodynamics and micromechanics are attractive for geomaterials, few efforts have been made for constructing models based upon the combination of these approaches (Zhu and Shao, 2016; Radjai *et al*., 2017). Recently, Zhu et al. (2008) introduced thermodynamics to discrete system based on weak sliding plane concept and applied this theory for modelling anisotropic coupled plastic-damage behaviour of cohesive geomaterials (Zhu *et al*., 2010). Misra and Singh (2014) and Misra and Poorsolhjouy (2015a) discussed a rate-dependent micromechanical model from the thermomechanical basis with kinematic hypothesis. However, the general procedure for constructing a thermodynamically consistent micromechanical model for granular soils has not been thoroughly addressed, especially considering that energy can be stored at particle contacts. In addition, the relation between dissipative energy distribution and material failure plane is also not investigated. For granular soils, if we do not consider the deformation of the grain itself, the energy can only be stored and dissipated at inter-particle contacts. The energy at the macro scale is the summation of the energy at all inter-particle contacts. Therefore, by

considering the energy dissipated through friction at the inter-particle contacts during loading, one can apply the principles of thermodynamics to micromechanical modelling.

To answer the question: how to construct a thermodynamically consistent micromechanical model, this chapter presents a thermomechanical framework for constructing micromechanical models for granular materials, in which elasto-plastic local laws can be defined at inter-particle contacts. Within this framework, free and dissipative energies are directly defined from force and displacement at the particle contact, based on which the yield criterion, the flow rule and the hardening law can be deduced by Legendre transformation. To demonstrate the applicability of this thermomechanical framework, on one hand, the static hypothesis suggested in the CH micromechanical model (Chang and Hicher, 2005) was derived from an energy perspective, which greatly enhanced the understanding of the micromechanical models based on this assumption. On the other hand, a thermodynamically consistent elasto-plastic micromechanical model has been constructed based on the static hypothesis. The model was then calibrated with the energy conservation and dissipation under loading analyzed at both micro and macro scales. For simplicity, we focused on dry granular materials under isothermal condition. The effective stress concept used in soil mechanics has been adopted throughout this chapter.

2.2 Thermomechanical framework

2.2.1 Thermodynamic preliminaries

Thermodynamics with internal variables has been adopted in this study, following the concepts elaborated in various studies (Rice, 1971; Ziegler and Wehrli, 1987; Collins and Houlsby, 1997; Collins and Hilder, 2002; Houslby and Puzrin, 2007; Li, 2007; Collins et al., 2010). The first law of thermodynamics states that the changes of internal energy, heat and work increments satisfy the following equation

$$\delta W + \delta Q = du \tag{2.1}$$

in which δW is the work increment, δQ is the heat increment and du is the internal energy increment. All these thermomechanical variables are defined per unit volume. Note that dx

denotes an exact differential while δx denotes an inexact one which represents an infinitesimal change of x. The Clausius-Plank inequality, as a form of the second law of thermodynamics for a soil element, states that the entropy increment should be non-negative, which can be written as

$$\gamma = d\eta - \delta Q / T \geq 0 \tag{2.2}$$

where γ is the entropy production increment, η is the entropy density, and T is the absolute temperature. Combining Eqs.(2.1) and (2.2), the energy conservation can be rewritten as

$$\delta W = \left(du - T d\eta \right) + T\gamma \tag{2.3}$$

The Helmholtz free energy ψ defined in terms of internal energy, entropy density and temperature, can be expressed as

$$\psi = u - T\eta \tag{2.4}$$

Differentiating Eq.(2.4), we obtain

$$d\psi = \left(du - T d\eta \right) - \eta dT \tag{2.5}$$

The dissipative energy increment per unit volume ϖ is defined as

$$\varpi = T\gamma \geq 0 \tag{2.6}$$

which should be non-negative (Collins and Houlsby, 1997). Inserting Eqs.(2.5) and (2.6) into Eq.(2.3), the energy conservation relation can be expressed as

$$\delta W - \varpi = d\psi + \eta dT \tag{2.7}$$

For the isothermal case with dT=0, Eq.(2.7) can be simplified as

$$\delta W - \varpi = d\psi \tag{2.8}$$

where the work increment δW is the product of stress and strain increments

$$\delta W = \boldsymbol{\sigma} : d\boldsymbol{\varepsilon} \tag{2.9}$$

Inserting Eq.(2.9) into Eq.(2.8), the relation between stress work increment, Helmholtz free energy increment, and dissipative energy increment, becomes

$$\boldsymbol{\sigma} : d\boldsymbol{\varepsilon} - \varpi = d\psi \tag{2.10}$$

In this study, only rate independent displacements of soil particles under isothermal condition are investigated.

2.2.2 Thermodynamics at micro scale

The Helmholtz free energy increment at inter-particle contact is noted as $d\psi^c$, where superscript c is used to represent contact. The micro Helmholtz free energy is a function of state variables, e.g. particle displacements. Since the macro energy quantities are expressed per unit volume, the macro Helmholtz free energy is calculated as the volumetric average of all contact summation, and the relation can be expressed as

$$d\psi = \frac{1}{V}\sum_{c=1}^{N} d\psi^c\left(\boldsymbol{\delta}^c\right) \tag{2.11}$$

Similarly, the dissipation increment at the macro scale is the volumetric average of all contact summation of the dissipation energy at the micro scale,

$$\varpi = \frac{1}{V}\sum_{c=1}^{N} \varpi^c\left(\dot{\boldsymbol{\delta}}^c\right) \tag{2.12}$$

The macro work increment is also the volumetric average of all work increment at inter-particle contacts (Misra and Singh, 2014)

$$\delta W = \frac{1}{V}\sum_{c=1}^{N} \delta W^c\left(\boldsymbol{\delta}^c\right) \tag{2.13}$$

in which, the micro work increment is defined by the product of force and displacement increments

$$\delta W^c = \mathbf{f}^c \cdot d\boldsymbol{\delta}^c \tag{2.14}$$

The energy conservation of Eq.(2.8) can be expressed by combining Eqs.(2.11), (2.12) and (2.13),

$$\frac{1}{V}\sum_{c=1}^{N} \delta W^c\left(\boldsymbol{\delta}^c\right) - \frac{1}{V}\sum_{c=1}^{N} \varpi^c\left(\dot{\boldsymbol{\delta}}^c\right) = \frac{1}{V}\sum_{c=1}^{N} d\psi^c\left(\boldsymbol{\delta}^c\right) \tag{2.15}$$

Assuming that energies are conserved at particle contacts, Eq.(2.15) can be satisfied for any number of grain-pair interactions, and the equality can be written in a term-by-term manner

$$\delta W^c - \varpi^c = d\psi^c \tag{2.16}$$

Eq.(2.16) cannot be adapted to real particle contact since particles are deformable and kinetic energy and heat exchange take place during mechanical loading. For small or infinitesimal deformation, the displacement increment can be decomposed into an elastic part and a plastic part

$$d\boldsymbol{\delta}^c = d\boldsymbol{\delta}^{ce} + d\boldsymbol{\delta}^{cp} \tag{2.17}$$

By substituting Eqs.(2.14) and (2.17) into Eq.(2.16) the micro Helmholtz free energy can be formulated as

$$d\psi^c = \mathbf{f}^c \cdot d\boldsymbol{\delta}^c - \varpi^c = \mathbf{f}^c \cdot \left(d\boldsymbol{\delta}^{ce} + d\boldsymbol{\delta}^{cp}\right) - \varpi^c = \underbrace{\mathbf{f}^c \cdot d\boldsymbol{\delta}^{ce} + \boldsymbol{\alpha}^c \cdot d\boldsymbol{\delta}^{cp}}_{d\psi^c} + \underbrace{\overbrace{\left(\mathbf{f}^c - \boldsymbol{\alpha}^c\right)}^{\boldsymbol{\chi}^c} \cdot d\boldsymbol{\delta}^{cp} - \varpi^c}_{0} \tag{2.18}$$

in which the back force $\boldsymbol{\alpha}^c$ and the dissipative force $\boldsymbol{\chi}^c$ are introduced. From Eq. (2.18), one can see the Helmholtz free energy can be decomposed into elastic and plastic parts (Collins and Hilder, 2002; Houlsby and Puzrin, 2007), in which the plastic part $d\psi_2^{cp}\left(\boldsymbol{\delta}^{cp}\right)$ is referred to as micro stored energy. When strain hardening occurs, the Helmholtz free energy can be decomposed into an elastic part that is equal to the elastic strain energy and the stored energy which cannot be recovered during the unloading process and is frozen by plastic hardening. The relation can be written as

$$d\psi^c = d\psi_1^{ce} + d\psi_2^{cp} = d\psi_1^{ce}\left(\boldsymbol{\delta}^{ce}\right) + d\psi_2^{cp}\left(\boldsymbol{\delta}^{cp}\right) \tag{2.19}$$

Combining Eqs.(2.16) and (2.19), the micro work can be decomposed into an elastic work which is equal to the elastic free energy

$$\delta W^{ce} = d\psi_1^{ce} = \frac{\partial \psi_1^{ce}\left(\boldsymbol{\delta}^{ce}\right)}{\partial \boldsymbol{\delta}^{ce}} d\boldsymbol{\delta}^{ce} \tag{2.20}$$

and plastic work, which is the summation of the micro stored energy and the dissipation energy

$$\delta W^{cp} = d\psi_2^{cp} + \varpi^c = \frac{\partial \psi_2^{cp}\left(\boldsymbol{\delta}^{cp}\right)}{\partial \boldsymbol{\delta}^{cp}} d\boldsymbol{\delta}^{cp} + \frac{\partial \varpi^c}{\partial \dot{\boldsymbol{\delta}}^{cp}} d\boldsymbol{\delta}^{cp} \tag{2.21}$$

Based on Eq.(2.21), the dissipative force and the back force can be defined as

$$\boldsymbol{\chi}^c = \frac{\partial \varpi^c}{\partial \boldsymbol{\delta}^{cp}} \text{ and } \boldsymbol{\alpha}^c = \frac{\partial \psi_2^{cp}\left(\boldsymbol{\delta}^{cp}\right)}{\partial \boldsymbol{\delta}^{cp}} \tag{2.22}$$

From Eq.(2.18), by using Legendre transformation, the yield criterion at the inter-particle contacts can be expressed in the dissipative force space by

$$\tilde{F}\left(\boldsymbol{\chi}^{c}\right)=\frac{1}{\lambda^{c}}\left[\boldsymbol{\chi}^{c}\cdot d\boldsymbol{\delta}^{cp}-\varpi^{c}\right]=0 \tag{2.23}$$

in which λ^{c} is a plastic multiplier defined at the inter-particle contact, and the yield function can also be formulated in the force space after defining the back force

$$F\left(\mathbf{f}^{c}\right)=\tilde{F}\underbrace{\left[\mathbf{f}^{c}-\boldsymbol{\alpha}^{c}\left(\mathbf{f}^{c}\right)\right]}_{\boldsymbol{\chi}^{c}}=0 \tag{2.24}$$

In the dissipative force space, the associated flow rule is obtained by adopting Ziegler's orthogonality condition (Ziegler and Wehrli, 1987), and the plastic displacement increment can be obtained by differentiating Eq.(2.23), given as

$$\delta\boldsymbol{\delta}^{cp}=\lambda^{c}\frac{\partial\tilde{F}\left(\boldsymbol{\chi}^{c}\right)}{\partial\boldsymbol{\chi}^{c}} \tag{2.25}$$

By using the consistency condition and replacing the back force by the inter-particle force, the flow rule in the force space can be deduced. It should be mentioned that the obtained flow rule can be either associated or non-associated.

2.2.3 Application of the thermomechanical formulation

For constructing a thermodynamically consistent model based on micromechanics, the micro-macro relations and the inter-particle contact law should be defined. For the micro-macro relations, a localization operator and an average operator should be given; these relations should satisfy the Hill-Mandel condition (Hill, 1963; Mandel, 1971; Geers *et al*., 2010; Nguyen *et al*., 2011). Additionally, the energy conservation conditions have to be taken into account in the local law. The procedure for defining the local law consists of: defining a Helmholtz free energy function $d\psi^{c}$ for elastic and plastic displacements, and a dissipation function ϖ^{c} which depends on the plastic displacement increment; obtaining the elastic part from the free energy by using Eq.(2.20); deducing the back force from the free energy by using Eq.(2.22); using Eq.(2.23) to obtain the yield criterion in the dissipative space and then using Eq.(2.24) to obtain the yield criterion in the force space; deducing an associate flow rule

in the dissipative space by Eq.(2.25); and lastly, differentiating the yield criterion to obtain the consistency equation.

From another perspective, if the elasto-plastic micromechanical model has already been constructed, its free energy and dissipation energy can be evaluated by using the inverse of the above procedure. Undoubtedly, the dissipation energy increment has to be non-negative. In the following section, a micromechanical model based on the thermomechanical formulation described above will be constructed, which will demonstrate the applicability of this framework for multi-scale modelling.

2.3 A thermomechanical micromechanical model

In this section, a micromechanical model has been constructed based on the proposed thermomechanical formulation. At first, inter-particle hyper-elasticity and hyper-plasticity are addressed in detail. Then, based on the strain tensor, the stress tensor is derived from Helmholtz free energy conservation relation. In addition, the static hypothesis is derived from the free energy, followed by an analysis of its connection to the Love-Weber micro-macro relation. A homogenization scheme is also presented.

2.3.1 Inter-particle contact law

Since the macro elastic and plastic behaviours originate from inter-particle contacts, the inter-particle displacement can be divided into two parts: elastic and plastic. To define elasticity and plasticity, a local coordinate system (*n, s, t*) has been defined, as shown in Figure 1.3, in which *n* is the normal to the contact plane, whereas *s* and *t* are orientations within the contact plane. The relationship between local and global coordinates can be defined by the angles β and γ, which can be expressed as by Eq.(1.31). With this relation, the quantities defined at inter-particle contacts can be expressed globally.

1) Inter-particle hyperelasticity

The hyper-elastic part is the means to guarantee the granular material obeys the first law of thermodynamics. The behaviour of the hyper-elastic granular material can be defined by the

Helmholtz free energy function (Collins *et al*., 2010; Misra and Singh, 2014). The Helmholtz free energy potential at the micro scale can be defined as

$$\psi^c\left(\delta^c\right)=\frac{1}{2}k_n^c\left(\delta_n^{ce}\right)^2+\frac{1}{2}k_r^c\left(\delta_r^{ce}\right)^2 \tag{2.26}$$

where k_n^c and k_r^c are stiffness in normal and tangential directions. By differentiating Eq.(2.26) with respect to displacements, the elastic inter-particle contact force-displacement relation can be obtained

$$\dot{f}_i^c=k_{ij}^c\dot{\delta}_j^{ce} \tag{2.27}$$

where k_{ij}^c is the elastic stiffness with the same tangential behaviour for each particle contact, given by Eq.(1.33).

2) *Inter-particle hyperplasticity*

Irrecoverable displacement between grains in contact during loading requires the mechanism of plasticity to be introduced at the local level. To define the hyper-plastic part of the local law, a dissipative energy potential at the micro scale should be given. However, the absence of experimental results at this scale makes it difficult to formulate this local law. Considering that the model proposed by Chang and Hicher (2005) has the ability to simulate with accuracy the soil response to various mechanical loadings and that only a few parameters need to be calibrated by elementary tests, its inter-particle plastic equations will be retained and its energy dissipation will be evaluated by the inverse procedure presented in section 2.2.

For examining the hyper-plasticity condition, the plastic work and the dissipative energy should be calculated. According to its definition in Eq.(2.21), the micro-scale plastic work can be written as

$$\delta W^{cp}=f_n^c d\delta_n^{cp}+f_r^c d\delta_r^{cp} \tag{2.28}$$

From the expression of the yield criterion in Eq.(1.35), we can write its partial derivatives as

$$\frac{\partial F}{\partial f_n^c}=-\frac{\kappa^2\left(\delta_r^{cp}\right)}{\tan\phi_p^c},\ \frac{\partial F}{\partial f_s^c}=\frac{f_s^c}{\sqrt{\left(f_s^c\right)^2+\left(f_t^c\right)^2}},\ \frac{\partial F}{\partial f_t^c}=\frac{f_t^c}{\sqrt{\left(f_s^c\right)^2+\left(f_t^c\right)^2}} \tag{2.29}$$

Since an associated flow rule has been adopted in the tangential direction, while a non-associated flow rule expressed by Eq.(1.40) has been adopted in the normal direction, the partial derivatives of the potential function can be expressed as

$$\frac{\partial G}{\partial f_s^c}=\frac{\partial F}{\partial f_s^c},\ \frac{\partial G}{\partial f_t^c}=\frac{\partial F}{\partial f_t^c},\ \frac{\partial G}{\partial f_n^c}=D\frac{\partial G}{\partial f_r^c}=D\sqrt{\left(\frac{\partial G}{\partial f_s^c}\right)+\left(\frac{\partial G}{\partial f_t^c}\right)}=D \tag{2.30}$$

where G is the potential function defined at the inter-particle contacts. Additionally, the plastic displacement increment can be calculated by

$$d\delta_i^{cp}=\lambda^c\frac{\partial G}{\partial f_i^c} \tag{2.31}$$

Combining Eqs.(2.29) and (2.30), we obtain

$$\frac{\partial G}{\partial f_r^c}=\sqrt{\left(\frac{\partial G}{\partial f_s^c}\right)^2+\left(\frac{\partial G}{\partial f_t^c}\right)^2}=1 \tag{2.32}$$

Thus from Eqs.(2.31) and (2.32)

$$\lambda^c=d\delta_r^{cp} \tag{2.33}$$

Inserting the dilatancy relationship assumed by Eq.(1.40) and Eq.(2.33) into Eq.(2.28), we obtain

$$\delta W^{cp}=f_i^c d\delta_i^{cp}=f_n^c d\delta_n^{cp}+f_r^c d\delta_r^{cp}=f_n^c\left(d\delta_r^{cp}\left(\tan\phi_d^c-\frac{f_r^c}{f_n^c}\right)\right)+f_r^c d\delta_r^{cp}=f_n^c\tan\phi_d^c d\delta_r^{cp} \tag{2.34}$$

The normal force f_n^c at particle contact is always compressive and, therefore, positive; $\tan\phi_d^c$ can be proved to be positive from Eq.(1.41) and $d\delta_r^{cp}$ being the tangential plastic increment is also positive, as shown in Eq.(1.36). Therefore, the plastic work increment calculated from Eq.(2.28) is non-negative. Thus, the dissipation energy increment is non-negative at both micro and macro scales, expressed as

$$\begin{cases}\varpi^c=\delta W^{cp}=f_n^c\tan\phi_d^c d\delta_r^{cp}\geq 0\\ \varpi=\dfrac{1}{V}\displaystyle\sum_{c=1}^{N}\varpi^c\left(\boldsymbol{\delta}^c\right)\geq 0\end{cases} \tag{2.35}$$

As shown in Eq.(2.21), the stored energy is a part of the plastic work increment and is a function of the state variables, so the integration of the stored energy increment over a closed

loading loop should be equal to zero. The stored energy increment should be positive for loading and negative for unloading condition (Collins and Hilder, 2002; Li, 2007). However, the plastic work is not integrable and is always positive; it prevents negative stored energy increment to exist. Consequently, the stored energy increment is equal to zero and the Helmholtz free energy depends only on the elastic displacement increment, which is consistent with the Helmholtz free energy potential given by Eq.(2.26)

$$d\psi^c = d\psi_1^{ce} + d\psi_2^{cp} = d\psi_1^{ce}(\boldsymbol{\delta}^{ce}) \tag{2.36}$$

Thus, the elastic work increment is equal to the free energy

$$\delta W^{ce} = f_i^c d\delta_i^{ce} = d\psi_1^{ce}\left(\boldsymbol{\delta}^{ce}\right) \tag{2.37}$$

From Eq.(2.35), the second law of thermodynamics is satisfied at the macro and micro scales, whereas Eq.(2.36) and Eq.(2.37) satisfy the condition of energy conservation. Hence, we can say that the micromechanical model is thermodynamically consistent.

2.3.2 Micro-macro relations

1) *Strain and stress tensors*

The micro-macro relations connect the local force and displacement to the overall stress and strain. For the relation between strain and relative displacement at contacts, the formulation based on the best-fit hypothesis suggested by Liao *et al*. (1997) has been adopted, expressed by Eq.(1.12). According to the definition of the strain energy, the stress can be derived as

$$\sigma_{ij} = \frac{\partial \psi\left(\varepsilon_{ij}^e\right)}{\partial \varepsilon_{ij}^e} = \frac{1}{V}\sum_{c=1}^{N} \frac{\partial \psi^c\left(\delta_i^{ce}\right)}{\partial \delta_i^{ce}} \frac{\partial \delta_i^{ce}}{\partial \varepsilon_{ij}^e} = \frac{1}{V}\sum_{c=1}^{N} f_i^c \bullet \frac{\partial \delta_i^{ce}}{\partial \varepsilon_{ij}^e} = \frac{1}{V}\sum_{c=1}^{N} f_i^c l_j^c \tag{2.38}$$

where

$$\frac{\partial \varepsilon_{ij}^e}{\partial \delta_i^{ce}} = \frac{\partial\left(\frac{1}{V}\sum_{c=1}^{N} \delta_i^{ce} l_n^c A_{jn}\right)}{\partial \delta_i^{ce}} = \frac{1}{V} l_n^c A_{jn} \tag{2.39}$$

It is found, therefore, that the stress is obtained by integrating the contact forces over the volume, which is consistent with the Love-Weber formula.

2) *Localization and averaging operators*

The stress tensor defined in Eq.(2.38) can be seen as an averaging operator; in addition, a localization operator is needed. From the micro-macro relations defined by Eqs.(1.12) and (2.38), however, the local variables are difficult to obtain since there is an innumerable number of contacts in the representative element volume. A localization operator, which can be deduced from the strain energy conservation and the complementary energy conservation, is needed to integrate the local law. Based on the thermomechanical analysis presented previously, the localization operator can be obtained by the Helmholtz free energy combined with the Gibbs free energy. The Helmholtz free energy at the macro scale is defined by the strain, $\psi(\boldsymbol{\varepsilon})$, which is also called strain energy. The complementary energy, known as Gibbs energy, ϕ, can be defined by the following Legendre transformation of the Helmholtz free energy

$$\phi(\boldsymbol{\sigma}) = \boldsymbol{\sigma} : \boldsymbol{\varepsilon} - \psi(\boldsymbol{\varepsilon}) \tag{2.40}$$

From the definition of the Helmholtz free energy and the Gibbs free energy, stress and strain can be expressed as

$$\sigma_{ij} = \frac{\partial \psi(\varepsilon_{ij})}{\partial \varepsilon_{ij}},\ \varepsilon_{ij} = \frac{\partial \phi(\sigma_{ij})}{\partial \sigma_{ij}} \tag{2.41}$$

Similarly, the Helmholtz free energy at the micro scale is defined by the displacement, which can be used to compute the Helmholtz free energy at the macro scale, as shown in Eq.(2.11). Additionally, the Gibbs energy can also be integrated from the micro to macro scales, expressed as

$$\phi = \frac{1}{V}\sum_{c=1}^{N} \phi^c\left(f_j^c\right) \tag{2.42}$$

Thus, force and displacement at the micro scale can be defined as

$$f_i^c = \frac{\partial \psi^c(\delta^c)}{\partial \delta_i^c},\ \delta_i^c = \frac{\partial \phi^c(f^c)}{\partial f_i^c} \tag{2.43}$$

According to the previous discussion, the stored energy increment is equal to zero at the micro scale. Therefore, the Helmholtz free energy and the Gibbs free energy at the macro scale are equal to the volumetric average of the free energy at the micro scale:

$$\begin{cases} \sigma_{ij} d\varepsilon_{ij} = \dfrac{1}{V} \sum_{c=1}^{N} f_i^c d\delta_i^c \\ d\sigma_{ij} \varepsilon_{ij} = \dfrac{1}{V} \sum_{c=1}^{N} df_j^c \delta_j^c \end{cases} \tag{2.44}$$

By inserting Eqs.(1.12) and (2.38) into Eq. (2.44), we obtain the localization operator expressed in Eq.(1.17) , which is referred to as the static hypothesis since the local force is calculated from the global stress as compared with the kinematic method in which the displacement is calculated from the strain (Nicot *et al*., 2005; Nicot and Darve, 2011; Misra and Singh, 2014, Xiong *et al*., 2017).

Since the derivation of the static hypothesis is based on free energy, the forces calculated from the stress increments are elastic. The plastic part of the inter-particle contacts implies the existence of an unbalanced force after the integration of the Love-Weber formula. Therefore, to make the global stress and the local force consistent, an iteration scheme is needed. The iterations force the first plane reaching the limit state to have the maximum dissipative energy, which will be demonstrated by the simulation of triaxial tests in Section 2.4.

2.3.3 Homogenization method

As demonstrated previously, the summation over all the contacts, for a given function F^c defined at inter-particle contact (any variable at contact level), should be performed. But, too many particle contacts in a representative elementary volume make it impossible to perform this summation. In this model, the integration method suggested in the CH model was adopted.

2.3.4 *Implementation* scheme

If the loading is under strain or mixed mode control, as shown in Figure 2.1, the linearization technique proposed by Bardet and Choucair (1991) is useful for obtaining the stress increment from which an elastic predictor can compute the displacement increment, then the stress can be obtained through the integration of the local law. To assure that the static hypothesis is consistent with the Love-Weber formula, an iteration process is needed until the unbalanced force increments dip below a given tolerance. Implicit or explicit integration methods, such as the closest point projection method or the cutting plane algorithm, can be adopted for

implementing the local law. This important point has not been well addressed in the previous version of the CH micromechanical model. The details of the implementation scheme for a micromechanical model based on static hypothesis will be discussed in detail in Chapter 4.

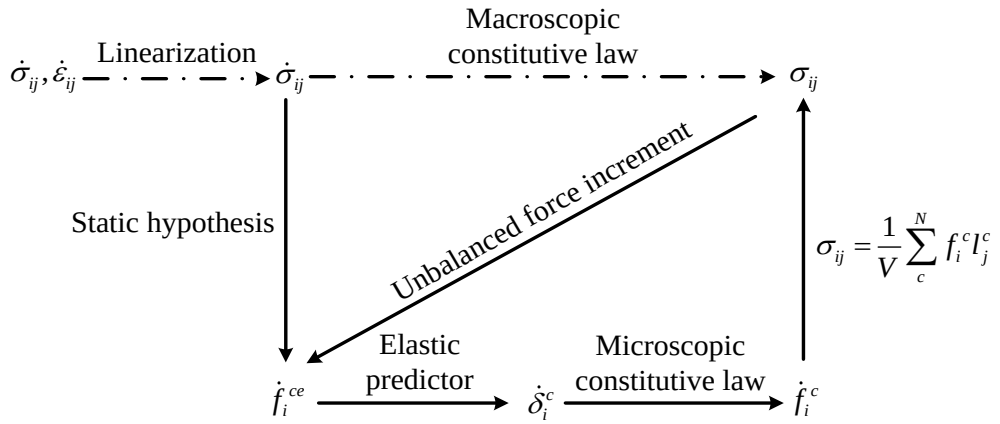

Figure 2.1 Implementation procedure of a micromechanical model based on static hypothesis

2.4 Numerical validation of the energy conservation

The thermodynamically consistent micromechanical model can be calibrated by simulating drained triaxial tests on loose and dense Hostun sand samples. The parameters used in this model can be divided into two categories: either macro or micro parameters, as shown in Table 2.1, in which d_{50} is taken as the diameter of the particle. The mean particle size of the tested Hostun sand is d_{50}=1.3mm. The inter-particle elastic constant k_{n0}=80N/mm was calibrated from an isotropic compression test. The macro parameters corresponding to the position of the critical state line in the e-logp' plane are: λ=0.06, p_{ref}=0.1MPa and e_{ref}=0.81. The inter-particle contact friction angle is ϕ_μ^c=33°. The ratio k_{pR}=0.4 representing the plastic stiffness was calibrated based on the stress-strain curves. Both experimental and simulated results are presented in Figure 2.2 for both loose and dense samples of Hostun sand. All the comparisons demonstrate a good performance of the model in describing the typical mechanical behaviour of a granular material.

Table 2.1 Parameters used in micromechanical model for Hostun sand

Macro		Micro				
e_{ref}	λ	k_{n0}^{c}(N/mm)	ϕ_{μ}^{c}(°)	d_{50}(mm)	k_{rR}	k_{pR}
0.81	0.06	80.0	33	1.3	0.4	0.4

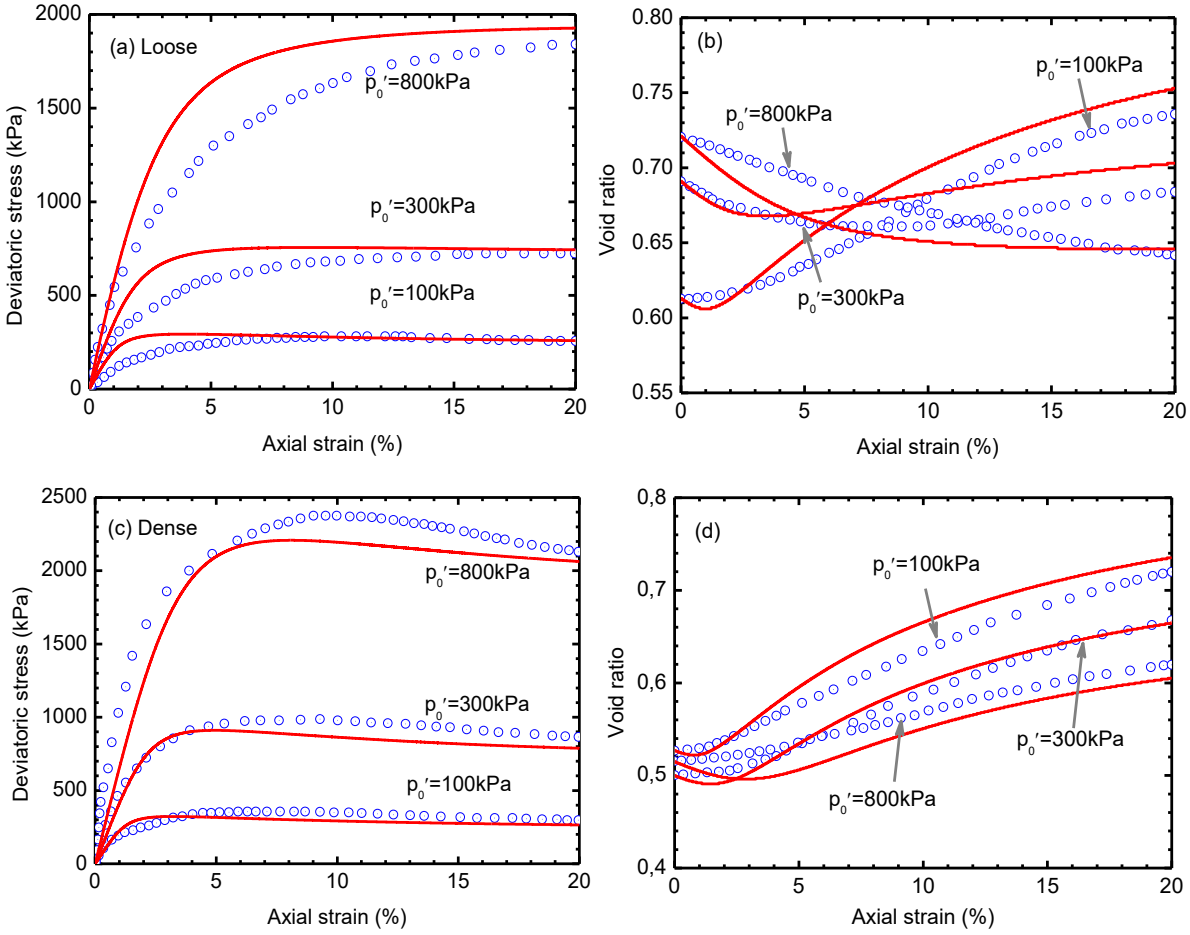

Figure 2.2 Experimental data and simulations for Hostun sand: triaxial drained testes (a) deviatoric stress versus axial strain for loose sand, (b) void ratio versus axial strain for loose sand, (c) deviatoric stress versus axial strain for dense sand, (d) void ratio versus axial strain for dense sand. (experimental data from Biarez and Hicher, 1994)

The force path at the micro level depends on the contact orientation, as shown in Figure 2.3(a). The 54° contact orientation contained the maximum force ratio and was the first one to reach the maximum strength condition at the micro scale. This angle comes closest to the macroscopic failure plane angle ($45°+\phi_{\mu}/2=61.5°$) among the selected angles of all the

integration points. Figure 2.3(b) shows clearly that the 54° direction underwent large displacement.

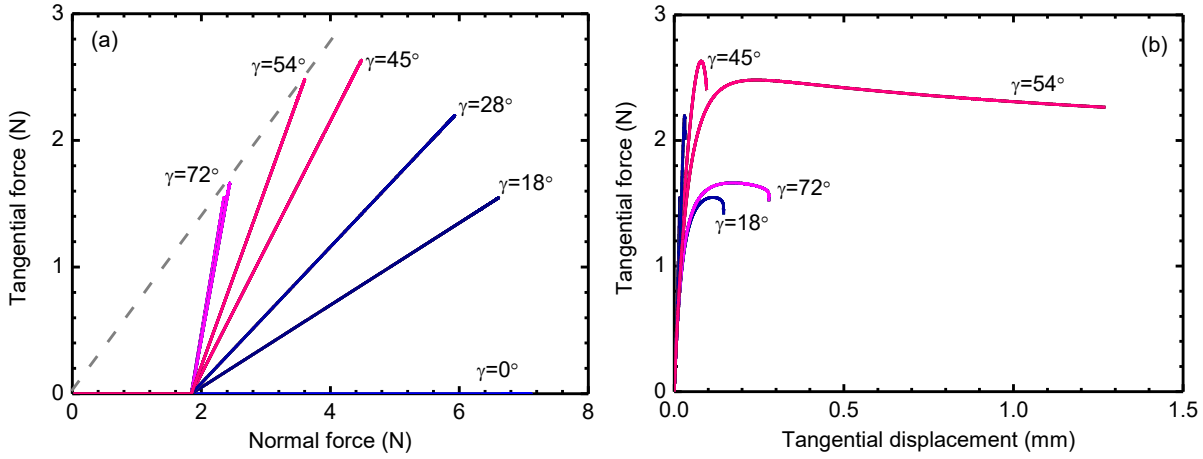

Figure 2.3 Local behaviour of dense sand ($p_0' = 800\,\text{kPa}$): (a) tangential force versus normal force; (b) tangential force versus tangential displacement

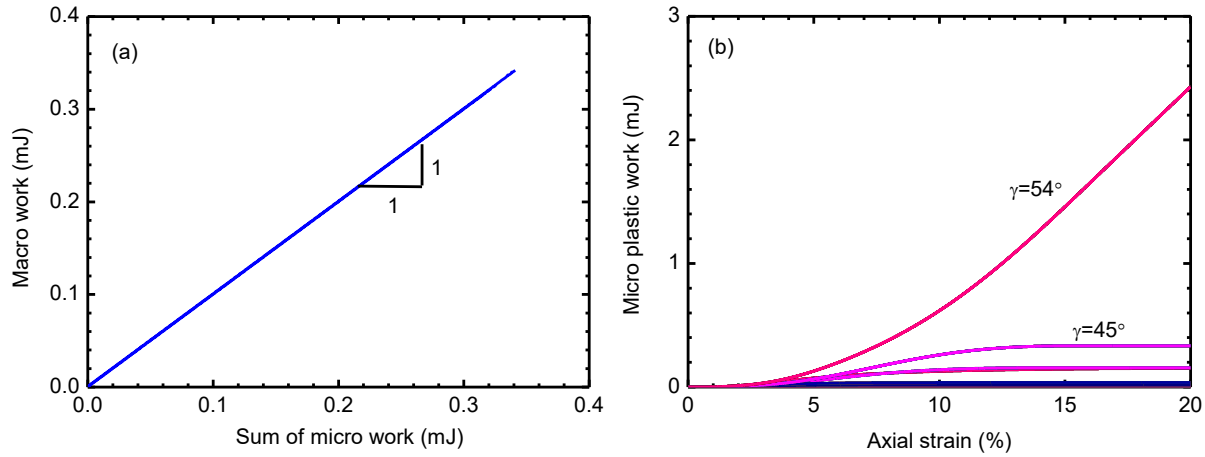

Figure 2.4 Total work and plastic work of dense sand ($p_0' = 800\,\text{kPa}$): (a) total work in macro scale and micro scale during loading, (b) plastic work evolution for various integration directions

As shown in Figure 2.4(a), the work input at the macro scale is equal to the volumetric average of the total work at the micro scale, which indicates that the energy dissipation is consistent at the two scales. At the micro scale, the evolution of the plastic work shows that the local plastic work is the highest in the 54° contact orientation, as shown in Figure 2.4(b). Figure 2.5(b)-(e) shows the distribution of the dissipative energy along each direction during

shearing. The maximum micro dissipation energy was found in the 54° direction, in agreement with the intensity of the tangential displacement in that direction. The direction of the failure plane corresponds to the direction of the maximum dissipation.

The isotropic compression stage was also simulated to evaluate the free energy in the micromechanical model. As shown in Figure 2.5(a), the increase of the free energy at micro scale is isotropic, whereas the dissipation energy is always zero. This is in agreement with the fact that the Helmholtz free energy depends only on elasticity but not on back force.

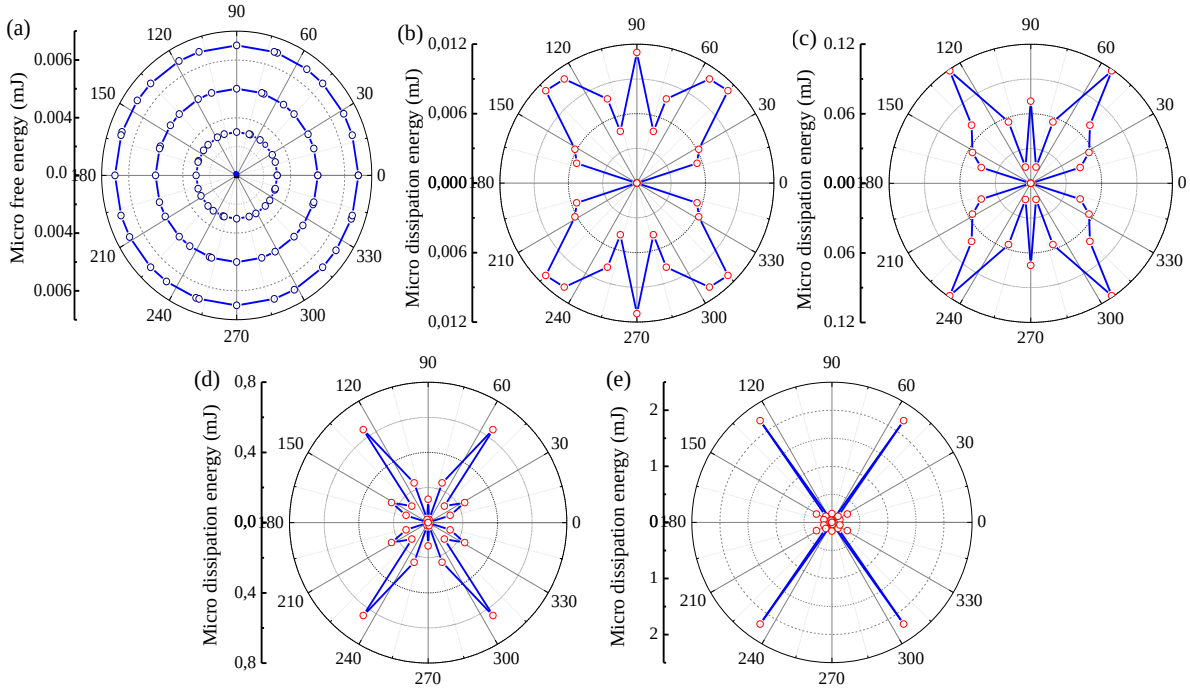

Figure 2.5 Free energy and dissipation energy evolution at the micro scale of dense sand under drained compression ($e_0 = 0.549$, $p'_0 = 800$ kPa): (a) free energy under isotropic compression, (b) dissipation energy at axial strain 2.14%, (c) dissipation energy at axial strain 4.94%, (d) dissipation energy at axial strain 10.14%, (e) dissipation energy at axial strain 20%

The evolution of the dissipation energy at the micro level under undrained triaxial conditions was also investigated by imposing the condition of a constant volumetric strain during loading. Figure 2.6(a) shows that at small strain levels, all the directions had a similar degree of dissipation. With the increase of the shearing strain, the maximum dissipation developed also in the 54° direction, as shown in Figure 2.6(b)-(e).

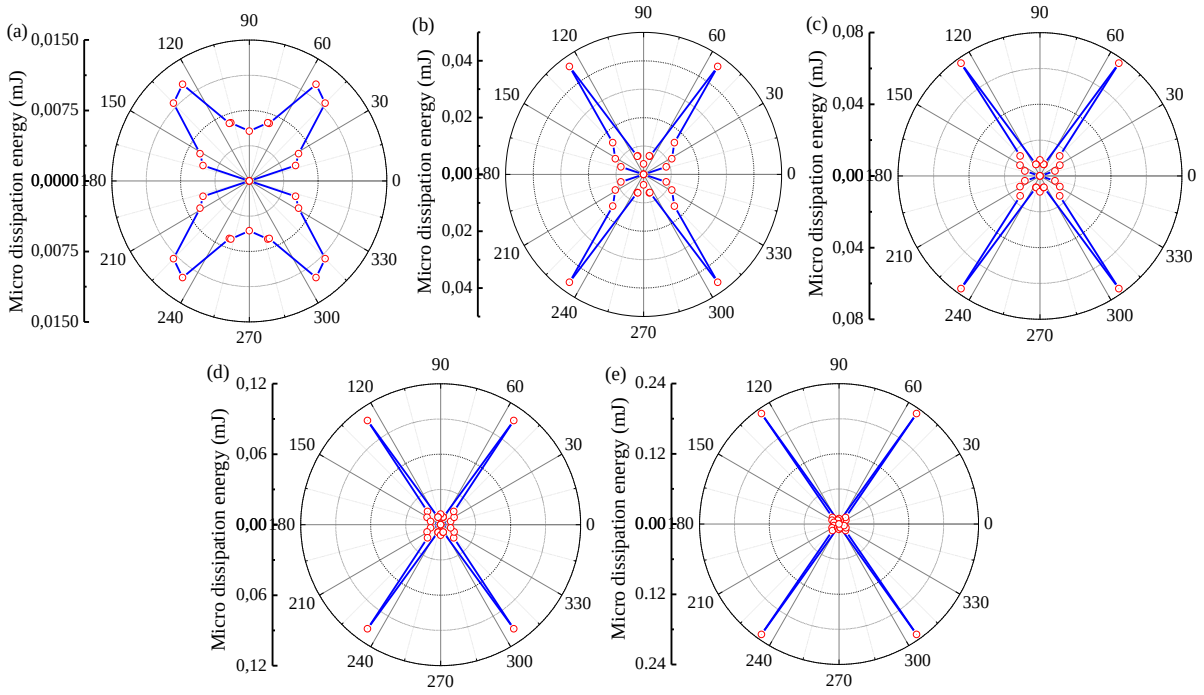

Figure 2.6 Dissipation energy evolution at the micro scale of loose sand under undrained compression ($e_0 = 0.9$, $p'_0 = 800\,\text{kPa}$): (a) dissipation energy at axial strain 1%, (b) dissipation energy at axial strain 3%, (c) dissipation energy at axial strain 6%, (d) dissipation energy at axial strain 12%, (e) dissipation energy at axial strain 20%

2.5 Concluding remarks

This chapter has presented a thermomechanical framework for micromechanical constitutive models of elastic-plastic granular materials, which can be applied to construct thermodynamically consistent models and to re-examine the existing micromechanical models, more specifically to clarify the assumptions in the derivations of the model suggested by Chang and Hicher (2005). The main achievements and conclusions of this chapter are as follow:

1) A thermomechanical framework for elasto-plastic micromechanical models has been presented. Based on conventional thermodynamics, energy conservation, free energy and dissipation potentials were formulated at the micro scale. Elasticity and plasticity at inter-particle contacts could be deduced from the two energy functions. The micro state variables, elastic and plastic displacements, were used to formulate the micro Helmholtz

free energy and the dissipation energy. Back force and dissipative force were defined from energy functions. The relationship between elastic work, free energy, plastic work, dissipation energy and stored energy were analysed at the micro scale. By using Legendre transformation, the micro yield criterion in the dissipative space could be deduced from the dissipative potential. This criterion could also be transferred into the force space after the back force was defined. Accordingly, the micro flow rule and the hardening law could be deduced from the dissipative potential.

2) Based on the thermomechanical formulation, a thermodynamically consistent micromechanical model for granular soils was constructed. The local laws of elasticity and plasticity, the micro-macro relationships, the micromechanical integration method and the implementation scheme were presented. The plastic work at the micro scale was computed, from which the micro stored energy increment was shown to be zero, i.e., all the plastic work is dissipated and the elastic work is equal to the free energy. The dissipation energy proved to be greater than zero, which shows that the micromechanical model satisfies thermodynamics. The validity of the static hypothesis adopted in this micromechanical model was also demonstrated through the expressions of the Helmholtz free energy and of the Gibbs free energy. The relation between the static hypothesis and the Love-Weber formula has also been analysed and an unbalanced iteration process was required for their consistence.

3) Isotropic compression and triaxial tests were simulated by the micromechanical model in order to analyse the energy conservation and dissipation during mechanical loading. The total input work is conserved both at the micro and macro scales. At the isotropic compression stage, the material remained in the elastic domain and, as a consequence, the plastic work in all directions was equal to zero. However, it increased significantly in the direction of 54° under shearing, whereas other directions showed a significantly smaller amount of plastic work. The micro free energy developed isotropically under isotropic loading, whereas the micro dissipation energy reached its maximum value in the 54° direction under shearing. The maximum micro dissipation energy was in agreement with

the static hypothesis which, if one direction reaches the limit state, predicts a global failure at the macro scale.

CHAPTER 3 MULTISCALE MODELLING OF UNSATURATED GRANULAR SOILS BASED ON THERMODYNAMIC PRINCIPLES

3.1 Introduction

The slope instability largely caused by precipitation and infiltration is strongly related to the behaviour of unsaturated granular soils (e.g., Ng and Shi, 1998; Cho and Lee, 2001; Fredlund *et al*., 2012). Unsaturated granular soils are three-phase granular materials composed of soil particles, water and air. Thus, the macroscopic behaviour of unsaturated granular soils is highly dependent on the characteristics of the components and on their interactions. Usually, solid particles and fluid are assumed to be incompressible, conversely air is compressible. Three interaction pairs, i.e. the interactions between solid and fluid, solid and air, as well as fluid and air exist. The cause of these interactions is typically understood from the capillary forces exerted by the water menisci between particles. The magnitude of the capillary forces, which relates to the degree of saturation, can cause significant changes in volume, shear strength and hydraulic properties of granular soils (Gens, 2010; Sheng, 2011).

For simulating the behaviour of unsaturated soils, phenomenological models have been developed in the last three decades (Alonso *et al*., 1990; Wheeler and Sivakumar, 1995; Cui and Delage, 1996; Sheng *et al*., 2004; Gens, 2010; Sheng, 2011; Fredlund *et al*., 2012). The earlier developments tended to adopt net stress and suction as independent stress variables and to extend the available elastoplastic models for saturated soils by introducing suction-dependent compressibility and yield surface (for instance, Alonso *et al*., 1990; Cui and Delage, 1996; Sheng *et al*., 2004). One result of this approach is the Barcelona Basic Model (BBM) suggested by Alonso *et al*. (1990), in which a suction-dependent loading collapse curve (LCC) was introduced based on the modified Cam-clay model. Alternatively, many attempts have been made to define an effective stress in order to represent the deformation of the soil skeleton for unsaturated soils (Bishop and Blight, 1963; Zhao *et al*., 2010; Buscarnera and Einav, 2012; Li *et al*., 2017). By using the effective stress concept, the hydraulic hysteresis

phenomenon and the transitional behaviour from the unsaturated to the saturated state can be effectively captured.

From a physical point of view, the formation of water menisci located between neighbouring grains produces capillary forces on the grains. Based on this observation, the CH micromechanical framework for saturated granular soils was extended to study the hydro-mechanical behaviour of unsaturated granular materials (Hicher and Chang, 2007). In this model, the capillary forces between inter-particle contacts are assumed to be dependent on the degree of saturation and integrated with the same homogenization method as for the mechanical forces. The Love-Weber formula that was adopted for the soil skeleton was also used to sum the capillary forces as a tensor-type capillary stress, meanwhile the same static hypothesis based localisation operator was used in the hydraulic part (Hicher and Chang, 2007; Scholtès *et al*., 2009). However, recent DEM simulations show that it is questionable to use the Love-Weber formula to determine a capillary stress tensor (Duriez and Wan, 2016; Chalak *et al*., 2017; Wang *et al*., 2017). In addition, the relation between the capillary force and the degree of saturation was given by an empirical formulation with several *ad hoc* parameters.

It should be mentioned that the capillary stress tensors were suggested as a stress state variable to replace the suction to represent the effect of water menisci since there are some limitations in using the suction (Li, 2003; Hicher and Chang, 2007; Lu, 2008; Scholtès *et al*., 2009; Duriez and Wan, 2016; Jiang *et al*., 2017). One of the limitations is that the microscale capillary forces are directional vectors which could not be always globally described by the scalar quantity suction. For instance, an initially isotropic unsaturated granular soil becomes anisotropic under shearing, thus the distribution of the capillary forces may also be anisotropic. However, it is difficult to measure the tensor-type capillary stress in laboratory tests and currently it is only possible to quantify it in discrete element simulations by using the Young-Laplace equation to describe the behaviour of capillary bridges in the pendular regime (Scholtès *et al*., 2009; Chalak *et al*., 2017; Wang *et al*., 2017).

Since the thermodynamics with internal variables (Houlsby and Puzrin, 2007) forms a coherent framework within which constitutive relations can be developed with few *ad hoc* assumptions and procedures, various studies have produced constitutive models which are thermodynamically consistent (Li, 2007; Coussy *et al*., 2010; Dangla and Pereira, 2014). By analysing the work input on an unsaturated representative volume element, the effective stress could be derived and conjugated to the deformation of the solid skeleton (Houlsby, 1997; Zhao *et al*., 2010; Coussy *et al*., 2010; Li *et al*., 2017). However, current thermodynamically consistent models for unsaturated granular soils are phenomenological (Sheng, 2004; Coussy *et al*., 2010; Li *et al*., 2017).

Given the described limitations of current constitutive relations for unsaturated granular soils, this chapter aims to construct a micromechanical model for unsaturated granular soils based on thermodynamic principles. For this purpose, the thermodynamic approach with internal variables has been developed to multiscale modelling of unsaturated granular soils by considering that the only source of energy dissipation is through friction at the inter-particle contacts during loading. The energy conservation at the micro and macro scales is first presented, before discussing the separation of the energy into a mechanical and a hydraulic part. The thermodynamically consistent micromechanical model constructed in Chapter 2 is adopted for the mechanical deformation of the solid skeleton, while a particle size dependent potential function is introduced for the hydraulic part.

3.2 Review of application of thermodynamic principles to unsaturated granular soils

At the continuum level, thermodynamic principles involving internal variables have been applied to construct constitutive relations for partially saturated granular soils (Houlsby, 1997; Zhao *et al*., 2010; Zhang, 2016; Li *et al*., 2017). In this study, the following assumptions used in these models are adopted: (1) solids and water are incompressible; (2) the RVE is subjected to small deformation; (3) capillary forces represent the effect of interactions between the components. For simplicity, this study considers only the RVE under iso-thermal boundary condition, as shown in Figure 3.1.

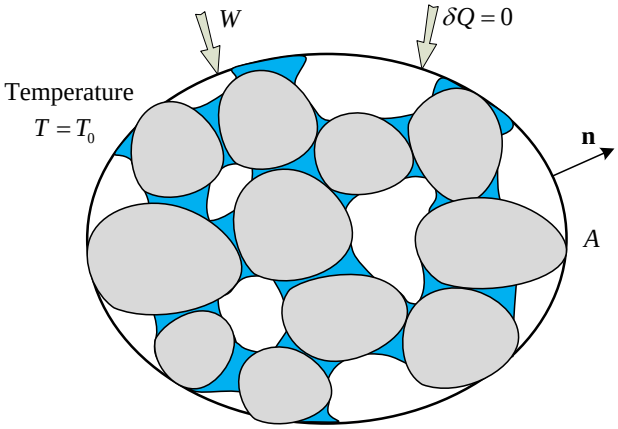

Figure 3.1 RVE of unsaturated granular soil as a closed thermodynamic system

3.2.1 The rate of work input

There are several derivations of work input in literature, each of which has the purpose of establishing the work conjugacy between effective stresses and strains (for instance, Hassanizadeh and Gray, 1980; Lewis and Schrefler, 1987; Houlsby, 1997; Sheng *et al*., 2004; Li, 2007; Coussy *et al*., 2010; Zhao *et al*., 2011; Li *et al*., 2017; Jiang *et al*., 2017). In this subsection, we will follow the formulation suggested by Houlsby (1997) with the tensor notations used by Zhang (2016). After denoting the porosity of RVE as n and its degree of saturation as S_r, the volume of solid, water and air can be expressed as $1\text{-}n$, nS_r and $(1\text{-}S_r)n$, as shown in Figure 3.2. At the continuum scale, the total stresses in the RVE originate from the solid stress **s**, from the air pressure u_a, from the water pressure u_w and from the water-air interactions **T**.

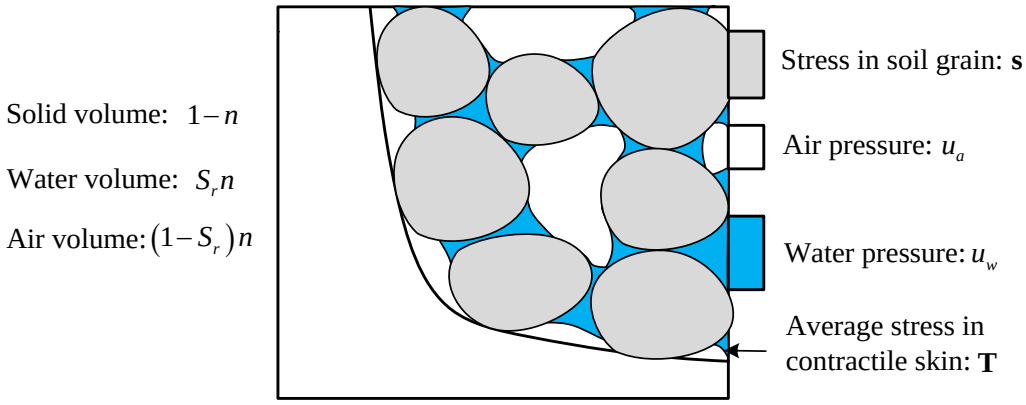

Figure 3.2 Total stresses in a RVE of unsaturated granular soils (figure from Zhang, 2016)

The total stress in the RVE can be obtained by adding the stresses in the described four components, expressed as

$$\boldsymbol{\sigma} = n\left[S_r u_w + \left(1-S_r\right)u_a\right]\mathbf{I} + \left(1-n\right)\mathbf{s} + \mathbf{T} \tag{3.1}$$

Similarly, the density of the RVE can be written as:

$$\rho = n\left[S_r \rho_w + \left(1-S_r\right)\rho_a\right] + \left(1-n\right)\rho_s \tag{3.2}$$

in which ρ_s, ρ_w and ρ_a are densities of the solid, water and air. Using the expressions of Eqs. (3.1) and (3.2), the equilibrium equation for the RVE can be given as

$$\nabla \cdot \boldsymbol{\sigma} - \rho \mathbf{g} = 0 \tag{3.3}$$

where **g** is the gravitational acceleration vector.

The mass balance equations for solid, water and air can be expressed as

$$\frac{d}{dt}\int_V \rho_s \left(1-n\right) dV = -\int_A \rho_s \left(1-n\right)\mathbf{v}\cdot\mathbf{n}dA \tag{3.4}$$

$$\frac{d}{dt}\int_V \rho_w n S_r dV = -\int_A \rho_w n S_r \mathbf{f_w}\cdot\mathbf{n}dA \tag{3.5}$$

$$\frac{d}{dt}\int_V \rho_a n\left(1-S_r\right) dV = -\int_A \rho_a n\left(1-S_r\right)\mathbf{f_a}\cdot\mathbf{n}dA \tag{3.6}$$

in which **v** is the velocity vector for the solids; $\mathbf{f_w}$ and $\mathbf{f_a}$ are the average velocities of the water and air phases; *V* is the volume of the RVE and *A* is the bounding area of the RVE; **n** is the outward normal to the surface *A*, as shown in Figure 3.1. Applying the Gauss divergence theorem, and noting that both ρ_s and ρ_w are constant (under the assumption of the incompressibility of the solids and water), and making use of the fact that *V* is arbitrary, we obtain

$$\nabla \cdot \mathbf{v} = \frac{\dot{n}}{1-n} \tag{3.7}$$

$$\nabla \cdot \mathbf{f_w} = -\frac{\dot{S}_r}{S_r} - \frac{\dot{n}}{n} \tag{3.8}$$

$$\nabla \cdot \mathbf{f_a} = \frac{\dot{S}_r}{(1-S_r)} - \frac{\dot{n}}{n} - \frac{\dot{\rho}_a}{\rho_a} \tag{3.9}$$

The power input for the RVE can be written as:

$$\begin{aligned} \int_V \delta W dV = -\int_A \left\{ n\left[S_r u_w \mathbf{f_w} + (1-S_r) u_a \mathbf{f_a} \right] + (1-n)\mathbf{v}\cdot\mathbf{s} + \mathbf{v}\cdot\mathbf{T} \right\} \cdot \mathbf{n} dA + \\ \int_V \left\{ n\left[S_r \rho_w \mathbf{f_w} + (1-S_r)\rho_a \mathbf{f_a} \right] + (1-n)\rho_s \mathbf{v} \right\} \cdot \mathbf{g} dV \end{aligned} \tag{3.10}$$

in which the four terms included in the surface integral are the power input driven by water, air, solids and contractile skin, whereas the three terms included in the volume integral are power input due to gravitational forces in connection with the mass flow of water, air and solids. Inserting Eqs. (3.1) and (3.2) into Eq. (3.10), we obtain

$$\begin{aligned} \int_V \delta W dV = -\int_A \left\{ n\left[S_r u_w (\mathbf{f_w} - \mathbf{v}) + (1-S_r) u_a (\mathbf{f_a} - \mathbf{v}) \right] + \mathbf{v}\cdot\boldsymbol{\sigma} \right\} \cdot \mathbf{n} dA + \\ \int_V \left\{ n\left[S_r \rho_w (\mathbf{f_w} - \mathbf{v}) + (1-S_r)\rho_a (\mathbf{f_a} - \mathbf{v}) \right] + \rho \mathbf{v} \right\} \cdot \mathbf{g} dV \end{aligned} \tag{3.11}$$

It is assumed that the spatial variations of n and S_r are negligible and that the seepage velocities of water and air phases can be defined as:

$$\mathbf{w_w} = nS_r(\mathbf{f_w} - \mathbf{v});\ \mathbf{w_a} = n(1-S_r)(\mathbf{f_a} - \mathbf{v}) \tag{3.12}$$

Substituting Eq. (3.12) into Eq. (3.11) leads to:

$$\int_V \delta W dV = -\int_A \{ u_w \mathbf{w_w} + u_a \mathbf{w}_a + \mathbf{v}\cdot\boldsymbol{\sigma} \} \cdot \mathbf{n} dA + \int_V \{ \rho_w \mathbf{w_w} + \rho_a \mathbf{w}_a + \rho \mathbf{v} \} \cdot \mathbf{g} dV \tag{3.13}$$

Eq. (3.13) can be written in the local form by using the divergence theorem:

$$\delta W = \mathbf{w_w} \cdot (\rho_w \mathbf{g} - \nabla u_w) + \mathbf{w_a} \cdot (\rho_a \mathbf{g} - \nabla u_a) + \rho \mathbf{v}\cdot\mathbf{g} - u_w \nabla\cdot\mathbf{w_w} - u_a \nabla\cdot\mathbf{w_a} - \nabla\cdot(\mathbf{v}\cdot\boldsymbol{\sigma}) \tag{3.14}$$

Eq. (3.14) can be simplified by inserting the equilibrium equation of Eq. (3.3):

$$\delta W = \mathbf{w_w} \cdot (\rho_w \mathbf{g} - \nabla u_w) + \mathbf{w_a} \cdot (\rho_a \mathbf{g} - \nabla u_a) - u_w \nabla\cdot\mathbf{w_w} - u_a \nabla\cdot\mathbf{w_a} - + \boldsymbol{\sigma} : \nabla \mathbf{v} \tag{3.15}$$

The gradients of seepage velocities of water and air phases in Eq. (3.15) can be replaced by inserting Eqs.(3.7), (3.8) and (3.9) into Eq. (3.12) and considering $\nabla\cdot\mathbf{v} = -\mathrm{tr}(\dot{\boldsymbol{\varepsilon}})$, given as

$$\nabla\cdot\mathbf{w_w} = -n\dot{S}_r + S_r \mathrm{tr}(\dot{\boldsymbol{\varepsilon}});\ \nabla\cdot\mathbf{w_a} = n\dot{S}_r + (1-S_r)\mathrm{tr}(\dot{\boldsymbol{\varepsilon}}) - n(1-S_r)\frac{\dot{\rho}_a}{\rho_a} \tag{3.16}$$

By substituting Eq. (3.16) into Eq. (3.15), and given that $\nabla\mathbf{v}=-\dot{\boldsymbol{\varepsilon}}$, the work input of RVE can be obtained

$$\delta W=-\mathbf{w}_{\mathbf{w}}\cdot\nabla u_w^e-\mathbf{w}_{\mathbf{a}}\cdot\nabla u_a^e+n\left(1-S_r\right)u_a\frac{\dot{\rho}_a}{\rho_a}-ns\dot{S}_r+\left[\boldsymbol{\sigma}-u_a\mathbf{I}+sS_r\mathbf{I}\right]:\dot{\boldsymbol{\varepsilon}} \tag{3.17}$$

in which $\nabla u_w^e=\nabla u_w-\rho_w\mathbf{g}$ and $\nabla u_a^e=\nabla u_a-\rho_a\mathbf{g}$ are gradients of excess pore pressure; s is the matric suction computed by $s=u_a-u_w$. Eq. (3.17) indicates that several work-conjugate pairs of external variables exist. The first two terms are the relative flow velocities and are work conjugated with the gradients of excess pore pressures. The third term demonstrates that the smeared air pressure $n\left(1-S_r\right)u_a$ is conjugated with the volumetric strain of air $\dot{\rho}_a/\rho_a$. The fourth term is the smeared suction ns work-conjugated with the rate of the degree of saturation $\dot{S}_r$. The last one displays that the quantity which is work conjugate with the strains is a stress term $\boldsymbol{\sigma}-u_a\mathbf{I}+sS_r\mathbf{I}$. This term is an expression of the effective stress tensor

$$\boldsymbol{\sigma}'=\boldsymbol{\sigma}-u_a\mathbf{I}+sS_r\mathbf{I}=\boldsymbol{\sigma}^{net}+sS_r\mathbf{I} \tag{3.18}$$

which corresponds to Bishop's expression (1963) of the effective stress with χ=S_r. It should be mentioned that Eq. (3.18) does not imply that unsaturated soils can be simply described by Bishop's effective stress tensor with χ=S_r, since it states that the mechanical behaviour of an unsaturated soil is also governed by the suction (Houlsby, 1997).

For rate-independent problems, the seepage velocities of the water and air phases are negligible, so the first two terms of Eq. (3.17) become zero. During conventional experimental loadings, air pressure is usually equal to atmosphere pressure, thus the air pressure can be further assumed to be constant, which implies that the third term of Eq. (3.17) can be neglected. With these hypotheses, Eq. (3.17) can be simplified as

$$\delta W=\boldsymbol{\sigma}':\dot{\boldsymbol{\varepsilon}}-ns\dot{S}_r \tag{3.19}$$

in which the first term represents the mechanical work input due to the deformation of the solid phase and the second term takes into account the hydraulic work input by means of changes in the water content (Houlsby, 1997; Zhang, 2016).

3.2.2 The Helmholtz free energy potential function

As discussed by Coussy *et al*. (2010), the free energy can be split into three parts: the recoverable elastic energy stored in the soil skeleton, the locked-in energy stored in the soil skeleton during an irreversible mechanical process and the hydraulic energy stored in the soil-water interface. In this study, we further assume that the locked-in energy is negligible and thus the Helmholtz free energy function is reversible and only depends on the elastic strain and on the degree of saturation. As suggested by Buscarnera and Einav (2012), this function can be further decomposed in a mechanical part and a hydraulic part, expressed as:

$$d\psi\left(\boldsymbol{\varepsilon}^{e}, S_{r}\right) = d\psi^{M}\left(\boldsymbol{\varepsilon}^{e}\right) + d\psi^{H}\left(S_{r}\right) \tag{3.20}$$

where $d\psi$ is the differential of the Helmholtz free energy; $d\psi^{M}$ represents the free energy held by the soil skeleton; $d\psi^{H}$ is the free energy stored in the water menisci. The mechanical part ψ^{M} is given as:

$$\psi^{M}\left(\boldsymbol{\varepsilon}^{e}\right) = \frac{1}{2}K\boldsymbol{\varepsilon}^{e} : \boldsymbol{\varepsilon}^{e} + G\mathbf{e}^{e} : \mathbf{e}^{e} \tag{3.21}$$

in which K and G are the effective bulk and shear moduli, whereas the elastic deviatoric strain is defined as $e_{ij}^{e} = \varepsilon_{ij}^{e} - \frac{1}{3}\delta_{ij}\varepsilon_{kk}^{e}$. In addition, a quadratic form of the hydraulic part, expressed as

$$\psi^{H}\left(S_{r}\right) = \frac{1}{2}K_{w}\left(1 - S_{r}\right)^{2} \tag{3.22}$$

was compared with a logarithmic form:

$$\psi^{H}\left(S_{r}\right) = K_{w}\left[S_{r} - \ln\left(S_{r}\right) - 1\right] \tag{3.23}$$

where K_{w} is a retention curve parameter associated with the value of the air entry suction (Buscarnera and Einav, 2012). It was found that the logarithmic form is closer to the experimental data, whereas they both share the same property of zero suction $s = 0$ at a fully saturated state $S_{r} = 1$.

Another direction for defining a free energy function is to analyse the energy of the constructed constitutive model. For instance, based on the analysis of the work input equation,

Sheng *et al*. (2004) suggested a stored energy potential under triaxial loading condition, given as

$$d\psi = \frac{1}{2} p_c d\varepsilon_v^p + \left(ns_I dS_r^p \text{ or } ns_D dS_r^p \right) \tag{3.24}$$

where p_c is the pre-consolidation pressure; s_I and s_D are the suction increase and decrease during loading; $d\varepsilon_v^p$ is the plastic volumetric strain increment; dS_r^p is the plastic increment of S_r.

3.2.3 The dissipative rate function

Since it is difficult to define a dissipative function to incorporate the frictional behaviour of granular soils, researchers attempted to construct constitutive models and then proved them to satisfy the thermodynamic principles. For example, to verify the satisfaction of the second law of thermodynamics of the constitutive models constructed by Sheng *et al*. (2004), dissipative rate functions were deduced. Sheng *et al*. (2004) obtained a dissipation function expressed as

$$\varpi = \frac{1}{2} p_c \frac{\left(d\varepsilon_v^p \right)^2 + \frac{M^2}{\zeta} \left(d\varepsilon_\gamma^p \right)^2}{\sqrt{\left(d\varepsilon_v^p \right)^2 + \frac{M^2}{\zeta} \left(d\varepsilon_\gamma^p \right)^2}} \geq 0 \tag{3.25}$$

where M and ζ are model parameters, $d\varepsilon_\gamma^p$ is the increment of deviatoric plastic strain. Similarly, Coussy *et al*. (2010) derived the dissipative rate function of the well-known Barcelona Basic Model (BBM), given as

$$\varpi = d\lambda \left(p_0 + p_s \right) \left(p_0 - p^B \right) \geq 0 \tag{3.26}$$

in which $d\lambda$ is the plastic multiplier thus it is always positive; p_s is the tensile strength which is a function of S_r; p^B is the extended Bishop's stress which is always less equal to the pre-consolidation pressure p_0. Therefore, the dissipative energy is always positive or null.

Given the difficulties in defining a dissipative rate function, the CH micromechanical model (Chang and Hicher, 2005) is modified to describe the deformation of the skeleton and it is proved that this model satisfies the thermodynamic principles, as described in Chapter 2.

3.3 A thermomechanical model for unsaturated granular soils

Since the deformation of a soil specimen originates from the relative displacement and rearrangements at the inter-particle contacts, the energy is dissipated and stored between these contacts. Given these considerations, it seems reasonable to construct a micromechanical model which is thermodynamically consistent at both the inter-particle contact and the representative volume levels.

3.3.1 A multiscale thermodynamic framework

3.3.1.1 Macroscopic energy conservation

In the following subsections, the aforementioned assumptions that soil particles and water are incompressible and that relative movement between grains and water menisci can be neglected, are also adopted. Additionally, the rate of work input, Eq.(3.19), introduced by Houlsby (1997) is adopted.

These assumptions imply that the dissipation related to the change of saturation is considered as negligible. In other words, the hydraulic energy appears only in the formulation of the Helmholtz free energy. Generally, the hyper-elastic expression is based on two kinematic state variables, i.e., the macro strain and the degree of saturation, and can be decomposed into two additive parts, as described by Eq. (3.20). In comparison, the dissipation energy increment is assumed to be a homogeneous function of degree 1 in terms of the increment of plastic strains:

$$\varpi\left(\dot{\boldsymbol{\varepsilon}}\right)=\varpi\left(\dot{\boldsymbol{\varepsilon}}^{p}\right)\geq 0 \tag{3.27}$$

By substituting the work input Eq.(3.19), the Helmholtz free energy function Eq. (3.20) and the dissipative rate function Eq. (3.27) into the energy conservation $\delta W = d\psi + \varpi$, one can obtain

$$\left(\boldsymbol{\sigma}' - \frac{\partial \psi}{\partial \boldsymbol{\varepsilon}^e}\right) : \dot{\boldsymbol{\varepsilon}}^e + \left(\boldsymbol{\sigma}' - \frac{\partial \varpi}{\partial \dot{\boldsymbol{\varepsilon}}^p}\right) : \dot{\boldsymbol{\varepsilon}}^p - \left(ns + \frac{\partial \psi}{\partial S_r}\right)\dot{S}_r = 0 \tag{3.28}$$

Since Eq. (3.28) is satisfied for the whole representative volume, the relationship between *ns* and the degree of saturation is given by:

$$ns = -\frac{\partial \psi}{\partial S_r} = -\frac{\partial \psi^H\left(S_r\right)}{\partial S_r} \tag{3.29}$$

And the effective stress can be obtained by:

$$\boldsymbol{\sigma}' = \frac{\partial \psi\left(\boldsymbol{\varepsilon}^e\right)}{\partial \boldsymbol{\varepsilon}^e} \tag{3.30}$$

3.3.1.2 Micro-macro energy relations

In order to derive the inter-particle contact law from thermomechanical considerations, the relations between the work input, the free energy and the dissipation energy at the micro and macro scales should be constructed. To this purpose, the volumetric techniques for relating energy at different scales used by Chang and Ma (1990) and Misra and Singh (2015) have been adopted. The macro energy quantities are assumed to be volumetric averages of micro energy quantities

$$\delta W = \frac{1}{V}\sum_{c=1}^{N}\delta W^c \ , \ d\psi = \frac{1}{V}\sum_{c=1}^{N} d\psi^c \ \text{ and } \ \varpi = \frac{1}{V}\sum_{c=1}^{N}\varpi^c \tag{3.31}$$

in which *c* is the interparticle contact defined as contacts between particles with or without the presence of liquid bridges; *N* is the number of particle contacts in a volume *V* of RVE.

Table 3.1 Micro-macro relations of energetic quantities

Work input	Helmholtz free energy	Dissipative energy
$\delta W = \frac{1}{V}\sum_{c=1}^{N}\delta W^c$	$d\psi = \frac{1}{V}\sum_{c=1}^{N} d\psi^c$	$\varpi = \frac{1}{V}\sum_{c=1}^{N}\varpi^c$
$\delta W^c = \delta W^{cM} + \delta W^{cH}$	$d\psi^c = d\psi^{cM} + d\psi^{cH}$	$\varpi^c = \varpi^{cM}$
$\delta W^{cM} = f_i^c \cdot \dot{\delta}_i^c$	$d\psi^{cM} = d\psi^{ce}\left(\boldsymbol{\delta}^{ce}\right)$	$\varpi^{cM} \geq 0$
δW^{cH}	$d\psi^{cH}$	–

Since the strain tensor can be calculated from the displacements at the inter-particle contacts, the displacement at the microscale level should be considered as an internal variable. Its work-conjugate is then the inter-particle contact force. According to experimental studies and analytical theories that are consistent with the Young-Laplace equation for capillary bridges between spheres of equal radii, capillary bridge forces depend on the capillary bridge volume and the distance between two particles, hence the two quantities can be used as hydraulic internal variables at the microscale. The relations of the work input, Helmholtz free energy and dissipative energy at the microscale and at the macroscale are shown in Table 3.1.

3.3.1.3 Microscopic energy conservation

In comparison to the macroscopic mechanical free energy that depends only on elastic strain, the microscopic mechanical elastic work input is equal to the microscopic mechanical Helmholtz free energy, expressed as

$$\delta W^{cMe} = f_i^c \dot{\delta}_i^{ce} = d\psi^{cM} = \frac{\partial \psi^{cM}\left(\boldsymbol{\delta}^{ce}\right)}{\partial \boldsymbol{\delta}^{ce}} d\boldsymbol{\delta}^{ce} \tag{3.32}$$

in which $\boldsymbol{\delta}^{ce}$ is elastic displacements at the interparticle contacts. Also at the micro scale, the plastic work input is equated to the dissipative energy, since the free energy does not depend on plastic displacements

$$\delta W^{cMp} = f_i^c \dot{\delta}_i^{cp} = \varpi^{cM} = \frac{\partial \varpi^{cM}(\dot{\boldsymbol{\delta}}^{cp})}{\partial \dot{\boldsymbol{\delta}}^{cp}} d\boldsymbol{\delta}^{cp} \tag{3.33}$$

where $\boldsymbol{\delta}^{cp}$ is plastic displacement at the interparticle contacts.

Given the capillary bridge volumes and the distances between particles, the capillary bridge forces can be calculated. Therefore, a potential expression for the hydraulic work input can be given as

$$\delta W^{cH} = f_d^{cap} \dot{\delta}^{cap} + f_v^{cap} \dot{v}^{cap} \tag{3.34}$$

in which δ^{cap} is the distance between two particles; $\dot{v}^{cap} = \dot{V}^{cap} / r^2$ with V^{cap} being the capillary bridge volume and r is the mean radius of particles which is a material constant; f_d^{cap} and f_v^{cap} are capillary bridge forces due to the change of the particle distance and of the

capillary bridge volume. Based on the adopted hypothesis that the change of amount of water will not dissipate the energy, the microscopic hydraulic work input is hence equal to the microscopic hydraulic free energy, given by

$$\delta W^{cH} = d\psi^{cH}(V^{cap}, \delta^{cap}) = \frac{\partial \psi^{cH}(V^{cap}, \delta^{cap})}{\partial \delta^{cap}} d\delta^{cap} + \frac{\partial \psi^{cH}(V^{cap}, \delta^{cap})}{\partial V^{cap}} dV^{cap} \qquad (3.35)$$

Substituting Eqs.(3.32), (3.33), (3.34) and (3.35) into the energy conservation $\delta W^c = d\psi^c + \varpi^c$ at the microscale, we obtain

$$\left(\mathbf{f}^c - \frac{\partial \psi^{cM}}{\partial \boldsymbol{\delta}^{ce}}\right)\dot{\boldsymbol{\delta}}^{ce} + \left(\mathbf{f}^c - \frac{\partial \varpi^{cM}}{\partial \dot{\boldsymbol{\delta}}^{cp}}\right)\dot{\boldsymbol{\delta}}^{cp} + \left(f_d^{cap} - \frac{\partial \psi^{cH}}{\partial \delta^{cap}}\right)\dot{\delta}^{cap} + \left(f_v^{cap} - r^2 \frac{\partial \psi^{cH}}{\partial V^{cap}}\right)\dot{v}^{cap} = 0 \qquad (3.36)$$

Since Eq.(3.36) is satisfying for any interparticle displacement, capillary bridge volume and particle distance, it follows that

$$\mathbf{f}^c = \frac{\partial \psi^{cM}\left(\boldsymbol{\delta}^{ce}\right)}{\partial \boldsymbol{\delta}^{ce}} \text{ and } f^{cap} = f_d^{cap} + f_v^{cap} = \frac{\partial \psi^{cH}\left(V^{cap}, \delta^{cap}\right)}{\partial \boldsymbol{\delta}^{cap}} + r^2 \frac{\partial \psi^{cH}\left(V^{cap}, \delta^{cap}\right)}{\partial V^{cap}} \qquad (3.37)$$

It should be noted that there is no available hydraulic free energy function $\psi^{cH}(V^{cap}, \delta^{cap})$ for a liquid bridge between two spherical particles of equal size in the literature. From an experimental perspective, measuring this hydraulic energy function is particularly difficult because the hysteresis in the contact angle arises from surface roughness and heterogeneity. Since the geometry of a steady capillary bridge surface can be described by the Young-Laplace equation, the hydraulic free energy $\psi^{cH}(V^{cap}, \delta^{cap})$ can be obtained by solving numerically the Young-Laplace equation with prescribed capillary bridge volume and particle distance. Because the numerical integration of the Young-Laplace equation for various capillary bridge volumes and particle distances is time-consuming, a simplified method to define the hydraulic free energy at the microscale will be used in the following section.

The procedure for constructing micromechanical models following the described multiscale thermomechanical framework include: (1) defining microscopic Helmholtz free energy potentials for both mechanical part and hydraulic part, and the dissipative rate function for the mechanical part; (2) deriving elastic/plastic relations from the energy potentials (it is worth mentioning that the Ziegler's orthogonality condition (Houlsby and Puzrin, 2007), according

to which the dissipative force is outward normal to the dissipation surface, has been adopted as a way of relating the dissipative variables to the dissipation potential, and to deduce the interparticle yield criterion and flow rule from the microscopic dissipative rate function; (3) establishing the micro-macro relation of strain in terms of the interparticle displacements; (4) deriving the effective stress tensor which is the work conjugate to the total strain tensor. In the following subsections, a micromechanical model will be constructed as an example to demonstrate the usefulness of this multiscale thermomechanical framework.

3.3.2 Mechanical potentials at the micro scale

The thermodynamically consistent microscopic free energy and dissipative energy constructed in Chapter 2 is adopted here to represent the mechanical behaviour of unsaturated granular soils. It should be mentioned that the stored energy is assumed to be zero, as a result, an increment of the elastic work is equal to the increment of the Helmholtz free energy whereas an increment of plastic work is equal to the dissipative energy.

3.3.3 Hydraulic potential at the micro scale

Assuming that the water bridges are isotropically distributed within the material, we can use the degree of saturation as a scalar quantity to describe the change of the capillary bridge volume. In addition, considering that the interparticle normal displacements and the capillary bridge separations are both distances between particles, the separations between particles can be approximated by the interparticle normal displacements. Therefore, the hydraulic free energy at the microscale $\psi^{cH}(V^{cap},\delta^{cap})$ can be equivalently replaced by $\psi^{cH}(S_r,\delta_n^c)$. As a result, the globally isotopic hydraulic behaviour of unsaturated granular soils can be captured by the change of the degree of saturation S_r, while the local anisotropic hydraulic property can be described by the distribution and evolution of the interparticle normal displacements.

Several attempts have been made to define the hydraulic energy potential for unsaturated soils at the macro scale using the soil water retention curve (SWRC) (Coussy *et al*., 2010; Buscarnera and Einav, 2012; Zhang and Buscarnera, 2014). Considering that the capillary

forces between two grains are represented by a decreasing function of the distance between the grains (Hicher and Chang, 2007), the following function can be retained for the hydraulic free energy at the inter-particle scale:

$$\psi^{cH}\left(S_r,\delta_n^c\right)=\psi_r^{cH}\left(S_r\right)\exp\left(\frac{L-2r}{r}\right) \tag{3.38}$$

where L is the distance between the centres of two neighbouring particles, r is a representative radius of the particles, taken as $r=d_{50}/2$, as shown in Figure 3.3. The value of $L-2r$ (also equal to δ^{cap}) is represented by interparticle displacements in normal direction δ_n^c with an initial value of $0.1r$.

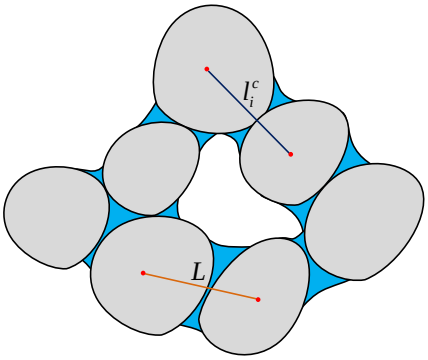

Figure 3.3 Branch vector and distance vector

The hydraulic potential $\psi_r^{cH}\left(S_r\right)$ at the microscale can be considered as equal to a reference hydraulic potential $\psi_r^{H}\left(S_r\right)$ at the macroscale, since it has been assumed that the water bridges are isotropically distributed in the specimen. The hydraulic potential $\psi_r^{H}\left(S_r\right)$ corresponds to the SWRC, which is usually expressed by empirical expressions (Brooks and Corey, 1964; van Genuchten, 1980; Fredlund and Xing, 1994). In this study, the simple logarithmic form introduced by Buscarnera and Einav (2012) has been adopted since it is a continuous and integrable function, given as:

$$\psi_r^{cH}\left(S_r\right)=\frac{1}{2}K_w\left(S_r\ln S_r+\left(2-S_r\right)\ln\left(2-S_r\right)\right) \tag{3.39}$$

in which K_w is a retention curve parameter associated with the value of the air entry suction. Based on Eq. (3.39), the reference free energy with respect to the degree of saturation is

comparable with the water retention curve, as shown in Figure 3.4(a). By inserting Eq. (3.39) into Eq. (3.29), we can obtain the relation between the smeared suction *ns* and the degree of saturation, as shown in Figure 3.4(b).

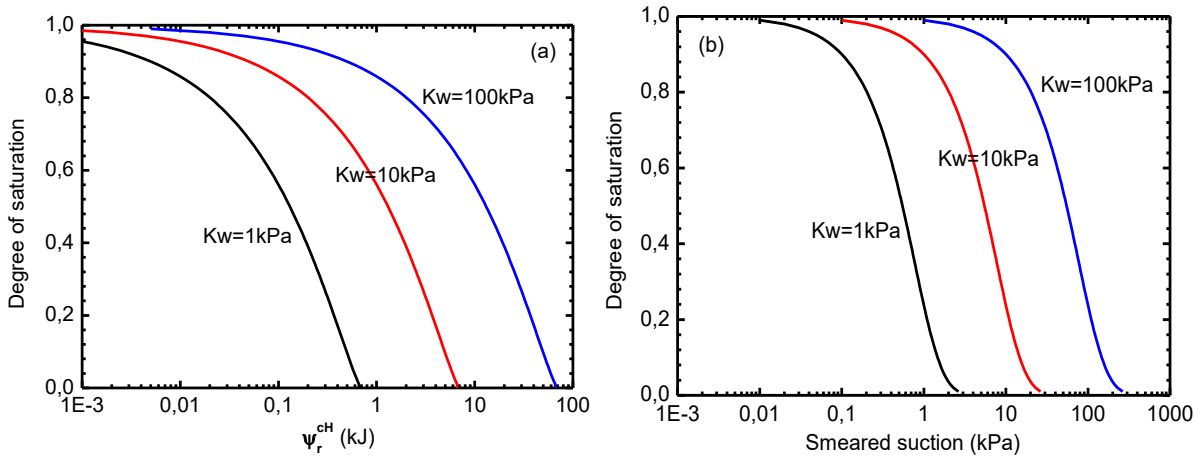

Figure 3.4 Performance of the reference hydraulic potential function

With the use of the principle of energy conservation, the behaviour of unsaturated granular soils can be obtained from two energy potentials, i.e. the mechanical part and the hydraulic part at inter-particle contacts. Accordingly, the constructed micromechanical model for unsaturated granular materials obeys the principles of thermodynamics.

3.3.4 Stress and strain tensors

The strain tensor suggested by Liao *et al*. (1997) is adopted to represent the relation between microscopic displacements and macroscopic strain, which represents the deformations of granular assemblies related to the displacements at interparticle contacts and the micro-topologies of particle clusters. Substituting Eq.(2.39) into the definition of the effective stress tensor based on the Helmholtz free energy, Eq. (3.30), and using the work input at the micro scale, we obtain

$$\boldsymbol{\sigma}' = \frac{\partial \psi\left(\boldsymbol{\varepsilon}^e, S_r\right)}{\partial \boldsymbol{\varepsilon}^e} = \frac{\partial \psi^M\left(\boldsymbol{\varepsilon}^e\right)}{\partial \boldsymbol{\varepsilon}^e} = \frac{1}{V}\sum_{c=1}^{N} \frac{\partial \psi^{cM}\left(\boldsymbol{\delta}^e\right)}{\partial \boldsymbol{\delta}^{ce}} \frac{\partial \boldsymbol{\delta}^{ce}}{\partial \boldsymbol{\varepsilon}^e} = \frac{1}{V}\sum_{c=1}^{N} f_i^c \cdot \frac{\partial \boldsymbol{\delta}^{ce}}{\partial \boldsymbol{\varepsilon}^e} = \frac{1}{V}\sum_{c=1}^{N} f_i^c l_j^c \qquad (3.40)$$

Eq. (3.40) indicates that the effective stress in unsaturated granular soils can be computed through the contact stress tensor, i.e. the Love-Weber formula, which is consistent with the stress tensor derived in Chapter 2. It should be mentioned that Eq. (3.40) is obtained on the

basis of the kinematic assumption of Eq.(1.12). The generalisation of Eq. (3.40) to be an effective stress tensor for partially saturated soils is a topic of current interest, which has been recently investigated through DEM simulations (Duriez and Wan, 2016; Chalak *et al*., 2017; Wang *et al*., 2017).

3.3.5 Homogenization method

In this model, the local variables of granular materials are random directional data, thus the statistics theory (Kanatani, 1984; Li and Yu, 2011) proposed to characterize the probability density distribution of such directional data is adopted. The summation of any local quantity over all interparticle contacts is computed using the same integration method as for dry granular materials based on the statistics theory (Kanatani, 1984; Li and Yu, 2011), as described in Chapter 2.

3.3.6 Implementation scheme

One of the difficulties in implementing the constitutive models for unsaturated soils expressed by the effective stress tensor is that the experiments usually consider other forms of stress variables such as the net stress tensors; therefore, the constraints imposed on laboratory specimens cannot be directly specified numerically. In addition, experiments with different combinations of net stress tensors and hydraulic controls, such as suction control, drying and wetting paths and constant water content require algebraic efforts in numerical simulations. A general approach to circumvent these difficulties is to express these constraints using the linearized integration method suggested by Bardet and Choucair (1991). This method has been successfully applied to integrate an effective tensor based model for partially saturated soils with the capability of imposing various loading programs (Zhang and Buscarnera, 2016), and has been adopted in this thesis to integrate the constructed micromechanical model. The integration of the local law, the micro-macro relations and the convergence criteria of the micromechanical model will be discussed in detail in Chapter 4.

3.4 Performance of the developed model for unsaturated granular soils

For saturated and dry conditions, the developed micromechanical model will be reduced to the one developed in Chapter 2. Its performance in describing the behaviour of granular Hostun sand has been well demonstrated. In order to demonstrate its capability in capturing the behaviour of unsaturated granular soils, the developed micromechanical model will be calibrated from triaxial compression test at constant water content on a partially saturated silica sand, the Chiba sand described by Fern *et al*. (2016).

3.4.1 Chiba sand

According to Fern *et al*. (2016), Chiba sand is a poorly graded silica sand with the particle size ranging from 0.01 to 1.00mm. It has a coefficient of uniformity of 2.1 and a coefficient of curvature of 1.1. The grain size distribution was obtained by sieving and sedimentation, as shown in Figure 3.5(a). The minimum and maximum void ratios are 0.500 and 0.946 respectively, and its specific gravity is 2.72. Its critical state friction angle was found to be $33°$, which is a typical value for silica sand.

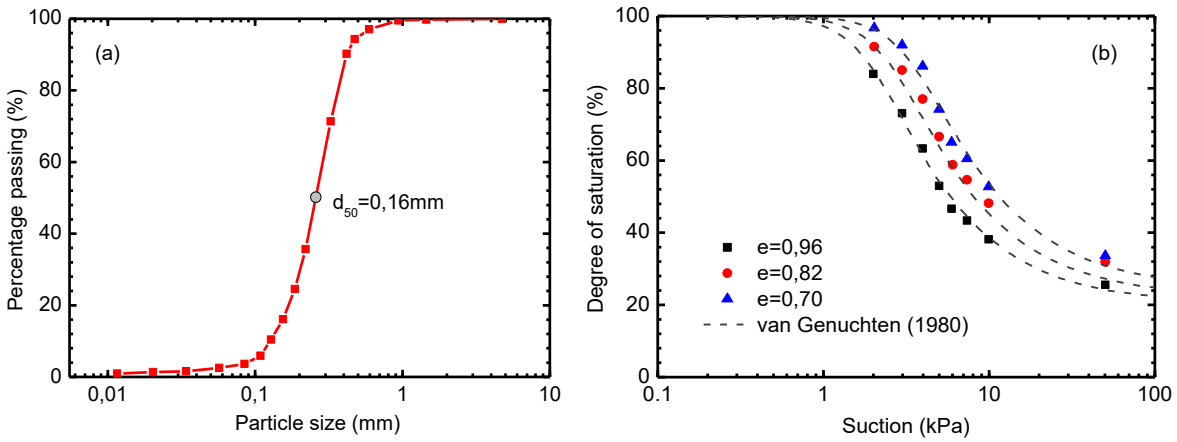

Figure 3.5 Chiba sand: (a) grain size distribution; (b) water retention curve

The water retention curve was obtained for the drying path with three different densities using the axis translation technique (Fern *et al*., 2016). The specimens were subjected to matric suctions of 2 to 60 kPa. Pressures ranging from 2 to 10 kPa were applied by means of negative water head and the 60 kPa with a pressure plate. Complimentary investigations were carried out on a loose specimen and the air entry value K_w, which was found to be 0.5kPa, the

residual degree of saturation around 20%, and a very small hysteresis was observed, as shown in Figure 3.5(b).

3.4.2 Triaxial compression tests with constant water content on Chiba sand

A series of triaxial tests at constant water contents were conducted on Chiba sand under vertical strain rates of 0.1%/min and 5.0%/min (Fern *et al*., 2016). In this study, the long duration tests that can be viewed as quasi-static loading tests will be adopted to calibrate the aforementioned micromechanical model. The specimens with various densities and gravimetric water contents of 10% and 17% were sheared until reaching an axial strain of 20%. For each water content, three tests were carried out with an initial net mean pressure of 20kPa, 40kPa and 80kPa, respectively. The detailed loading program is shown in Table 3.2.

Table 3.2 Initial condition of constant water content triaxial compression tests on Chiba sand

Group	$w(\%)$	e_0	$S_r(\%)$	$p_0^{net}(\mathrm{kPa})$
Loose	10	0.842	32	20
	10	0.818	33	40
	10	0.808	34	80
	17	0.845	55	20
	17	0.830	56	40
	17	0.820	56	80
Medium dense	10	0.742	37	20
	10	0.738	37	40
	10	0.725	38	80
	17	0.745	62	20
	17	0.734	63	40
	17	0.719	64	80
Dense	10	0.656	41	20
	10	0.659	41	40
	10	0.653	42	80
	17	0.657	70	20
	17	0.648	71	40
	17	0.641	72	80

3.4.3 Simulations of constant water content triaxial compression tests

The maximum effective stress ratio q/p' was found to be 1.455 (Figure 3.6(a)), which corresponds to a critical state friction angle of 33º. Accordingly, the friction angle at

interparticle contacts is assumed to be 33º. The critical state line was calibrated from the $e-\log p'$ plot (Figure 3.6(b)), which gave e_{ref}=1.23, λ=0.25 and $\xi=0.2$ with the reference pressure of $p_{ref}=10\,\text{kPa}$. The radius of the particles r is half of the diameter d_{50}=0.16mm. The air entry value for the hydraulic free energy K_w is 0.5 kPa. The parameters at the interparticle contact k_{n0}^c, k_{rR} and k_{pR} were calibrated from the constant water content triaxial compression tests. A total of eight parameters were required in the micromechanical model for Chiba sand, as summarized in Table 3.3.

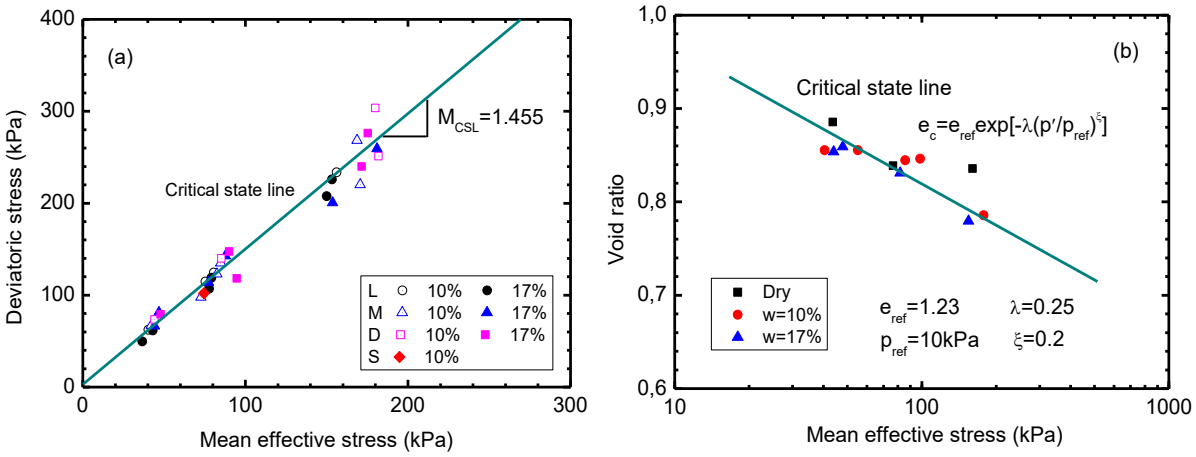

Figure 3.6 Critical state of Chiba sand in (a) $p'-q$ plane and (b) $e-\log p'$ plane

Table 3.3 Parameters used in the micromechanical model for Chiba sand

e_{ref}	λ	k_{n0}^c(N/mm)	ϕ_μ^c(°)	d_{50}(mm)	k_{rR}	k_{pR}	K_w(kPa)
1.23	0.25	800	33	0.16	1.0	2.0	0.5

The constraints used to simulate the constant water content triaxial compression tests are: $\Delta\sigma_2^{net}=\Delta\sigma_3^{net}=0$, $\Delta\varepsilon_1=20\%$, and $\Delta e_w=0$ with e_w being the void ratio of water which is given as

$$e_w=eS_r \tag{3.41}$$

With Eq. (3.41), the constant water content Δw=0 is equivalently controlled by Δe_w=0. The net stress term $\Delta\sigma_2^{net}=\Delta\sigma_3^{net}=0$ was rewritten as $\Delta\sigma_2'-sS_r=\Delta\sigma_3'-sS_r=0$, thus the

effective stress can be obtained. With these boundary conditions, the model was integrated through the linearized integration method suggested by Bardet and Choucair (1991).

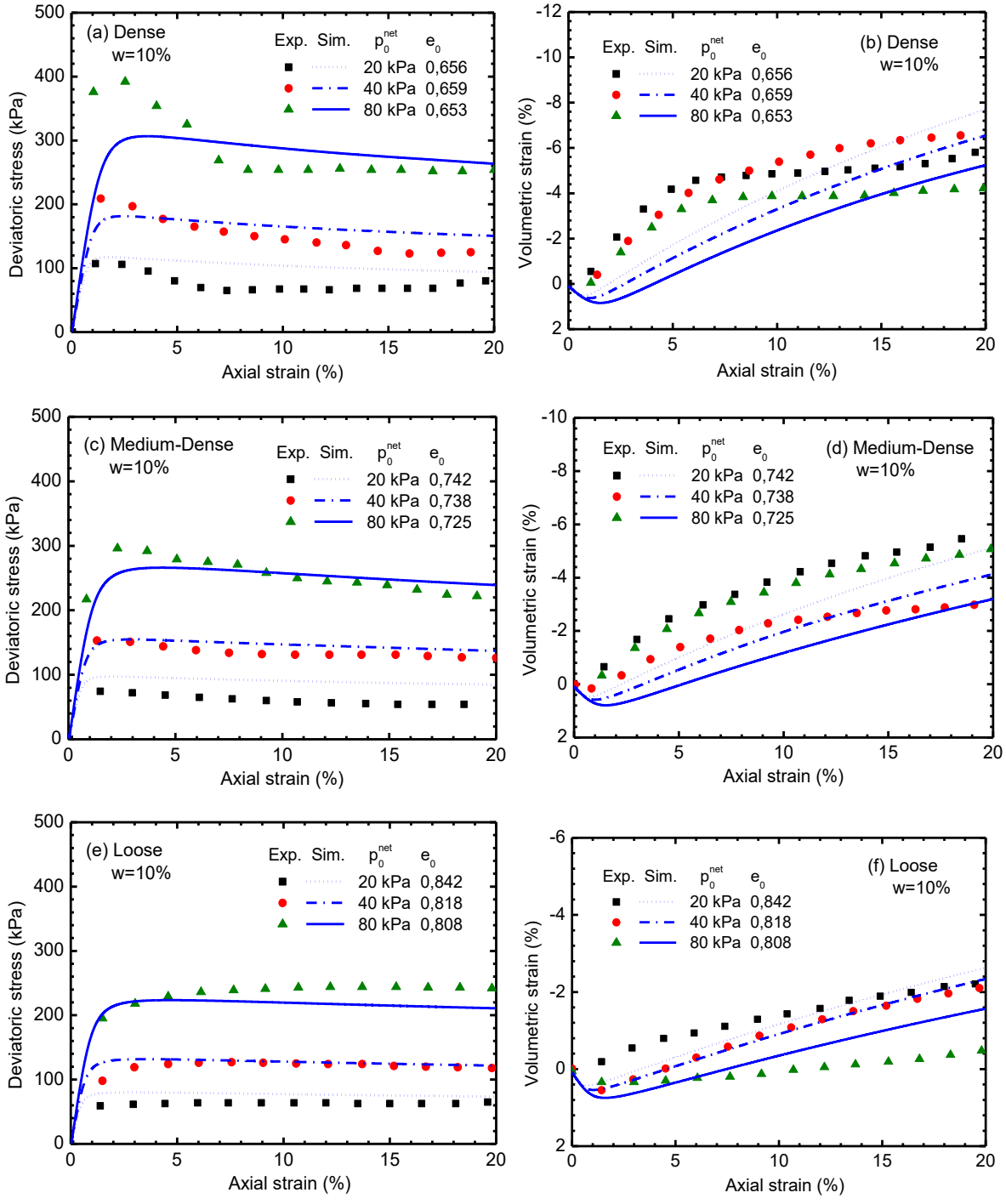

Figure 3.7 Simulation of the constant water content triaxial compression tests on unsaturated Chiba sand ($w = 10\%$)

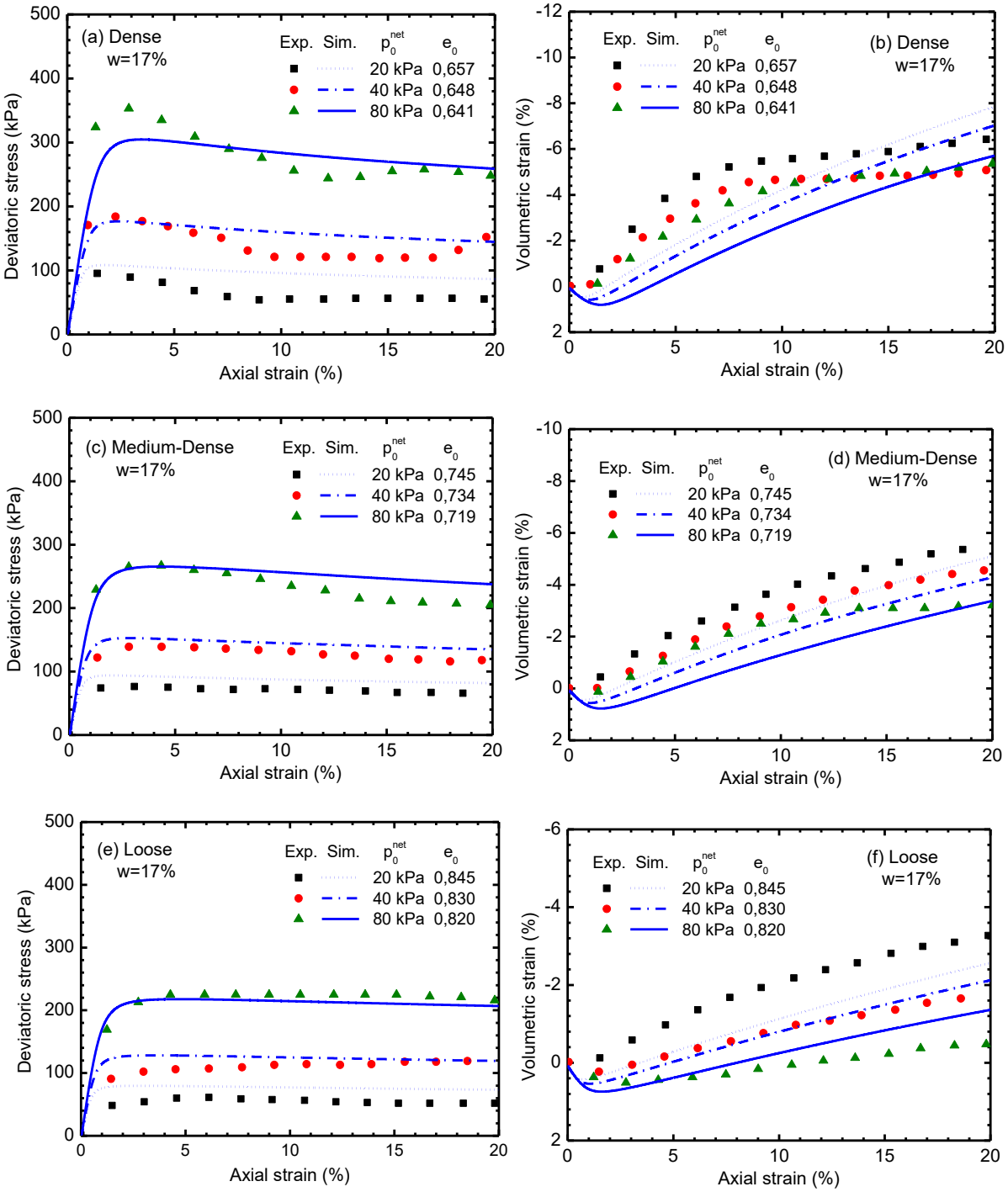

Figure 3.8 Simulation of the constant water content triaxial compression tests on unsaturated Chiba sand ($w = 17\%$)

The simulation results are presented with experimental data in Figures 3.7 and 3.8. The strain hardening and dilative behaviour, the peak strength and the softening behaviour are well captured by the micromechanical model. In terms of the plots of the shearing stress with respect to the axial loading, the model demonstrates a very good predictive capability over

wide ranges of densities, confining pressures and water contents (Figure 3.7(a, c, e) and Figure 3.8(a, c, e)). In contrast, the model reproduces the volumetric deformation with acceptable differences between the simulation results and the experimental data. As explained by Fern *et al*. (2016), the differences obtained for the dense sample are largely due to the occurrence of strain localization. In comparison with the elasto-plastic models based upon classical continuum mechanics (Wheeler and Sivakumar, 1995; Sheng *et al*., 2004; Fern *et al*., 2016), only few parameters are required in this model and all of them have a physical basis.

It should be noted that both the current model and the model of Hicher and Chang (2007) have adopted the strain tensor of Liao *et al*. (1997) and the same Coulomb type yield criterion at the interparticle scale. The main differences between these two models are: (1) the interparticle elastic relation; (2) the scalar suction s with the current model instead of the capillary stress tensor $\boldsymbol{\sigma}^{cap}$ in Hicher and Chang (2007); (3) a free energy function for the hydraulic behaviour instead of an empirical function of the degree of saturation S_r in Hicher and Chang (2007). Consequently, thermodynamic principles are satisfied by the current model.

3.5 Concluding remarks

This chapter reviewed briefly the application of the thermodynamic approach with internal variables for constitutive modelling of unsaturated granular soils. Particular attention has been given to the work input derived by Houlsby (1997) and the Helmholtz free energy functions related to the water retention curve, which were the basis of the multiscale model constructed by extending the thermodynamic principles to the micromechanical modelling of unsaturated granular soils.

A micromechanical model for unsaturated granular soils was constructed based on the suggested multiscale thermodynamic framework. The energy quantities defined at the micro and macro scales were analysed, and then the Helmholtz free energy at the microscale was defined as the sum of a mechanical part and a hydraulic part. The free energy is dependent on the elastic strains and on the degree of saturation at the macro scale, and it is related to the

elastic displacements and the degree of saturation at the micro scale. The dissipation energy is of frictional origin and is a function of the plastic displacements at the micro scale and of the plastic strains at the macro scale. For the mechanical part, the micromechanical model constructed in Chapter 2 was adopted, since it has been proved to be consistent with thermodynamic principles. A particle-size dependency function has been suggested to consider the water retention in the hydraulic free energy potential at the micro scale. The model was calibrated and its satisfactory performance in capturing the behaviour of unsaturated Chiba sand under constant water content triaxial compression was demonstrated.

CHAPTER 4 INTEGRATING A MICROMECHANICAL MODEL FOR MULTISCALE MODELLING OF GRANULAR SOILS

4.1 Introduction

One of the most rewarding tasks in geomechanics is to be able to construct an efficient constitutive model. Until now, the favoured models are the ones that reveal soil physics and are capable of predicting soil behaviour with a limited number of parameters. Based on continuum mechanics, phenomenological models have been widely used to describe soil behaviour obtained from elementary tests. Quite recently, however, there has been a growth of micromechanical models that consider the force-displacement relationships at the inter-particle contacts. These models (Chang and Hicher, 2005; Nicot and Darve, 2005; Yin and Chang, 2009; Nicot and Darve, 2011) have the advantage of treating the fundamentals of granular physics and to reproduce the main aspects of soil behaviour. It seems beneficial, therefore, to implement these models into finite element codes in order to analyse geotechnical problems on the basis of multi-scales.

Two types of micromechanical models, based on either a kinematic or a static hypothesis, can be increasingly found in the literature. The models based on the latter (Chang and Hicher, 2005; Yin and Chang, 2009; Yin *et al*., 2009; Yin *et al*., 2010; Yin *et al*., 2011; Yin *et al*., 2013; Yin *et al*., 2014) have proved to perform well in predicting soil behaviour. This chapter, therefore, will discuss the numerical implementation of the static hypothesis into finite element codes. Under the static hypothesis, the micro-macro relationship can be derived by linking the force increments to the stress increments. The force-displacement relations defined at inter-particle contacts are displacement driven contact laws. After the forces at each contact have been updated, the stress can then be integrated with the Love-Weber expression.

One of the difficulties in implementing these models is how to calculate the displacement increment in the case of strain softening. Since the displacement cannot be directly calculated by the strain increment but only through the relations between force and stress increments, it is therefore not easy to calculate the stress increment for any given loading constraint or to

ensure the consistency of the static hypothesis with the stress integration formula, in an effort to maintain the static equilibrium at both the local and the global levels. Until now, these issues have not been thoroughly addressed.

Besides an effective algorithm for assuring the micro-macro balance, the local force-displacement laws need to be accurately integrated. The local laws driven by displacement are force-displacement ordinary differential equations (ODEs) resembling strain increment controlled stress-strain ODEs. For solving these ODEs, two categories: the explicit forward Euler and the implicit backward Euler integration schemes have been developed. The former belongs to one of a large family of explicit methods and is often used with automatic sub-stepping methods (Sloan 1987; Sloan *et al.*, 2001; Lloret-Cabot *et al*., 2016). But since the single step forward Euler method is not highly accurate, it has been necessary to develop high-order procedures such as the Modified Euler and the Runge-Kutta methods. The implicit backward Euler schemes attract usage because they do not require calculating the stress intersection with the yield surface and permit the calculated stress to automatically satisfy the yield criterion under a specified tolerance. The closest point projection method (CPPM) suggested by Simo and Taylor (1985) has proven to be effective in the case of complex models. However, as the Newton-Raphson procedure is currently used to solve these equations iteratively, it is necessary to derive a consistent tangential modulus, which is difficult to obtain in the case of complex models. To circumvent this problem, it has been suggested to use the cutting-plane algorithm (CPA) for calculating the plastic corrector (Ortiz and Simo, 1986). For the implicit integration of the micromechanical model, CPPM and CPA can both be used at the micro level, and their efficiency readily tested.

In this chapter, the Chang and Hicher micromechanical model (2005) based on a static hypothesis is first briefly reviewed. The linearized control constraints solved by a predictor-corrector iterative procedure can also be used with homogeneous stress and strain fields to simulate laboratory tests. A trial stress driven scheme has been proposed for implementing the micro-macro relations, which will guarantee the consistency of the static hypothesis with the integrated stress tensor. Two return mapping algorithms (CPPM and CPA) have been

alternatively adopted to integrate the inter-particle force-displacement relations. Several conventional loading paths, i.e. drained and undrained triaxial compression tests, have been simulated to probe the accuracy and efficiency of the numerical approaches. Finally, the model was implemented into a finite element code and the numerical procedure validated by elementary tests. Two typical boundary value problems: a biaxial test and a square footing were numerically analysed to evaluate how the micromechanical model can be applied to multiscale modelling.

4.2 A static hypothesis based micromechanical model

The CH model (Chang and Hicher, 2005) was initially proposed for sand. Further developments by Yin and Chang (2009) and Yin *et al*. (2009, 2010, 2011, 2013, 2014) demonstrated its good performance in modelling the mechanical behaviour of sand and clay. In this chapter, it is used as an example of integrating a micromechanical model into a finite element code.

4.3 Implicit multiscale integration methods

Three levels of implicit integration methods for obtaining the stress increment, consistent with the stress-force relation and the local inter-particle contact law, are presented in this section.

4.3.1 Global mixed control

As mentioned previously, the difficulty of implementing a micromechanical model based on a static hypothesis is how to obtain the stress increment under general loadings. For this, it is necessary to adopt a strategy which combines the implicit algorithms with a general loading control. To achieve these goals conveniently, we can express the loading control by means of linearized constraints. The expression suggested by Bardet and Choucair (1991) can be deployed, in which a loading condition can be expressed as

$$\mathbf{S}\Delta\boldsymbol{\sigma}_{n+1} + \mathbf{E}\Delta\boldsymbol{\varepsilon}_{n+1} = \Delta\mathbf{X}_{n+1} \tag{4.1}$$

where **S** and **E** are constraint matrices given by elementary tests, as shown in Table 4.1 for typical loading paths, whereas $\Delta\mathbf{X}_{n+1} = \left[\Delta x_1, \Delta x_2, \cdots, \Delta x_i\right]_{\mathrm{n+1}}^{T}$ is the imposed driving vector, and

i is the number of freedoms. Since there are 12 unknowns in Eq. (4.1) but only 6 equations, the relation between strain and stress increments has to be added, expressed as

$$\Delta\boldsymbol{\sigma}_{n+1} = \mathbf{D}_{n+1}^{ep}\Delta\boldsymbol{\varepsilon}_{n+1} \tag{4.2}$$

where $\mathbf{D}_{n+1}^{ep}$ is the elastoplastic matrix. To solve Eqs.(4.1) and (4.2), two separate levels of the

Table 4.1 Constraint matrices for mixed controls

Type of tests	**S**	**E**	$\mathbf{\Delta X_{n+1}}$
ISO: Stress controlled isotropic compression	$\begin{bmatrix}1&0&0&0&0&0\\0&1&0&0&0&0\\0&0&1&0&0&0\\0&0&0&1&0&0\\0&0&0&0&1&0\\0&0&0&0&0&1\end{bmatrix}$	$\begin{bmatrix}0&0&0&0&0&0\\0&0&0&0&0&0\\0&0&0&0&0&0\\0&0&0&0&0&0\\0&0&0&0&0&0\\0&0&0&0&0&0\end{bmatrix}$	$\begin{bmatrix}\Delta x_1\\\Delta x_1\\\Delta x_1\\0\\0\\0\end{bmatrix}$
ASO: Stress controlled anisotropic compression	$\begin{bmatrix}1&0&0&0&0&0\\0&1&0&0&0&0\\0&0&1&0&0&0\\0&0&0&1&0&0\\0&0&0&0&1&0\\0&0&0&0&0&1\end{bmatrix}$	$\begin{bmatrix}0&0&0&0&0&0\\0&0&0&0&0&0\\0&0&0&0&0&0\\0&0&0&0&0&0\\0&0&0&0&0&0\\0&0&0&0&0&0\end{bmatrix}$	$\begin{bmatrix}\Delta x_1\\\Delta x_2\\\Delta x_3\\0\\0\\0\end{bmatrix}$
TXD: Strain controlled drained triaxial	$\begin{bmatrix}0&1&0&0&0&0\\0&0&1&0&0&0\\0&0&0&1&0&0\\0&0&0&0&1&0\\0&0&0&0&0&1\\0&0&0&0&0&0\end{bmatrix}$	$\begin{bmatrix}0&0&0&0&0&0\\0&0&0&0&0&0\\0&0&0&0&0&0\\0&0&0&0&0&0\\0&0&0&0&0&0\\1&0&0&0&0&0\end{bmatrix}$	$\begin{bmatrix}0\\0\\0\\0\\0\\\Delta x_1\end{bmatrix}$
TXU: Strain controlled undrained triaxial	$\begin{bmatrix}0&0&0&0&0&0\\0&1&-1&0&0&0\\0&0&0&1&0&0\\0&0&0&0&1&0\\0&0&0&0&0&1\\0&0&0&0&0&0\end{bmatrix}$	$\begin{bmatrix}1&1&1&0&0&0\\0&0&0&0&0&0\\0&0&0&0&0&0\\0&0&0&0&0&0\\0&0&0&0&0&0\\1&0&0&0&0&0\end{bmatrix}$	$\begin{bmatrix}0\\0\\0\\0\\0\\\Delta x_1\end{bmatrix}$
FE: Finite element implementation	$\begin{bmatrix}0&0&0&0&0&0\\0&0&0&0&0&0\\0&0&0&0&0&0\\0&0&0&0&0&0\\0&0&0&0&0&0\\0&0&0&0&0&0\end{bmatrix}$	$\begin{bmatrix}1&0&0&0&0&0\\0&1&0&0&0&0\\0&0&1&0&0&0\\0&0&0&1&0&0\\0&0&0&0&1&0\\0&0&0&0&0&1\end{bmatrix}$	$\begin{bmatrix}\Delta x_1\\\Delta x_2\\\Delta x_3\\\Delta x_4\\\Delta x_5\\\Delta x_6\end{bmatrix}$

Newton iteration have been proposed by Zhang and Buscarnera (2015); the first one solves the control condition, whereas the other solves the constitutive equations. However, this

procedure is not well adapted to a micromechanical model, because of the difficulty in obtaining a consistent matrix. This study suggests two different levels of predictor-corrector algorithms to solve Eqs.(4.1) and (4.2). To solve the equation of the linearized constraints, Eq.(4.1) can be rewritten as

$$\mathbf{R}_{n+1} = \mathbf{S}\Delta\boldsymbol{\sigma}_{n+1} + \mathbf{E}\Delta\boldsymbol{\varepsilon}_{n+1} - \Delta\mathbf{X}_{n+1} \tag{4.3}$$

where the residual $\mathbf{R}_{n+1}$=0 contains the same solution as in Eq.(4.1). For each increment, 6 unknown stress increments and 6 unknown strain increments need to be solved by Eq.(4.3).

Table 4.2 Algorithm for mixed control

1) Initialise $k=0$, given the initial value of $\boldsymbol{\sigma}_{n+1}^{(0)} = \boldsymbol{\sigma}_n$, $\boldsymbol{\varepsilon}_{n+1}^{(0)} = \boldsymbol{\varepsilon}_n$ and $\Delta\mathbf{X}_{n+1}^{(0)}$

2) Set $\mathbf{R}_{n+1}^{(\mathrm{k})} = 0$ and solve equation

$$\begin{cases} \mathbf{R}_{n+1}^{(\mathrm{k})} = \mathbf{S}\Delta\boldsymbol{\sigma}_{n+1}^{(\mathrm{k})} + \mathbf{E}\Delta\boldsymbol{\varepsilon}_{n+1}^{(\mathrm{k})} - \Delta\mathbf{X}_{n+1}^{(\mathrm{k})} \\ \Delta\boldsymbol{\sigma}_{n+1}^{(\mathrm{k})} = \left(\mathbf{D}^e\right)_{n+1}^{(k)} \Delta\boldsymbol{\varepsilon}_{n+1}^{(\mathrm{k})} \end{cases}$$

3) Calculate force increment from stress increment

$$\left(\Delta\mathbf{f}^c\right)_{n+1}^{(\mathrm{k})} = \Delta\boldsymbol{\sigma}_{n+1}^{(\mathrm{k})} \left(\mathbf{l}^c\right)_{n+1}^{(\mathrm{k})} \mathbf{A}_{n+1}^{(\mathrm{k})}$$

4) Use macro-micro algorithm to update stress $\boldsymbol{\sigma}_{n+1}^{(\mathrm{k}+1)}$, calculate stress increment $\Delta\boldsymbol{\sigma}_{n+1}^{(\mathrm{k}+1)} = \boldsymbol{\sigma}_{n+1}^{(\mathrm{k}+1)} - \boldsymbol{\sigma}_{n+1}^{(\mathrm{k})}$, and strain increment $\Delta\boldsymbol{\varepsilon}_{n+1}^{(\mathrm{k}+1)} = \Delta\boldsymbol{\varepsilon}_{n+1}^{(\mathrm{k})}$

5) Calculate residual constraints

$$\mathbf{R}_{n+1}^{(\mathrm{k}+1)} = \Delta\mathbf{X}_{n+1}^{(0)} - \left(\mathbf{S}\Delta\boldsymbol{\sigma}_{n+1}^{(\mathrm{k}+1)} + \mathbf{E}\Delta\boldsymbol{\varepsilon}_{n+1}^{(\mathrm{k}+1)}\right)$$

IF $\dfrac{\left\|\mathbf{R}_{n+1}^{(\mathrm{k}+1)}\right\|}{\left\|\boldsymbol{\sigma}_{n+1}^{(\mathrm{k}+1)}\right\|} \le RTOL$, THEN: EXIT

6) Set

$$\Delta\mathbf{X}_{n+1}^{(\mathrm{k}+1)} = \mathbf{R}_{n+1}^{(\mathrm{k}+1)}$$

Set $k \leftarrow k+1$ and GO TO step 2.

Combining Eqs.(4.2) and (4.3), the strain or stress increments can first be predicted through the use of the elastic matrix $\mathbf{D}^e$. The obtained stress increments, used to calculate the force increments, are then corrected to take into account the plastic condition by the local corrector which will be presented in the following section. At the end of the kth elastic prediction, the residuals need to be calculated

$$\mathbf{R}_{n+1}^{(k+1)} = \Delta\mathbf{X}_{n+1}^{(0)} - \left(\mathbf{S}\Delta\boldsymbol{\sigma}_{n+1}^{(k+1)} + \mathbf{E}\Delta\boldsymbol{\varepsilon}_{n+1}^{(k+1)}\right) \tag{4.4}$$

The relative error $\left\|\mathbf{R}_{n+1}^{(k+1)}\right\| / \left\|\boldsymbol{\sigma}_{n+1}^{(k+1)}\right\| \leq RTOL$ is computed at the end of each iteration to guarantee that the constraints are fully imposed. The relative error should satisfy the given tolerance *RTOL* set as 10^{-4}. If this is not the case, the residuals, viewed as correctors, are imposed as new constraints

$$\Delta\mathbf{X}_{n+1}^{(k+1)} = \mathbf{R}_{n+1}^{(k+1)} \tag{4.5}$$

Stress and strain are also updated after each iteration. The flowchart of the mixed control programme is given in Table 4.2. For a displacement driven finite element code, the strain increments at each Gauss point are given. Under this condition, **S** is null in Eq.(4.1), the constraints are strain increments; thus, no iteration is needed to solve Eq.(4.1).

4.3.1 Micro-macro integration

The micro-macro relation is the bridge connecting the behaviour at inter-particle contacts to the behaviour of the representative elementary volume. This relation consists of a localisation operator and an averaging operator. In the CH model, the localisation operator is based on the static hypothesis, whereas the averaging operator is based on the Love-Weber formula. Given that the two operators are relations between stress and force, they should be consistent with each other during the calculation process. For isotropic loading, no plastic displacement occurs according to the local law, and the stress integration is the inverse of the static expression. However, plastic displacements under shearing lead the updated forces to be smaller than are the forces calculated by the static hypothesis. The difference causes the static hypothesis and the Love-Weber formula to be inconsistent. Therefore, an iteration procedure needs to be conducted.

Since the static expression has been deduced from the best-fit hypothesis, which can be used as a predictor for calculating the trial force increments, the trial displacement increments can be calculated by the force increments, written as

$$\left(\Delta\mathbf{f}^c\right)_{n+1} = \Delta\boldsymbol{\sigma}_{n+1}\left(\mathbf{l}^c\right)_{n+1}\mathbf{A}_{n+1},\ \left(\Delta\boldsymbol{\delta}^c\right)_{n+1} = \left(\left(\mathbf{k}^c\right)^{-1}\right)_{n+1}\left(\Delta\mathbf{f}^c\right)_{n+1} \tag{4.6}$$

where $\mathbf{k}^c$ is the elastic stiffness tensor defined at the inter-particle contacts. If there is a deviatoric loading, it will be necessary to conduct an out-of-balance force iteration process. Noting the force after the kth iteration in local law as $\left(\mathbf{f}^c\right)^k$, the stress integrated by Eq.(1.14) is correspondingly denoted as $\boldsymbol{\sigma}^k$. Meanwhile, the force $\left(\mathbf{f}^c\right)^{k+1}$ could be calculated by the expression of Eq.(1.17). If the updated force $\left(\mathbf{f}^c\right)^k$ is equal to the force $\left(\mathbf{f}^c\right)^{k+1}$, the integration procedure will be terminated. Otherwise the out-of-balance force

$$\left(\mathbf{f}_{unb}^c\right)^{k+1} = \left(\mathbf{f}^c\right)^k - \left(\mathbf{f}^c\right)^{k+1} \tag{4.7}$$

will be imposed on the (k+1) th iteration until the out-of-balance force drops below the given tolerance. The following relative error is proposed to evaluate the magnitude of the out-of-balance force:

$$\frac{1}{NP}\sqrt{\sum_{i=1}^{NP}\left(\left(\mathbf{f}_{unb}^c\right)^{k+1}\right)^2} \Bigg/ \frac{1}{6}\sqrt{\sum_{i=1}^{6}\left(\boldsymbol{\sigma}^{(k)}\right)^2} \le UFTOL \tag{4.8}$$

in which the unbalanced force tolerance $UFTOL$ is chosen between 10^{-3} and 10^{-6}, depending on the non-linearity of the local law. The procedure for the micro-macro integration can be found in Table 4.3.

Table 4.3 Implicit integration of macro-micro relation

1) Calculate force increment and displacement increment

$$\left(\Delta\mathbf{f}^c\right)_{n+1} = \Delta\boldsymbol{\sigma}_{n+1}\left(\mathbf{l}^c\right)_{n+1}\mathbf{A}_{n+1},\ \left(\Delta\boldsymbol{\delta}^c\right)_{n+1} = \left(\left(\mathbf{k}^c\right)^{-1}\right)_{n+1}\left(\Delta\mathbf{f}^c\right)_{n+1}$$

2) Return mapping algorithm to update force $\left(\mathbf{f}^c\right)_{n+1}$

3) Initialise $k=0$, integrate force to obtain stress

$$\boldsymbol{\sigma}_{n+1}^{(k)} = \frac{1}{V}\sum_{c=1}^{N}\left(\mathbf{f}^c\right)_{n+1}^{(k)}\left(\mathbf{l}^c\right)_{n+1}^{(k)}$$

4) Calculate force from updated stress

$$\left(\mathbf{f}^c\right)_{n+1}^{(k)} = \boldsymbol{\sigma}_{n+1}^{(k)}\left(\mathbf{l}^c\right)_{n+1}^{(k)}\mathbf{A}_{n+1}^{(k)}$$

5) Calculate unbalance force

$$\left(\mathbf{f}^c\right)_{unb}^{(k)} = \left(\mathbf{f}^c\right)_{n+1}^{(k)} - \left(\mathbf{f}^c\right)_{n+1},\ \left(\Delta\boldsymbol{\delta}^c\right)_{n+1}^{(k)} = \left(\left(\mathbf{k}^c\right)^{-1}\right)_{n+1}\left(\mathbf{f}^c\right)_{unb}^{(k)}$$

And check the convergence criterion

$$\frac{1}{NP}\sqrt{\sum_{i=1}^{NP}\left(\left(\mathbf{f}^{c}\right)_{unb}^{(k)}\right)^{2}}\Bigg/\frac{1}{6}\sqrt{\sum_{i=1}^{6}\left(\boldsymbol{\sigma}^{(k)}\right)^{2}}\leq UFTOL$$

IF above equation is satisfied, THEN: EXIT

6) Return mapping algorithm to update force $\left(\mathbf{f}^{c}\right)_{n+1}^{(k)}$

Set $k \leftarrow k+1$ and GO TO step 4.

4.3.2 Implicit integration of the local law

The displacement driven local law can be similarly integrated by the strain driven ordinary differential equations. The single step backward Euler can be used to integrate the incremental stress-strain equations, but its accuracy depends on the amplitude of the loading increments because the plastic corrector is very elementary. To solve this problem, we have proposed return mapping schemes to find more accurately the plastic corrector. The calculations are performed essentially as a two-step process: the increment is first considered as elastic and the trial variables are calculated as an elastic predictor; the trial variables will then be relaxed on the yield surface and referred to as the plastic corrector. Within the return mapping framework, several algorithms to calculate the plastic corrector have been suggested: among them, the Closest Point Projection Method (CPPM) developed by Simo and Taylor (1985) and the cutting plane algorithm (CPA) suggested by Ortiz and Simo (1986) have been widely used.

Each implicit integration method carries its specific advantages. However, the integration of only a limited number of models has been subjected to comparison through the two above mentioned methods. Additional comparisons should be made to assess the efficiency of these two methods for a specific micromechanical model.

4.3.3.1 Closest point projection method (CPPM)

CPPM solves the plastic multiplier equation in conjunction with Newton's iterative technique**.** Consequently, a consistent tangential modulus needs to be derived to obtain the quadric convergence speed. For complex models, it is not easy to derive the second gradients, but for

a Coulomb type inter-particle contact law, it is possible to determine the first and the second derivatives. Since the yield criterion is plastic displacement dependent, the residual can be expressed as

$$R_{n+1}^{(k)} = -\left(\Delta\boldsymbol{\delta}^{cp}\right)_{n+1}^{(k)} + \left(\Delta\lambda^{c}\right)_{n+1}^{(k)} \mathbf{b}_{n+1}^{k} \tag{4.9}$$

where the first order derivatives of the potential function **b** are defined in Eq.(A2). If the yield point satisfies the condition $F_{n+1}^{(k)} \le TOL_1$ and the residual satisfies the condition $\left\|R_{n+1}^{(k)}\right\| \le TOL_2$, it will not be necessary to calculate the plastic corrector. Otherwise, the consistent tangential modulus is computed by

$$\mathbf{C}_{n+1}^{(k)} = \left[\mathbf{I} + \left(\Delta\lambda^{c}\right)_{n+1}^{(k)} \left[\frac{\partial \mathbf{b}}{\partial \mathbf{f}}\right]_{n+1}^{(k)}\right] \mathbf{k}_{n+1}^{ce} \tag{4.10}$$

in which $\mathbf{k}_{n+1}^{ce}$ is the force-displacement elastic matrix, as shown in Eq.(1.43), and the second derivatives of the potential function $\partial \mathbf{b} / \partial \mathbf{f}^{c}$ can be found in Appendix A. The consistency parameter increment can be obtained by

$$\left(\Delta^2\lambda^{c}\right)_{n+1}^{(k)} = \frac{F_{n+1}^{(k)} - \mathbf{a}_{n+1}^{(k)} \mathbf{C}_{n+1}^{(k)} R_{n+1}^{(k)}}{\mathbf{a}_{n+1}^{(k)} \mathbf{C}_{n+1}^{(k)} \mathbf{b}_{n+1}^{(k)}} \tag{4.11}$$

The force increments can be obtained by

$$\left(\Delta\mathbf{f}^{c}\right)_{n+1}^{(k)} = -\mathbf{C}_{n+1}^{(k)} R_{n+1}^{(k)} - \left(\Delta^2\lambda^{c}\right)_{n+1}^{(k)} \mathbf{C}_{n+1}^{(k)} \mathbf{a}_{n+1}^{(k)} \tag{4.12}$$

Then, the plastic multiplier can be updated by

$$\left(\Delta\lambda^{c}\right)_{n+1}^{(k+1)} = \left(\Delta\lambda^{c}\right)_{n+1}^{(k)} + \left(\Delta^2\lambda^{c}\right)_{n+1}^{(k)} \tag{4.13}$$

The incremental plastic displacements can be calculated by

$$\left(\Delta\boldsymbol{\delta}^{cp}\right)_{n+1}^{(k+1)} = -\left(\left(\mathbf{k}^{c}\right)^{-1}\right)_{n+1}^{(k)} \left(\Delta\mathbf{f}^{c}\right)_{n+1}^{(k)} \tag{4.14}$$

Finally, the forces can be updated by

$$\left(\mathbf{f}^{c}\right)_{n+1}^{(k+1)} = \left(\mathbf{f}^{c}\right)_{n+1}^{(k)} + \left(\Delta\mathbf{f}^{c}\right)_{n+1}^{(k)} \tag{4.15}$$

The flowchart for implementing the local law by CPPM is presented in Table 4.4.

Table 4.4 Closest point projection method (CPPM) for local law

1) Initialise: $k=0$, $\left(\boldsymbol{\delta}^{cp}\right)_{n+1}^{(0)}=\left(\boldsymbol{\delta}^{cp}\right)_{n}$, $\left(\Delta\boldsymbol{\delta}^{cp}\right)_{n+1}^{(k)}=0$, $\left(\Delta\lambda^{c}\right)_{n+1}^{(k)}=0$.

2) Compute yield condition and evaluate hardening law residuals,

$$\left(\Delta\mathbf{f}^{c}\right)_{n+1}^{(k)}=\left(\mathbf{k}^{c}\right)_{n+1}^{(k)}\left(\left(\Delta\boldsymbol{\delta}^{c}\right)_{n+1}-\left(\Delta\boldsymbol{\delta}^{cp}\right)_{n+1}^{(k)}\right),\ \left(\mathbf{f}^{c}\right)_{n+1}^{(k)}=\left(\mathbf{f}^{c}\right)_{n}+\left(\Delta\mathbf{f}^{c}\right)_{n+1}^{(k)}$$

$$F_{n+1}^{(k)}=F\left(\left(\mathbf{f}^{c}\right)_{n+1}^{(k)},\left(\boldsymbol{\delta}^{c}\right)_{n+1}^{(k)}\right)$$

$$R_{n+1}^{(k)}=-\left(\Delta\boldsymbol{\delta}^{cp}\right)_{n+1}^{(k)}+\left(\Delta\lambda^{c}\right)_{n+1}^{(k)}\mathbf{b}_{n+1}^{k}$$

IF: $F_{n+1}^{(k)}\le FTOL$ and $\left\|R_{n+1}^{(k)}\right\|\le RTOL$, THEN: EXIT.

3) Compute consistent tangent moduli

$$\mathbf{C}_{n+1}^{-1^{(k)}}=\left(\left(\mathbf{k}^{c}\right)^{-1}\right)_{n+1}^{(k)}+\left(\Delta\lambda^{c}\right)_{n+1}^{(k)}\mathbf{b}_{n+1}^{(k)}$$

4) Obtain increment to consistency parameter

$$\left(\Delta^{2}\lambda^{c}\right)_{n+1}^{(k)}=\frac{F_{n+1}^{(k)}-\mathbf{a}_{n+1}^{(k)}\mathbf{C}_{n+1}^{(k)}R_{n+1}^{(k)}}{\mathbf{a}_{n+1}^{(k)}\mathbf{C}_{n+1}^{(k)}\mathbf{b}_{n+1}^{(k)}}$$

5) Calculate force increments

$$\left(\Delta\mathbf{f}^{c}\right)_{n+1}^{(k)}=-\mathbf{C}_{n+1}^{(k)}R_{n+1}^{(k)}-\left(\Delta^{2}\lambda^{c}\right)_{n+1}^{(k)}\mathbf{C}_{n+1}^{(k)}\mathbf{a}_{n+1}^{(k)}$$

6) Obtain incremental plastic strains and internal variables

$$\left(\Delta\lambda^{c}\right)_{n+1}^{(k+1)}=\left(\Delta\lambda^{c}\right)_{n+1}^{(k)}+\left(\Delta^{2}\lambda^{c}\right)_{n+1}^{(k)}$$

7) Incremental plastic displacements

$$\left(\Delta\boldsymbol{\delta}^{cp}\right)_{n+1}^{(k+1)}=-\left(\left(\mathbf{k}^{c}\right)^{-1}\right)_{n+1}^{(k)}\left(\Delta\mathbf{f}^{c}\right)_{n+1}^{(k)}$$

8) Update forces at inter-particle contact

$$\left(\mathbf{f}^{c}\right)_{n+1}^{(k+1)}=\left(\mathbf{f}^{c}\right)_{n+1}^{(k)}+\left(\Delta\mathbf{f}^{c}\right)_{n+1}^{(k)}$$

Set $k\leftarrow k+1$ and GO TO step 2.

4.3.3.2 Cutting plane algorithm (CPA)

Alternatively, the CPA proposed by Ortiz and Simo (1986) has been selected and its performance compared to CPPM. The CPA is convivial to use since it does not require the

evaluation of moduli based on internal variables. The plastic multiplier can be calculated by

$$\left(\Delta\lambda^c\right)_{n+1}^{(k)} = \frac{F_{n+1}^{(k)}}{H_{n+1}^{(k)} + \mathbf{a}_{n+1}^{T(k)} \left(\mathbf{k}^c\right)_{n+1}^{(k)} \mathbf{b}_{n+1}^{(k)}} \tag{4.16}$$

where $H_{n+1}^{(k)}$ can be calculated by

$$H_{n+1}^{(k)} = -\frac{\partial F}{\partial \delta_r^{cp}} \frac{\Delta \delta_r^{cp}}{\Delta \lambda^c} \tag{4.17}$$

The detailed calculations of Eqs.(4.16) and (4.17) are given in Appendix B. The plastic displacement can be updated by

$$\left(\Delta\boldsymbol{\delta}^{cp}\right)_{n+1}^{(k+1)} = \left(\Delta\boldsymbol{\delta}^{cp}\right)_{n+1}^{(k)} + \left(\Delta\lambda^c\right)_{n+1}^{(k)} \mathbf{b}_{n+1}^{(k)} \tag{4.18}$$

The flowchart of this method is presented in Table 4.5.

Table 4.5 Cutting-plane algorithm (CPA) for local law

1) Initialise: $k = 0$, $\left(\boldsymbol{\delta}^{cp}\right)_{n+1}^{(0)} = \left(\boldsymbol{\delta}^{cp}\right)_n$, $\left(\Delta\boldsymbol{\delta}^{cp}\right)_{n+1}^{(k)} = 0$.

2) Compute the force increment, hardening moduli, and yield function

$$\left(\Delta\mathbf{f}^c\right)_{n+1}^{(k)} = \left(\mathbf{k}^c\right)_{n+1}^{(k)} \left(\left(\Delta\boldsymbol{\delta}^c\right)_{n+1} - \left(\Delta\boldsymbol{\delta}^{cp}\right)_{n+1}^{(k)}\right), \quad \left(\mathbf{f}^c\right)_{n+1}^{(k)} = \left(\mathbf{f}^c\right)_n + \left(\Delta\mathbf{f}^c\right)_{n+1}^{(k)}$$

IF $F\left(\left(\mathbf{f}^c\right)_{n+1}^{(k)}, \left(\boldsymbol{\delta}^c\right)_{n+1}^{(k)}\right) \le FTOL$, THEN: EXIT.

ELSE

3) Compute the plastic multiplier

$$\left(\Delta\lambda^c\right)_{n+1}^{(k)} = \frac{F_{n+1}^{(k)}}{C_{n+1}^{(k)} + \mathbf{a}_{n+1}^{T(k)} \left(\mathbf{k}^c\right)_{n+1}^{(k)} \mathbf{b}_{n+1}^{(k)}}$$

4) Update force and plastic displacement

$$\left(\boldsymbol{\delta}^{cp}\right)_{n+1}^{(k+1)} = \left(\boldsymbol{\delta}^{cp}\right)_{n+1}^{(k)} + \left(\Delta\lambda^c\right)_{n+1}^{(k)} \mathbf{b}_{n+1}^{(k)}$$

Set $k \leftarrow k+1$ and GO TO step 2.

ENDIF

Overall, the micromechanical model based on a static hypothesis can be integrated with three

levels of implicit integrations. The accuracy and efficiency of the described scheme will be evaluated based on elementary tests and boundary value problems. The implemented micromechanical model will be further applied for multiscale analyses.

4.4 Accuracy and efficiency of the integration scheme

To assess the performances of the implicit algorithms for integrating the micromechanical model, a series of loading constraints from single element tests to boundary value problems were conducted. The analyses focused on the accuracy and convergence speed for different loading increments. The numerical simulations were performed on an Intel Core i5-4590 at 3.30 GHz processor with internal memory of 8.0 GB. To evaluate the accuracy of the implicit algorithms, we defined the relative error as

$$ERR = \left\| ERR^{\boldsymbol{\sigma}}, ERR^{\boldsymbol{\varepsilon}} \right\| = \sqrt{\frac{\left(\boldsymbol{\sigma}-\boldsymbol{\sigma}^{*}\right):\left(\boldsymbol{\sigma}-\boldsymbol{\sigma}^{*}\right)}{\boldsymbol{\sigma}^{*}:\boldsymbol{\sigma}^{*}} + \frac{\left(\boldsymbol{\varepsilon}-\boldsymbol{\varepsilon}^{*}\right):\left(\boldsymbol{\varepsilon}-\boldsymbol{\varepsilon}^{*}\right)}{\boldsymbol{\varepsilon}^{*}:\boldsymbol{\varepsilon}^{*}}} \tag{4.19}$$

where $ERR^{\boldsymbol{\sigma}}$ and $ERR^{\boldsymbol{\varepsilon}}$ are relative errors for stress and strain, respectively; $\boldsymbol{\sigma}$ and $\boldsymbol{\varepsilon}$ are the results obtained by using the implicit algorithm, whereas $\boldsymbol{\sigma}^{*}$ and $\boldsymbol{\varepsilon}^{*}$ are the exact solutions corresponding to the specified stress or strain increments. The exact values were obtained by decreasing the given tolerance and the incremental size up to a point where the numerical results no longer changed.

4.4.1 Elementary test simulations

To investigate the efficiency and accuracy of the proposed numerical schemes, two kinds of elementary tests were simulated to observe the strength softening behaviour using the parameters calibrated by drained triaxial test results on Hostun sand (Table 2.1). First, triaxial drained compression tests were conducted to check the performance of the proposed integration schemes under mixed control loading conditions. The samples with an initial void ratio of 0.515 were isotropically compressed up to 800kPa and then subjected to an axial strain-controlled loading under a constant confining stress. The exact solutions were obtained by a sub-increment of strain equal to 0.002%. The drained triaxial test simulations for dense sand integrated by CPA (Figure 4.1 (a)-(b)) and by CPPM produced a good agreement (Figure

4.2(a)-(b)). It should be noted that CPPM required less computational cost and showed even more accuracy in the case of an imposed strain increment of 2%, as presented in Table 4.6. Undrained triaxial tests in compression were also conducted by full strain controlled constraints with no iteration for the mixed control procedure, which is a useful example of testing the efficiency of the micro-macro iterations and of the local integration schemes. The samples with an initial void ratio of 0.818 were isotropically compressed up to 800kPa, and then an axial strain-controlled loading at a constant void ratio was performed; the exact solution was obtained by a sub-increment of strain equal to 0.002%. The undrained triaxial test simulations for loose sand both integrated by CPA, shown in Figure 4.1(c) and (d), and by CPPM, shown in Figure 4.2(c) and (d), demonstrated that the methods are hardly different in terms of accuracy, but CPPM is superior in terms of computational cost efficiency.

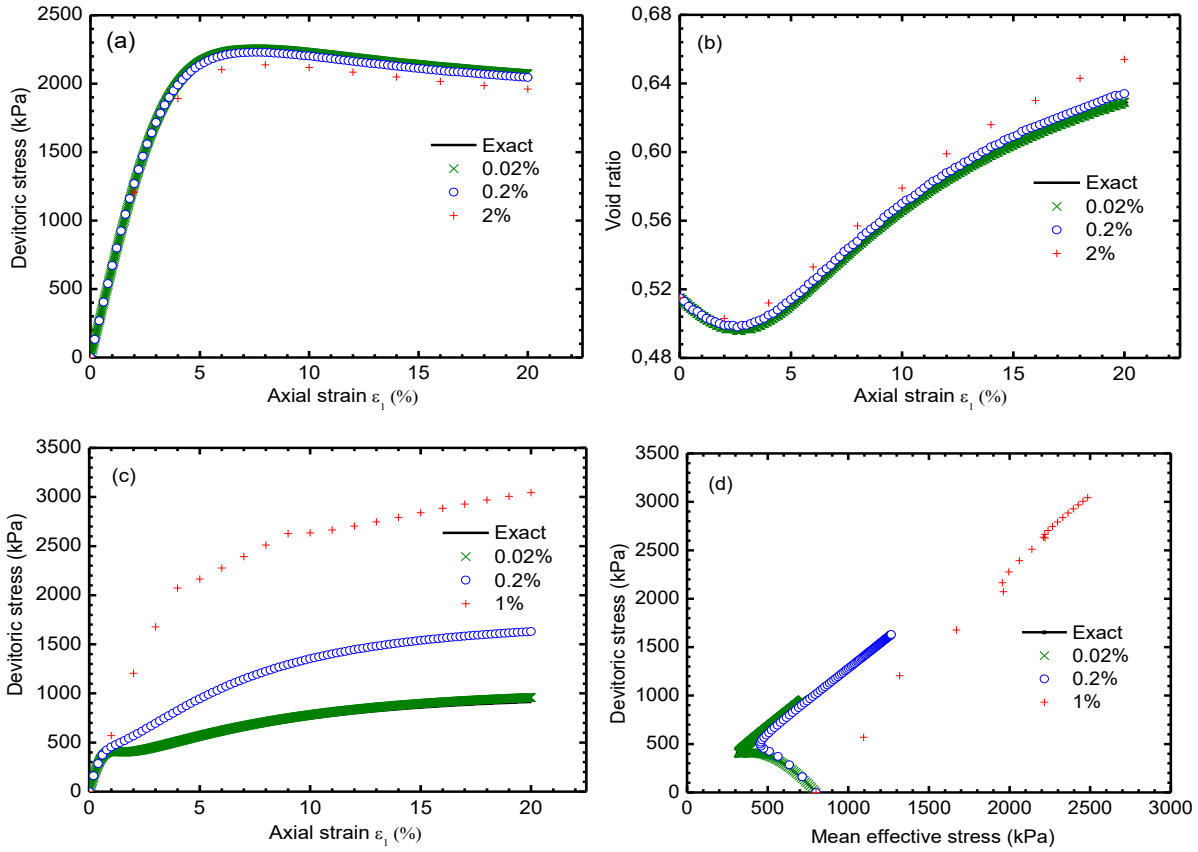

Figure 4.1 Performances of CPA for dense sand and loose sand under drained and undrained compressions: (a) deviatoric stress versus axial strain, (b) void ratio versus axial strain for dense sand, (c) deviatoric stress versus axial strain for loose sand, (d) deviatoric stress versus mean effective stress for loose sand

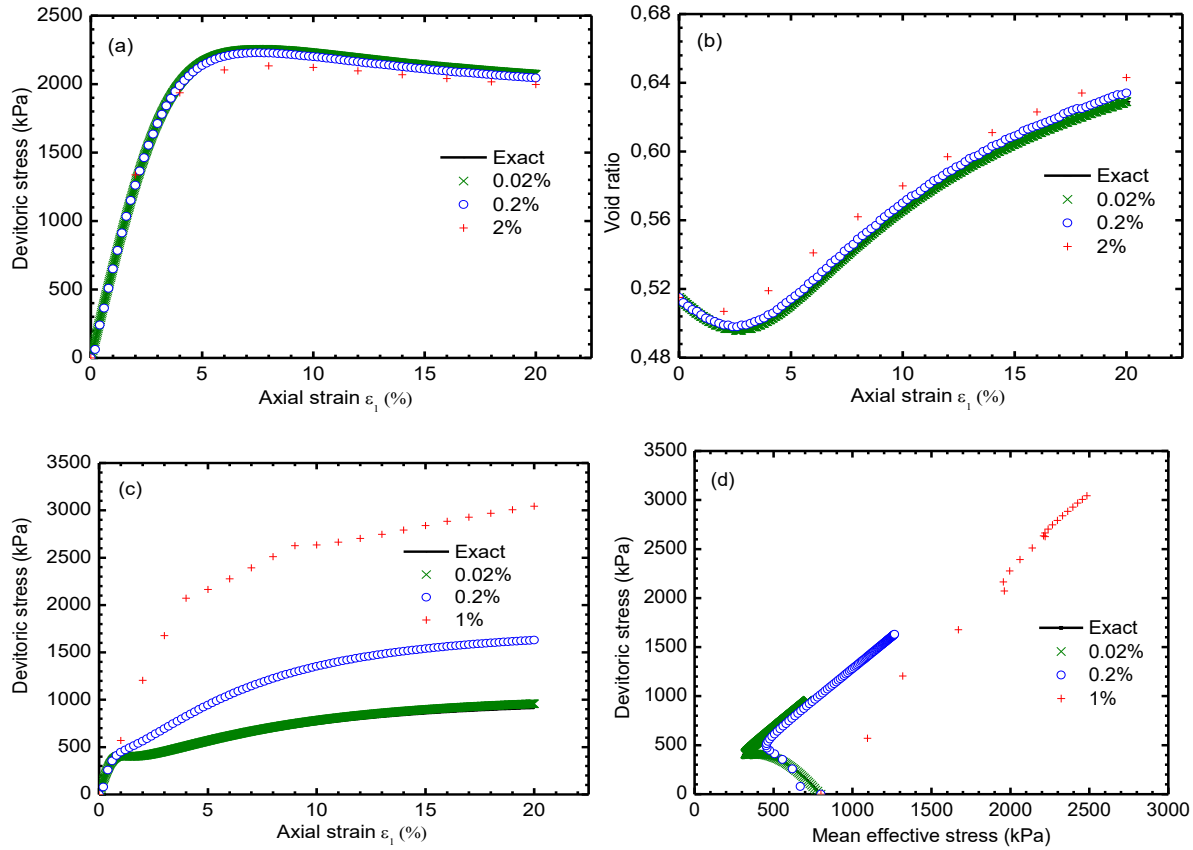

Figure 4.2 Performances of CPPM for dense sand and loose sand under drained and undrained compressions: (a) deviatoric stress versus axial strain, (b) void ratio versus axial strain for dense sand, (c) deviatoric stress versus axial strain for loose sand, (d) deviatoric stress versus mean effective stress for loose sand

Table 4.6 Performances of implicit algorithms on triaxial drained and undrained tests

Test information			CPA			CPPM		
Test no.	Initial void ratio	Strain increments	Iterations	CPU time (s)	ERR (%)	Iterations	CPU time (s)	ERR (%)
TXD	0.515	0.002%	311258	81.734	Exact	313912	70.984	Exact
TXD	0.515	0.02%	111231	26.406	0.178	112004	22.453	0.178
TXD	0.515	0.2%	27441	6.328	1.459	27658	5.438	1.454
TXD	0.515	2%	5102	1.25	3.787	5092	1.172	5.533
TXU	0.721	0.002%	261504	65.328	Exact	263003	56.821	Exact
TXU	0.721	0.02%	38648	9.328	5.000	38898	8.219	5.000
TXU	0.721	0.2%	4737	1.29	77.659	4785	1.125	77.661
TXU	0.721	1%	1048	0.391	233.490	541	0.219	233.492

4.4.2 Iso-error maps

The accuracy of the implicit integration scheme can be evaluated by iso-error maps as proposed by Krieg and Krieg (1977), Ortiz and Simo (1986) and Simo and Taylor (1986). The numerical errors due to different loading step increments in various loading directions can be analysed by plotting these iso-error maps. An iso-error map, corresponding to a specific stress state, can be generated by plotting the relative errors calculated by Eq.(4.19) for all the integrations performed by imposing different step increments upon the selected constraints. The remaining degrees of freedom can be kept either constant or equal to the prescribed increments.

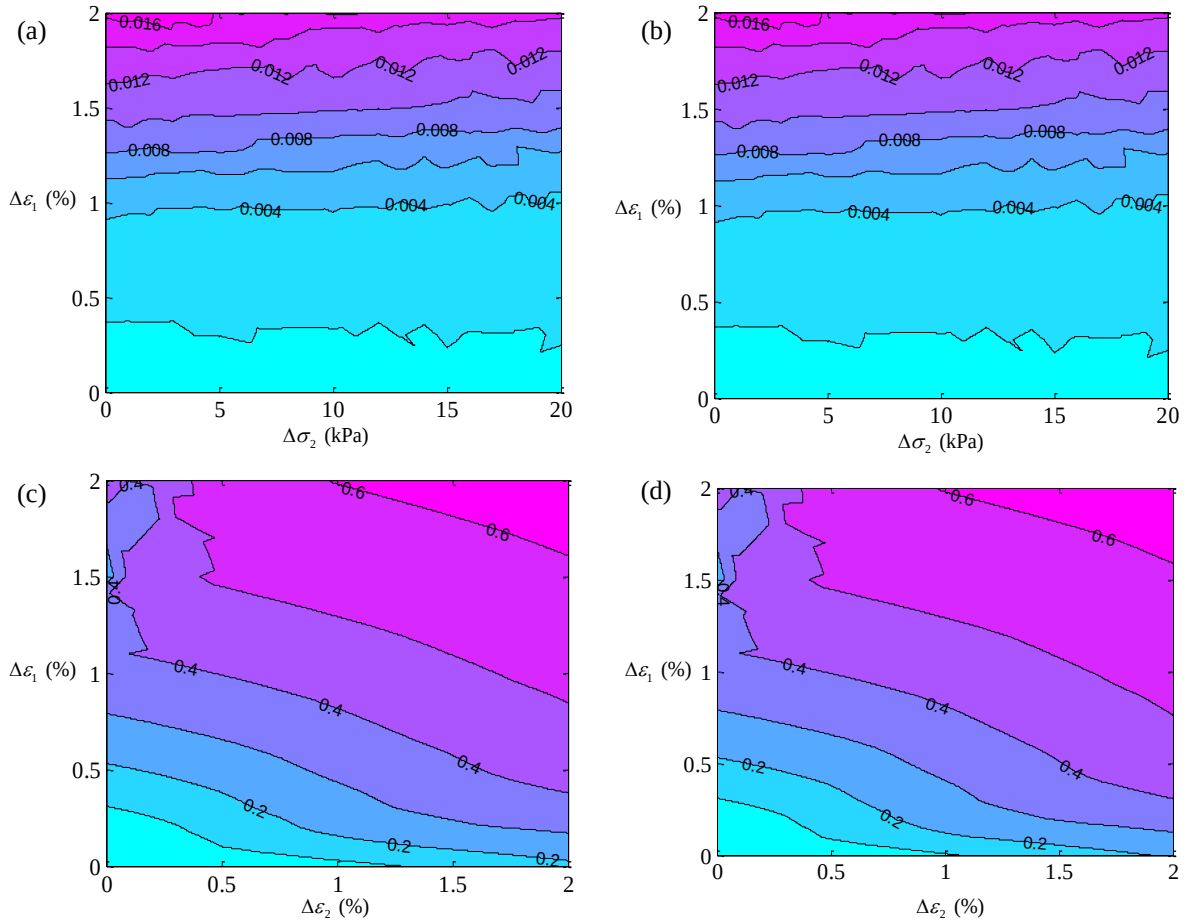

Figure 4.3 Isoerror maps plotted under mixed controls and strain controls: (a) CPA for drained triaxial test, (b) CPPM for drained triaxial, (c) CPA for undrained triaxial test, (d) CPPM for undrained triaxial test

To obtain the distribution of errors under mixed control and strain control, respectively, the

aforementioned triaxial drained and undrained tests with an initial void ratio of 0.515 and a confining pressure of 800kPa were performed for a second time. Given the performances of the implicit schemes with CPA and CPPM shown in Figure 4.1 and Figure 4.2, the stress state at the softening stage was selected to generate the iso-error maps. Figure 4.3(a) presents the iso-error map calculated with CPA by the mixed control at the state of p'=1545kPa, q=2331kPa and ε_d =11%, and Figure 4.3(b) shows the iso-error map computed by CPPM under the same condition. The obtained relative errors are in the same range as those obtained by typical return mapping schemes, with smaller loading increments leading to lower errors (Simo and Taylor, 1986; Zhang and Buscarnera, 2015). The proposed two schemes have the same performance with the changes of the vertical strains and the lateral stresses, and are much more sensitive to strain increments than to stress step sizes.

The iso-error maps for the undrained triaxial loading path were obtained, as shown in Figure 4.3(c) and (d), by imposing different strain step sizes at the state of p'=320.7kPa, q=393.2kPa and ε_d =1.5%. Compared to the mixed control case, the strain controlled integration contains larger errors since there is no global iteration; thus, the macro variables such as the void ratio were not updated during the iterations of the local law. The differences between the two iso-error maps plotted by using CPPM and CPA can hardly be distinguished.

4.5 Application to boundary value problems

This section discusses the use of the CH model, implemented in the form of a user subroutine, in finite element simulations. The efficiency of the procedure has been validated by single-element tests, multi-element tests and boundary value calculations.

4.5.1 Finite element implementation

The micromechanical model has been implemented into Abaqus/Standard 6.11 as a user material (UMAT) and the implementation has been validated by simulating single element tests with the implicit integration schemes along various loading paths. Under a given loading condition, the results were the same as the ones obtained by direct simulations of the model coded in the previous section, which demonstrated the success of the implementation into the

finite element code.

4.5.2 Biaxial test simulation

The implicit integration schemes were further verified by simulating biaxial tests, in which the strain increments inside and outside the shear band are not the same. The simulated biaxial test was performed on dense sand as its behaviour is highly dilative with strain softening occurring rapidly under a small range of strain. The influence of the mesh size was investigated, and a reasonable mesh size was generated. The specimen was composed of 2501 elements and 2583 nodes with the dimension of 200mm × 100mm × 10mm, as shown in Figure 4.4. The specimen was first isotropically compressed up to a pressure of 800kPa and then loaded with different vertical displacement increments, maintaining a constant lateral stress. An accurate result was obtained for a maximum vertical displacement increment of 0.02mm (Table 4.7). The integration schemes with CPPM and CPA had a similar performance, as shown in Figure 4.5(a) for CPPM and Figure 4.5(b) for CPA.

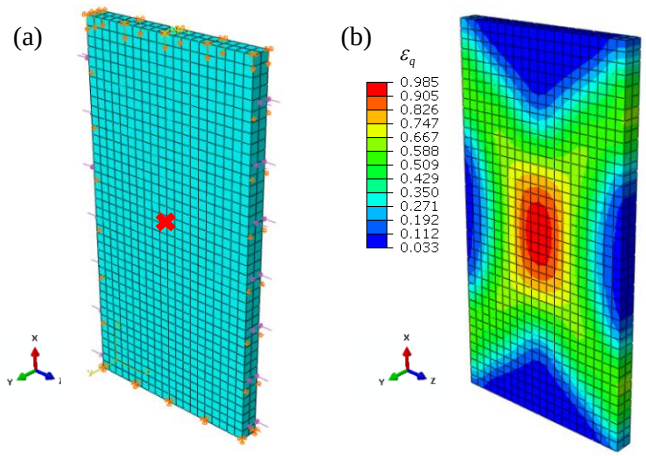

Figure 4.4 Biaxial test simulation: (a) meshes and boundary conditions, (b) distribution of equivalent plastic strain

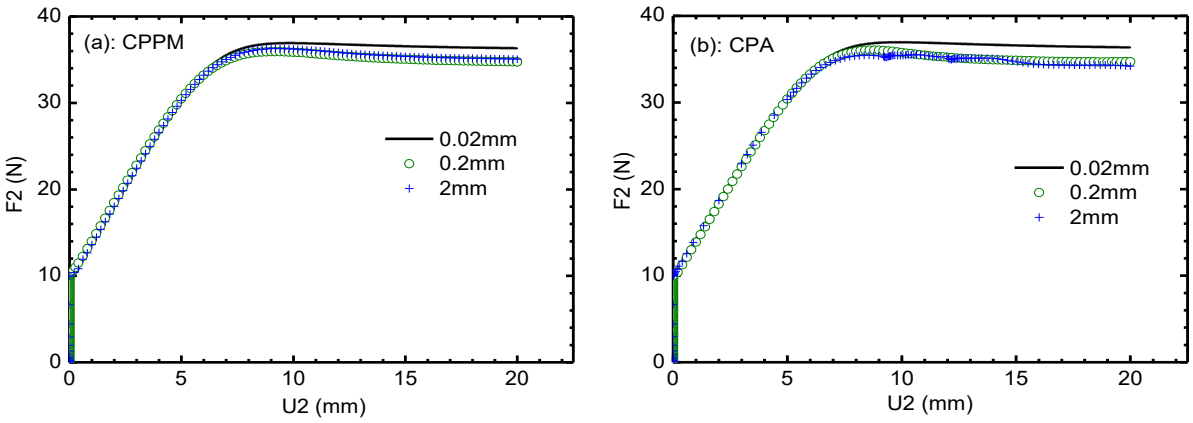

Figure 4.5 Biaxial tests by various increments using (a) CPPM, (b) CPA to integrate force-displacement relations

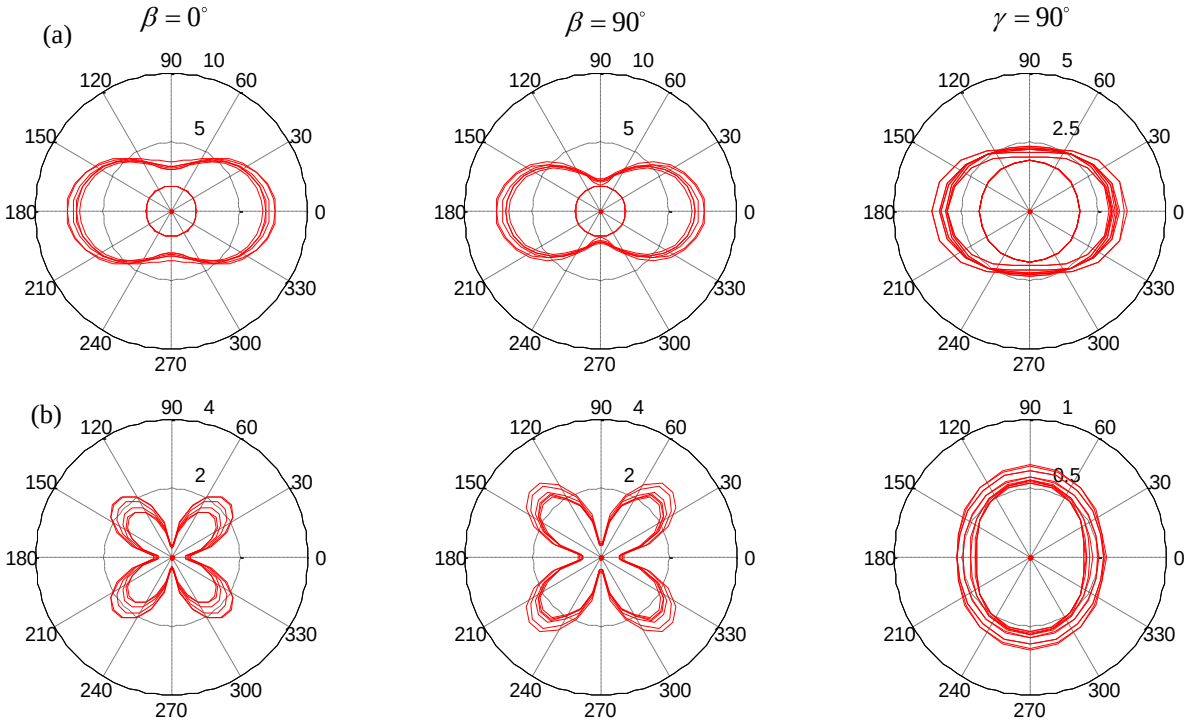

Figure 4.6 Evolution of interparticle contact forces of the selected element: (a) normal forces (N), (b) tangential forces (N)

A shear band was observed from the distribution of the deviatoric plastic strain. To understand the formation of the shear band, it was decided to undertake a multiscale analysis by examining the evolution of the inter-particle normal and tangential force distributions for a central element inside the shear band. During the development of the shear band, the normal force pointed its maximum value in the vertical direction, whereas the shear force pointed its

maximum value towards the direction of the shear band, as shown in Figure 4.6(a) and (b). Note that this study is focused on the predictive performances of the numerical integrations; other problems such as instability, bifurcation, strain localization regulation, etc., will be studied at a later stage.

Table 4.7 Performances of implicit algorithms in biaxial drained test simulations

Test information			CPPM		CPA	
Test no.	Initial void ratio	Maximum increments	CPU time (s)	ERR (%)	CPU time (s)	ERR (%)
BXD	0.6	0.02mm	6921.3	Exact	7980.5	Exact
BXD	0.6	0.2mm	1997.7	4.420	2056.4	4.580
BXD	0.6	2mm	1833.7	3.898	1944.8	4.012

Table 4.8 Performances of implicit algorithms in finite element analysis of square footing

Test information		CPPM		CPA	
Test no.	Initial void ratio	CPU time (s)	ERR (%)	CPU time (s)	ERR (%)
FT1	0.5	83273	Exact	1.068E5	Exact

4.5.3 Finite element analysis of a square footing

The ultimate bearing capacity of a rigid footing is a typical problem for numerical validation, due to the complex loading stress paths inside the soil foundation. During loading, the values of the strain increments span a very large range within the soil volume beneath the footing, which requires solid constitutive integration schemes over all the Gauss points. To assess each performance of the implicit integration of the micromechanical model, we performed a finite element analysis of a square footing. As shown in Figure 4.7(a), the finite element model is composed of 8819 C3D8R elements and 9261 nodes, and only a quarter of the volume is considered for the calculation, due to the symmetry of the problem. The dimensions of the soils are $10\text{m} \times 10\text{m} \times 10\text{m}$, whereas the bottom of the footing is $1\text{m} \times 1\text{m}$. The lower boundary of the soil is fixed in the directions x, y and z, whereas the lateral soil boundaries are only fixed in the y and z directions. As for the boundary of the footing, only the vertical displacement has not been prevented. The model parameters used in the previous example were selected with an initial void ratio of 0.5 and 0.7, respectively. Considering that the

footing can be regarded as a rigid body, a single element can be used to represent the footing, which prevents the influence of the soil-footing interaction on the performance of the studied algorithms.

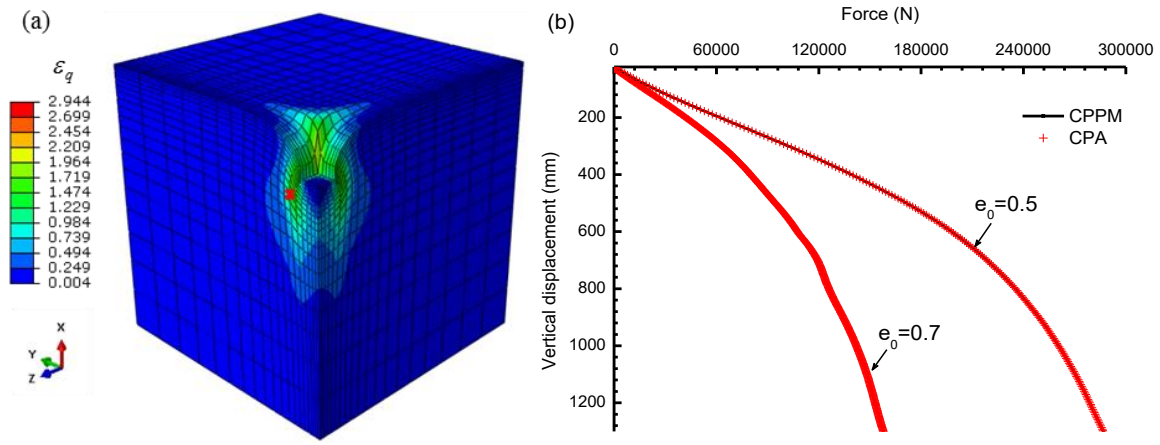

Figure 4.7 Finite element model of a square footing: (a) equivalent plastic strain of dense sand, (b) reaction force and vertical displacement of the square footing

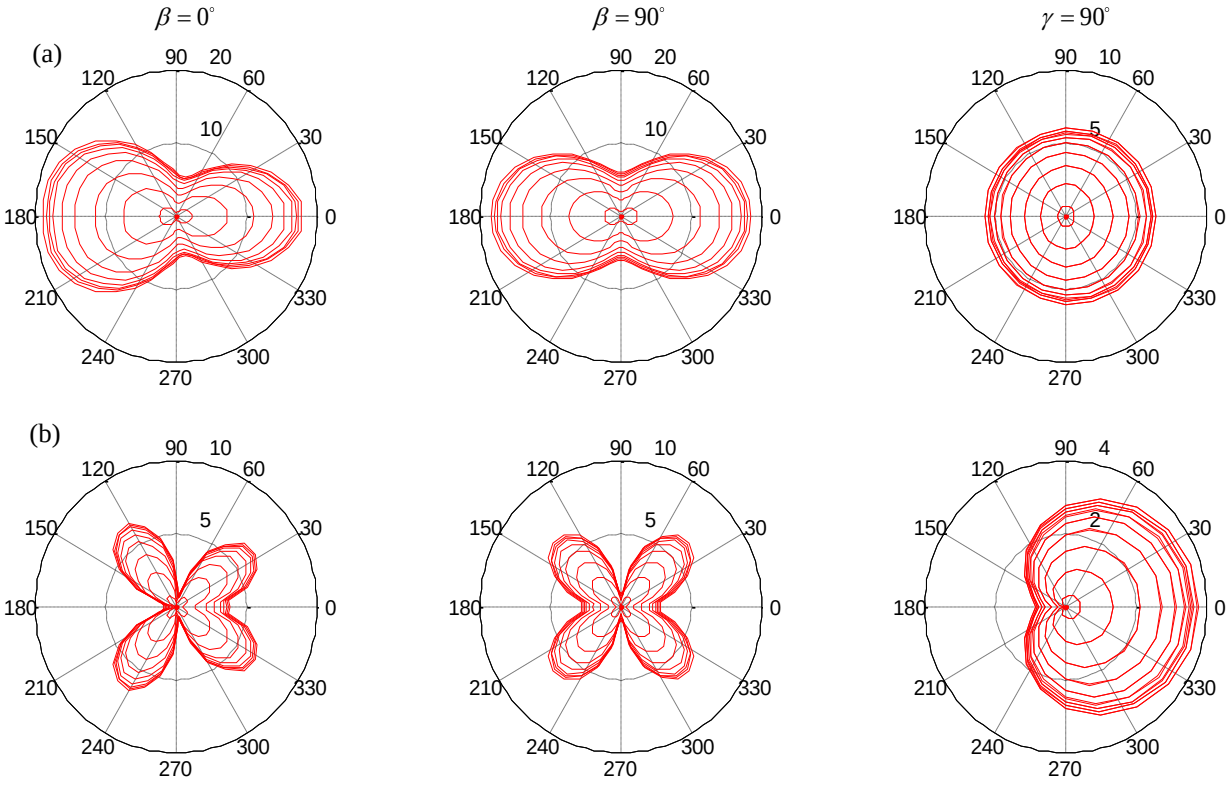

Figure 4.8 Evolution of interparticle contact forces of the selected element: (a) normal forces (N), (b) tangential forces (N)

At first, the soil underwent a geostatic loading in order to simulate the *in-situ* gravity and, then, a 50kPa surcharge was imposed on the ground surface to avoid the singularities at the edge of the footing. The footing was then loaded by imposing a vertical displacement with different maximum increments of 0.15mm, 1.5mm, 15mm and 150mm. The distribution of the deviatoric plastic strain, shown in Figure 4.7(a) for dense sand, is quite similar to the results obtained in the literature (Gourvenec *et al*., 2006; Lyamin *et al.*, 2007). Since most of the incremental loadings were very small and under the tolerance requirements of the finite element code, the same force-displacement curves were obtained for different methods of integration (CPPM, CPA) and different loading increments, as shown in Figure 4.7(b). However, the CPPM procedure needed less computational time than the CPA procedure, as shown in Table 4.6. To demonstrate that the approach could perform multiscale analyses, one element inside the shear band of the soil with an initial void ratio of 0.5 (Figure 4.8(a)) was selected to show the evolution of the normal and tangential force distributions. As shown in Figure 4.8(a) and (b), the normal and tangential forces were non-symmetric, which agrees with the existence of principal stress rotations during loading.

4.6 Concluding remarks

This chapter has presented an implicit method for integrating the micromechanical models based on a static hypothesis. A predictor-corrector method was proposed to solve linearized constraint equations under mixed controls. An iterative scheme was constructed to implement the stress-driven micro-macro relations. Two return mapping algorithms, i.e., the closest point projection method (CPPM) and the cutting plane algorithm (CPA) with the backward Euler method, were alternatively adopted to implement the local law at the micro level. The model was then implemented into a finite element code in order to perform multiscale analyses of boundary value problems. The main findings can be summarised as follows:

1) The predictor-corrector method is efficient for solving linearised mixed control constraint equations. The effectiveness of this method has been validated by simulating drained triaxial compression tests, in which the boundary conditions consisted in imposing the vertical strain and the lateral stresses.

2) The static hypothesis was implemented consistently with the stress homogenisation formula by an out-of-balance iteration scheme, which rendered consistent the localisation and averaging operators.
3) The local force-displacement relations were integrated by CPPM and CPA, respectively. Consistent results were obtained by using the two integration schemes with small strain or stress increments. In comparison to CPA, CPPM provided a better computational cost efficiency without any loss of accuracy, either for elementary tests or boundary value problems.
4) The CH model was implemented into a finite element code and firstly validated by elementary tests. Then, two typical boundary value problems, i.e., a biaxial test and a square footing, were simulated, and the applicability of this method for multiscale analyses was demonstrated.

The CH model belongs to the family of micromechanical models which use the static approach. This work could, therefore, provide guidance for similar attempts on micromechanical models of the same type.

CHAPTER 5 MULTISCALE STUDY OF INSTABILITIES IN GRANULAR ASSEMBLIES

5.1 Introduction

The phenomenon of failure at various scales has been widely observed in geotechnical engineering. Much effort has been devoted to understanding this mechanism in granular materials (Vardoulakis *et al*., 1978; Vardoulakis, 1980; Gudehus, 1986; Tejchman and Wu, 1993; Nova, 1989, 1994; Desrues *et al*., 1996; Tejchman 1997; Oda and Kazama, 1998; Lade, 2002; Desrues and Viggiani, 2004; Nicot *et al*., 2007; Chang *et al*., 2011; Daouadji *et al*., 2011, 2013; Ando *et al*., 2012; Sze and Yang, 2013; Bouscarnera and Mihalache, 2014; Desrues and Ando, 2015). Experimental studies have shown that global failure can depend on various elements such as material density, degree of saturation, mechanical state and loading history, *etc*. (Desrues and Viggiani, 2004; Gudehus and Nübel, 2004; Mirone and Corallo, 2010; Daouadji *et al*., 2011, 2013; Ando *et al*., 2012; Gao and Zhao, 2013; Bouscarnera and Mihalache, 2014; Misra and Poorsolhjouy, 2015b). Micromechanical investigations have demonstrated that global instabilities in granular materials originate from the rearrangements of grain-loops and the collapses of force-chains (Nicot *et al*., 2007; Radjai, 2008; Rechenmacher, 2006; Tordesillas *et al*., 2009; Welker and McNamara, 2009; Rechenmacher *et al*., 2010; Ando, 2012; Desrues and Ando, 2015; Ardeljan *et al*., 2015; Hadda *et al*., 2013, 2015, 2016). Given these findings, two questions can be raised: what criterion can be used to characterise the instabilities at various scales and how is the extent of global instability related to elementary and microstructural instabilities in granular materials?

Various criteria have been proposed to characterise global and local failures (Rudnicki and Rice, 1975; Darve and Laouafa, 2000; Lade, 2002; Staron *et al*., 2005; Nicot *et al*., 2007, Prunier *et al*., 2016; Nicot *et al*., 2017; Wan *et al*., 2017). In engineering practice, the factor of safety used to design geo-structures is based on the plastic limit condition. However, this method is inoperative in certain situations where material failure may occur before the plastic limit state is attained. A most typical example is that of the diffuse failure observed before the

Mohr-Coulomb plastic limit (Darve and Laouafa, 2000; Darve *et al*., 2004; Desrues and Viggiani, 2004; Nicot *et al*., 2007; Daouadji *et al*., 2011; Daouadji *et al*., 2013; Wan *et al*., 2013). Therefore, it is of crucial importance to improve understanding of the mechanism of material instability in order to improve the safety of geotechnical structures. Several researchers have attempted to give precise definitions of material failure (Lyapunov, 1907; Hill, 1958; Rudnicki and Rice, 1975; Nova, 1994; Nicot *et al*., 2007; Nicot and Darve, 2007; Prunier *et al*., 2016; Nicot *et al*., 2017). Lyapunov (1907), in particular, was a pioneer in defining instability in solid mechanics within a mathematical framework. Under his definition, a rate-independent mechanical system subjected to a given loading path reaches failure state if the loading path is limited to a given load level for at least one control mode. However, this definition is difficult to apply in engineering practice. By contrast, Hill's sufficient condition of stability (Hill, 1958) is a criterion easier to manipulate. It states that a given material at an equilibrium state is reputedly unstable if, under a prescribed strain increment $d\boldsymbol{\varepsilon}$, the second-order work $d^2w=d\boldsymbol{\sigma}:d\boldsymbol{\varepsilon}\leq 0$ for at least one stress increment $d\boldsymbol{\sigma}$. Based on elastoplasticity theory, Nova (1994) suggested a convenient framework referred to as the loss of controllability which describes the existence of a unique solution for a mechanical system under a prescribed loading program. What are the physical meanings of Hill's stability criterion and the approach consisting of the loss of controllability? Nicot *et al*. (2007) answered this question from the perspective of energy and, in so doing, demonstrated that, for a quasi-static system, the second-order work can be a uniform quantity in capturing the bifurcation point in granular materials (Nicot *et al*., 2009). More recently, the second-order work criterion has been applied to investigate material instability from the particle scale to boundary value problems (Nicot *et al*., 2009; Nicot *et al*., 2011; Prunier *et al*., 2016; Wan *et al*., 2017; Kakogiannou *et al*., 2016; Nicot *et al*., 2017).

The microstructure of a granular material has a significant impact on its macroscopic behaviour. When an external force is applied on the boundary of a specimen, it is transmitted from the particles at the boundary to the inside of the sample through a network of inter-particle contact forces. These forces are the main ingredient that governs the kinematics of

particles through local laws, which leads to the macroscopic strain. Once grain loops collapse, the force chain will be broken and significant displacements will appear (Nicot *et al*., 2007; Radjai, 2008; Rechenmacher, 2006; Tordesillas *et al*., 2009; Welker and McNamara, 2009; Rechenmacher *et al*., 2010; Ando, 2012; Desrues and Ando, 2015; Ardeljan *et al*., 2015). Therefore, the failure of the sample is triggered by the instability of the grain loops. However, a local failure may not destabilise the whole system. For instance, a soil sample extracted from a local failed slope is in a failed state, while the whole slope remains stable. Following the development of the micromechanics of granular materials, the extent of global instability arising from microstructural instability was recently examined by the discrete element method (Rechenmacher, 2006; Nicot and Darve, 2007; Sibille *et al*., 2007; Hall *et al*., 2010; Nguyen, 2016; Zhao *et al*., 2016). It was found that micro instabilities precede a global failure. However, the relation between local instability and global failure has not been explicitly considered with computational models (Chang *et al*., 2010; Daouadji *et al*., 2011). To this purpose, a micromechanical model describing the behaviour of granular materials at both the micro and macro scales is necessary. Furthermore, the criterion of instability at different scales should be consistently quantified in accordance with the micromechanical model.

Micromechanical models have been developed through the definition of inter-particle contact laws and homogenisation schemes (Chang and Hicher, 2005; Nicot and Darve, 2005, 2011; Li *et al*., 2009; Yin and Chang, 2009; Yin *et al*., 2011, 2013, 2014; Xiong *et al*., 2017). Discrete features of granular materials are embedded within these models which describe the stress-strain relations of granular assemblies. In terms of a homogenisation scheme, the Love-Weber formula has been widely used as the average operator thanks to its effectiveness in aggregating inter-particle forces to assembly stresses. However, various localisation operators have been suggested to compute local variables from global ones. Two types of localised operators: the kinematic method and the static hypothesis can be found in the literature. The kinematic method relates global strains to inter-particle displacements, based on which micromechanical models were constructed by Nicot and Darve (2005, 2011), Misra and Singh (2014), Misra and Poorsolhjouy (2015a) and Xiong *et al*. (2017). The static hypothesis

deduces inter-particle forces from global stresses, which gives rise to a family of micromechanical models (Chang and Hicher, 2005; Yin and Chang, 2009; Yin *et al*., 2011, 2013, 2014). Among these models, the CH model has proved to be effective in predicting the overall behaviour of granular materials (Chang and Hicher, 2005).

This chapter focuses on the second-order work criterion to characterise failure at various scales. The CH micromechanical model has been adopted because it is one of the few models that can accurately reproduce the behaviour of granular materials at both the representative volume and the inter-particle contact levels. The chapter, divided into three parts, will present the following discussion: first, the second-order work is defined at different scales and its relations between these different scales are derived. Then, the rationality of the micromechanical model expressed by the Cauchy stresses and the Euler strains to calculate the second-order work is tested. Finally, simulations of triaxial tests as REV scale problems and biaxial tests as boundary value problems are conducted to demonstrate that this method is capable of describing the extent of global failure originating from microstructural instabilities.

5.2 Second-order work as a failure criterion

5.2.1 Loss of sustainability

Failure modes of granular materials and their different mechanisms have been widely studied (see for example: Chambon *et al*., 2004; Welker and McNamara, 2009; Sze and Yang, 2013; Hadda *et al*., 2015). Generally, two specific failure modes: localised and diffuse failures have been observed (Darve and Laouafa, 2000; Darve *et al*., 2004; Nicot *et al*., 2007). In localised failure, the strain is concentrated in shear bands; the displacement field is highly heterogeneous and organised. The diffuse failure is characterised by the absence of a specific failure pattern; the displacement field is chaotic, without any apparent organisation. The present study investigates localised and diffuse failures in non-viscous granular materials at small deformations. Neither the geometric nor the divergence instability will be discussed.

Failure occurs with an outburst of kinetic energy (Hadda *et al*., 2016; Nguyen *et al*., 2016). From this energy perspective, Nicot and Darve (2007) suggested that the sign of the second-

order work can be used to detect the transition from a quasi-static to a dynamic system. Using the Lagrangian description, the kinetic energy increment can be expressed as

$$\delta E_c(t) = \int_{\Gamma_0} F_i \delta u_i dS_o + \int_{V_0} b_{o,i} \delta u_i dV_o - \int_{V_0} \Pi_{ij} \frac{\partial(\delta u_i)}{\partial X_j} dV_o \tag{5.1}$$

where $\delta E_c(t)$ represents the current change in kinetic energy of the system; F_i is the surface density of the forces applied to the boundary; **u** is the displacement field imposed along the boundary; b_0 is the density of the body force in the volume; **Π** denotes the first Piola-Kirchhoff stress tensor; the operator $\partial \cdot / \partial X_i$ denotes spatial differentiation whereas δ represents particulate time derivative; Γ_0 is the boundary of the volume V_0. The differentiation with time of Eq.(5.1) results in

$$\delta^2 E_c(t) = \int_{\Gamma_0} \delta\Pi_{ij} N_j \delta u_i dS_o + \int_{V_0} \delta b_{o,i} \delta u_i dV_o - \int_{V_0} \delta\Pi_{ij} \frac{\partial(\delta u_i)}{\partial X_j} dV_o \tag{5.2}$$

in which **N** is the normal to the boundary. The kinetic energy can be expressed by a two-order Taylor expansion

$$E_c(t+\delta t) = E_c(t) + \dot{E}_c(t)\delta t + \frac{1}{2}\ddot{E}_c(t)\delta t^2 + o(\delta t)^3 \tag{5.3}$$

Noting that $E_c(t) = \int_{V_0} \rho_0 \left\|\dot{\mathbf{u}}\right\|^2 dV_0$ and the system is in an equilibrium state at a time t, then $E_c(t) = 0$, similarly $\dot{E}_c(t) = \int_{V_0} \rho_0 \dot{\mathbf{u}} \cdot \ddot{\mathbf{u}} dV_0$ at time t satisfies $\dot{E}_c(t) = 0$. Therefore, Eq.(5.3) can be expressed as

$$E_c(t+\delta t) = \frac{1}{2}\ddot{E}_c(t)\delta t^2 + o(\delta t)^3 \tag{5.4}$$

Ignoring the third-order terms, then $2E_c(t+\delta t) = \ddot{E}_c(t)\delta t^2$. The system evolves if and only if the kinetic energy is greater than zero, i.e. $E_c(t+\delta t) > 0$. Thus by combining with Eq.(5.2), it follows that

$$\delta^2 E_c(t) = \underbrace{\int_{\Gamma_0} \delta\Pi_{ij} N_j \delta u_i dS_o + \int_{V_0} \delta b_{o,i} \delta u_i dV_o}_{W_2^{ext}} - \underbrace{\int_{V_0} \delta\Pi_{ij} \frac{\partial(\delta u_i)}{\partial X_j} dV_o}_{W_2^{\text{int}}} > 0 \tag{5.5}$$

For non-viscous materials, the external second-order work W_2^{ext} is zero during a quasi-static loading. Therefore, the kinetic energy bursts out only if the internal second-order work W_2^{int} is negative. In other words, the instability of the system can be detected by a change of sign of the second-order work.

5.2.2 Lagrangian and Euler description

The second-order work can be expressed with a material and spatial description. A given material, with a volume V_0 and a surface boundary S_0, initially in a configuration C_0, is considered. Under a loading history, the system is in a strained configuration C, with a volume V and a boundary surface S, in equilibrium under a prescribed external load. Each material point in volume V_0 is transformed into a material point in volume V. All the material points in volume V_0 are displaced along with pure strain induced by stretching and spinning deformations. If large deformations take place, the initial configuration C_0 and the current configuration C cannot be merged. The second-order work defined in configuration C_0 is obtained by a Lagrangian description, whereas when defined in configuration C it is obtained by a Euler description (see details in Nicot *et al*., 2007). Based on a Lagrangian description, the stability of elastoplastic solids has been defined by Hill (1958):

$$W_2 = \int_{V_0} \dot{s}_{ij} \frac{\partial \dot{U}_j}{\partial x_i} dV_0 > 0 \tag{5.6}$$

in which $\dot{s}_{ij}$ is the rate of the nominal stress tensor, which is the transposed form of the non-symmetric Piola-Kirchhoff stress tensor; $\partial \dot{U}_j / \partial x_i$ is the kinematic velocity field conjugated with $\dot{s}_{ij}$. Nicot *et al*. (2007) have clarified the link between the violation of Hill's criterion and an increase of kinetic energy. The expression of the internal second-order work by a Lagrangian description can be rewritten as

$$W_2 = \int_{V_0} \delta\Pi_{ij} \delta F_{ij} dV_0 \tag{5.7}$$

in which **F** is the deformation tensor in a Lagrangian description. For the case of small deformations and negligible geometrical effects, the second-order work can be equivalently expressed by a Euler description

$$W_2 = \int_V \delta\sigma_{ij}\delta\varepsilon_{ij} dV \tag{5.8}$$

where **σ** is the Cauchy stress tensor and **ε** is the Euler strain tensor.

5.2.3 Definitions of second-order work at various scales

At the inter-particle contact level, the second-order work for non-viscous materials can be expressed as (Nicot and Darve, 2007; Nicot *et al*., 2007)

$$W_2^c = \delta f_i^c \cdot \delta l_i^c + \delta M_i^c \cdot \delta w_i^c \tag{5.9}$$

in which δf_i^c is the interparticle force increment, δl_i^c is the change of branch length for two connecting grains, δM_i^c is the increment of the contact couple, and δw_i^c is the radian of particle rotation. The first term considers the relative displacement of the particle, whereas the second term describes the effects of particle rotation. Since the CH micromechanical model does not consider the interlocking effect directly but only through global corrections, the second-order work at the inter-particle contacts can be expressed as (Chang *et al*., 2010)

$$W_2^c = \delta f_i^c \cdot \delta\delta_i^c \tag{5.10}$$

where $\delta\delta_i^c$ is the displacement increments defined at the inter-particle contacts.

At the material point (or REV) level, the second-order work expressed by the Euler description is given by

$$W_2^{el} = \delta\sigma_{ij} : \delta\varepsilon_{ij} \tag{5.11}$$

Hence, the global second-order work can be integrated over all elements and can be adopted as an indicator to characterise the stability in boundary value problems. With the finite element method, the global second-order work can be calculated as

$$W_2 = \int_{V_{el}} d\varepsilon^t d\sigma dV_{el} = \int_{V_{el}} \left(Bdq\right)^t D^{ep} Bdq dV_{el} = dq^t \left(\int_{V_{el}} B^t D^{ep} B dV_{el} \right) dq = dq^t k_{el} dq \tag{5.12}$$

where k_{el} is the elementary consistent tangent stiffness matrix. Once all the meshes are assembled, we obtain

$$W_2 = \int_V d\varepsilon^t d\sigma dV = dQ^t K dQ = dQ^t dF \tag{5.13}$$

in which *dQ* and *dF* are the global nodal incremental displacement and force, *K* is the global consistent tangent matrix (Prunier *et al.*, 2016; Nicot *et al.*, 2017).

5.3 Multiscale approach and the second-order work

To analyse the instability occurring at various scales, a multiscale approach is necessary. Through this approach, the second-order work can be defined at different scales and linked up and down the scales. The efficiency of the multiscale analysis of the second-order work for capturing instability will be evaluated by a directional analysis.

5.3.1 Micromechanical model

In this study, the CH model (Chang and Hicher, 2005) has been adopted to describe the granular material behaviour. Details of this model can be found in Chapter 1. The model could be calibrated by simulating drained triaxial tests on loose and dense Hostun sand samples. The parameters used in this model are given in Table 2.1.

5.3.2 Directional analysis

For a given material at an equilibrium state, a small perturbation can be imposed to detect whether this state is sustainable. A convenient method for conducting the perturbation is the directional analysis proposed by Gudehus (1979). Incremental stress probes or strain probes are imposed along all loading directions, and their conjugate incremental strains or stresses are calculated (Figure 5.1(a-b)). If there is a loading direction for which the second-order work is negative, a loss of sustainability will occur under this loading program, otherwise the equilibrium is unconditionally sustainable.

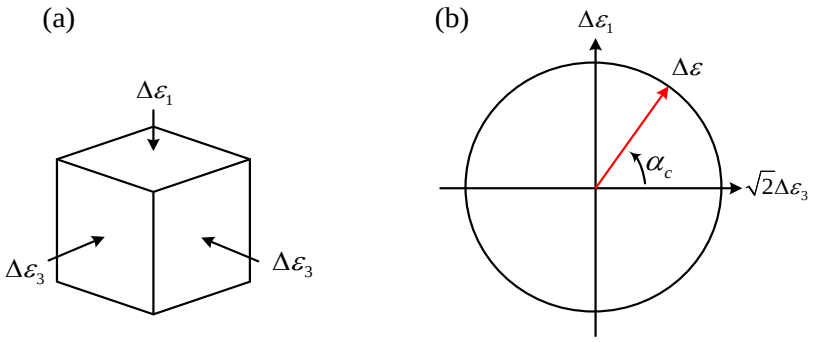

Figure 5.1 Rendulic plane: (a) triaxial probe, (b) strain probe circle

We began by imposing a strain probe of a magnitude 1% on a dense sample at different stages of a drained triaxial test. Four points A, B, C and D, at axial strains of 1%, 4%, 6.5% and 12%, respectively, were selected to analyse the second-order work in the Rendulic plane, shown in Figure 5.2(a) and (b). At point A, the second-order work is positive in all loading directions, whereas at point B the second-order work vanishes in the 150° loading direction while remaining positive in all the other directions (Figure 5.3(a-b)). This explains that in certain loading schemes the material is stable despite the existence of latent instability. Point C corresponds to the peak stress state where instability occurs around the direction of 150°, which is consistent with the directional analysis by Nicot *et al*. (2007). After the peak, the instability zone becomes wider, as shown at point D (Figure 5.3(c-d)).

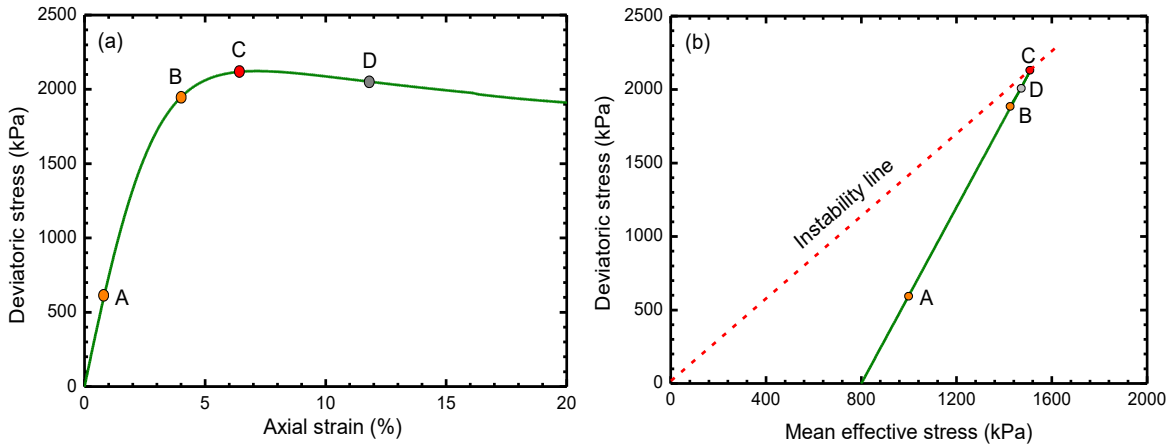

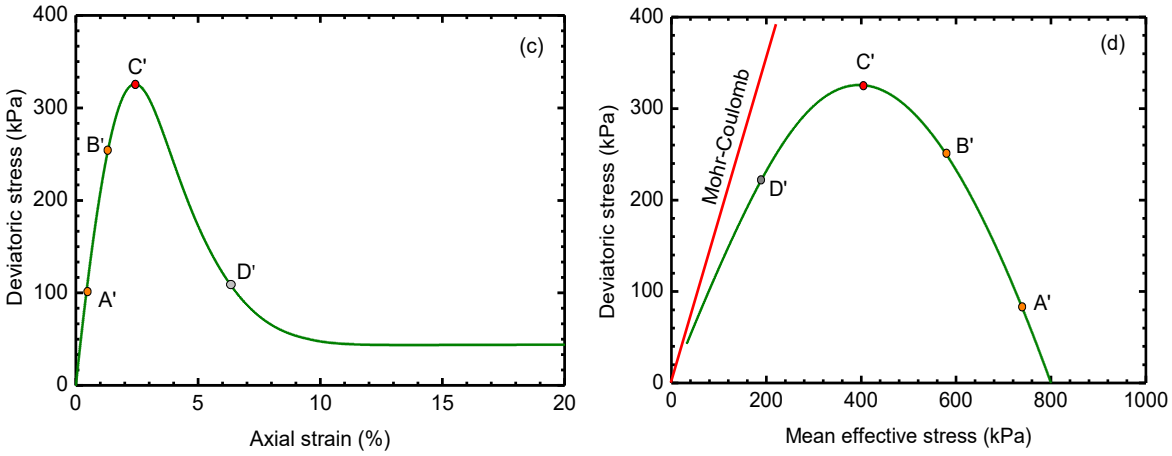

Figure 5.2 Stress-strain relation with confining pressure of 800kPa: (a) deviatoric stress versus axial strain of dense sand (e_0=0.5), (b) deviatoric stress versus mean effective pressure of dense sand (e_0=0.5), (c) deviatoric stress versus axial strain of loose sand (e_0=0.885), (d) deviatoric stress versus mean effective pressure of loose sand (e_0=0.885)

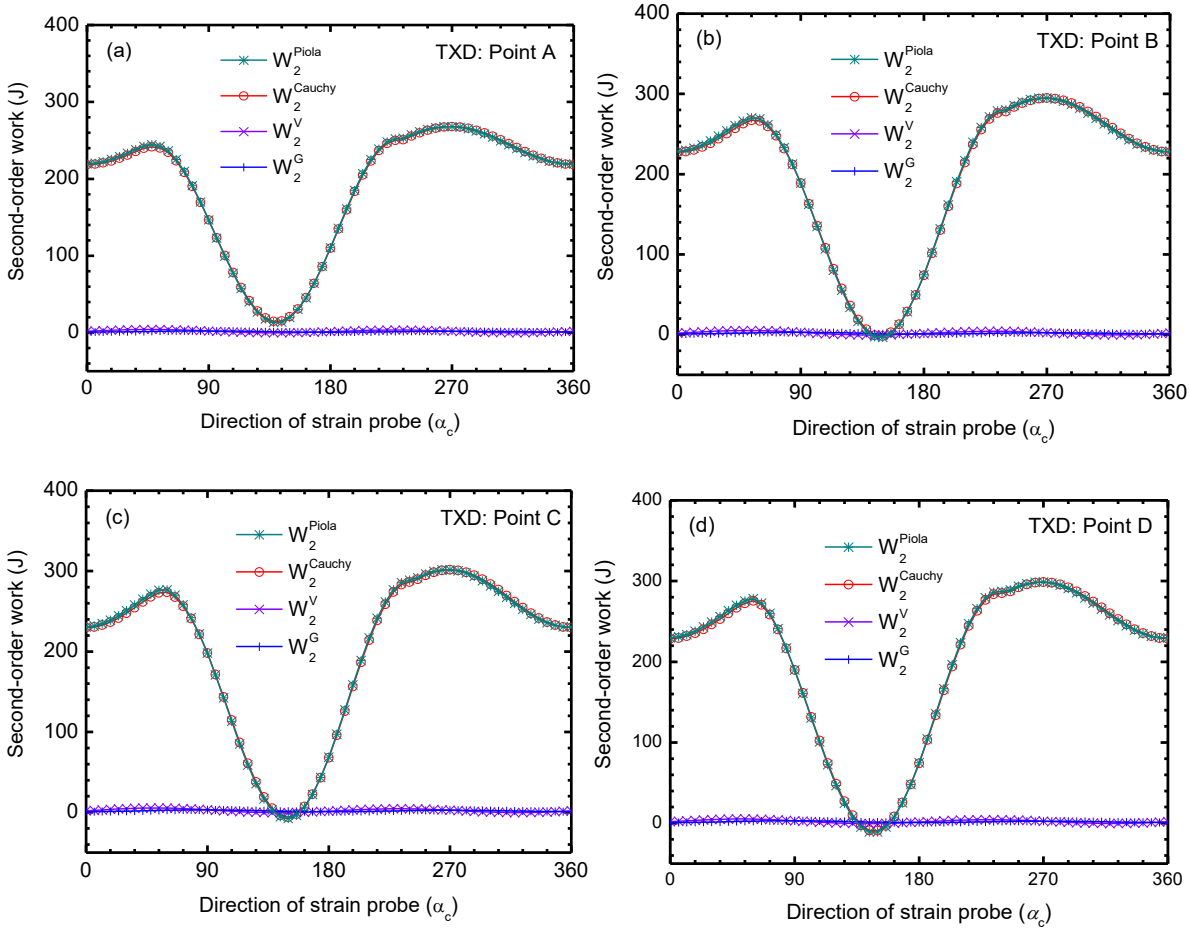

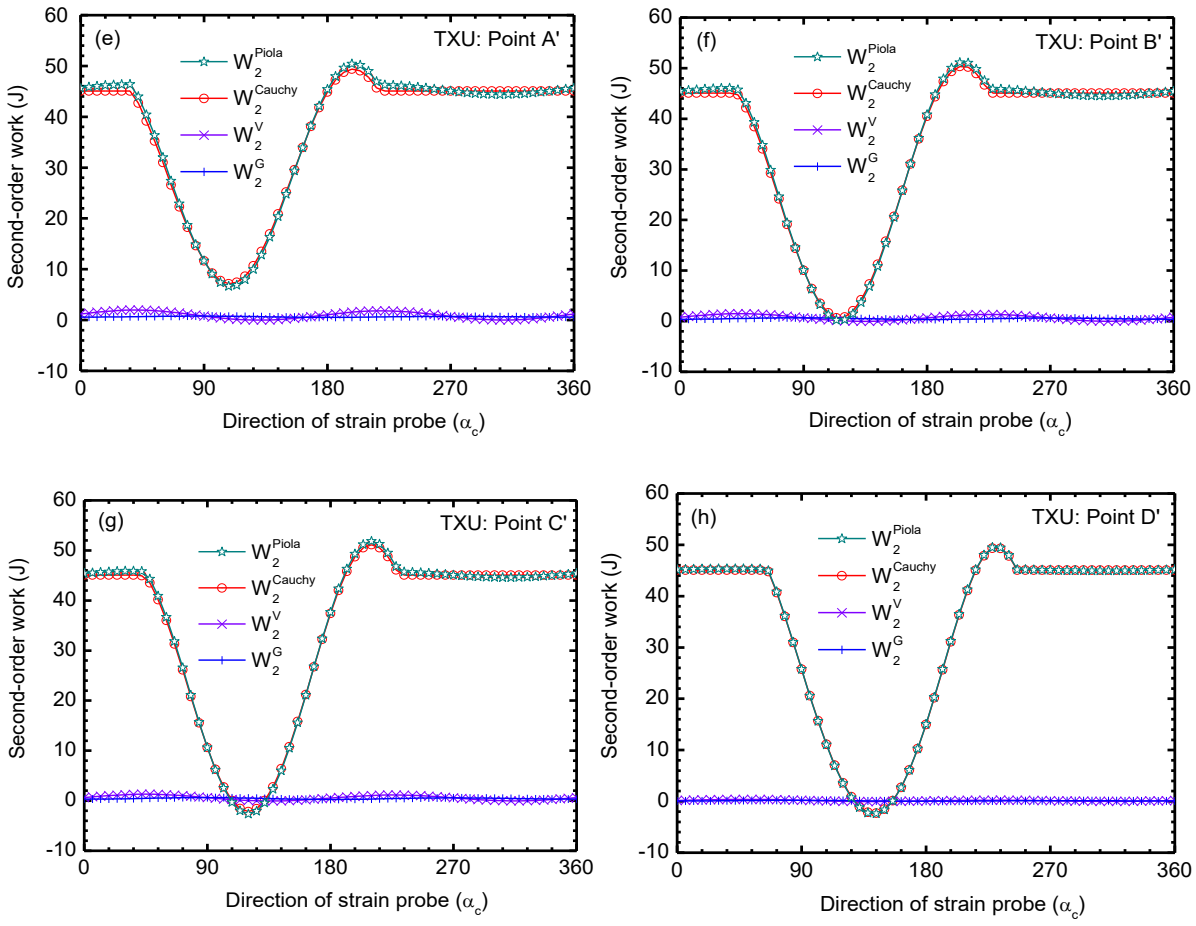

Figure 5.3 Second-order work calculated by Piola-Kirchhoff stress and Cauchy stress, and its volumetric part and geometrical parts at point A, B, C and D by Rendulic strain probe

The above directional analysis was also conducted at different stages for a loose specimen under undrained triaxial compression. The second-order work was calculated at axial strains of 1%, 2%, 2.42% and 6%, noted as points A', B', C' and D', respectively. The latent instability at point B' was also detected and was followed by a diffuse failure at point C'. Most interestingly, the transition from diffuse to localised failure was well captured by the second-order work, and the localised direction was included within the range formed by all the directions of instability (Figure 5.3(e-h)). Based on these analyses, it can be confirmed that the CH model is capable of detecting instability in granular materials based on the second-order work criterion.

5.3.3 Comparing Lagrangian and Euler descriptions

The expression of the second-order work was given by a Lagrangian description (Hill, 1958; Nicot *et al*., 2007; Nicot and Darve, 2009). However, since the Cauchy stress tensor and the Euler strain tensor are widely adopted in constitutive models and finite element codes, it is useful to express the second-order work by a Eulerian description. With the use of Nanson's formula (Nicot *et al*., 2007), the second-order work in a Lagrangian description can be expressed by a Eulerian description. The second-order work calculated through the Piola-Kirchhoff stress tensor can be written as

$$W_2^{Piola} = \underbrace{V\delta\boldsymbol{\sigma} : \delta\boldsymbol{\varepsilon}}_{W_2^{Cauchy}} + \underbrace{\delta V\boldsymbol{\sigma} : \delta\boldsymbol{\varepsilon}}_{W_2^{V}} - \underbrace{V\boldsymbol{\sigma}\left(\delta\boldsymbol{\varepsilon}\right) : \delta\boldsymbol{\varepsilon}}_{W_2^{G}} \tag{5.14}$$

in which, on the right-hand side, the first term is the second-order work in a Eulerian description, denoting as W_2^{Cauchy}; whereas the second term W_2^V is related to the change of volume and the third term W_2^G is treating geometrical changes. It is necessary to calculate the difference between these two definitions, since the Eulerian description has been adopted within the CH micromechanical model.

The contributions of the different terms W_2^{Piola}, W_2^{Cauchy}, W_2^V and W_2^G are analysed in Figure 5.3. The difference in the second-order work expressed by a Lagrangian or by a Eulerian description was investigated under the same loading procedure as the one conducted in the directional analysis. As shown in Figure 5.3, the contributions of both terms W_2^V and W_2^G are negligible at the selected points A(A'), B(B'), C(C') and D(D'), which demonstrates that the difference between the two descriptions is very small. Therefore, we can use the Eulerian instead of the Lagrangian description to compute the second-order work in the following analyses.

5.3.4 Micro-macro relation of the second-order work

As previously described, the second-order work can be seen as an ideal indicator for detecting material instability at the specimen scale. To investigate the role of microstructural instabilities on the global failure of granular materials, a consistent indicator should be

constructed at different scales. Based on the adopted micromechanical model, we inserted the static expression of Eq.(1.17) into Eq.(5.10) and made a summation over all inter-particle contacts, expressed as

$$\sum_{c=1}^{N} \dot{f}_i^c \dot{\delta}_i^c = \sum_{c=1}^{N} \left(\dot{\sigma}_{ij} l_n^c A_{jn} \right) \dot{\delta}_i^c = \dot{\sigma}_{ij} \sum_{c=1}^{N} \dot{\delta}_i^c l_n^c A_{jn} \tag{5.15}$$

in which the stress increment is a common denominator and can be taken out of the summation since the calculation is based on the REV. By volumetrically averaging Eq.(5.15) and taking into account the best-fit hypothesis expressed by Eq.(1.12), the relation between the second-order work at micro and macro scales can be obtained

$$\frac{1}{V} \sum_{c=1}^{N} \dot{f}_i^c \dot{\delta}_i^c = \dot{\sigma}_{ij} \left(\frac{1}{V} \sum_{c=1}^{N} \dot{\delta}_i^c l_n^c A_{jn} \right) = \dot{\sigma}_{ij} : \dot{\varepsilon}_{ij} \tag{5.16}$$

According to the definition of the second-order work at various scales, Eq.(5.16) can be further written as

$$W_2^{el} = \frac{1}{V} \sum_{c=1}^{N} W_2^c \tag{5.17}$$

which indicates that the instability of the specimen originates from the instability of the inter-particle contacts. Note that Eq.(5.17) cannot be generalised to all kinds of micromechanical models since the previous derivations are based on the best-fit hypothesis adopted within the CH model. Other kinds of micromechanical models should be carefully investigated when this connection is being considered.

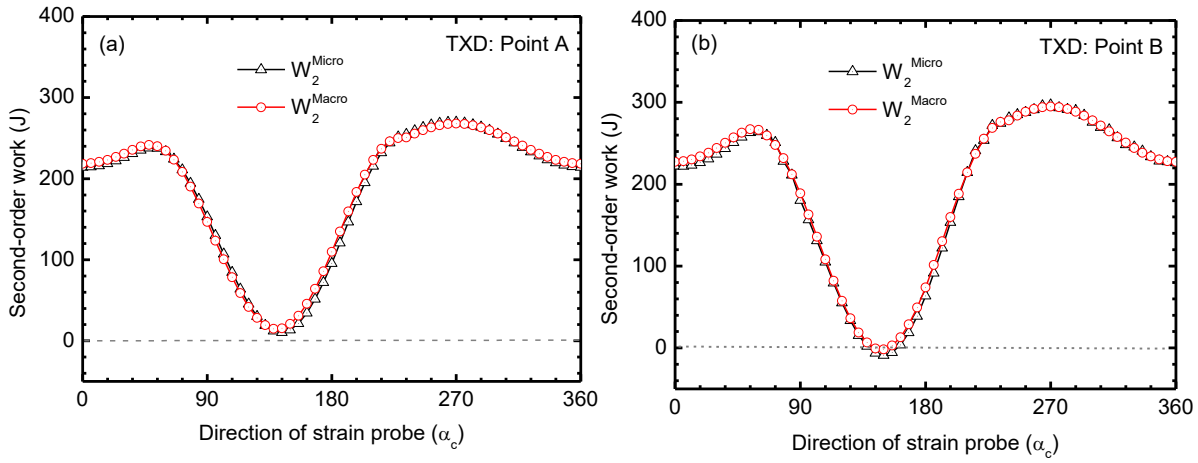

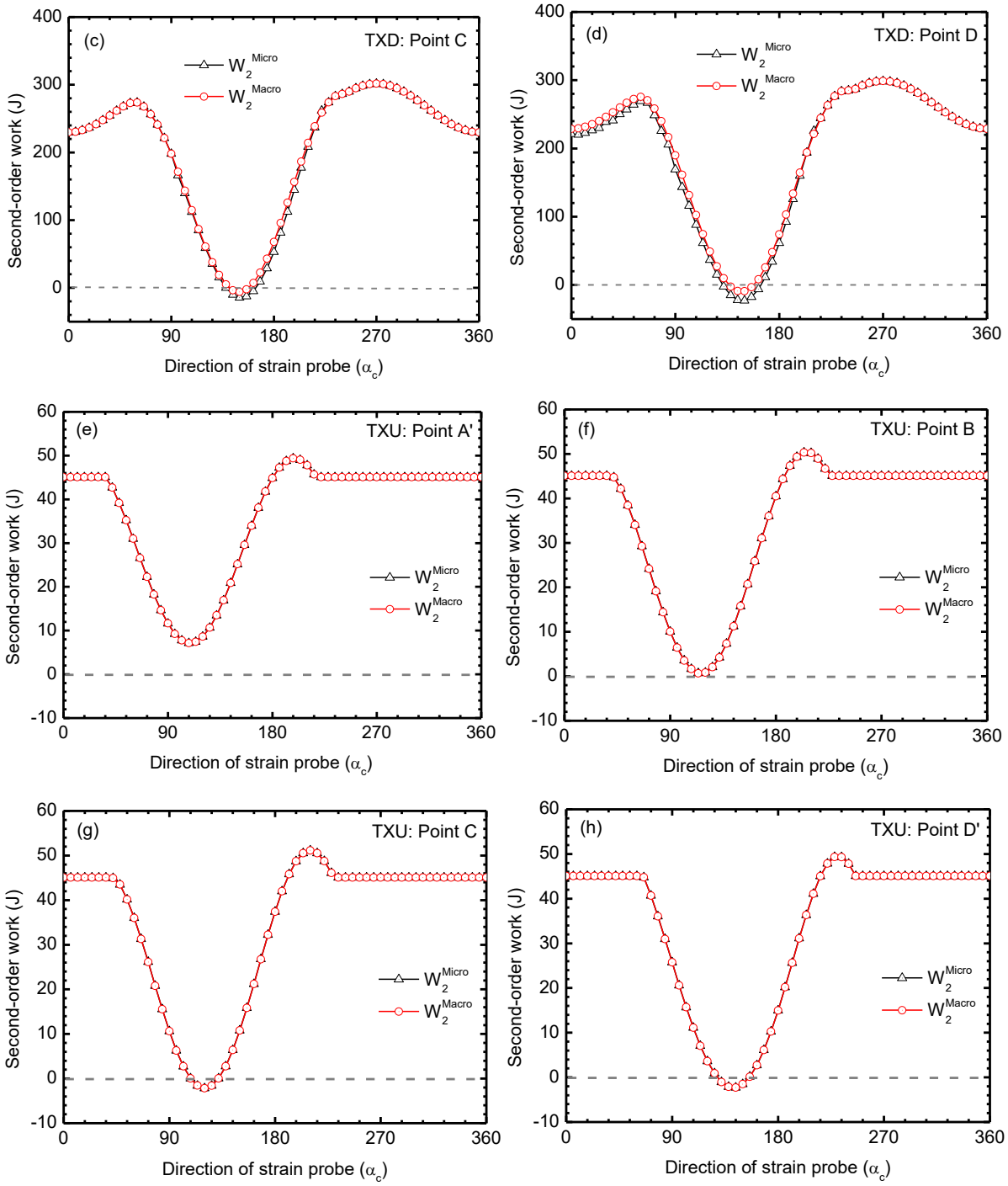

Figure 5.4 Second-order work calculated by stress-strain and summation of microscale second-order work at points A, B, C and D by Rendulic strain probe

The consistency between the second-order works calculated by macro scale stress and strain increments, on one hand, and by the summation of all micro scale second-order works computed by force and displacement increments, on the other hand, is demonstrated in Figure 5.4. By imposing the same strain increments as previously done during the directional

analysis at the selected stress states A(A'), B(B'), C(C') and D(D'), in the Rendulic plane, it was possible to obtain a consistent second-order work. With the help of consistent expressions of the second-order work at various scales, the extent of particle instability to global instability can be quantitatively analysed.

5.4 Analyses of the influence of microstructural instabilities on global failure

The effectiveness of the micromechanical approach in characterising the mechanism of granular material failure will be illustrated at the specimen scale and for boundary value problems. At each scale, both localised and diffuse failures will be analysed.

5.4.1 Instability of material points

5.4.1.1 Drained triaxial test on dense sand

A conventional drained triaxial compression test was first performed on a dense sand sample with an initial void ratio of 0.5 under a confining pressure of 800 kPa (Figure 5.2(a) and (b)). As expected, a strain softening behaviour was obtained, accompanied by a localised failure of the specimen. To better understand the occurrence of failure, Figure 5.5 presents the evolution of the inter-particle contact forces, of the displacements, and of the force ratios at the selected stress states A, B, C and D. At these specific points, the normal forces reached maximum values along the x-axis with an isotropic distribution in the y-z plane, whereas the tangential forces reached their maximum values in the direction of γ=45° (Figure 5.5(a-b)). The normal displacements showed a distribution similar to the one obtained for the normal forces, except at stage D where the normal displacements were affected by large tangential deformations. Indeed, the plastic deformations were relatively small before the bifurcation point (stage C), compared to the ones in the post failure stage, such as at point D. Moreover, the plastic behaviour of the granular material was described by a non-associated local law which leads to a different distribution of the normal displacements, compared to the distribution of the normal forces. Unlike the normal displacements, the tangential displacements revealed maximum values along the direction of γ=60° with an isotropic distribution in the y-z plane (Figure 5.5(d)). Again, this direction was not the one corresponding to the maximum

tangential force since a non-associated inter-particle flow rule has been adopted. Force ratios, given as tangential forces over normal forces, were also computed at these four stages. Their maximum values were obtained along the direction of γ=45° with an isotropic distribution in the y-z plane (Figure 5.5(e)).

(a) x-y plane (β=0°) x-z plane (β=90°) y-z plane (γ=90°)

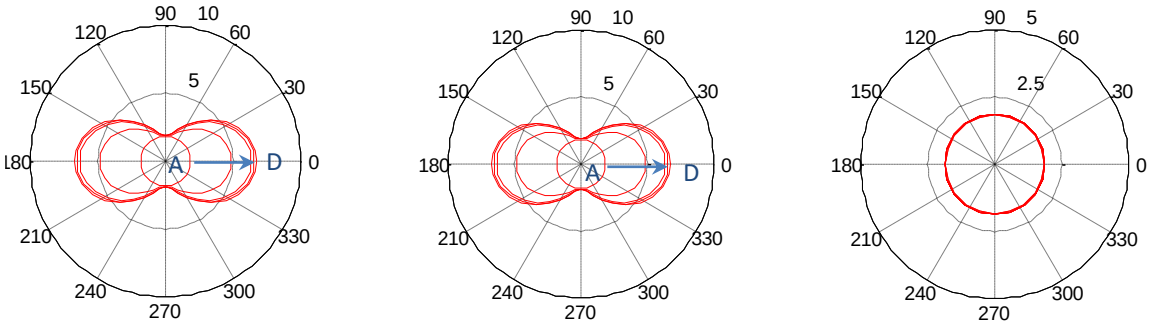

(b) x-y plane (β=0°) x-z plane (β=90°) y-z plane (γ=90°)

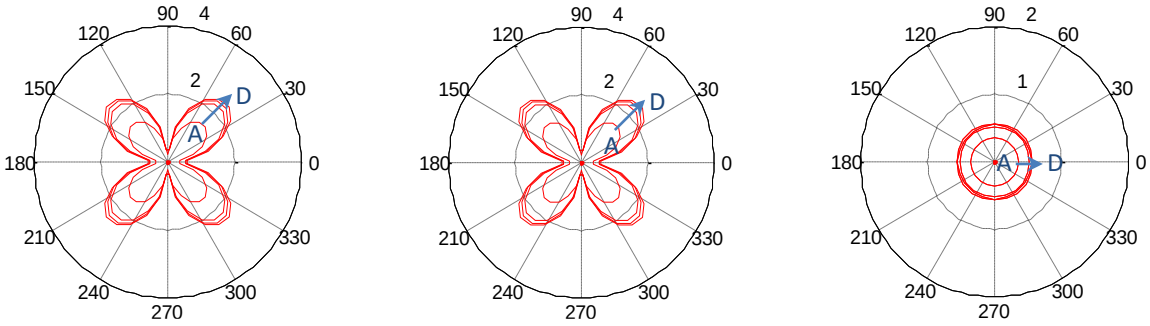

(c) x-y plane (β=0°) x-z plane (β=90°) y-z plane (γ=90°)

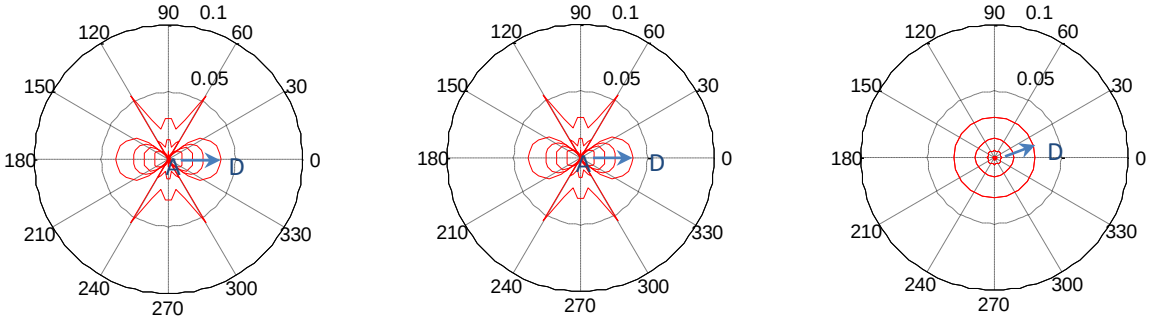

(d) x-y plane (β=0°) x-z plane (β=90°) y-z plane (γ=90°)

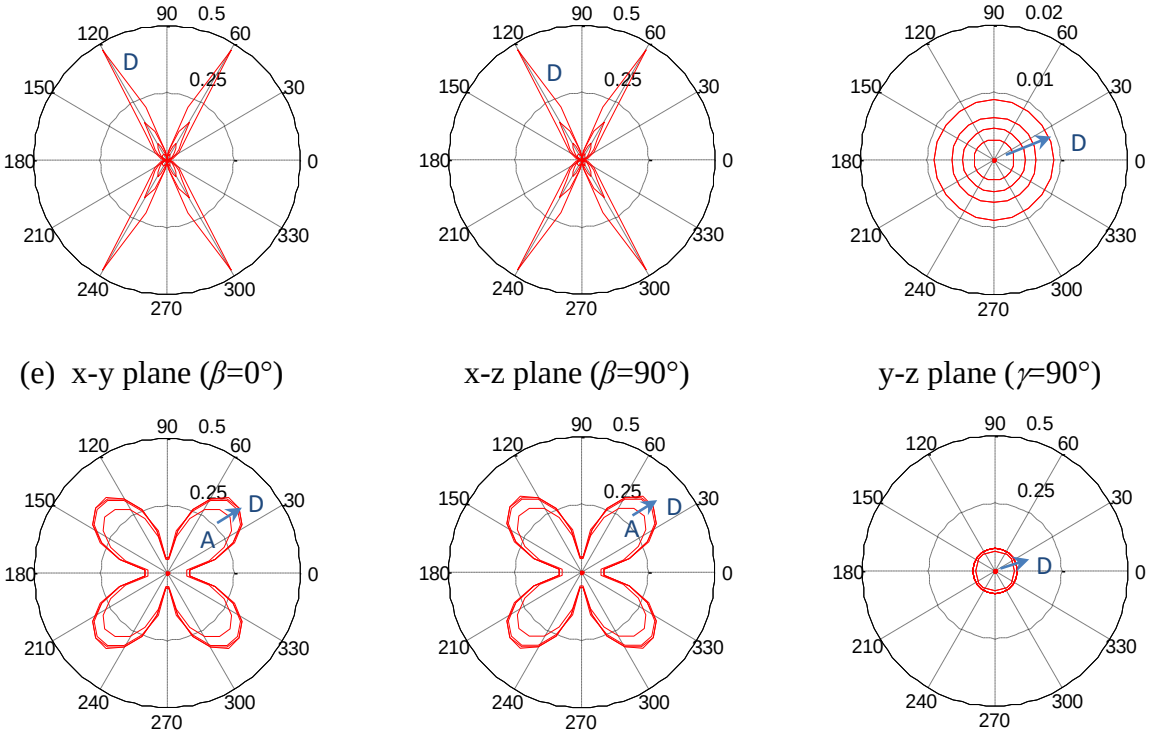

(e) x-y plane (β=0°) x-z plane (β=90°) y-z plane (γ=90°)

Figure 5.5 Force, displacement and force ratio distributions of triaxial drained test at initial stage and stages A, B, C and D: (a) normal forces on x-y plane, x-z plane and y-z plane (N); (b) tangential forces on x-y plane, x-z plane and y-z plane (N); (c) normal displacements on x-y plane, x-z plane and y-z plane (mm); (d) tangential displacements on x-y plane, x-z plane and y-z plane (mm); (e) force ratios on x-y plane, x-z plane and y-z plane

(a) x-y plane (β=0°) x-z plane (β=90°) y-z plane (γ=90°)

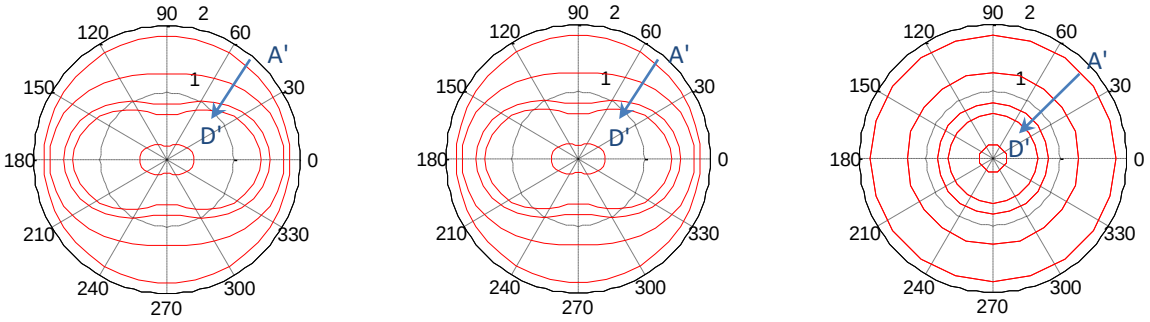

(b) x-y plane (β=0°) x-z plane (β=90°) y-z plane (γ=90°)

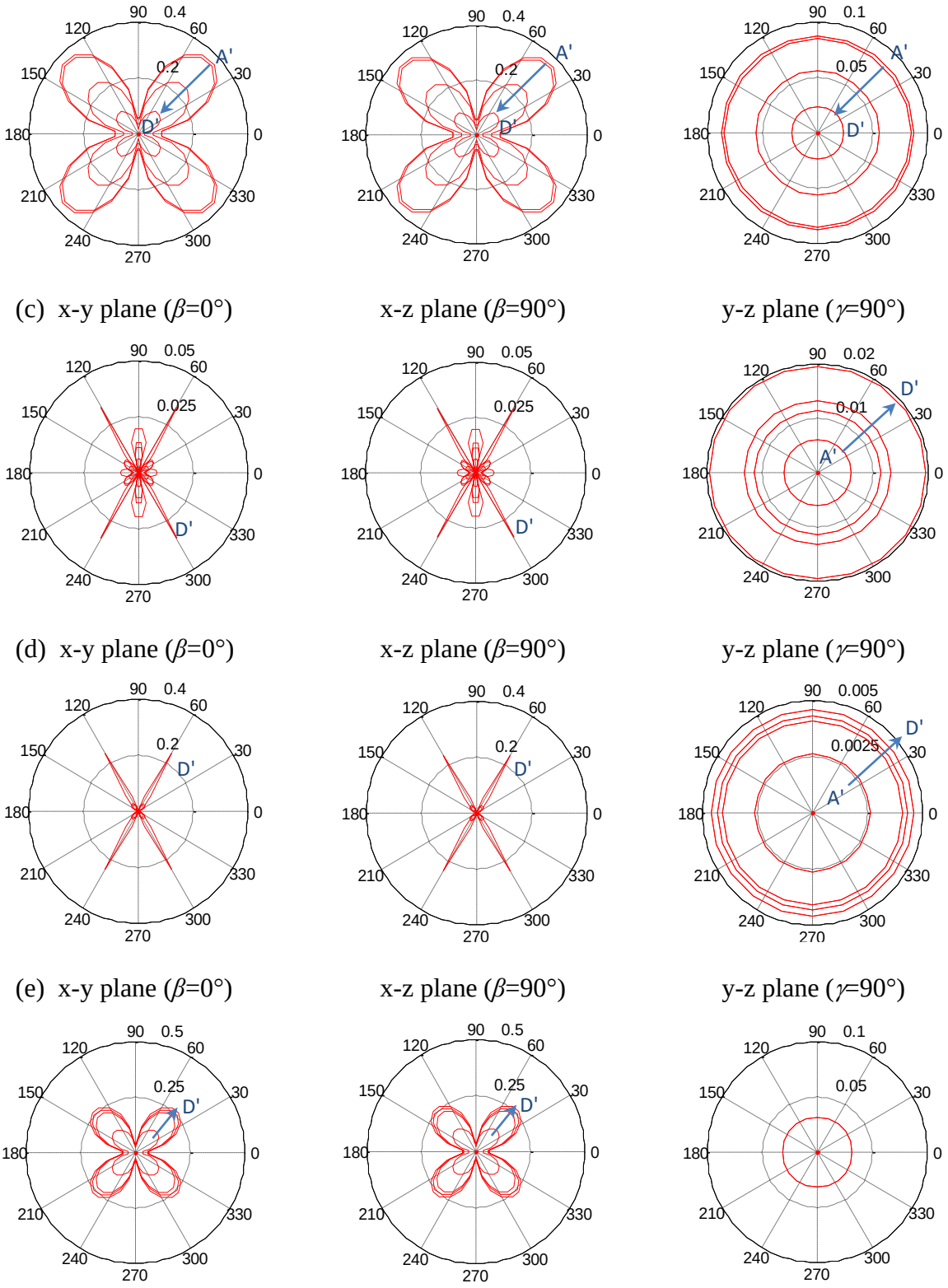

Figure 5.6 Force, displacement and force ratio distributions of triaxial undrained test at initial stage and stages A, B, C and D: (a) normal forces on x-y plane, x-z plane and y-z plane (N); (b) tangential forces on x-y plane, x-z plane and y-z plane (N); (c) normal displacements on x-y plane, x-z plane and y-z plane (mm); (d) tangential displacements on x-y plane, x-z plane

and y-z plane (mm); (e) force ratios on x-y plane, x-z plane and y-z plane

With the CH model, the second-order work can be used to detect material instability. At the macro scale, the specimen was always stable before reaching the peak stress with a positive value of the macroscale second-order work. At point C, the second-order work vanished and then took negative values, which denoted the instability of the specimen (Figure 5.2(a)). In fact, if the loading had been stress-controlled, sudden collapse of the specimen would have occurred and the system would have evolved from a static to a dynamic regime. As expected, the second-order work calculated at the macro scale is equal to the volumetric summation of the second-order work at the micro scale (Figure 5.7(a)). The macroscale instability can, therefore, be explained by the magnitude of the instabilities at the inter-particle contacts. The failure plane of the specimen calculated by the Coulomb failure criterion, with $\alpha=45°+33°/2=61.5°$, is consistent with the direction of the plane where the second-order work reaches its highest negative value (Figure 5.8(b)).

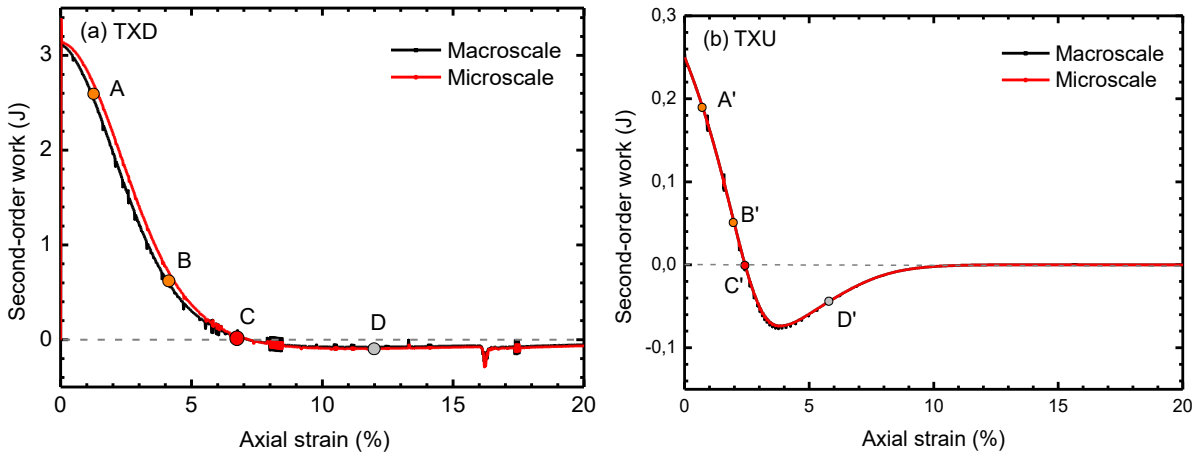

Figure 5.7 Macro and micro second-order work: (a) second-order work calculated by stress-strain and summation of microscale second-order work of dense sand (e_0=0.5); (b) second-order work calculated by stress-strain and summation of microscale second-order work of loose sand (e_0=0.885)

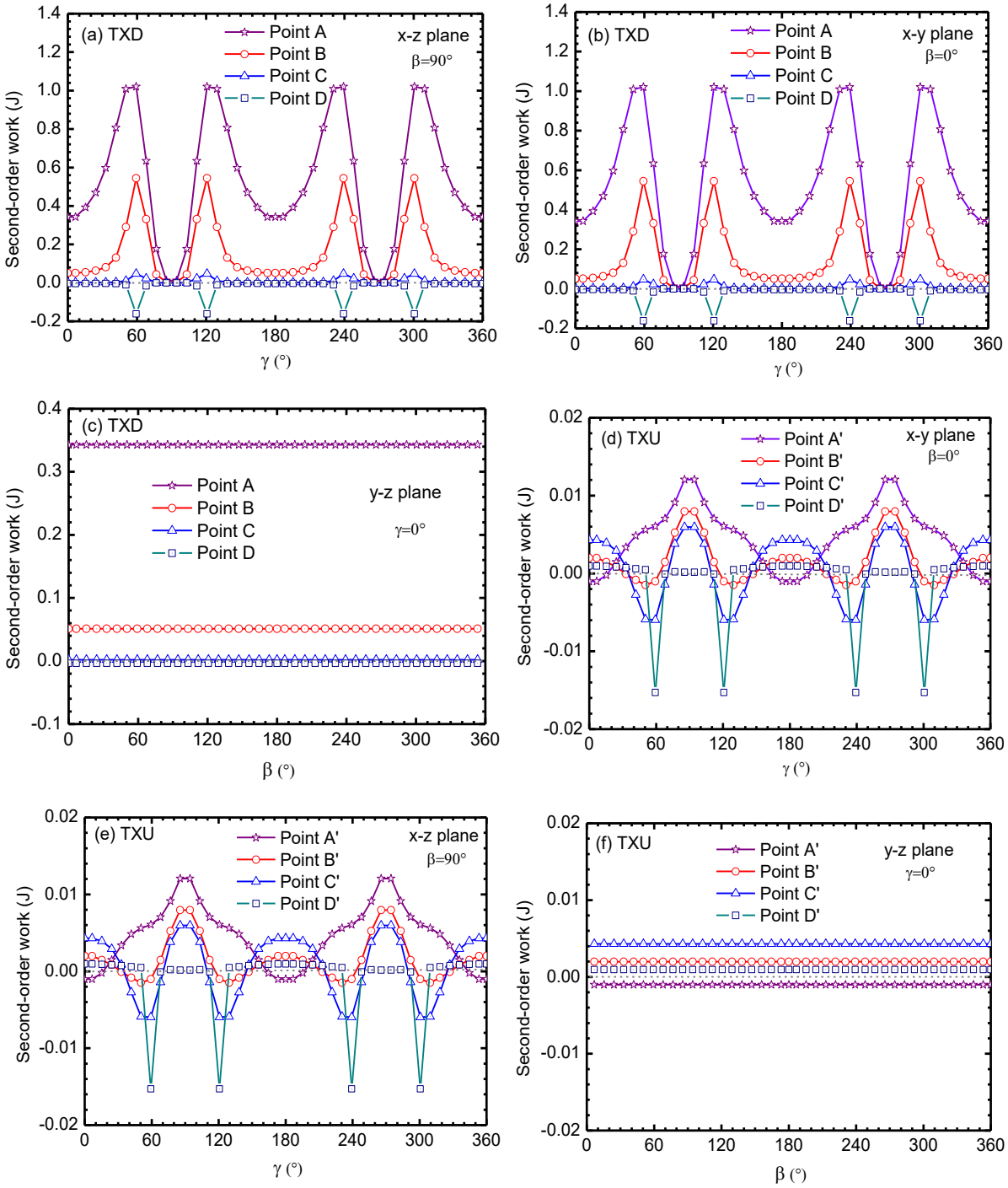

Figure 5.8 Micro second-order work at stages A, B, C and D on x-y plane, x-z plane and y-z plane

5.4.1.2 Undrained triaxial test on loose sand

To demonstrate the effectiveness of this approach in describing diffuse failure, a conventional undrained triaxial compression test on a loose sand sample with an initial void ratio of 0.885 under a confining pressure of 800 kPa (Figure 5.2(c)-(d)) was also performed. Before

analysing the instability at micro and macro scales, the evolution of the inter-particle forces, displacements and force ratios at the selected stages A', B', C' and D' were studied. The normal forces were isotropically distributed at the end of the consolidation stage, and then decreased anisotropically under shearing, whereas the tangential forces increased from zero to the maximum values obtained along the direction γ=45°, as shown in Figure 5.6(a-b). Normal and tangential displacements had small values before the bifurcation point C', where diffuse failure would have occurred under stress control (Figure 5.6(a-b)). Due to the non-associated inter-particle flow rule, the normal displacements at point D' reached their maximum values in the direction γ=60°, concordantly with the tangential displacements. During shearing, the specimen lost its homogeneity gradually, particularly from a diffuse state at point C' to a localised state at point D' (see also Wan *et al*., 2013). This feature was well characterised via the CH micromechanical model, as demonstrated by the distribution of normal and tangential displacements (Figure 5.6(a-b)). The distribution of the force ratios also showed maximum values along the direction γ=45° (Figure 5.6(e)).

At the specimen scale, the diffuse failure at point C' was well captured by the vanishing of the macroscale second-order work (Figure 5.7(b)). Before point C', the specimen was stable and the macroscale second-order work was positive, whereas after this point the second-order work became negative. Since the macroscale second-order work is equal to the volumetric summation of all the microscale second-order works (Figure 5.7(b)), the particulate origin of the macroscale instability can be analysed by observing the evolution of the microscale second-order work in all local directions. Before the peak stress point C', instability could be observed for certain directions even though the whole specimen remained stable. Moreover, a high degree of negative second-order work occurred at point D', corresponding to a localised state. The direction of the localised zone predicted by the maximum negative second-order work was around γ=60°, consistent with the Coulomb failure direction.

5.4.2 Failure in boundary value problems

The above analysis was then extended from the material point scale to boundary value problems. With the finite element method, instability at the grain scale can be linked to the

failure of engineering geo-structures through the material points, i.e. the Gauss integration points. The biaxial test as a boundary value problem was chosen to demonstrate the predictability of this method for cases of localised and diffuse failures.

The CH model was implemented into the finite element code Abaqus/Standard 6.14-1. For one element, the second-order work can be calculated by the incremental node displacements and the consistent stiffness matrix by Eq.(5.11). The global second-order work can also be computed by the incremental node displacements and forces by Eq.(5.13). Therefore, the global second-order work can be obtained by connecting elementary second-order works at the grain scale.

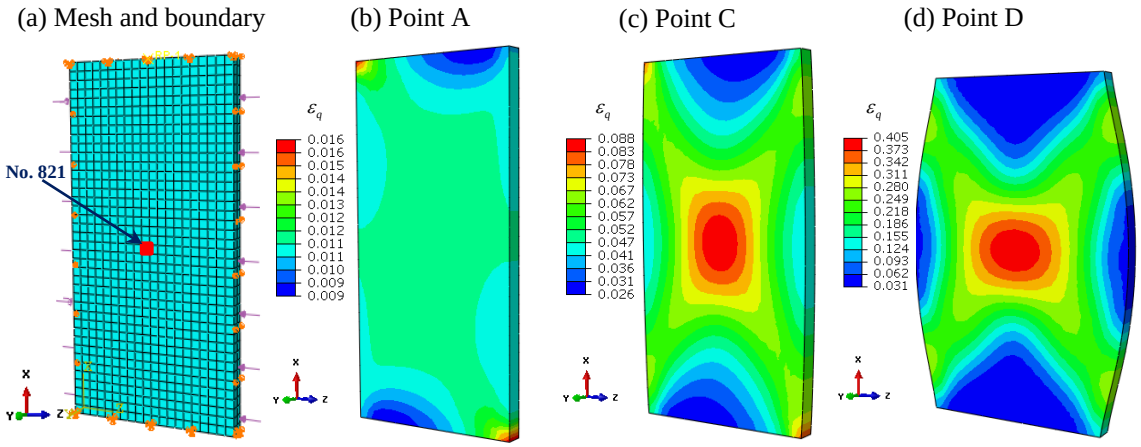

Figure 5.9 Drained biaxial tests of dense sand (e_0=0.5): (a) mesh and boundary conditions; (b) deviatoric plastic strain at stage A; (c) deviatoric plastic strain at stage C; (d) deviatoric plastic strain at stage D

5.4.2.1 Biaxial test under drained condition on dense sand

A biaxial test on dense sand under drained condition was first conducted. The dimension of the finite element model was 200mm×100mm×10mm. The FEM model did not consider any regularisation technique, since the current study focuses mainly on the outset of the instability condition. A preliminary study of the influence of the mesh size on the computational cost and on the thickness of the shear band led to the choice of the discretisation of the problem by 1600 three-dimensional eight-node trilinear displacement elements with reduced integration

C3D8R, as shown in Figure 5.9(a). The imposed boundary conditions were the following: the left and right sides were constrained with a constant pressure of 800 kPa; the bottom and top were restricted in x, y and z directions; the front and back surfaces were fixed in the y direction. The boundaries were referred to as rough boundaries, since the bottom and top surfaces were limited in the x, y and z directions (Guo and Zhao, 2014). The material parameters were the same as the ones used in the aforementioned triaxial drained test. All elements were initiated with an isotropic stress of 800 kPa, corresponding to the confining pressure. Then, a vertical displacement was imposed at the top surface.

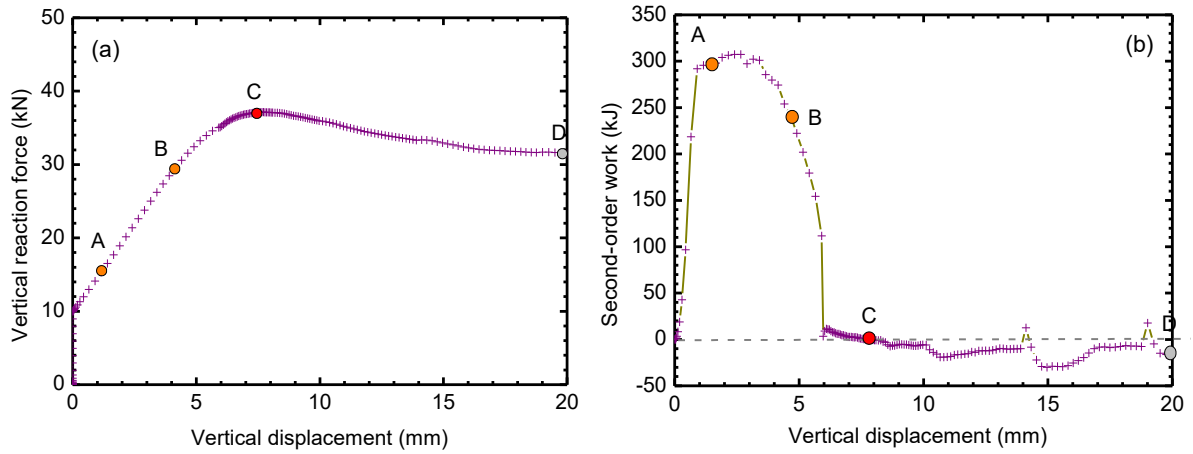

Figure 5.10 Drained biaxial tests of dense sand (e_0=0.5): (a) vertical reaction force versus vertical displacement; (b) global second-order work

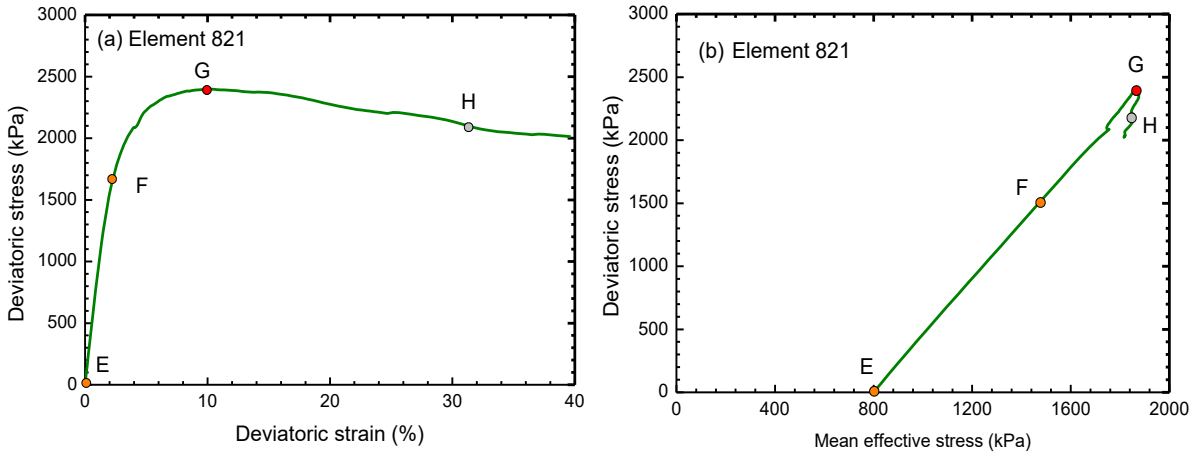

Figure 5.11 Stress-strain of the selected element of biaxial test during loading (e_0=0.5): (a) deviatoric stress versus axial strain, (b) deviatoric stress versus mean effective pressure

After a 20mm vertical displacement at the top surface, a distinct shear band could be observed,

as shown by the deviatoric plastic strain field in Figure 5.9(d). This localised behaviour was characterised by the vertical force-displacement curve, in which a softening stage could be noticed. Concordantly, the global second-order work, positive before the peak force point G, vanished at that point (Figure 5.10). This result demonstrates that the global second-order work can be an efficient indicator for detecting localisation in boundary value problems. The element 821, placed near the centre of the specimen, was selected due to its significant plastic deformation developed in the course of loading. Its micro quantities were closely analysed throughout the loading. The stress-strain behaviour was obtained (Figure 5.11), and the evolution of forces, displacements and force ratios were plotted at the selected stress stages E, F, G and H (see Figure 5.12). Distributions similar to those in the previous drained triaxial test were obtained. However, these variables have much larger values on the x-z plane if compared to the x-y plane, since the boundary conditions are non-symmetric (Figure 5.12).

(a) x-y plane (β=0°) x-z plane (β=90°) y-z plane (γ=90°)

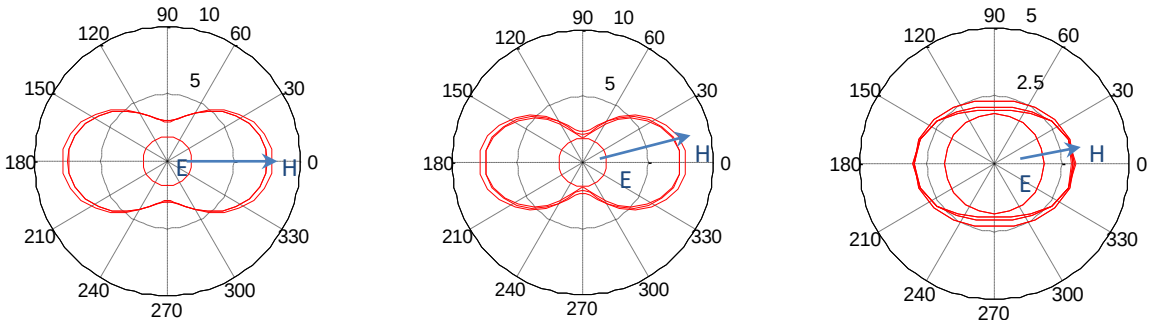

(b) x-y plane (β=0°) x-z plane (β=90°) y-z plane (γ=90°)

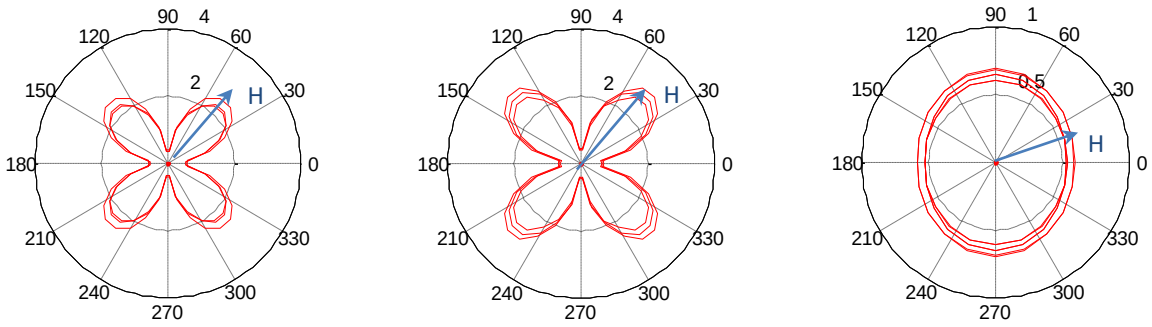

(c) x-y plane (β=0°) x-z plane (β=90°) y-z plane (γ=90°)

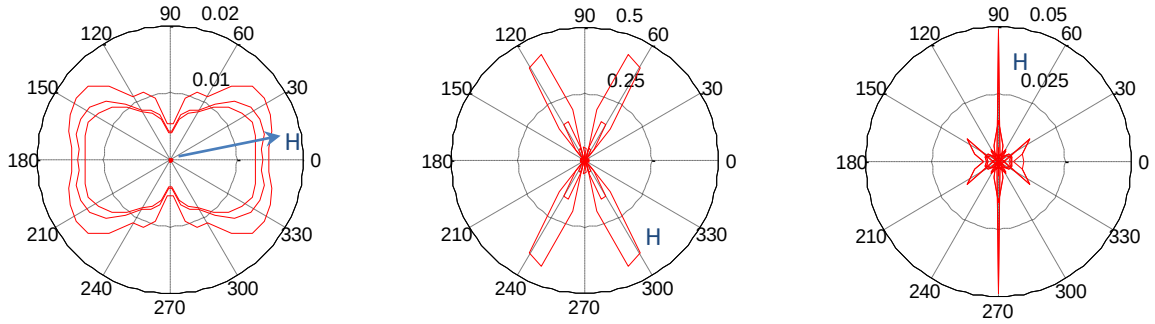

(d) x-y plane (β=0°) x-z plane (β=90°) y-z plane (γ=90°)

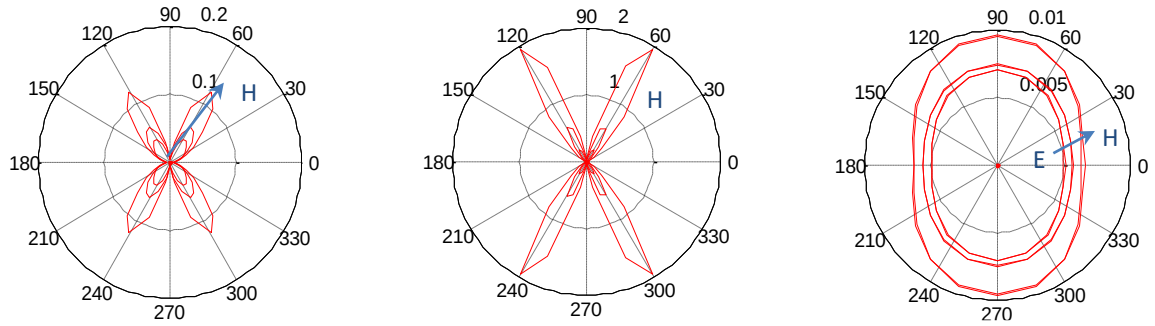

(e) x-y plane (β=0°) x-z plane (β=90°) y-z plane (γ=90°)

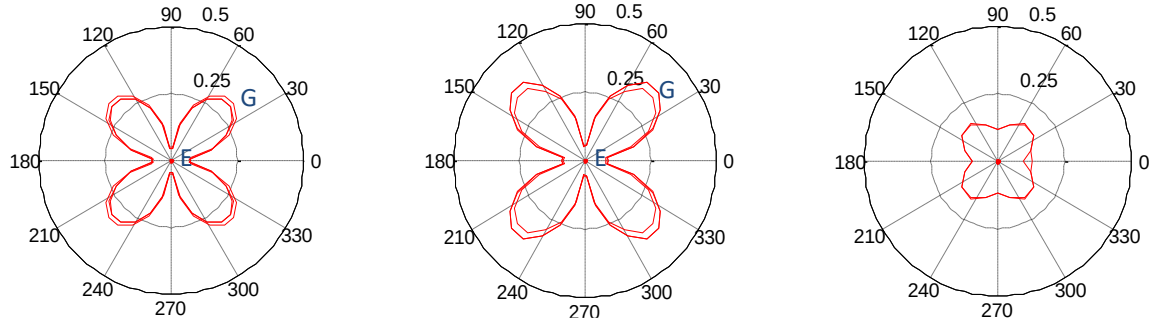

Figure 5.12 Force, displacement and force ratio distributions at initial stage and stages E, F and G of selected element of biaxial test: (a) normal forces on x-y plane, x-z plane and y-z plane (N); (b) tangential forces on x-y plane, x-z plane and y-z plane (N); (c) normal displacements on x-y plane, x-z plane and y-z plane (mm); (d) tangential displacements on x-y plane, x-z plane and y-z plane (mm); (e) force ratios on x-y plane, x-z plane and y-z plane

For the selected element, the second-order works have the same values calculated, on the one hand, from macro stress and strain increments and, on the other hand, by the integration of the micro force and displacement increments (Figure 5.13(a)). Before point G, the second-order work was positive and, after this point, it became negative, which corresponds to strain softening behaviour (Figure 5.11(a)). The instability of the material can be further explained

by the instability at inter-particle contacts. It was found that the direction of the shear band (around 60°) was the direction of the inter-particle second-order work having the maximum negative value (Figure 5.13(c) and Figure 5.19 (a)). The simulation results are consistent with DEM simulations of a drained biaxial compression test on a dense sample by Nicot *et al.* (2013) and Nguyen (2016), which demonstrated that the multiscale approach does explain the localised failure of granular assemblies.

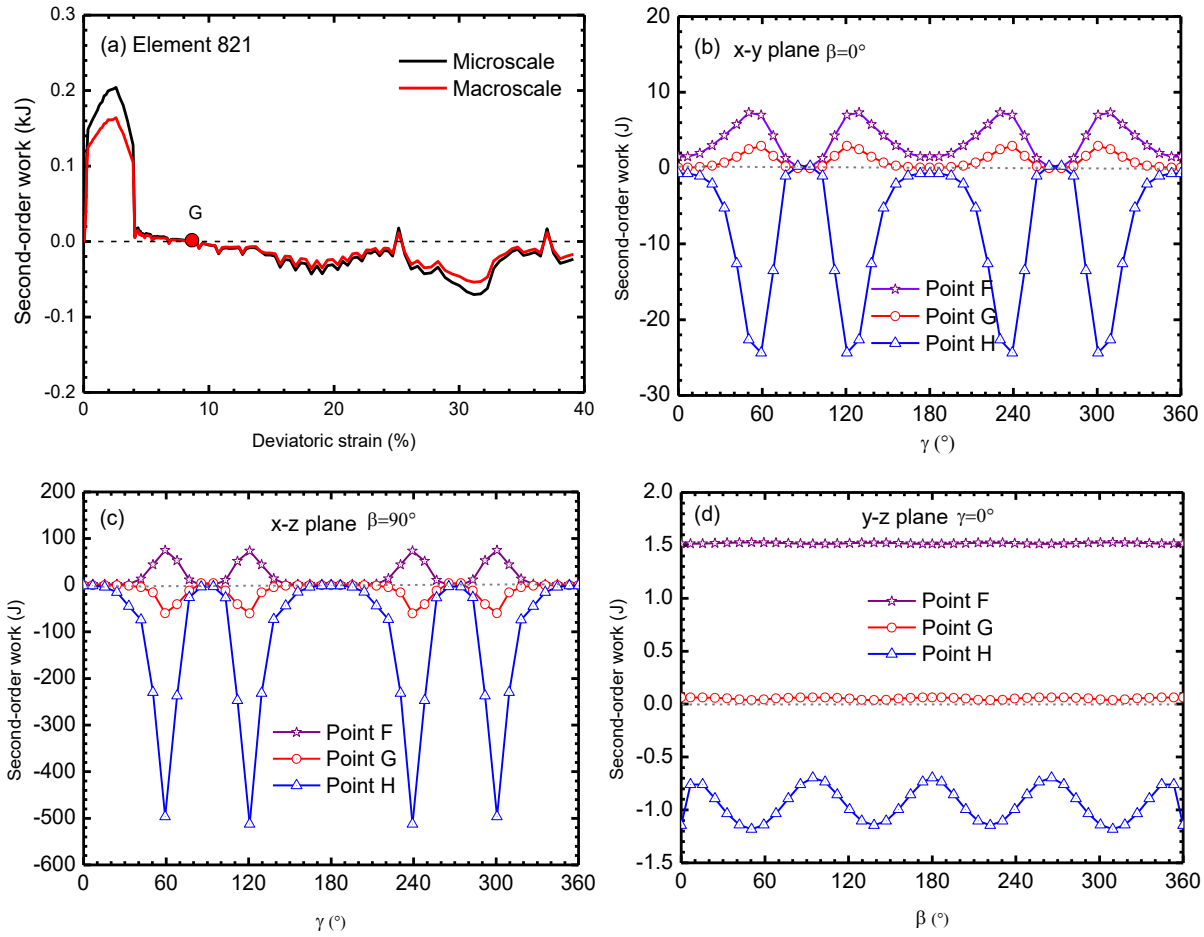

Figure 5.13 Macro and micro second-order work of selected element during loading and failure plane of biaxial test (e_0=0.5): (a) second-order work calculated by stress-strain and summation of microscale second-order work; (b-d) micro second-order work at stages E, F and G on x-y plane, x-z plane and y-z plane

5.4.2.2 Biaxial test under undrained condition on loose sand

To determine if the proposed method is capable of predicting diffuse failure, a biaxial test under undrained condition was conducted. 1600 elements with C3D8RP mesh were used to

simulate soil-water interaction. The rough boundary conditions previously used in the biaxial drained test were imposed. Darcy's law with an intrinsic permeability of 1.0×10^{-4} m/s, as suggested by Feia *et al*. (2016), was adopted to describe the flow of water inside the granular assembly. The initial void ratio of the loose Hostun sand was 0.885. The material was first subjected to an isotropic stress of 800 kPa. Then, a displacement of 15mm was imposed on the top surface along the x axis.

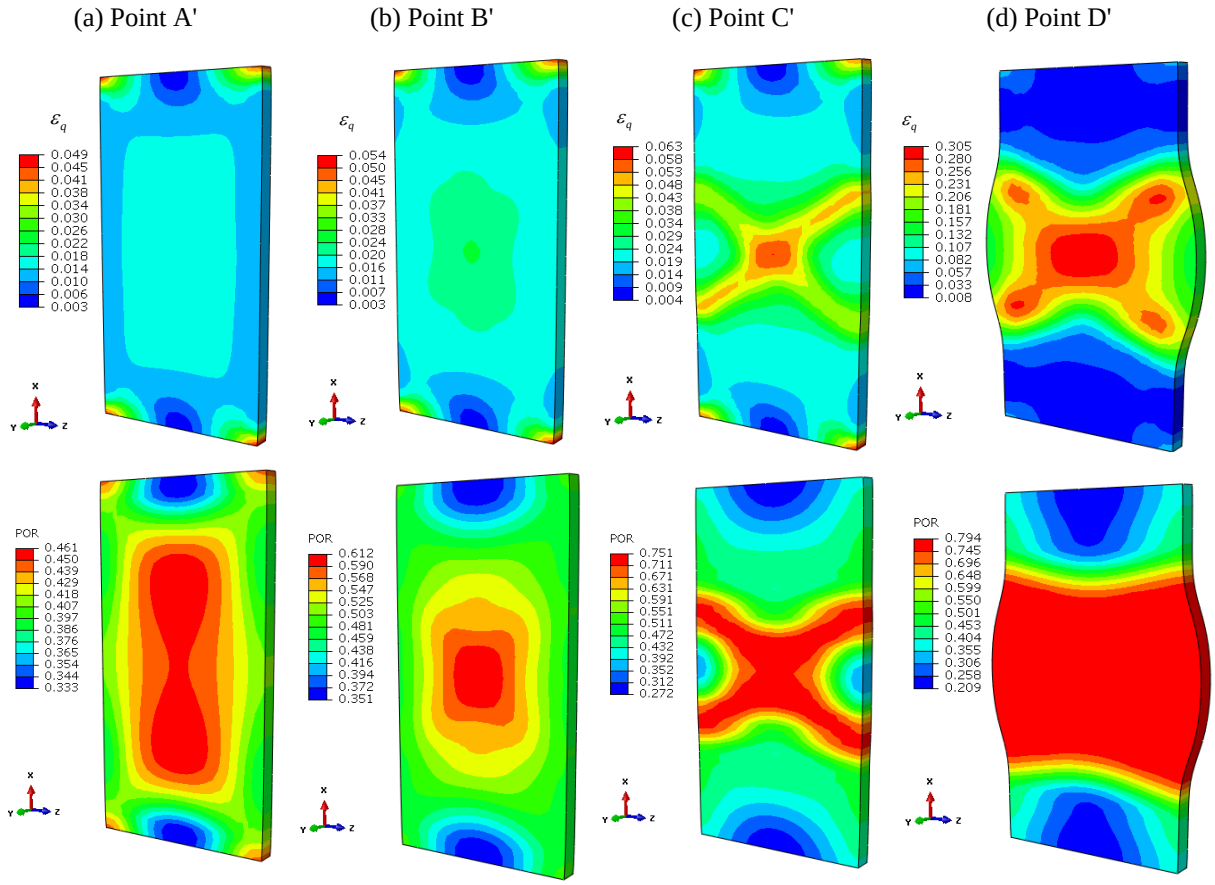

Figure 5.14 Undrained biaxial tests of loose sand (e_0=0.885): (a) deviatoric plastic strain at stage A'; (b) deviatoric plastic strain at stage B'; (c) deviatoric plastic strain at stage C'; (d) deviatoric plastic strain at stage D'

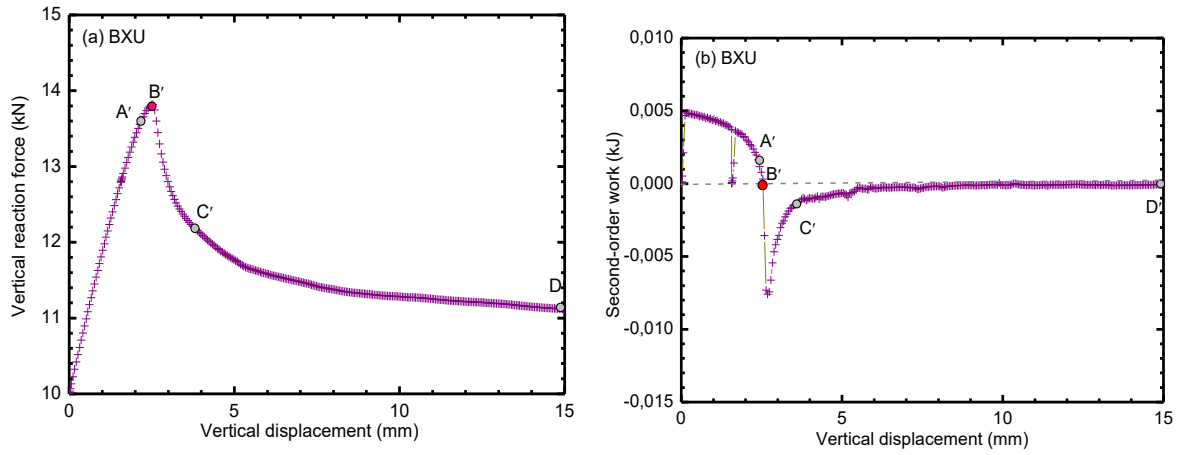

Figure 5.15 Biaxial tests of dense sand (e_0=0.885): (a) vertical reaction force versus vertical displacement; (b) global second-order work

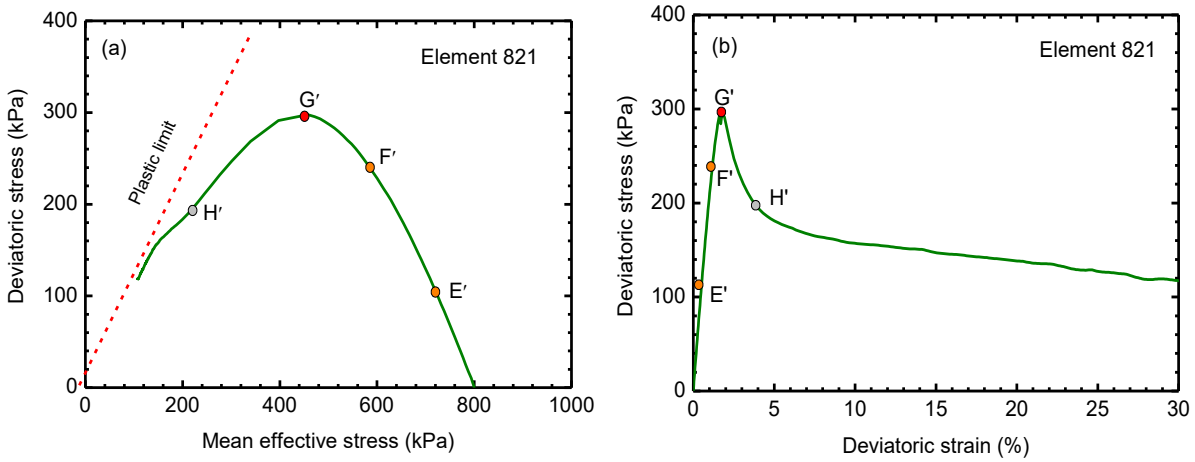

Figure 5.16 Stress-strain of the selected element of biaxial test during loading (e_0=0.885): (a) deviatoric stress versus axial strain, (b) deviatoric stress versus mean effective pressure

The granular assembly reached its maximum strength at point B' (Figure 5.15(a)), where a diffuse failure occurred (Figure 5.14(b)). Very close to this stage, at point A', the material was homogeneous if the boundary effects were neglected. However, diffuse failure transited towards a localised failure under a continuing vertical displacement (Figure 5.14(c) and (d)). The sequence of the occurrence of instability can be explained by the order of the instability criteria. As discussed by Wan *et al.* (2013), with the increment of shear loading, the loss of positive definiteness where diffuse failure can be observed is first encountered, and then the singularity of the acoustic tensor, which represents the occurrence of a shear band, follows. As for the biaxial test under undrained condition, the second-order work demonstrated also its

ability to predict diffuse failure (Figure 5.15). The diffuse failure condition can be well understood by examining the stress-strain behaviour of element 821, in which failure occurred, obviously, before the plastic limit. The evolutions of forces, displacements and force ratios were presented at the selected stages E', F', G' and H' (Figure 5.17). Distributions similar to those of the previous triaxial undrained test were obtained. However, these variables have much larger values on the x-z plane if compared to the x-y plane, since the boundary conditions are non-symmetric.

(a) x-y plane (β=0°) x-z plane (β=90°) y-z plane (γ=90°)

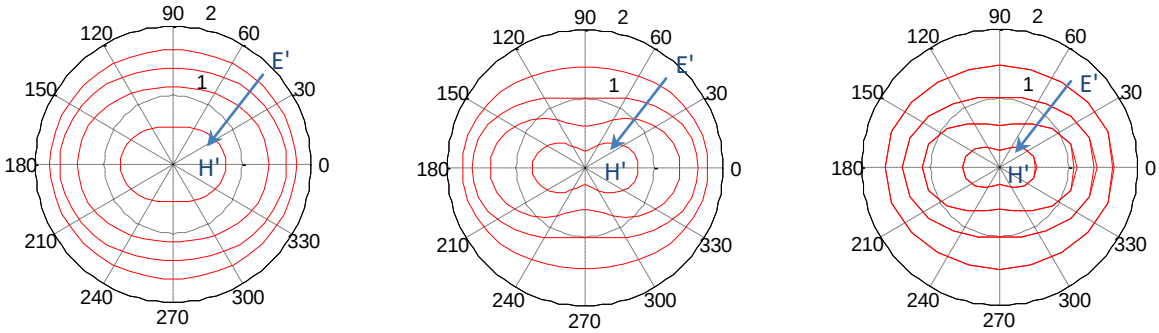

(b) x-y plane (β=0°) x-z plane (β=90°) y-z plane (γ=90°)

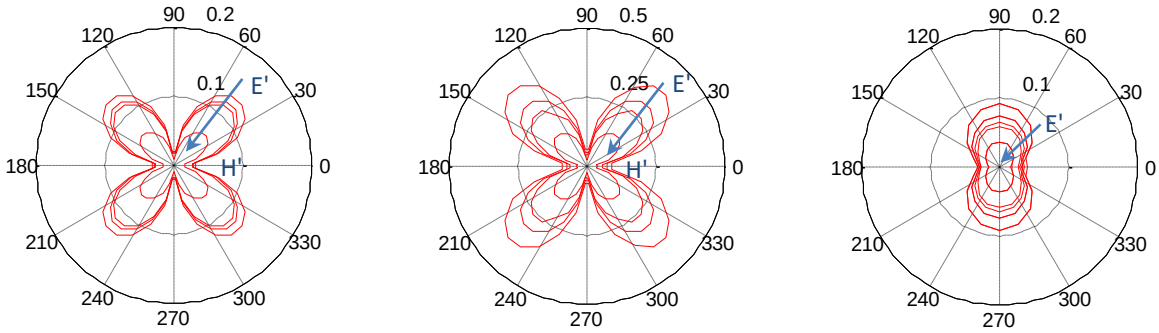

(c) x-y plane (β=0°) x-z plane (β=90°) y-z plane (γ=90°)

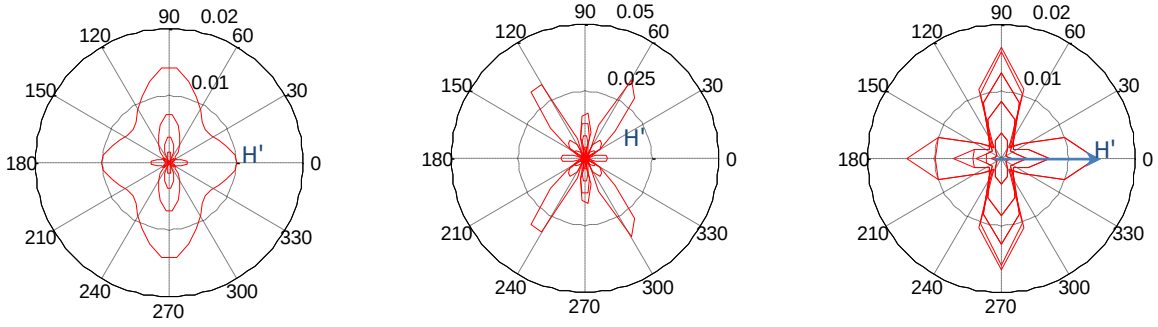

(d) x-y plane (β=0°) x-z plane (β=90°) y-z plane (γ=90°)

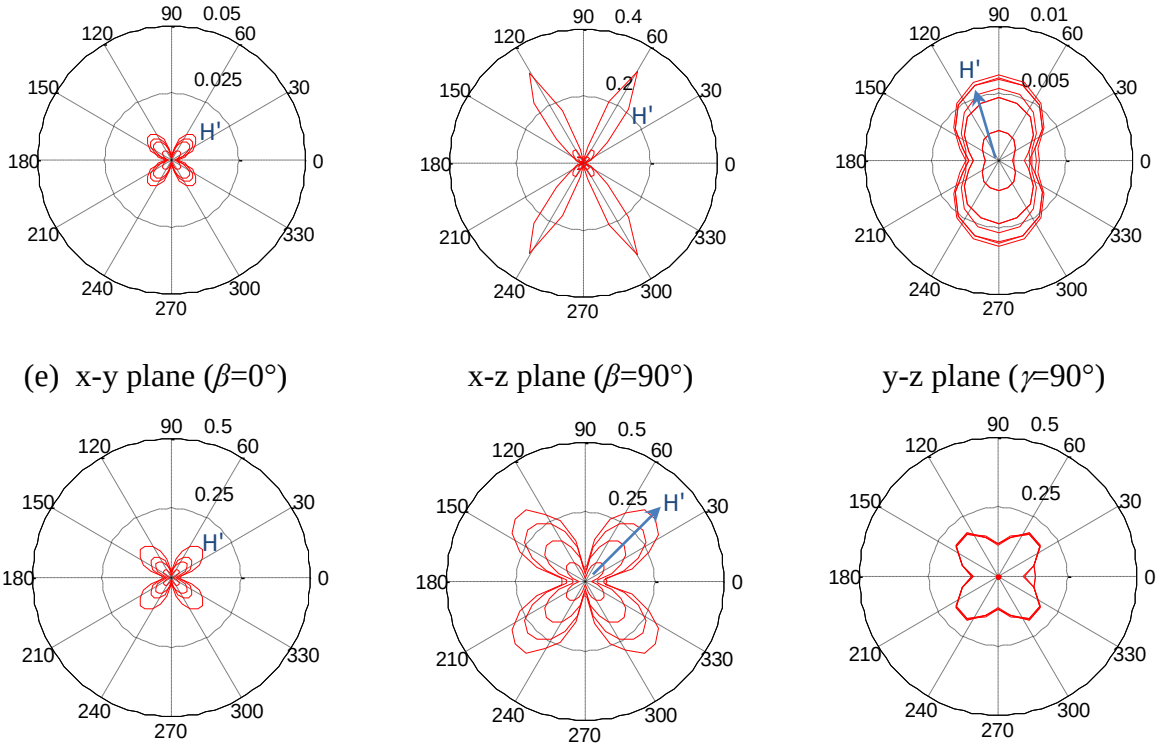

Figure 5.17 Force, displacement and force ratio distributions at initial stage and stages E, F and G of selected element of biaxial test: (a) normal forces on x-y plane, x-z plane and y-z plane (N); (b) tangential forces on x-y plane, x-z plane and y-z plane (N); (c) normal displacements on x-y plane, x-z plane and y-z plane (mm); (d) tangential displacements on x-y plane, x-z plane and y-z plane (mm); (e) force ratios on x-y plane, x-z plane and y-z plane

Likewise, consistent second-order work values were obtained for the selected element (Figure 5.18(a)). Before point G', the second-order work was positive, whereas after this point it became negative (Figure 5.16(b)). The instability of the material can be further explained by the instability at the inter-particle contacts. It was found that the direction of the shear band (around 55°) was close to the direction of the maximum negative value of the inter-particle second-order work (Figure 5.18(c) and Figure 5.19 (b)). The simulation demonstrated that the multiscale approach could explain the occurrence of diffuse failure in a granular assembly.

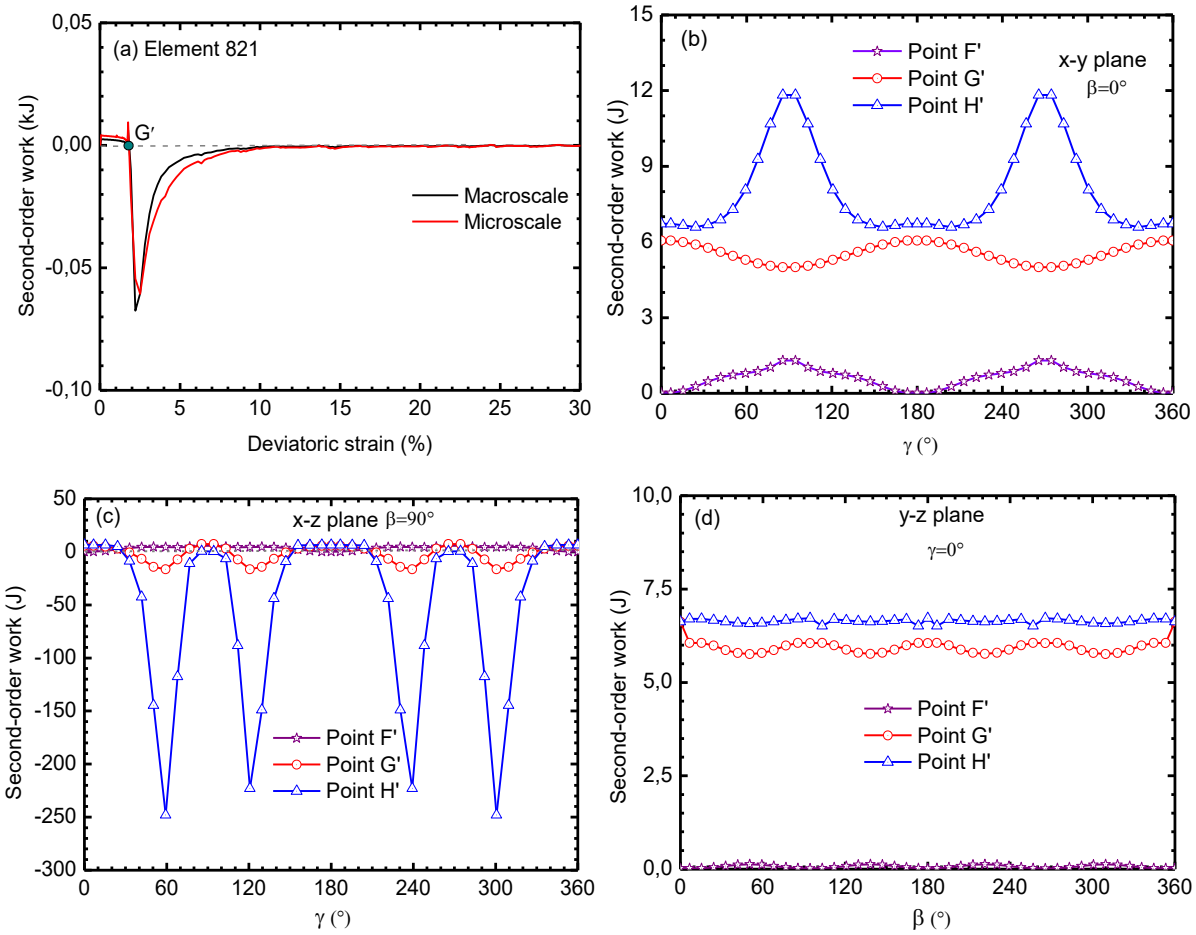

Figure 5.18 Macro and micro second-order work of selected element during loading and failure plane of biaxial test (e_0=0.885): (a) second-order work calculated by stress-strain and summation of microscale second-order word; (b-d) micro second-order work at stages E, F and G on x-y plane, x-z plane and y-z plane

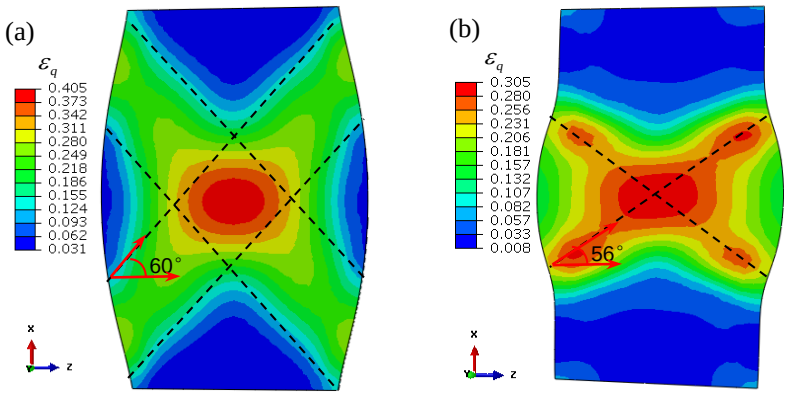

Figure 5.19 Direction of strain localisation at the end of biaxial tests: (a) dense sand (e_0=0.5) under drained condition; (b) loose sand (e_0=0.885) under undrained condition

5.4.2.3 Effect of boundary condition on the failure mode

Since failures of granular materials are strongly related to boundary conditions, it is of no slight interest to compare the failure modes in biaxial tests with different boundary conditions. For comparison, the constraints in the z direction of the aforementioned rough boundaries were relieved, whereas the other conditions were kept the same, a condition corresponding to the so-called smooth boundaries. For the biaxial test with smooth boundaries, the symmetry should be broken through a random initial void ratio (Andrade and Borja, 2006; Andrade *et al*., 2008), artificial imperfections or material inherent fabric anisotropy (Gao and Zhao, 2013; Guo and Zhao, 2014).

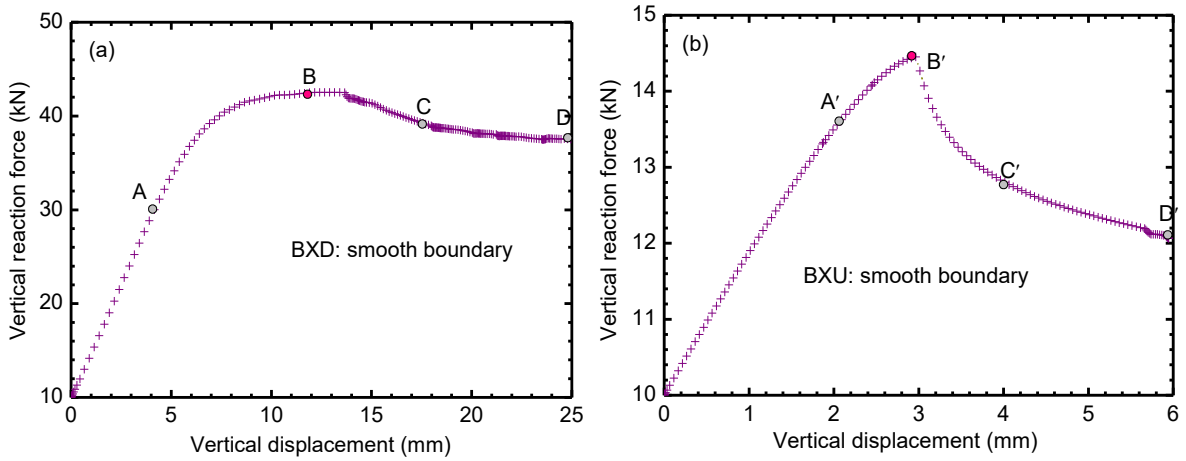

Figure 5.20 Force-displacement of biaxial tests with smooth boundaries: (a) dense sand (e_0=0.5) under drained condition; (b) loose sand (e_0=0.885) under undrained condition

In this study, an initially homogeneous granular assembly was considered and the central element 821 was set as a weak element with an initial void ratio of 0.6 (compared to 0.5 for the whole assembly) for drained condition and of 0.9 (compared to 0.885 for the whole assembly) for undrained conditions. The shape of the localised contour was apparently very different from the one obtained with rough boundaries (Figure 5.9 and Figure 5.21). Only one branch of the shear band could be observed at the end of the loading, in agreement with the results obtained by DEM simulations (Guo and Zhao, 2014) and finite element modelling (Gao and Zhao, 2013). Under undrained condition (Figure 5.14 and Figure 5.22), the assembly was homogenous at point A' and continued to be homogeneous until point B', where a diffuse failure occurred. This bifurcation point B' can be clearly observed throughout the

evolution of the plastic strain and the pore water pressure of the selected elements and nodes, as shown in Figure 5.23. Afterwards, the failure mode became localised at stages C' and D'. Given this comparison, it can be concluded that the boundary conditions have significant effects on the failure mode of granular materials.

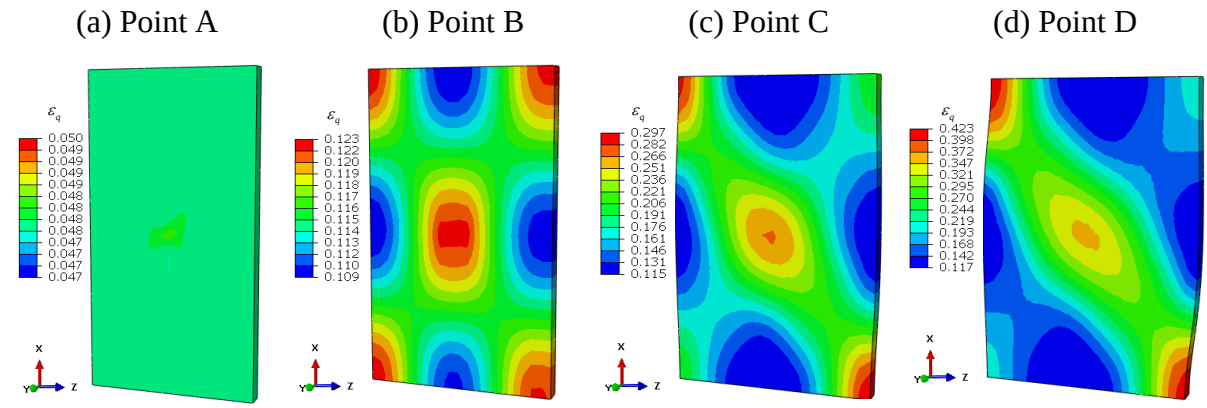

Figure 5.21 Drained biaxial tests of dense sand (e_0=0.5) with smooth boundary: (a) deviatoric plastic strain at stage A; (b) deviatoric plastic strain at stage B; (c) deviatoric plastic strain at stage C; (d) deviatoric plastic strain at stage D

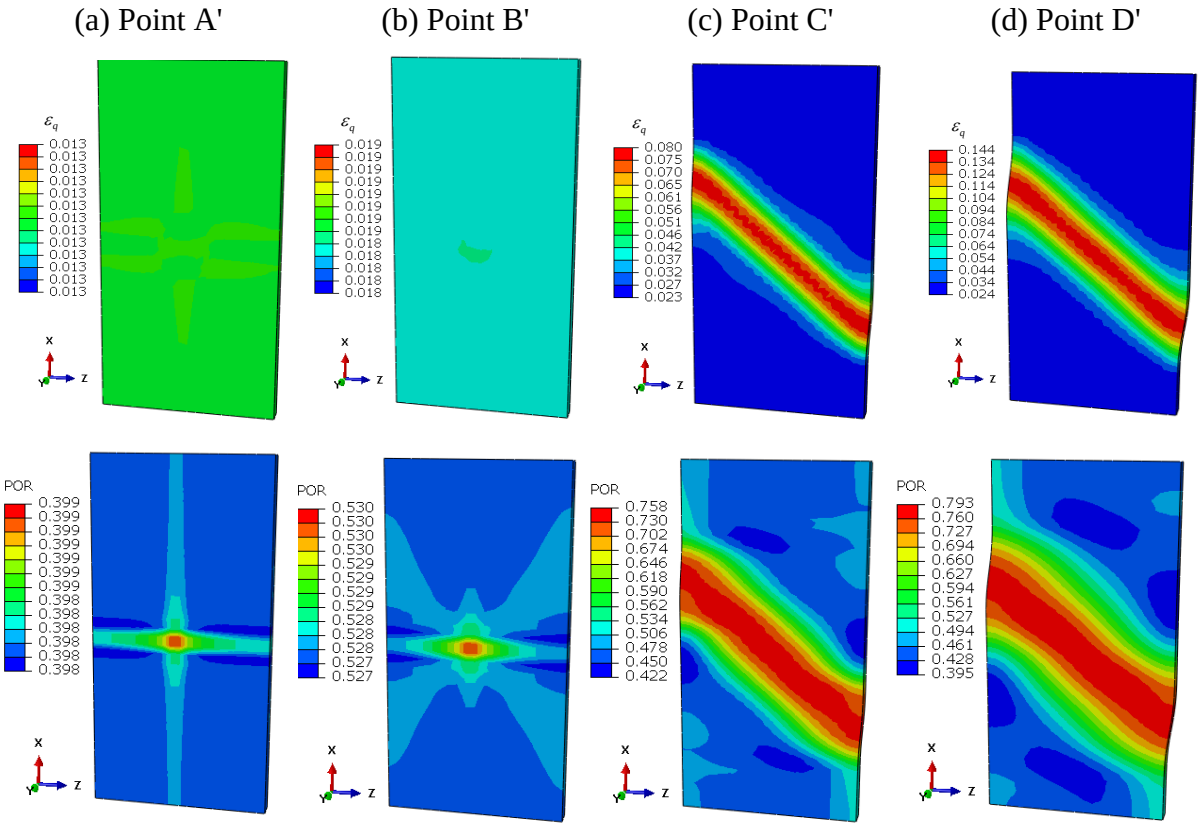

Figure 5.22 Undrained biaxial tests of loose sand (e_0=0.885) with smooth boundary:

deviatoric plastic strain and pore pressure at (a) stage A'; (b) stage B'; (c) stage C'; and (d) stage D'

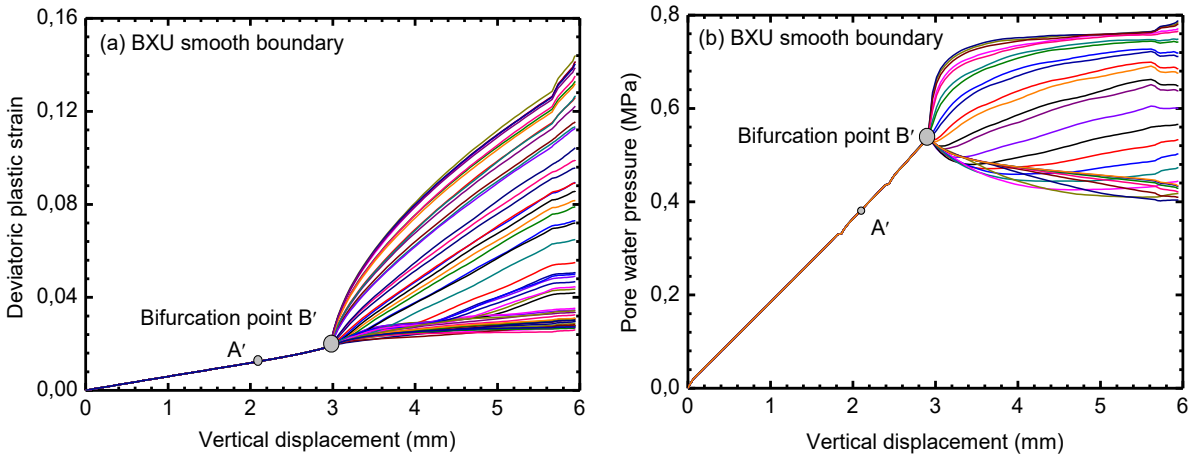

Figure 5.23 Deviatoric plastic strain and pore water pressure of selected elements of the undrained biaxial tests with smooth boundary: (a) plastic strain; (b) pore water pressure

5.4.2.4 Influence of the porosity field on the failure mode

The stress paths have significant impact on the failure mode of granular materials. A specimen tends towards a diffuse failure if the stress path is inclined to approach the origin of the *p'-q* plane, whereas its tendency is to localise if the stress path is far away from the origin, as discussed by Nicot *et al*. (2009). In addition to the previously investigated loading programs with different stress paths, the porosity of the assembly inherently influences the evolution of the stress path. This has been confirmed by the evidence that a loose sand sample is more likely to contract, whereas a dense one is prone to dilate (Wan *et al*., 2017). Accordingly, one can infer that the porosity field of a granular assembly influences, at least to some extent, its failure mode.

A limited number of studies devoted to examining the effect of the porosity field on the failure mode of granular assemblies is available in the literature. Andrade and Borja (2006) adopted a truncated exponential density function, whereas Andrade *et al*. (2008) used a probability density function to describe the non-uniformity of the granular assemblies. Their studies present the strain localisation of specimens under plane strain compressions. The results indicate that the strength of the specimen was affected by both the degree of

heterogeneity and the orientation of the anisotropy of the porosity field, while distinct shear bands were observed at the peak strength point. Wan *et al*. (2017) generated granular assemblies with non-uniform initial void ratios using the Gauss distribution. The average void ratios were the same as in the homogeneous ones, whereas the standard deviation was set at a small value of μ=0.01. Localised and diffuse failures at the peak strength point were obtained, in agreement with the homogeneous cases. However, the range of the void ratios in these simulations was small and all the void ratio values were largely close to the average value.

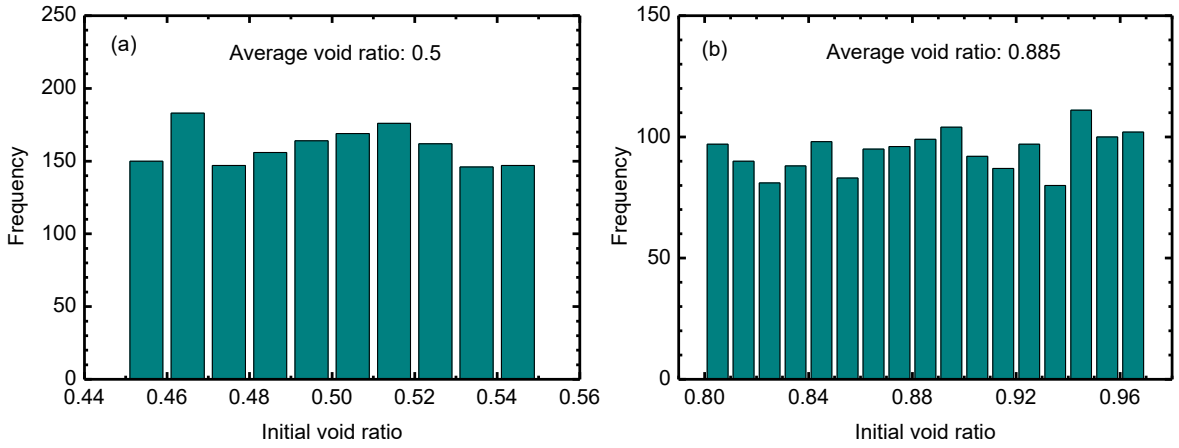

Figure 5.24 Distribution of random initial void ratio of granular assembly: (a) dense; (b) loose

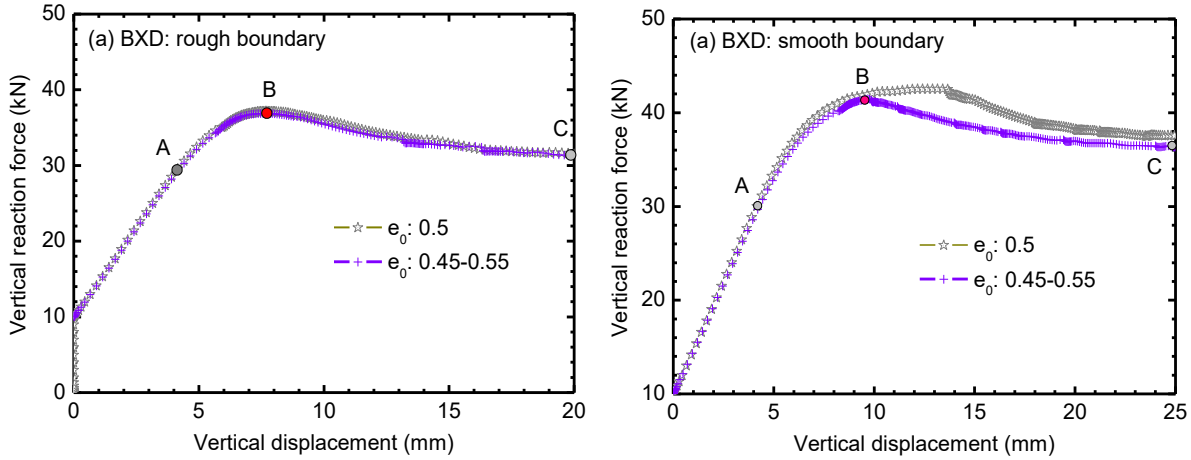

Figure 5.25 Force-displacement of biaxial tests on dense sand (e_0=0.45-0.55): (a) rough boundary; (b) smooth boundary

To examine the influence of a given range of void ratios on the failure mode of granular materials, it was decided to use a uniform distribution function to generate randomly distributed void ratios in granular assemblies. The same average values as previously used

were maintained, i.e. 0.5 for drained tests and 0.885 for undrained tests, with the range of 0.45-0.55 for drained tests and 0.8-0.97 for undrained tests. Same simulation results were obtained by using different randomly distributed initial void ratios within the given range. We present here only one example of the simulation results based on the initial void ratios given in Figure 5.24. Both drained and undrained simulations were conducted with the aforementioned rough and smooth boundary conditions. For the drained test with rough boundaries, a shear band was formed, similar to the one obtained in the homogenous case; the force-displacement relationship was also similar to the one obtained in the homogenous case, see Figure 5.25(a) and Figure 5.26. For a drained test with smooth boundaries, only one shear band developed at peak point B, unlike the localised pattern obtained for the homogenous assembly (Figure 5.21). In addition, the peak strength of the assembly was slightly smaller than in the homogenous case, as indicated in Figure 5.25(b) and the stress-strain relationship differed from the one obtained in the homogeneous granular assembly.

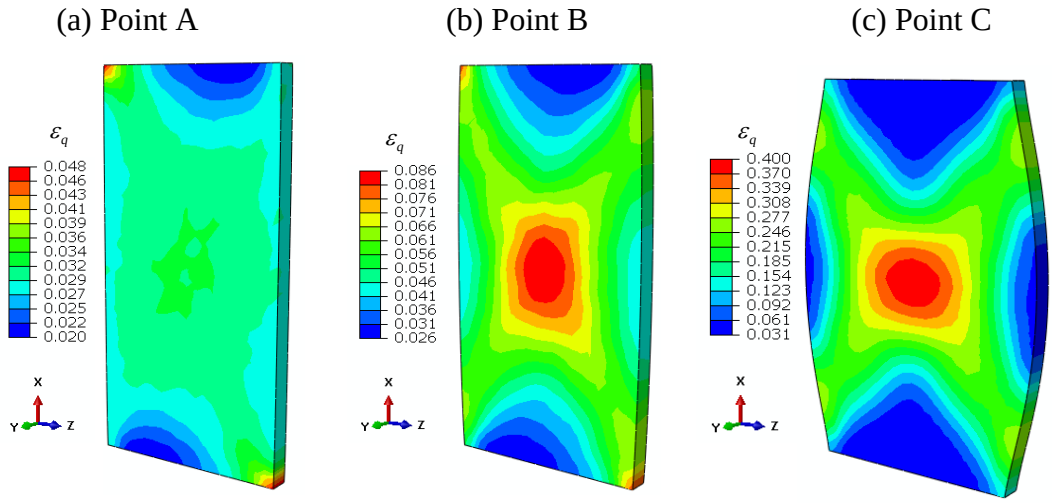

Figure 5.26 Drained biaxial tests of dense sand (e_0=0.45-0.55) with rough boundary: (a) deviatoric plastic strain at stage A; (b) deviatoric plastic strain at stage B; (c) deviatoric plastic strain at stage C

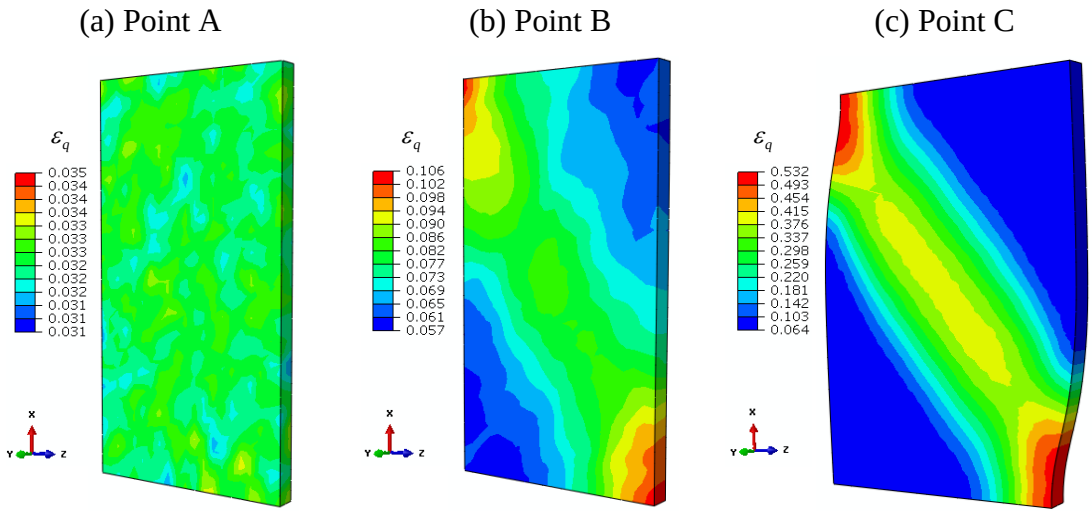

Figure 5.27 Drained biaxial tests of dense sand (e_0=0.45-0.55) with smooth boundary: (a) deviatoric plastic strain at stage A; (b) deviatoric plastic strain at stage B; (c) deviatoric plastic strain at stage C

Diffuse failures were obtained in the undrained cases with both rough and smooth boundaries. The peak strength with the rough boundaries was about the same as in the homogenous assembly, whereas for the smooth boundaries it was found to be lower. In the case of rough boundaries for a non-uniform initial void ratio, only one shear band developed at point C', which was not the case for a homogenous void ratio. However, the 'X-shape' shear band that developed in the homogenous case also occurred at point D' (Figure 5.29), which indicates that the boundary condition controls the failure mode highly. For the undrained test with smooth boundaries, only one shear band developed after the diffuse failure point B', which is consistent with the results obtained in the uniform case. However, the location and direction of the shear band differed from the ones observed in the homogenous case (Figure 5.21 and Figure 5.30). The results demonstrate that the heterogeneity of the initial void ratio within the granular assembly can affect the failure behaviour of granular materials. In the studied cases, the peak strengths were not highly influenced by the heterogeneity of the initial void ratio, but this heterogeneity had significant impact on the shape and direction of the shear bands.

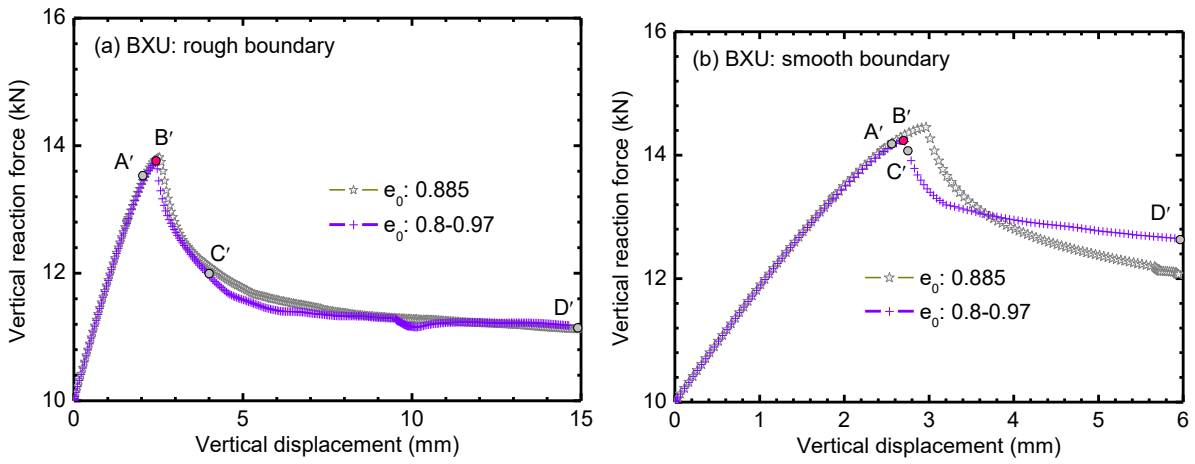

Figure 5.28 Force-displacement of biaxial tests on loose sand (e_0=0.80-0.97): (a) rough boundary; (b) smooth boundary

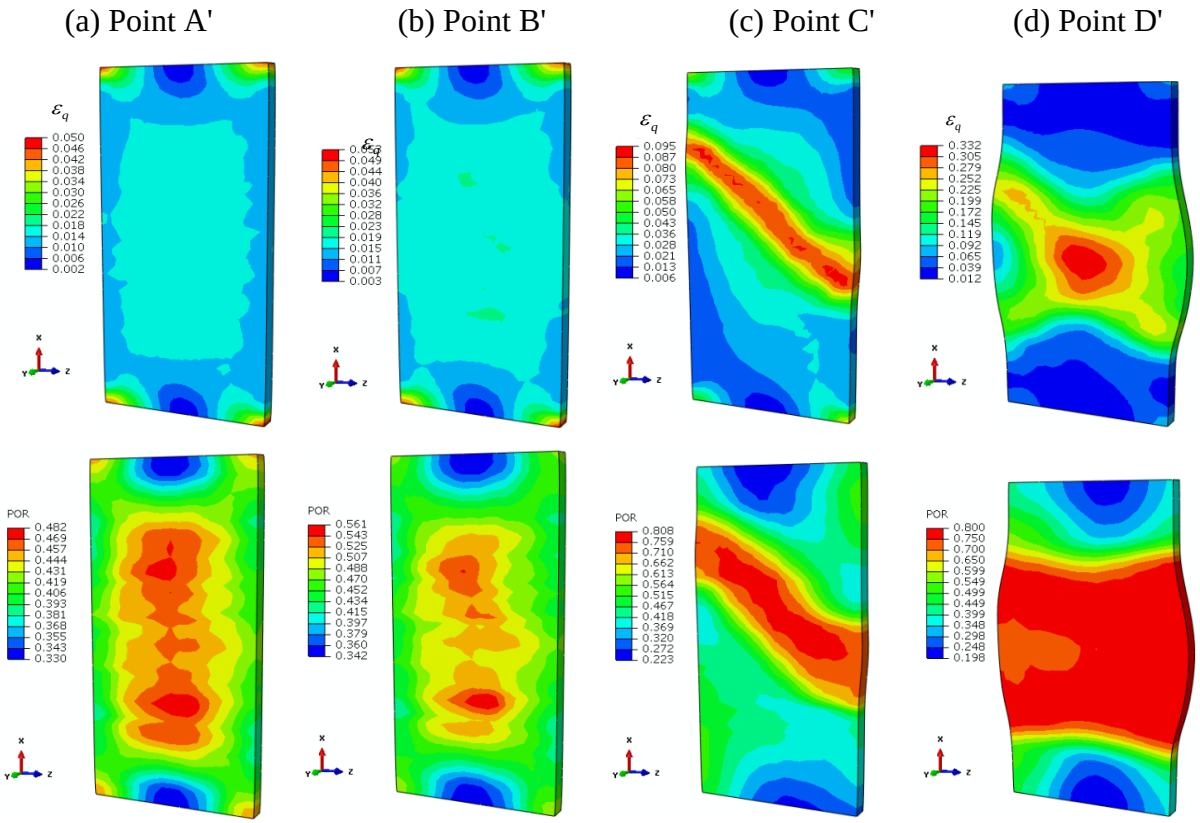

Figure 5.29 Undrained biaxial tests of loose sand (e_0=0.80-0.97) with rough boundary: deviatoric plastic strain and pore pressure at (a) stage A'; (b) stage B'; (c) stage C'

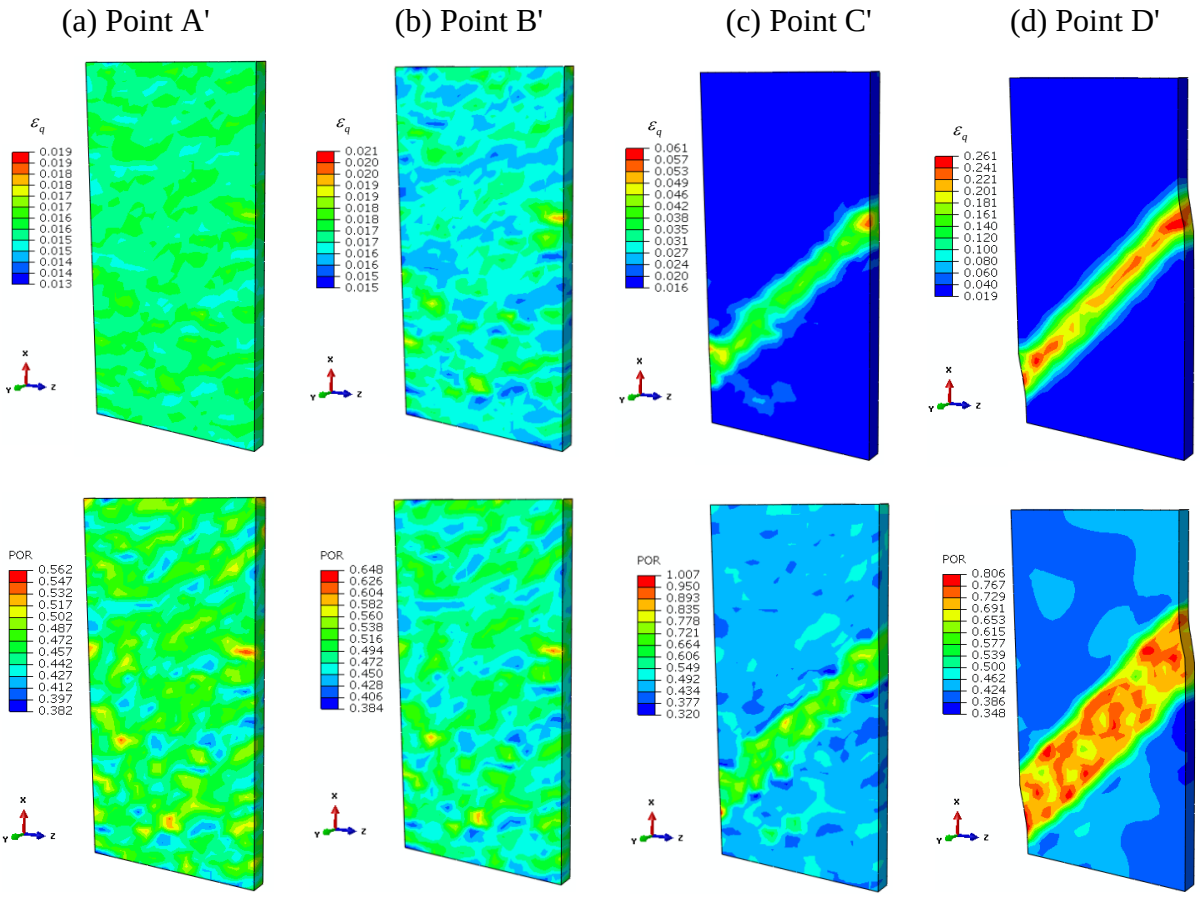

Figure 5.30 Undrained biaxial tests of loose sand (e_0=0.80-0.97) with smooth boundary: deviatoric plastic strain and pore pressure at (a) stage A'; (b) stage B'; (c) stage C'

5.5 Concluding remarks

This chapter investigated the influence of microstructural instabilities on the global failure of granular materials through the use of second-order work as the instability criterion. Based on the above analyses, the following conclusions can be drawn:

1) Adopting the vanishing of the second-order work as the condition for the effective failure of a granular material is a more rigorous approach than any other one which considers the traditional factor of safety based on the material plastic limit. To examine the extent to which inter-particle contact instability has upon the influence of the macroscale material instability, the second-order work at different scales was defined. The relation between the second-order work at the micro and macro scales was derived,

based on the CH model, and extended to the scale of boundary value problems via the finite element method.

2) The effects of volumetric and geometric changes on the second-order work calculated by the CH model were examined. The results show that there was no significant influence in the studied problems, which justifies the adoption of the Cauchy stress and the Euler strain for calculating the second-order work.
3) Drained and undrained triaxial tests were simulated to validate the consistency of the second-order work computed at micro and macro levels. The particulate origin of the specimen instability was well captured, which demonstrates the validity of this method for predicting localised and diffuse failures in a granular material.
4) The extent of the global material failure originating from microstructural instabilities was analysed. The second-order work in boundary value problems was computed for the case of drained and undrained biaxial tests. Localised failure in dense specimens and diffuse failure in loose specimens were obtained and analysed. It has been shown that the suggested method was adequate for predicting the instability of a granular assembly subjected to homogeneous and inhomogeneous loading conditions.
5) The influence of the boundary conditions as well as the heterogeneity of the initial porosity on the failure mode was examined. Results show that these two aspects can have significant effects on the failure mode of granular materials.

The suggested approach has contributed in describing the instability in granular assemblies, and can now be further applied to investigate the stability of geotechnical structures.

CHAPTER 6 MICROMECHANICS-BASED FINITE ELEMENT ANALYSIS OF GEOTECHNICAL PROBLEMS

6.1 Introduction

The performance of geotechnical structures such as dams, structural fills, earth retaining structures, and solid waste landfills are vital to human's activities. To improve the safety of the geo-structures and to predict their long-term performances after construction, reliable computational methods should be used to accurately and efficiently calculate their bearing capacity under various loadings. The current design methods including the empirical equations, the finite element method, the finite difference method and the discrete element method have been used in scientific research as well as in engineering practice. Among these approaches, the finite element method based upon the classical continuum mechanics has been widely adopted. In this method, the constitutive model controls the physics of the problem which requires a model reliable enough for describing the behaviour of granular soils.

A large number of constitutive models have been proposed to describe various aspects of soil behaviour. However, many advanced models require many parameters that are difficult to calibrate and thus they are difficult to use in engineering practice. With the increasing constructions of underground, the planed engineering facilities are required to have small enough imperfections on the constructions, which demands more sophisticated meanwhile applicable models to be used.

Typically, problems involving small and large deformations of granular soils need to be solved in engineering practice. The former ones can be solved by the classical finite element method. However, this method may encounter huge mesh distortions in large deformation problems which results in non-convergence of the numerical simulations. One method to solve this problem is to re-mesh the computational domain with the Arbitrary Lagrangian Eulerian (ALE) technique (Tolooiyan and Gavin, 2011; Zhang *et al*., 2014). However, the new meshes are highly dependent on the initial mesh size. Alternatively, the Coupled Eulerian

Lagrangian (CEL) based finite element method sticks granular soils that have large deformations as Euler mesh, while taking the structures as Lagrangian mesh. The efficiency of this approach has been demonstrated in simulating the closed-ended displacement piles (Qiu *et al*., 2011; Zhang *et al*., 2014; Wang *et al*., 2015; Ko *et al*., 2016). Other methods in solving large deformation problems based on the FEM include the Material Point Method (Soga *et al*., 2015) and the Smoothed Particle Hydrodynamics (SPH) method (Bui *et al*., 2008, 2011; Liu and Liu, 2010).

Regarding the multiscale nature of granular soils, it is preferable to use a constitutive model that can well consider the characteristics of granular soils with physical insights and fewer *ad hoc* assumptions in finite element modelling (Schweiger, 2008). In this study, some classical geotechnical problems will be revisited through implementing the aforementioned CH (Chang and Hicher, 2005) micromechanical model into the FEM code Abaqus/Explicit 6.14-2. The applicability of the CH micromechanical model to engineering applications will be demonstrated by solving geotechnical problems that involve both small and large deformations.

6.2 Implementation of the CH model into Abaqus/Explicit

As demonstrated in Chapter 4, the CH model was successfully implemented into the implicit finite element code Abaqus/Standard 6.11. In comparison with the Abaqus/Standard that uses an implicit method to solve the weak form of the FEM differentiating equations, Abaqus/Explicit employs an explicit scheme to solve these equations. Therefore, there is no convergence problem in Abaqus/Explicit often encountered in the implicit FEM and hence it can be used to solve large deformation problems. In this chapter, the CH model is implemented in the Abaqus/Explicit 6.14-2 in the form of a user subroutine VUMAT.

According to Hibbitt *et al*. (2001), the numerical scheme of Abaqus/Explicit is presented in Figure 6.1. The equilibrium condition is expressed by the inertial force, the internal force and the external force:

$$M\ddot{u}_{(t)} = P_{(t)} - I_{(t)} \tag{6.1}$$

where M is the mass matrix; $\ddot{u}$ is the acceleration; P is the applied external force vector, and I is the internal force vector. For each time increment, the accelerations and velocities at a material point due to external loads are assumed to be constant. The equations of motion for the body are then integrated using the explicit time central-difference integration algorithm, expressed as

$$\begin{cases} \dot{u}_{\left(t+\frac{\Delta t}{2}\right)} = \dot{u}_{\left(t-\frac{\Delta t}{2}\right)} + \dfrac{\Delta t_{(t+\Delta t)} + \Delta t_{(t)}}{2} \ddot{u}_{(t)} \\ u_{(t+\Delta t)} = u_{(t)} + \Delta t_{(t+\Delta t)} \dot{u}_{\left(t+\frac{\Delta t}{2}\right)} \end{cases} \tag{6.2}$$

where u is the displacement and $\dot{u}$ is the velocity; the subscript t refers to the time in an explicit dynamic step and Δt is the time increment. To guarantee the stability of the calculation, the time increment Δt should be smaller than a critical value $\Delta t_{critical} = L_{\min}/c_d$ with $L_{\min}$ is the smallest mesh size and $c_d = [(\lambda+2\mu)/\rho]^{0.5}$ where λ and μ are the Lamé elastic constants, and ρ is the material density. The incremental displacements Δu are used to calculate the incremental strain by the compatibility equations, which will be used to drive the constitutive model to update the stresses and the internal forces, until reaching a new equilibrium state. Using VUMAT in ABAQUS/Explicit, the strain increment in the element at time t is first solved by ABAQUS using the presented explicit time central-differential integration method, and then the stress increments are updated through VUMAT.

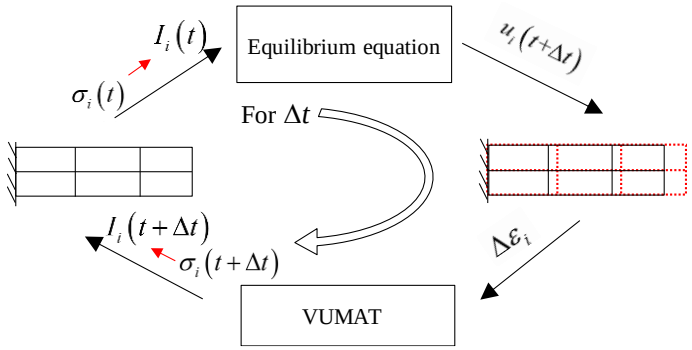

Figure 6.1 Flow chart of explicit finite element analysis based on the ABAQUS/Explicit

To verify the validity of the implementation, three triaxial drained compression tests were conducted at the elementary levels. Since there is no available element with pore pressure in the module of Abaqus/Explicit, only drained tests were modelled. In addition, the biaxial tests

and the settlement of a square footing conducted in Chapter 4 were simulated with the Abaqus/Explicit 6.14-2 solver to further demonstrate the success of the implementation in calculating boundary value problems.

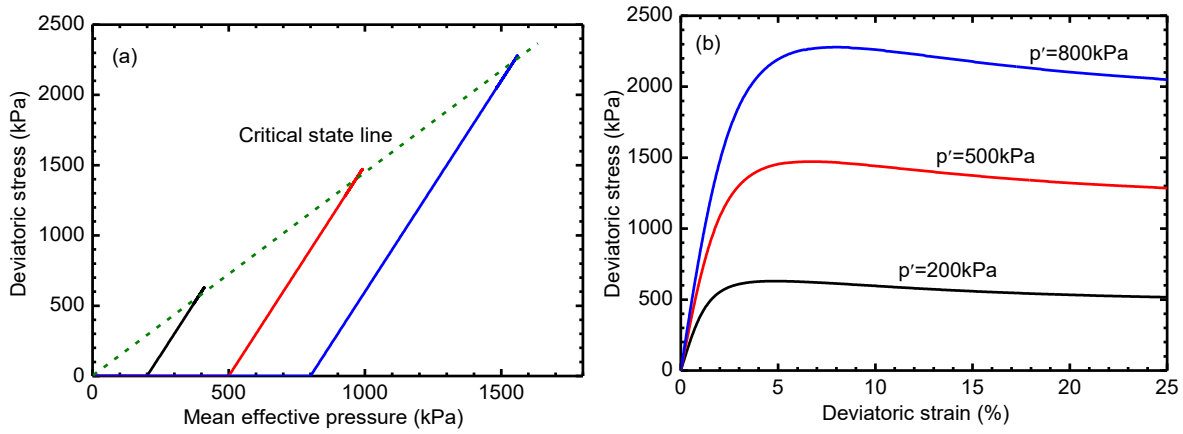

Figure 6.2 Simulations of drained triaxial compression tests using IPP, UMAT and VUMAT

6.2.1 Drained triaxial compression tests

Drained triaxial compression tests on dense Hostun sand were simulated for which a strain softening behaviour could be observed. The simulations were conducted on a single element with the dimension of 1m×1m×1m by using Abaqus/Explicit 6.14-2. The material was represented by VUMAT with the material parameters calibrated in Chapter 2 and with an initial void ratio of 0.5. The samples were isotropically compressed up to 200kPa, 500kPa and 800kPa and then axial velocity-controlled loadings were imposed under constant confining stresses. As shown in Figure 6.2, the simulation results are consistent with the ones obtained by UMAT and IPP (Integration Point Program that was described in Chapter 4). The same responses were obtained by the three methods, which demonstrate the correctness of the implementation for single element tests.

6.2.2 Biaxial test on dense sand

In biaxial test on dense sand, the strain increments inside and outside the shear band are not the same. The simulation of a biaxial test was performed on dense sand as its behaviour is highly dilative with strain softening occurring rapidly under a small range of strain. The specimen was composed of 2501 eight-node trilinear displacement elements with reduced

integration (C3D8R) and 2583 nodes with the dimension of 200mm×100mm×10mm, as shown in Figure 6.3(a). The material parameters used for the single element test were adopted again, with the initial void ratio of 0.5. The specimen was first isotropically compressed up to a pressure of 800kPa and then loaded with different vertical displacement increments, maintaining a constant lateral stress. The hardening and softening behaviour of the granular assembly was well captured, accompanying with the localisation of the specimen, as shown in Figure 6.3(b-c). A shear band was observed from the distribution of the deviatoric plastic strain, which is comparable to the results obtained from literature (Gao and Zhao, 2013; Guo and Zhao, 2016).

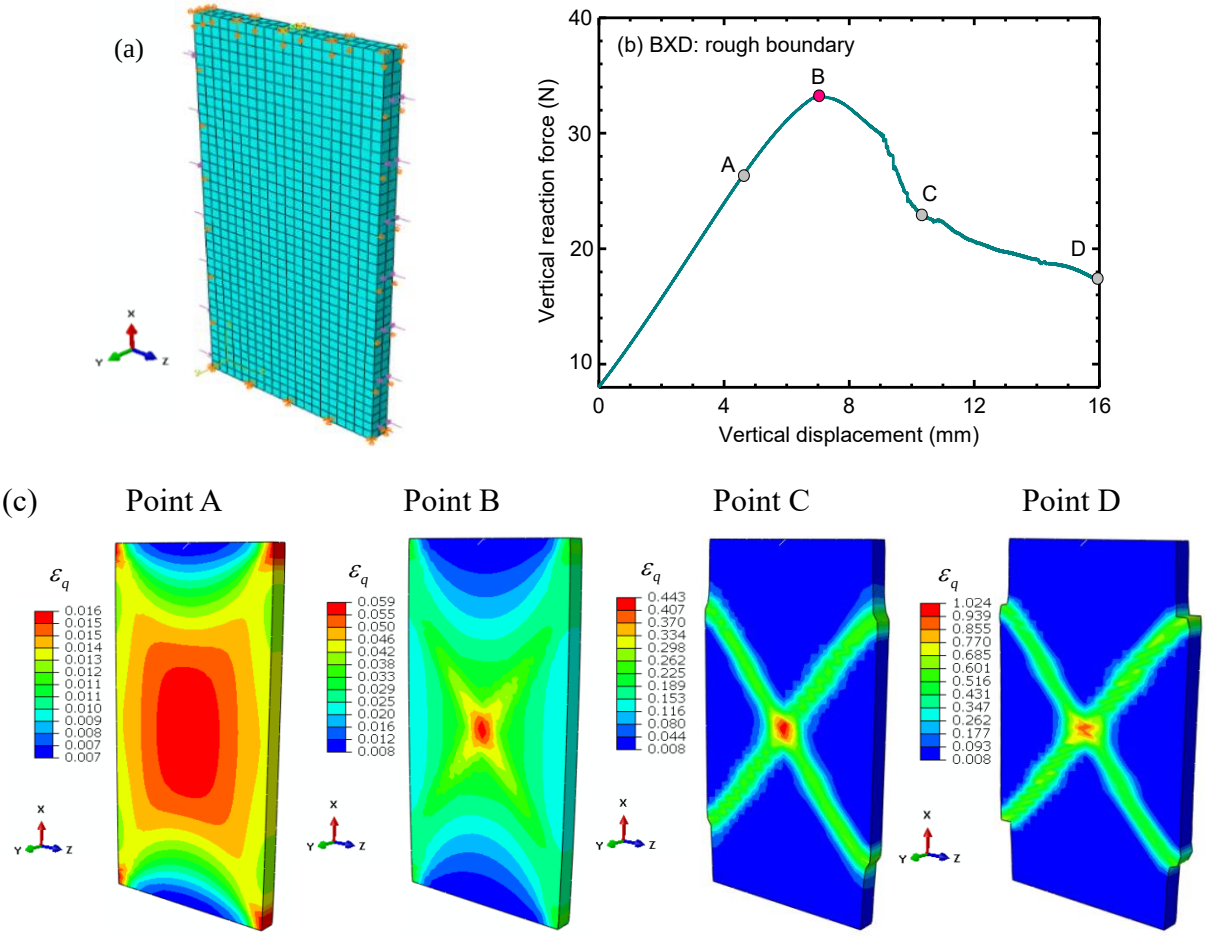

Figure 6.3 Simulation of biaxial test: (a) mesh and boundary condition (b) distribution of deviatoric strain

6.2.3 Settlement of a square footing under vertical loading

The ultimate bearing capacity of a rigid footing is a typical problem for numerical validation,

due to the complex loading stress paths inside the foundation soil. During loading, the values of the strain increments span a very large range within the soil volume beneath the footing, which requires a solid constitutive integration scheme over all the Gauss points. To assess the performance of the implemented CH model in Abaqus/Explicit 6.14-2, a finite element analysis of a square footing was analysed.

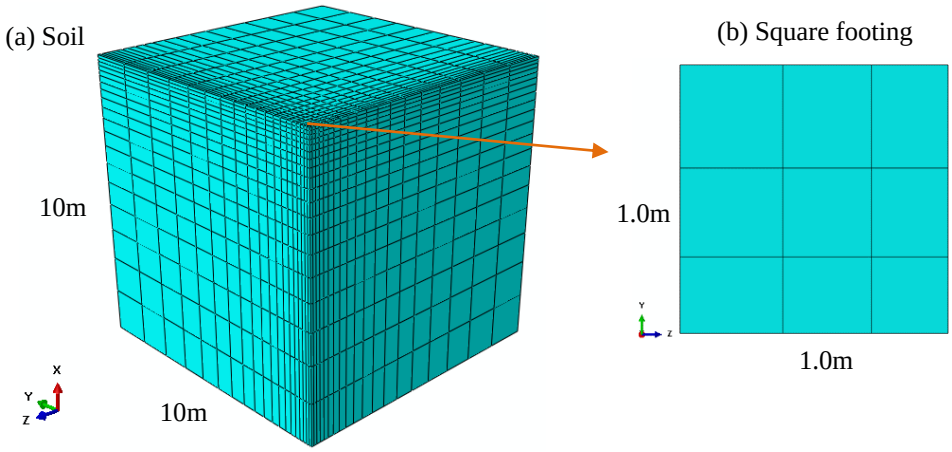

Figure 6.4 Dimension of the FE model: (a) foundation and (b) square footing area

The FE model used in Chapter 4 was adopted again. As shown in Figure 6.4, the finite element model is composed of 8819 C3D8R elements and 9261 nodes, and only a quarter of the volume is considered for the calculation, due to the symmetry of the problem. The dimensions of the soils are $10\text{m}\times 10\text{m}\times 10\text{m}$, whereas the bottom of the footing is $1\text{m}\times 1\text{m}$. The lower boundary of the soil is fixed in the directions x, y and z, whereas the lateral soil boundaries are only fixed in the y and z directions. As for the boundary of the footing, only the vertical displacement has not been prevented.

The model parameters used in the previous example were adopted with an initial void ratio of 0.42. Considering that the footing can be regarded as a rigid body, a single element can be used to represent the footing, which prevents the influence of the soil-footing interaction on the performance of the studied problem. At first, the soil underwent a geostatic loading in order to simulate the *in-situ* gravity and, then, the footing was loaded by imposing a vertical velocity at the speed of 0.05mm/s, which is slow enough to ensure that the loading corresponds to a static condition. The distribution of the deviatoric plastic strain, shown in

Figure 6.5(b), is quite similar to the results obtained in the literature (Gourvenec *et al*., 2006; Lyamin *et al.*, 2007). A typical p-s curve obtained in the field test and in other numerical simulations is also obtained in this simulation, as shown in Figure 6.6.

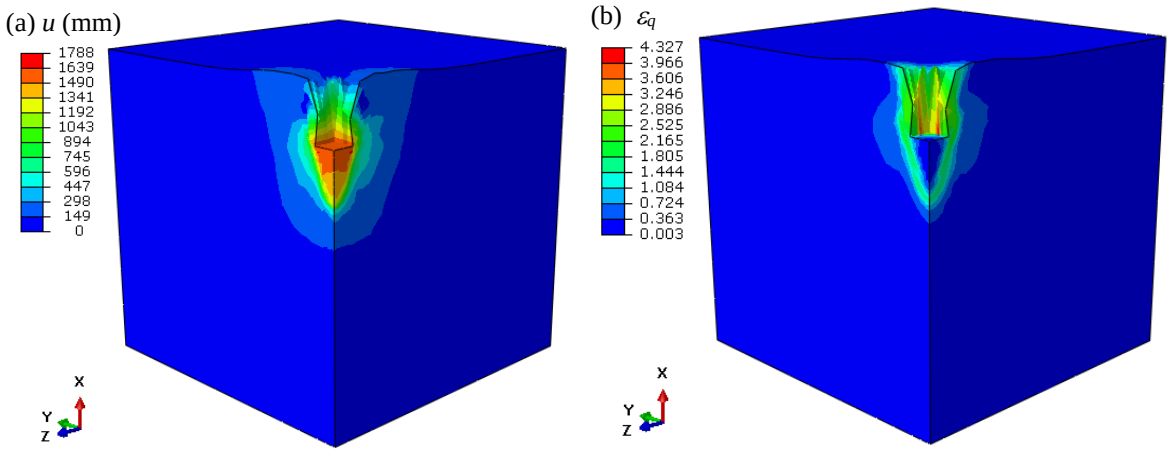

Figure 6.5 Settlement of a square footing: (a) total displacement and (b) accumulated deviatoric shear strain

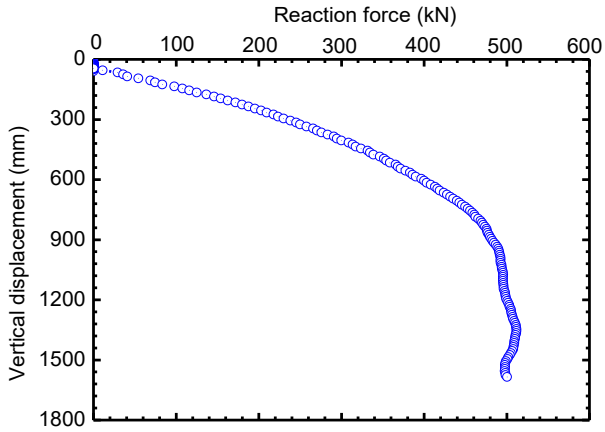

Figure 6.6 Force-displacement relation of the square footing

Overall, based on the analyses of drained triaxial compression tests, a biaxial test and a square footing, one can conclude that the CH micromechanical model has been successfully implemented into Abaqus/Explicit 6.14-2. In the following subsections, this multiscale approach will be applied to solve some engineering problems with small and large deformations by comparing the numerical results to experimental results as well as to analytical solutions.

6.3 Tunnel excavation

Tunnelling is one of the major construction methods to sustain the increasing demand on construction of highways and metros in cities. Improper excavations may endanger human life and cause catastrophic damage to the structures within the influence zone. Over the decades, numerous theoretical and experimental studies have been performed for the prediction of the ground surface settlement during and after tunnelling (Fang *et al*., 1994; Mair, 2008; Kirsch, 2010; Marshall and Mair, 2011; Jiang *et al*., 2012; Wong *et al*., 2012; Li *et al*., 2014; Jiang *et al*., 2014; Shen *et al*., 2014; Wu *et al*., 2015; Cui *et al*., 2016; Zhang *et al*., 2017). On one hand, very large settlement of ground surface destroys the constructed roads, pipelines and high-rises. On the other hand, the displacements largely originating from the non-equilibrium pressure at the excavation face of tunnel may arise risks for the workers. Therefore, it is of importance to predict the settlement of ground surface after tunnelling by the finite element analysis that has demonstrated its priority in engineering design. However, only relatively simple constitutive models have been used in the engineering practice. In view of this, this study adopts the aforementioned CH micromechanical model to compute the excavation of a shallow tunnel in sand. The obtained ground settlement curve was compared with the classical analytical solution, i.e. the Peck's method (Peck, 1969). By doing so, it can be inferred that the CH micromechanical model can be potentially used in the design of tunnel excavation in granular soils.

6.3.1 Model calibration on Hostun sand

The CH micromechanical model was calibrated on Hostun sand over a wide range of densities and confining pressures with a total of 8 parameters, and demonstrated a good performance in reproducing the behaviour of Hostun sand, as described in Chapter 2.

6.3.2 Finite element analysis

A two-dimensional finite element model was built by using the Abaqus/Explicit 6.14-2 by considering that the tunnel excavation is a plane strain problem. The dimension of the soil domain is in the length of 80m and in the height of 40m, as shown in Figure 6.7. A total of 1680 four-node bilinear displacement CPE4 elements were generated for the soil. The

distance from the top of the tunnel to the earth ground is 10.5m. The bottom of the soil domain is fixed in all directions while the lateral boundaries are only constrained in the x direction. After the soil underwent a geo-static process, a tunnel with the radius of 3.135m was excavated by deactivating the soil elements within the tunnel, meanwhile keeping the displacements of the tunnel boundary as zero. In order to simulate the ground settlement due to the excavation, the tunnel boundary was shrunk towards the centre of the tunnel with the radium displacement of 0.035m, which corresponds to the volume loss rate of 2%. After that, a lining with an inner radius of 2.75m and an outer radius of 3.1m was added to support the soil.

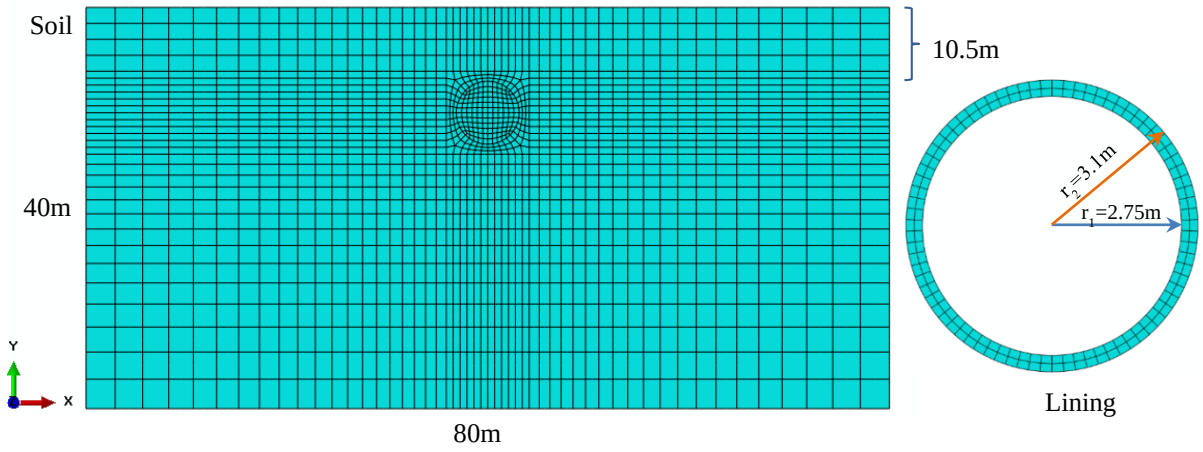

Figure 6.7 Finite element model of soil and tunnel lining

The distribution of the total displacement at the end of the construction is shown in Figure 6.8(a). One can see that the top of the tunnel displays the largest displacement; above this point the displacement reduces with a funnel-shaped distribution. Interestingly, the upheaved behaviour of the soil under the tunnel after the excavation was well captured, as demonstrated in Figure 6.8(b). In addition, the typical vertical displacement distribution observed in the field was also obtained. After adding the lining, the largest shear strains were distributed mainly around the lining, whereas the other elements displayed relatively smaller deviatoric shear strains (Figure 6.8(c)).

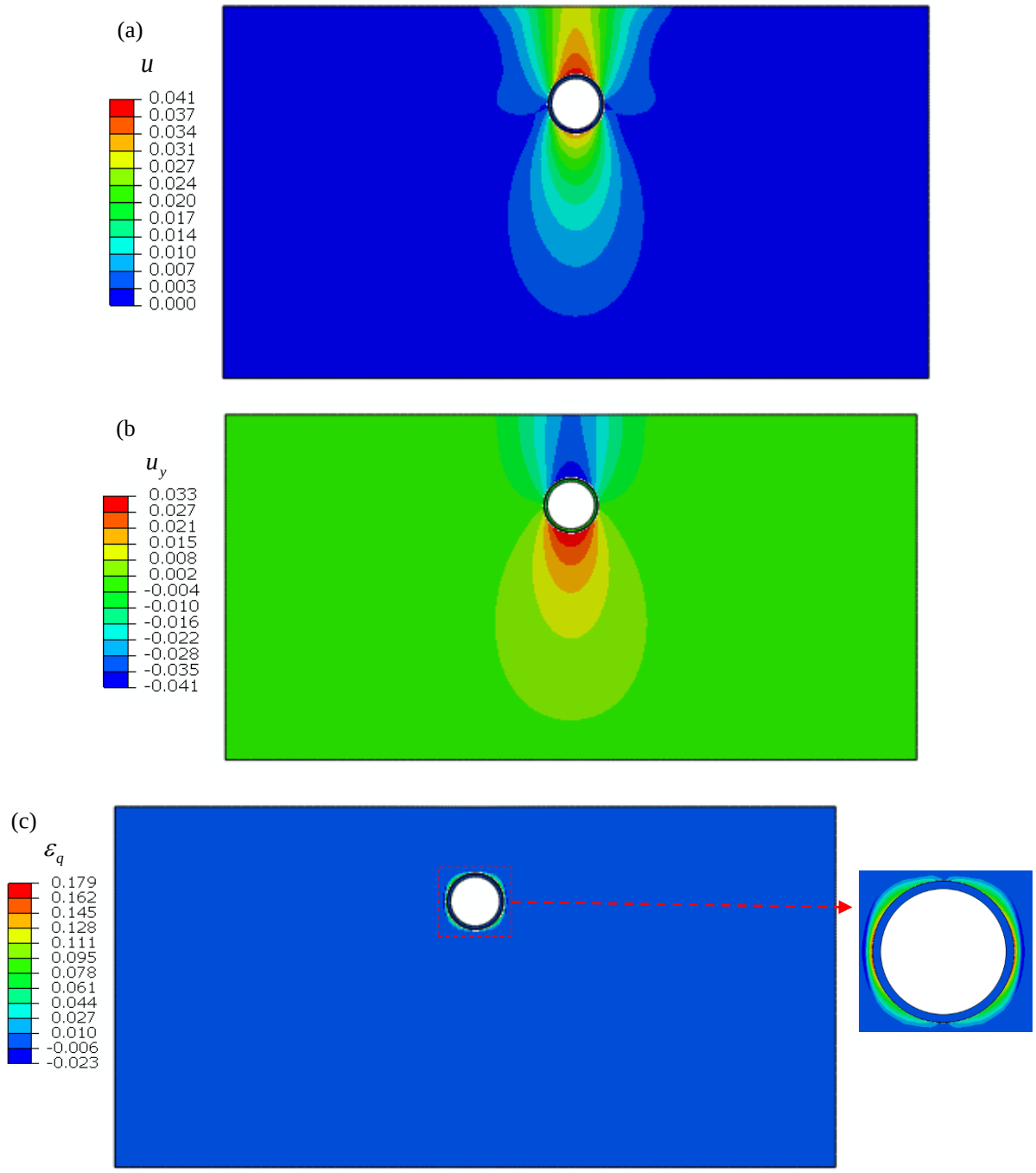

Figure 6.8 Distributions of the (a) displacement (m); (b) vertical displacement (m); (c) shear strain at the end of lining

6.3.3 Comparison with Peck's method

The ground settlements caused by an excavation obtained by using the CH micromechanical model were compared with the Peck analytical solution (Peck, 1969) since it has been proved to have the ability to describe the ground settlement after excavation, as discussed by Dang

and Meguid (2008). Based on field data, Peck (1969) suggested that the surface settlement over a single tunnel could be approximated by the following expression:

$$S(y) = S_{max} \exp\left(\frac{-y^2}{2i^2}\right) \tag{6.3}$$

in which $S(y)$ is the settlement at the offset distance y from the tunnel centre line, S_{max} is the maximum settlement above the tunnel centre line, and i is the distance from the inflection point of the trough to the tunnel centre line, which is commonly used to represent the width of the settlement trough, as shown in Figure 6.9(a). According to the computed results, the value of S_{max} is taken to be 20.12mm, while the parameter i is equal to 4.24m. As shown in Figure 6.9(b), the numerical simulation results fit well with the analytical solution, which indicates that the CH micromechanical model has the capability to capture the settlement of geotechnical excavations.

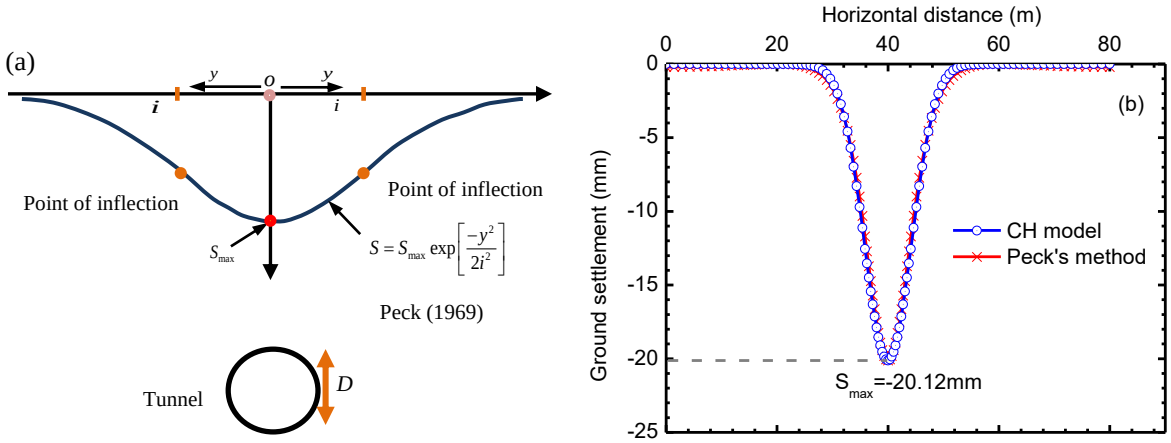

Figure 6.9 Ground settlement: (a) Peck's method and (b) CH model and Peck's prediction

6.4 Deformation of retaining walls under various loadings

The deformation of the soil behind a retaining wall is a typical large deformation problem which involves strain localisation of granular soils. This problem has been widely investigated in the literature, such as the classical Rankine and Coulomb theories, and more recently studied by X-rays tomographic (Niedostatkiewicz *et al.*, 2011), finite element analysis with elasto-plastic models (Hicks *et al.*, 2001) and micro-polar hypo-plastic constitutive relations

(Tejchman *et al*., 2007) and by DEM simulations (Tejchman *et al*., 2011; Guo and Zhao, 2016).

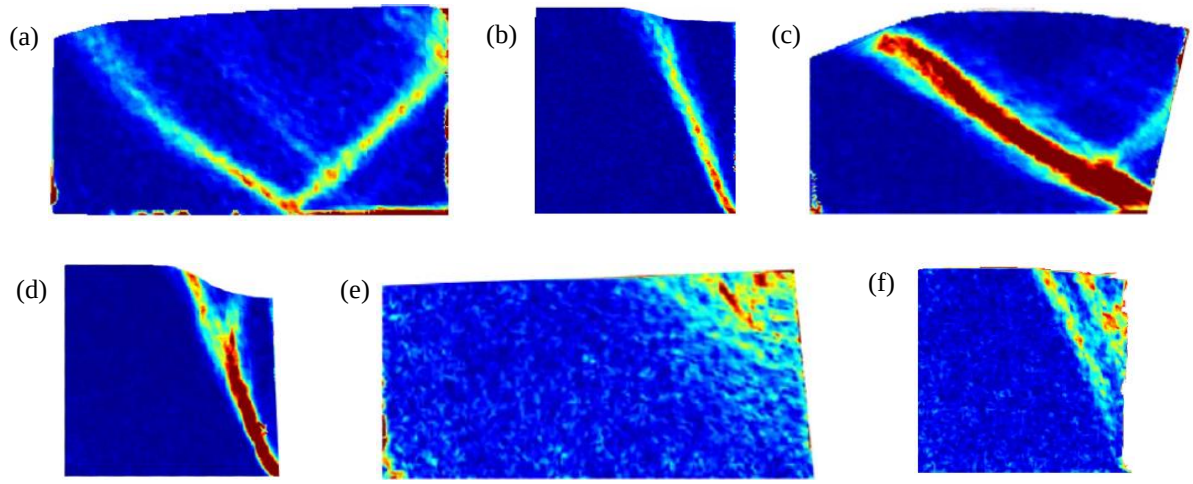

Figure 6.10 Shear strain observed in the experiments on sand by moving a retaining wall: (a) translation, passive (b) translation, active (c) rotation about the top, passive (d) rotation about the top, active (e) rotation about the toe, passive (f) rotation about the toe, active (figures from Niedostatkiewicz *et al*., 2010)

To demonstrate the ability of the CH micromechanical model in capturing the behaviour of strain localisation around retaining walls under various loading conditions, the experiments on dry cohesionless sand performed by Niedostatkiewicz *et al*. (2010) were simulated by the described FEM×CH numerical approach. Based on the experimental description of Niedostatkiewicz *et al*. (2010), the plane strain experiments were calculated by three-dimensional finite element models undergoing passive and active movements: horizontal translation, rotation about the tops and rotation relative to the toes. In passive mode, the retaining walls were moved towards the backfill, whereas in an active mode they were moved away from it.

6.4.1 Calibration of the CH micromechanical model with Karlsruhe sand

The experimental results of drained triaxial compression tests on Karlsruhe sand conducted by Kolymbas and Wu (1990) and also reported by Widuliński *et al*. (2009) were chosen to calibrate the CH micromechanical model. Karlsruhe sand consists mainly of sub-round quartz particles, with minimum void ratio of 0.53 and maximum void ratio of 0.84. According to the

grain size distribution presented by Kolymbas and Wu (1990), d_{50} is equal to 0.4 mm. As conducted by Tejchman *et al*. (2011) in calibrating the DEM parameters, the dense sand with an initial void ratio of 0.53 was adopted in this calibration. The hardening and softening as well as the dilatant behaviour of the Karlsruhe sand was well captured by the CH micromechanical model, as shown in Figure 6.11, with a total of 8 parameters listed in Table 6.1.

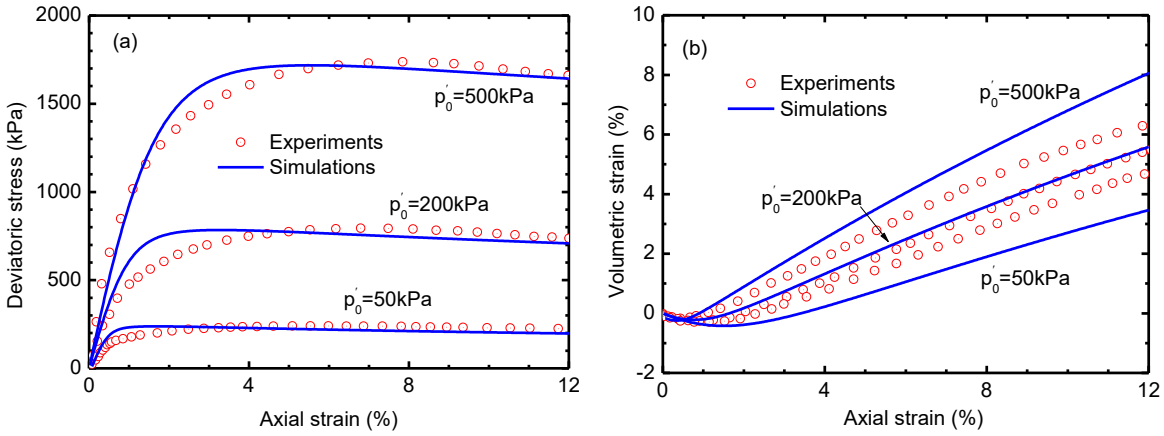

Figure 6.11 Calibration of the CH micromechanical model (data from Kolymbas and Wu, 1990)

Table 6.1 Parameters used in the CH micromechanical model for Karlsrule sand

Macro		Micro				
e_{ref}	λ	$k_{n0}^{c}(N/mm)$	$\phi_{\mu}^{c}(°)$	$d_{50}(mm)$	k_{rR}	k_{pR}
0.95	0.1	1000	33	0.40	0.5	0.5

6.4.2 Finite element model

The dimension of the finite element model is the same as the experimental set-up made by Niedostatkiewicz *et al*. (2010), which has been also used in the simulations of Tejchman *et al*. (2011) and Guo and Zhao (2016). As shown in Figure 6.12(a), the dimension of the simulated domain is 0.4m×0.2m×0.01m. The height of the wall is 0.17m and it was simulated by a set of surface elements, i.e. a virtual retaining wall with rough boundary, and hence there is no need to define the soil-wall interactions. The soil domain is discretised by a total of 800 eight-node

trilinear displacement elements with reduced integration elements, i.e. C3D8R. The boundary conditions are: the bottom is fixed in all directions; the top surface is free; the left side is fixed only in the x direction; the front and the back surfaces are fixed in the z direction and the right side is constrained in the x direction. Three kinds of loading modes of the virtual wall were conducted and for each loading, both active and passive modes were controlled, as shown in Figure 6.12(b).

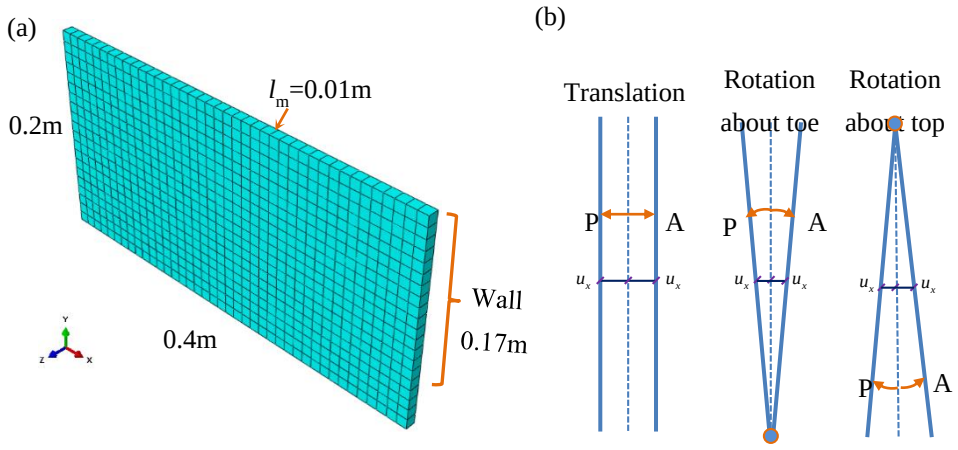

Figure 6.12 Simulation of the retaining wall: (a) the finite element model and (b) loading modes

6.4.3 Patterns of shear zones

1) Passive failure

The passive strain localisation behaviour of the soil was observed by moving the wall towards the soil. The displacement u and the accumulated deviatoric shear strain ε_q of the soil are presented in Figures 6.12, 6.13 and 6.14. For the case of a horizontal translation of the wall, as shown in Figure 6.13, two localised bands were observed at the end of the wall movement. In contrast, only one localisation band was developed from the top corner close to the wall after rotating the wall around the toe, whereas only one shear band was formed in the case of rotating the wall around the top. The shape of the contour agrees well with the ones of rough soil-wall boundaries obtained in experiments shown in Figure 6.10, in the finite element modelling with a micro-polar hypo-plastic model (Tejchman *et al.*, 2007) and coupling with DEM (Guo and Zhao, 2016) as well as through the DEM simulations (Tejchman *et al.*, 2011).

According to the Rankine's passive earth pressure theory (Rankine, 1857), the failure angle of the passive failure slip line with respect to the horizontal plane is given as 45°-φ'/2=28.5°. Interestingly, the failure angle given by this simulation is about 30°, as shown in Figure 6.13, which is very close to the value predicted by Rankine's theory.

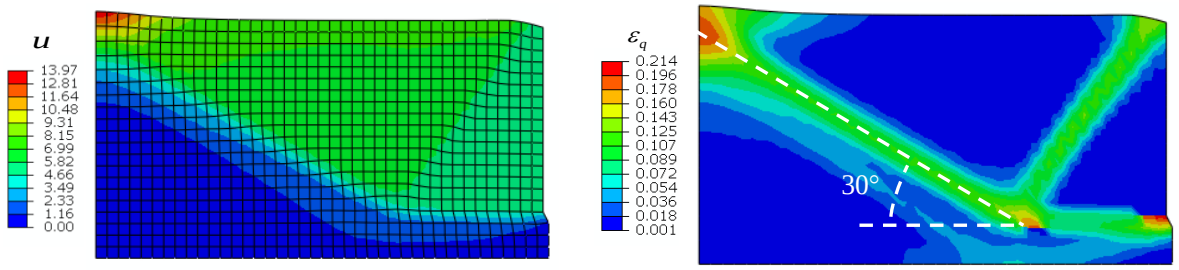

Figure 6.13 Transition, passive

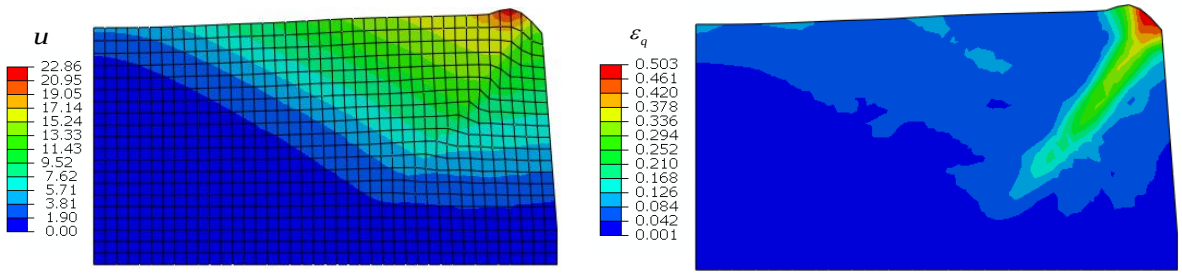

Figure 6.14 Rotation about bottom, passive

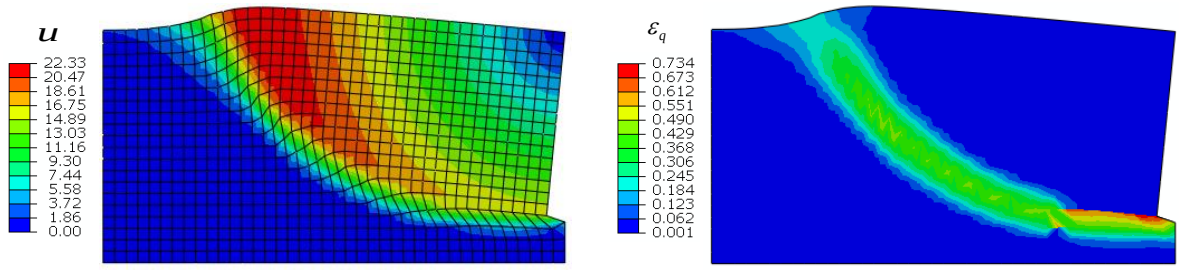

Figure 6.15 Rotation about top, passive

2) Active failure

Figures 6.15, 6.16 and 6.17 present the displacement u and the accumulated shear strain ε_q of the soil at the end of the displacement of the wall away from the soil. For the case of a horizontal translation of the wall, as shown in Figure 6.16, two localisation bands were also observed at the end of the wall movement. In comparison, on the one hand, large deformations in one area close to the wall were observed for the case of rotation around the

bottom, as shown in Figure 6.17. On the other hand, the large deformation area was developed at the bottom in the case of rotating the wall around the top, as shown in Figure 6.18. Again, the distribution of both displacement and accumulated shear strain is consistent with the ones of rough soil-wall boundaries obtained in the experiments displayed in Figure 6.10, and the finite element modelling with a micro-polar hypo-plastic model (Tejchman *et al*., 2007) and coupling with DEM (Guo and Zhao, 2016) as well as through the DEM simulations (Tejchman *et al*., 2011).

Based on the Rankine's active earth pressure theory (Rankine, 1857), the failure angle of the active failure slip line with respect to the horizontal plane is given as $45^\circ+\varphi'/2=61.5^\circ$. In comparison, as shown in Figure 6.16, the failure angle computed by this simulation is about 67°, which is close to the value predicted by Rankine's theory.

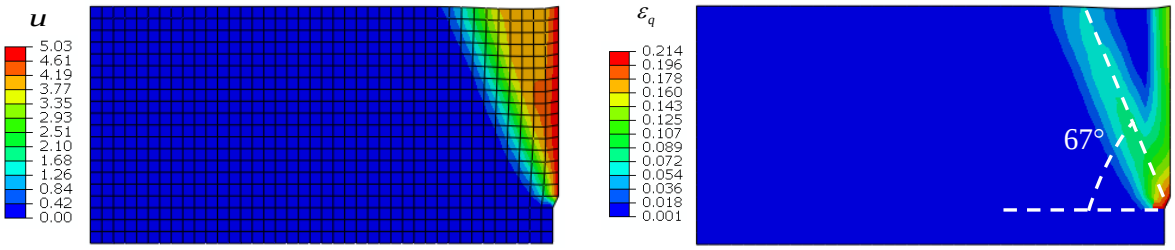

Figure 6.16 Transition, active

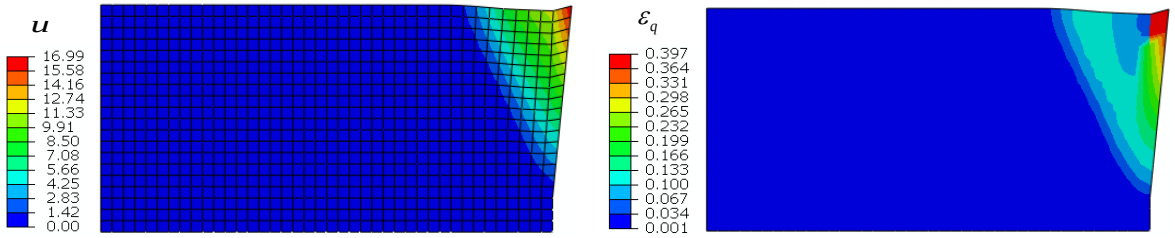

Figure 6.17 Rotation about bottom, active

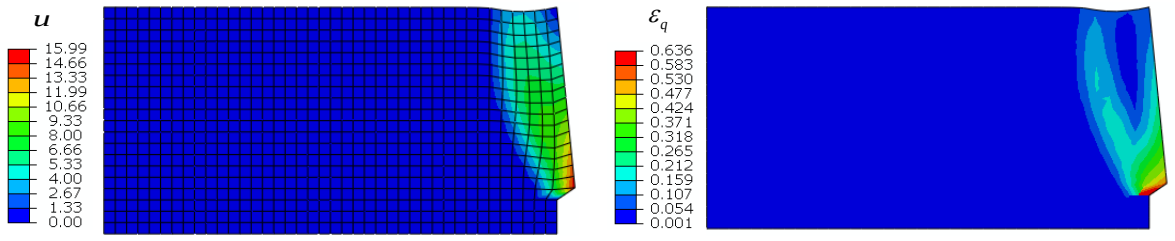

Figure 6.18 Rotation about top, active

6.5 Closed-ended pile driven in sand

Predicting the behaviour of piles driven in sand is important in major bridges, harbours and offshore engineering applications since it has significant effect on the practicality and construction costs. Axial capacity predictions are crucial to for example, tension leg, tripod or jacket offshore structures (Overy, 2007; Merritt *et al*., 2012; Jardine, 2013). Current design methods of axially driven piles include empirical equations based on field data and methods based on CPT experiments. The 'Main Text' method (API, 2014) dominates the former type of methods, whereas the widely used CPT based methods include the design methods of ICP-05 (Imperial College London, Jardine *et al*., 2005), UWA-05 (University of Western Australia, Lehane *et al*., 2005), NGI-05 (Norwegian Geotechnical Institute, Clausen *et al*., 2005) and Fugro-05 (Kolk *et al*., 2005). Although these methods have demonstrated their capabilities in predicting the capacity of piles, there were, and still are, limitations in these methods particularly for the 'Main Text' method as indicated through the rigorous field test database presented by Yang *et al*. (2015a, 2015b). In addition, these methods roughly consider the stress distribution such as the h/R effect during pile installations, which has been experimentally found to be important for the pile capacity (Jardine *et al*., 2013a, 2013b). In order to improve the design method, the numerical simulation method is a suitable candidate by which the stress field during and after pile installation can be obtained. To this end, numerical simulations were conducted by using different constitutive models and computational techniques that have the potential to solve mesh distortion which may cause convergence problems. One type of these simulations is conducted by combining the finite element method with the Arbitrary Lagrangian Eulerian (ALE), such as in the work of Zhang *et al*. (2013, 2014) and Wang *et al*. (2015). Since the ALE method still possesses some limitations inherently presented in the initial meshes, the Coupled Eulerian-Lagrangian (CEL) approach has been alternatively utilized by Henke *et al*. (2010), Qiu *et al*. (2011), Wang *et al*. (2015) and Ko *et al*. (2016), *etc*.

Besides these numerical methods, another important aspect is the adopted constitutive model. It is well known that the soil around the pile exhibits distinct strain localisation under

shearing. However, the models used in the aforementioned analyses cannot well describe the behaviour of sand. For instance, the Modified Cam-Clay (MCC) model which is a typical model for clay was used for sand by Sheng *et al*. (2005) and it failed to capture the non-associated dilatancy behaviour of sand; a linear elastic breakage model was used for sand by Zhang *et al*. (2013) in order to investigate the effect of particle breakage on pile capacity during pile driving; the Mohr-Coulomb model which could not describe the softening behaviour of soils was adopted by Ko *et al*. (2016), etc. It is, therefore, of interest to use the CH micromechanical model that has the ability to capture accurately the soil behaviour combined with the finite element method to investigate the capacity of a closed-ended pile.

In this study, the CEL method that has the advantages of both Lagrangian and Eulerian methods was adopted. The Eulerian domain can be used to describe the material with large deformations, whereas the Lagrangian domain is suitable for the material with small deformations, as demonstrated in Figure 6.19. Accordingly, the pile is simulated by Lagrangian meshes whereas the soil is partitioned by Eulerian meshes.

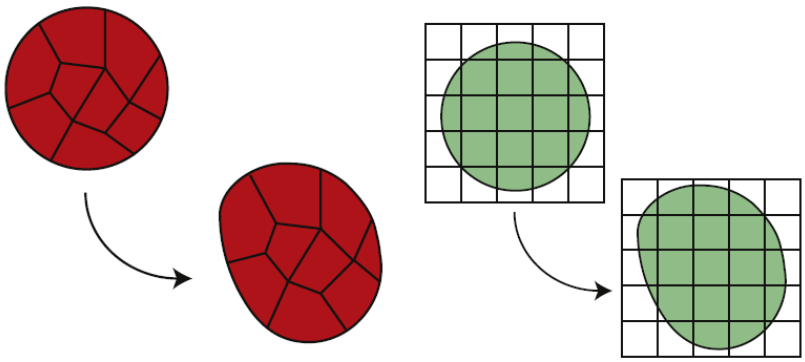

Figure 6.19 Deformation of a continuum in a Lagrangian (left) and a Eulerian analysis (right) (figure from Qiu *et al*., 2011)

6.5.1 Model calibration for Dog's bay sand

To simulate the capacity of a closed-ended pile driven in Dog's bay sand (Klotz and Coop, 2001; Kuwajima *et al*., 2009), the CH micromechanical model was calibrated from laboratory tests on Dog's bay sand. According to Kuwajima *et al*. (2009), Dog's bay sand is a carbonate sand from the west coast of Eire. Its specific gravity is 2.72, and its maximum and minimum

void ratios are 2.451 and 1.621 respectively. One can see that its d_{50} is 0.22mm from the particle size distribution curve shown in Figure 6.20.

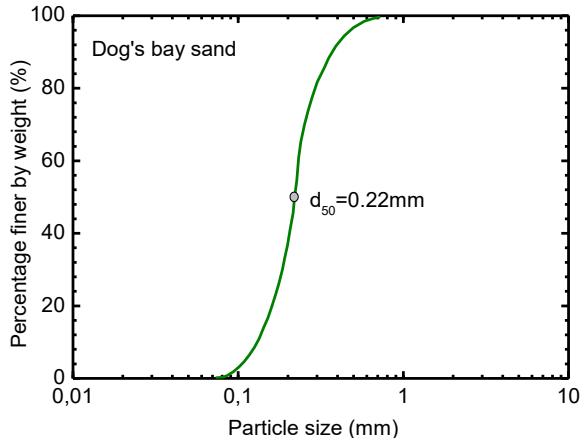

Figure 6.20 Particle size distribution of Dog's bay sand (data from Kuwajima *et al*., 2009)

The critical state lines were obtained by Coop (1990) through constant mean effective stress tests, as shown in Figure 6.21. The critical state curve in the $e-\log p'$ plane is given by the following expression

$$e_c = e_{ref} \exp\left(-\lambda\left(\frac{p'}{p_{ref}}\right)^{\xi}\right) \tag{6.4}$$

where the parameters can be calibrated as e_{ref} =3.35, λ=0.31, ξ=0.29 with p_{ref} =10 kPa. Through Eq.(6.4), the grain breakage mechanism can be considered implicitly introduced by simulating the curvilinear critical state line with pressure higher than 3000 kPa. The critical state line in the p'-q plane has a slope M =1.60, which corresponds to a friction angle of 39°.

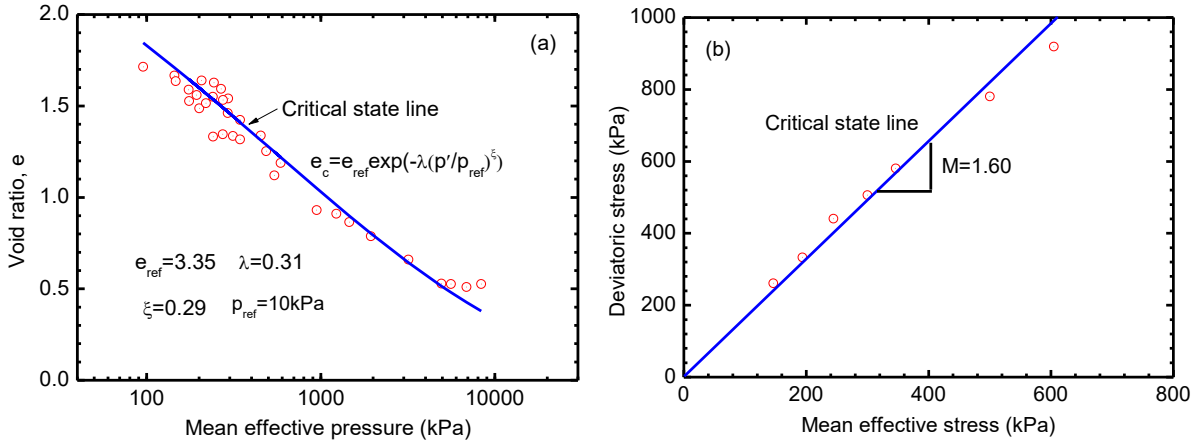

Figure 6.21 Critical state lines of Dog's bay sand: (a) $e-\log p'$ plane; (b) $p'-q$ plane

(experimental data from Coop, 1990)

Given that the radius of the particles r is half of the diameter d_{50}=0.22 mm, the parameters at the inter-particle contact k_{n0}^{c}, k_{rR} and k_{pR} were calibrated from drained triaxial compression tests performed by Kuwajima *et al*. (2009) on dense Dog's bay sand with a relative density of 90%. As shown in Figure 6.22, the CH model demonstrated good performance in simulating the behaviour of Dog's bay sand at various confining pressures. A total of 8 parameters were required in the CH micromechanical model for Dog's bay sand, as summarized in Table 6.2.

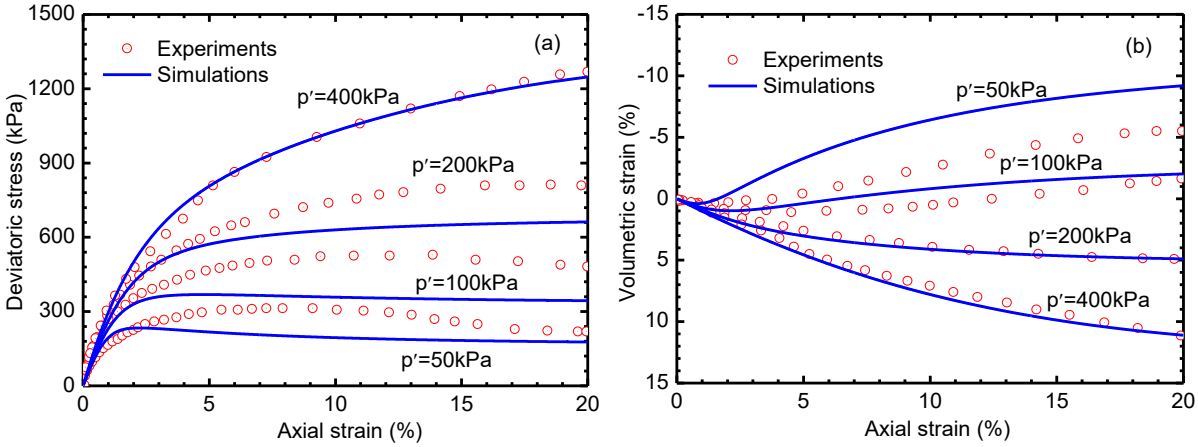

Figure 6.22 Simulations of drained triaxial compression tests on Dog's bay sand: (a) deviatoric stress vs axial strain (b) volumetric strain vs axial strain (experimental data from Kuwajima *et al*., 2009)

Table 6.2 Parameters used in the CH model for Dog's bay sand

Macro		Micro				
e_{ref}	λ	$k_{n0}^{c}(N/mm)$	$\phi_{\mu}^{c}(°)$	$d_{50}(mm)$	k_{rR}	k_{pR}
3.35	0.31	3000	39	0.22	0.6	0.4

6.5.2 Finite element analysis

To simulate the centrifuge tests of 100g on medium-dense Dog's bay sand, only a quarter of the experimental set-up was calculated due to the symmetry of the problem. The radius of the soil domain was 15m and its height 49m, as show in Figure 6.23. The bottom of the FE model was fixed in all directions, and the lateral boundaries were constrained in horizontal

directions. The soil was represented by 62000 Eulerian EC3D8R elements, whereas 7448 Lagrangian C3D8R elements were used for the 37m length pile. The soil behaviour was represented by the CH micromechanical model, whereas the pile was considered as a rigid body. The soil-pile interaction was defined by a Coulomb friction law, in which the effective friction angle was taken as 33º according to the ring shear test conducted by Klotz and Coop (2001). The soil firstly underwent a vertical gravity without any vertical settlement and then the pile was axially driven at a vertical velocity of 0.02m/s as in the experiments. As indicated by Klotz and Coop (2001), this loading rate is small enough to guarantee that the installation can be viewed as a quasi-static process.

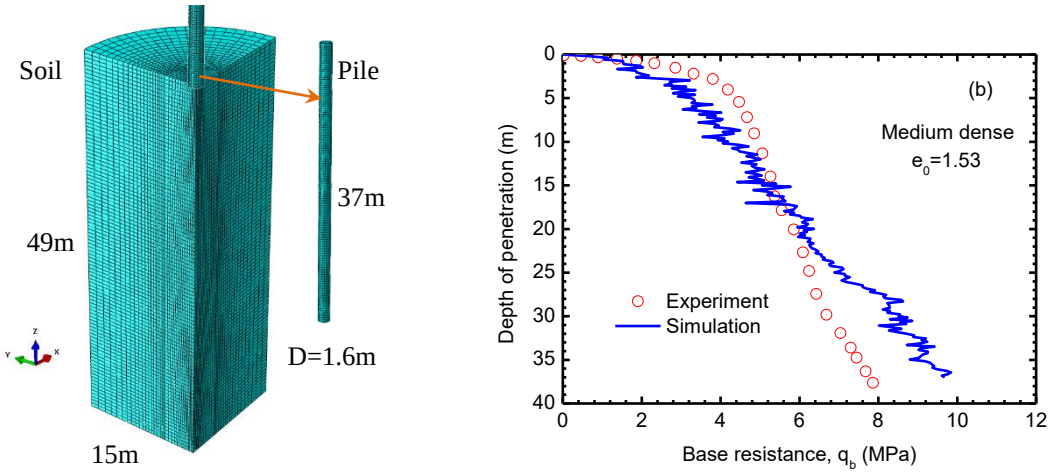

Figure 6.23 Closed-ended pile driven in sand (a) finite element model and (b) base resistance

With the penetration of the pile, the soil elements that are adjacent to the pile display large deformations, as shown in Figure 6.24 (a) and (c). It can be found that significant shear stresses developed around the pile tip while the shaft stresses are much smaller, as shown in Figure 6.24(d), which is consistent with the experimental observations by jacking a CPT probe into pressurised, air-pluviated Fontainebleau NE34 sand in the well instrumented INPG calibration chamber (Jardine *et al*., 2013). High stresses around the pile tip as shown in Figure 6.24(b) may induce soil particle breakage and hence reduce the capacity of pile (Klotz and Coop, 2001; Yang *et al*., 2011; Zhang *et al*., 2013, 2014).

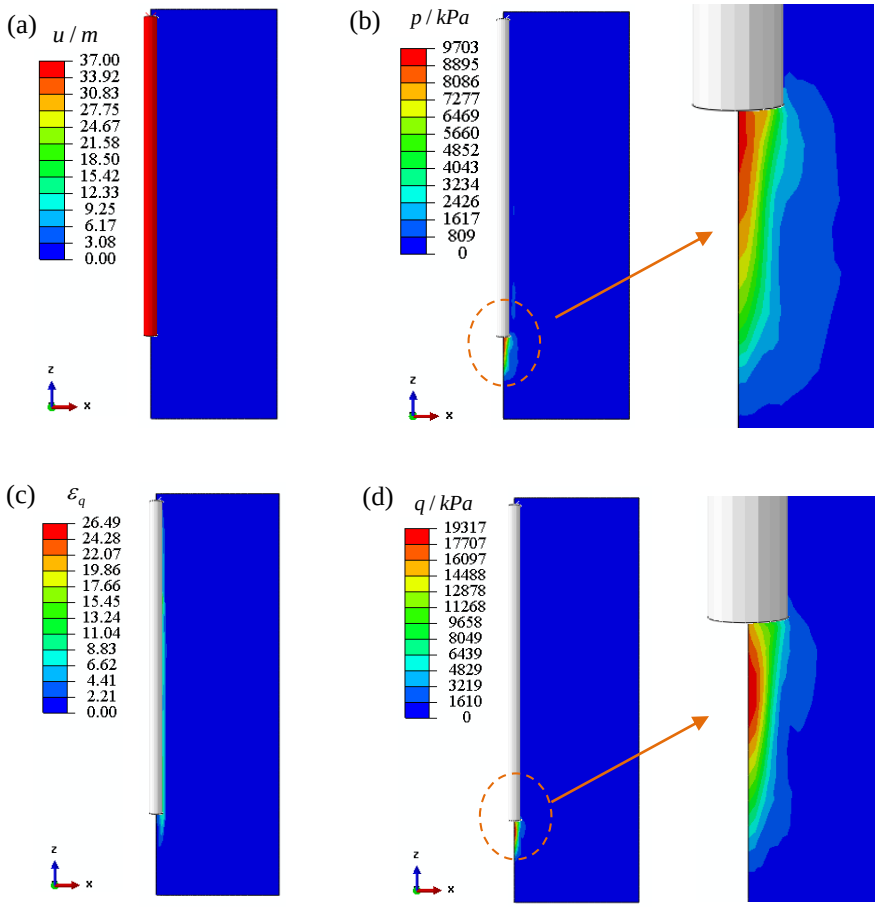

Figure 6.24 Finial state of the closed-ended pile: (a) total displacement (b) mean effective stress (c) deviatoric shear strain (d) deviatoric stress

The base resistance calculated by this simulation was compared with the centrifuge test results conducted by Klotz and Coop (2001). As shown in Figure 6.23(b), the overall good agreement between the numerical results and the experimental data demonstrates that the CH micromechanical model can be used to compute the capacity of piles. With the increase of the penetration depth, the simulated base resistance shows a relatively slow softening behaviour compared with the experiments. This is largely due to the fact that the CH model does not consider the effect of particle breakage. It seems that using the critical state line of Eq.(6.4) calibrated at low stress level (less than 1 MPa) and applying it to high stress levels (more than 5 MPa) is not sufficient.

6.6 Concluding remarks

This chapter presented the modelling capability of the described multiscale approach, conducted by implementing the CH micromechanical model into an explicit finite element code Abaqus/Explicit, in solving classical geotechnical problems with small and large deformations. At first, the validity of this approach was verified through a single-element test, a biaxial test and the settlement of a square footing. Then, the small deformation problem, consisting in the excavation of a tunnel, was analysed. The ground settlement caused by the excavation agrees well with the analytical solution suggested by Peck (1969). Two large deformation problems were investigated in which significant strain localisations were observed. The retaining walls were moved with or without rotations, which corresponds to active and passive loading modes. The distributions of the localised shear bands were consistent with the results obtained in experiments, in DEM simulations and in finite element simulations using a micro-polar hypo-plastic constitutive model. Finally, an axially loaded closed-ended pile was analysed and the capacity of the pile was computed, which was in good agreement with the centrifuge experimental results. All these investigations demonstrate that the FEM×CH multiscale approach can be applied to geotechnical engineering designs.

CONCLUSIONS AND PERSPECTIVES

1. Conclusions

This thesis presents an application of the thermodynamic principles for constructing micromechanical models for dry and unsaturated granular soils, and the implementation of these models in the finite element codes to fulfil multiscale modelling of geotechnical problems. The main contributions of this thesis can be summarised as follows.

1) Thermodynamics with internal variables has been extended to construct micromechanical models by considering the energy stored and dissipated at the inter-particle contacts. In the suggested framework, the Helmholtz free energy and the dissipation energy at the macro scale are equated to the volumetric average of the Helmholtz free energy and the dissipation energy at the micro scale. Consequently, the elasto-plastic formulation at inter-particle contacts can be obtained from the expressions of the micro free energy and the micro dissipation potentials. A thermodynamically consistent micromechanical model has been constructed on the basis of the static hypothesis. An isotropic compression and several triaxial tests were simulated with the model to analyse the energy conservation and dissipation under loading. Free energy and dissipation energy were computed at both micro and macro scales, and the orientations of the failure planes were explained by the evolution of the local dissipation energy. The maximum micro dissipation energy agreed with the static hypothesis for which, when one direction reaches the limit state, the rupture at the macro scale is obtained.

2) A micromechanical model for unsaturated granular soils based on thermodynamic principles has been constructed. The energy quantities defined at the micro and macro scales were firstly analysed, and then the Helmholtz free energy at the microscale was defined as the sum of a mechanical part and a hydraulic part. The free energy is dependent on the elastic strains and on the degree of saturation at the macro scale, and it is related to the elastic displacements and the degree of saturation at the micro scale. The dissipation energy is of frictional origin and is a function of the plastic displacements at the micro

scale and of the plastic strains at the macro scale. For the mechanical part, the CH model has been modified and its satisfaction of thermodynamic principles has been verified. A particle-size dependency function has been suggested to consider the water retention in the hydraulic free energy potential at the micro scale.

3) An implicit method for integrating the micromechanical models based on a static hypothesis has been presented. A predictor-corrector method was proposed to solve linearized constraint equations under mixed controls. An iterative scheme was constructed to implement the stress-driven micro-macro relations. Two return mapping algorithms, i.e., the closest point projection method (CPPM) and the cutting plane algorithm (CPA) with the backward Euler method, were alternatively adopted to implement the local law at the micro level. The model was then implemented into a finite element code in order to perform multiscale analyses of boundary value problems. It was found that the predictor-corrector method is efficient for solving linearized mixed control constraint equations. The effectiveness of this method has been validated by simulating drained triaxial compression tests, in which the boundary conditions consisted in imposing the vertical strain and the lateral stresses. The static hypothesis was implemented consistently with the stress homogenisation formula by an out-of-balance iteration scheme, which rendered consistent the localisation and averaging operators. The local force-displacement relations were integrated by CPPM and CPA, respectively. Consistent results were obtained by using the two integration schemes with small strain or stress increments. In comparison to CPA, CPPM provided a better computational cost efficiency without any loss of accuracy, either for elementary tests or boundary value problems. The CH model was implemented into a finite element code and firstly validated by elementary tests. Then, two typical boundary value problems, i.e., a biaxial test and a square footing, were simulated, and the applicability of this method for multiscale analyses was demonstrated.

4) The influence of microstructural instabilities on the global failure of granular materials has been investigated by using the second-order work as an instability criterion. Adopting the vanishing of the second-order work as a quantity to detect the effective failure of a

granular material is a more rigorous approach than the one considering the traditional factor of safety based on the material plastic limit. To investigate the extent of inter-particle contact instabilities on the influence of the macroscale material instability, the second-order work at different scales was defined. The relation between the second-order work at the micro and macro scales was derived in connection with the CH model, and extended to the scale of boundary value problems via the finite element method. The effects of volumetric and geometrical changes on the second-order work calculated by the CH model were investigated. The results showed that there was no significant influence in the investigated problems, which validated the rationality of adopting the Cauchy stress and the Euler strain to calculate the second-order work. Drained and undrained triaxial tests were simulated to validate the consistency of the second-order work computed at micro and macro levels and the particulate origin of the specimen instability was well captured, demonstrating the validity of this method to predict localised and diffuse failures of a granular material. The extent of the global material failure originating from microstructural instabilities was analysed. The second-order work for boundary value problems was integrated into the case of drained and undrained biaxial tests, by which localised failure in dense specimen and diffuse failure in loose specimen were obtained and analysed. It was shown that the suggested method is adapted to predict the instability of a granular assembly subjected to homogeneous and inhomogeneous loading conditions.

5) The modelling capability of the described multiscale approach conducted by implementing the CH micromechanical model into an explicit finite element code Abaqus/Explicit was demonstrated by solving several classical geotechnical problems at small and large deformations. First, the validity of this approach was verified through a single-element test, a biaxial test and the settlements of a square footing. The obtained results are consistent with the benchmark results obtained by using the implicit integration point program and the implicit finite element code Abaqus/Standard. Then, a small-deformation problem, the excavation of a tunnel, was analysed. The ground settlement of the tunnel caused by excavation agrees well with the analytical solution of Peck (1969). In

addition, two large-deformation problems were investigated in which significant strain localisation were observed. Retaining walls were moved transitionally with or without rotations, corresponding to active and passive loading modes. The distributions of localisation bands were consistent with the results obtained in experiments, in DEM simulations and in finite element simulations using a micro-polar hypo-plastic constitutive model. Finally, an axially loaded closed-ended pile was analysed and the capacity of the pile was computed, which was in good agreement with the results of centrifuge experimental tests. These investigations demonstrate that the FEM×CH micromechanical model multiscale approach is efficient in solving geotechnical problems.

2. Perspectives

Although some efforts have been made on multiscale modelling of granular soils in this thesis, more studies should be done to further develop this multiscale approach. More specifically, on one hand the developed micromechanical models should be improved to simulate the behaviour of granular soils under more complex loading conditions. On the other hand, the developed models should be applied to solve more complicated boundary value problems in order to demonstrate their effectiveness and efficiency. The potential directions for further developments are suggested below.

1) Throughout this thesis, the adopted density function is equal to $1/4\pi$, which corresponds to an isotropic fabric of the granular soils. Since the internal structure has significant effect on non-coaxial deformation of granular soils, the evolution of the fabric tensor should be introduced to capture the phenomenon. With this feature, responses of granular soils under principal stress rotation could be naturally described. In addition, this thesis investigated only the behaviour of granular soils under quasi-static monotonic loadings. However, in engineering practice, it is more usual to encounter cyclic and dynamic loadings. Therefore, the described micromechanical approach should be developed to reproduce the behaviour of granular soils under cyclic and dynamic loadings.

2) Since the Euler strain tensor and the Cauchy stress tensor have been used in the micromechanical approach, the results obtained in finite element analysis with this method are dependent on the employed mesh size. To solve this problem, the models should be extended to high-gradient models accounting for the internal length of the granular soils.

3) Natural soils have inherent anisotropy under the gravity field. The inherent anisotropy will evolve under shearing and this will influence the deformations of geotechnical structures constructed on soils. By using the micromechanical approach with fabric evolution, the deformations could be well predicted, which will improve the accurateness of the factor of safety that has been widely adopted in engineering designs.

4) The high-gradient micromechanical models could be very useful to accurately capture the behaviour of granular soils after the bifurcation point. Hence studies are suggested to focus on the application of these models to calculate large deformation problems where strain localisation often occurs.

APPENDIX A: PARTIAL DERIVATIVES IN THE IMPLEMENTATION OF CPPM AND CPA

A.1 First-order derivatives

The first-order derivatives of the yield criterion **a** and the first order derivatives of the potential function **b** defined at inter-particle contacts can be written as

$$\mathbf{a} = \frac{\partial F}{\partial f_i^c} = \left\{ \frac{\partial F}{\partial f_n^c} \quad \frac{\partial F}{\partial f_s^c} \quad \frac{\partial F}{\partial f_t^c} \right\} \tag{A1}$$

$$\mathbf{b} = \frac{\partial G}{\partial f_i^c} = \left\{ \frac{\partial G}{\partial f_n^c} \quad \frac{\partial G}{\partial f_s^c} \quad \frac{\partial G}{\partial f_t^c} \right\} \tag{A2}$$

in which the partial derivations of the yield criterion can be expressed as

$$\begin{cases} \dfrac{\partial F}{\partial f_n^c} = -\dfrac{k_p^c \tan\phi_p^c \delta_r^{cp}}{f_n^c \tan\phi_p^c + k_p^c \delta_r^{cp}} - f_n^c \left(\dfrac{-k_p^c (\tan\phi_p^c)^2 \delta_r^{cp}}{(f_n^c \tan\phi_p^c + k_p^c \delta_r^{cp})^2} \right) = -\dfrac{\kappa^2}{\tan\phi_p^c} \\ \dfrac{\partial F}{\partial f_s^c} = \dfrac{f_s^c}{\sqrt{\left(f_s^c\right)^2 + \left(f_t^c\right)^2}}, \quad \dfrac{\partial F}{\partial f_t^c} = \dfrac{f_t^c}{\sqrt{\left(f_s^c\right)^2 + \left(f_t^c\right)^2}} \end{cases} \tag{A3}$$

As a non-associated flow rule has been adopted for the normal direction, whereas an associated flow rule has been chosen for the tangential direction, the first order derivatives of the potential function can be obtained by

$$\frac{\partial G}{\partial f_n^c} = D\,, \quad \frac{\partial G}{\partial f_s^c} = \frac{\partial F}{\partial f_s^c}\,, \quad \frac{\partial G}{\partial f_t^c} = \frac{\partial F}{\partial f_t^c} \tag{A4}$$

where D is the dilatancy coefficient defined in Eq.(1.40).

A.2 Second-order derivatives

The second-order derivatives of the potential function can be written as

$$\frac{\partial \mathbf{b}}{\partial \mathbf{f}^c} = \begin{bmatrix} \dfrac{\partial^2 G}{\partial f_n^c \partial f_n^c} & \dfrac{\partial^2 G}{\partial f_n^c \partial f_s^c} & \dfrac{\partial^2 G}{\partial f_n^c \partial f_t^c} \\ \dfrac{\partial^2 G}{\partial f_s^c \partial f_n^c} & \dfrac{\partial^2 G}{\partial f_s^c \partial f_s^c} & \dfrac{\partial^2 G}{\partial f_s^c \partial f_t^c} \\ \dfrac{\partial^2 G}{\partial f_t^c \partial f_n^c} & \dfrac{\partial^2 G}{\partial f_t^c \partial f_s^c} & \dfrac{\partial^2 G}{\partial f_t^c \partial f_t^c} \end{bmatrix} \tag{A5}$$

in which the components of the matrix defined in Eq.(A5) can be derived from Eq.(A2),

$$\frac{\partial^2 G}{\partial f_n^c \partial f_n^c} = \frac{\sqrt{\left(f_s^c\right)^2 + \left(f_t^c\right)^2}}{f_n^c},\ \frac{\partial^2 G}{\partial f_n^c \partial f_s^c} = -\frac{1}{f_n^c}\frac{f_s^c}{\sqrt{\left(f_s^c\right)^2 + \left(f_t^c\right)^2}},\ \frac{\partial^2 G}{\partial f_n^c \partial f_t^c} = -\frac{1}{f_n^c}\frac{f_t^c}{\sqrt{\left(f_s^c\right)^2 + \left(f_t^c\right)^2}} \quad \text{(A6)}$$

$$\frac{\partial^2 G}{\partial f_s^c \partial f_n^c} = 0,\ \frac{\partial^2 G}{\partial f_s^c \partial f_s^c} = \frac{\left(f_t^c\right)^2}{\left(\left(f_s^c\right)^2 + \left(f_t^c\right)^2\right)^{\frac{3}{2}}},\ \frac{\partial^2 G}{\partial f_s^c \partial f_t^c} = \frac{-f_s^c f_t^c}{\left(\left(f_s^c\right)^2 + \left(f_t^c\right)^2\right)^{\frac{3}{2}}} \quad \text{(A7)}$$

$$\frac{\partial^2 G}{\partial f_t^c \partial f_n^c} = 0,\ \frac{\partial^2 G}{\partial f_t^c \partial f_s^c} = \frac{-f_s^c f_t^c}{\left(\left(f_s^c\right)^2 + \left(f_t^c\right)^2\right)^{\frac{3}{2}}},\ \frac{\partial^2 G}{\partial f_t^c \partial f_t^c} = \frac{\left(f_s^c\right)^2}{\left(\left(f_s^c\right)^2 + \left(f_t^c\right)^2\right)^{\frac{3}{2}}} \quad \text{(A8)}$$

APPENDIX B: CALCULATION OF THE PLASTIC MULTIPLIER BY CPA

The plastic multiplier used in CPA, as shown in Eq. (4.16) and Table 4.5, can be rewritten as

$$\Delta\lambda^c = \frac{\dfrac{\partial F}{\partial f_i^c} k_{ij}^c d\delta_j^c}{\dfrac{\partial F}{\partial f_i^c} k_{ij}^c \dfrac{\partial G}{\partial f_i^c} - \dfrac{\partial F}{\partial \kappa}\dfrac{\partial \kappa}{\partial \delta_i^{cp}}\dfrac{\partial G}{\partial f_i^c}} = \frac{\dfrac{\partial F}{\partial f_i^c} k_{ij}^c d\delta_j^c}{\dfrac{\partial F}{\partial f_i^c} k_{ij}^c \dfrac{\partial G}{\partial f_i^c} - \dfrac{\partial F}{\partial \kappa}\dfrac{\partial \kappa}{\partial \delta_r^{cp}}\dfrac{\partial \delta_r^{cp}}{\partial \delta_i^{p}}\dfrac{\partial G}{\partial f_i^c}} \tag{B1}$$

in which k_{ij}^c is the elastic matrix defined by Eq.(1.33), and the derivatives of the tangential plastic displacements can be derived from Eq.(1.36)

$$\frac{\partial \delta_r^{cp}}{\partial \delta_s^{cp}} = \frac{\delta_s^{cp}}{\sqrt{(\delta_s^{cp})^2 + (\delta_t^{cp})^2}}, \quad \frac{\partial \delta_r^{cp}}{\partial \delta_t^{cp}} = \frac{\delta_t^{cp}}{\sqrt{(\delta_s^{cp})^2 + (\delta_t^{cp})^2}} \tag{B2}$$

Eq.(B2) will cause numerical difficulties at the beginning of the shearing loading, since the dominator is equal to zero. To circumvent this problem, we can rewrite the plastic multiplier as

$$\Delta\lambda^c = \frac{\dfrac{\partial F}{\partial f_i^c} k_{ij}^c d\delta_j^c}{\dfrac{\partial F}{\partial f_i^c} k_{ij}^c \dfrac{\partial G}{\partial f_i^c} - \dfrac{\partial F}{\partial \kappa}\dfrac{\partial \kappa}{\partial \delta_i^{cp}}\dfrac{\partial G}{\partial f_i^c}} = \frac{\dfrac{\partial F}{\partial f_i^c} k_{ij}^c d\delta_j^c}{\dfrac{\partial F}{\partial f_i^c} k_{ij}^c \dfrac{\partial G}{\partial f_i^c} - \dfrac{\partial F}{\partial \delta_r^{cp}}\dfrac{\partial G}{\partial f_r^c}} \tag{B3}$$

where the following expression can be demonstrated:

$$\frac{\partial F}{\partial \kappa}\frac{\partial \kappa}{\partial \delta_i^{cp}}\frac{\partial G}{\partial f_i^c} = \frac{\partial F}{\partial \delta_r^{cp}}\frac{\partial G}{\partial f_r^c} \tag{B4}$$

Eq.(B4) can be expressed equivalently by

$$\frac{\partial F}{\partial \delta_i^{cp}}\frac{\partial G}{\partial f_i^c} = \frac{\partial F}{\partial \delta_r^{cp}}\frac{\partial G}{\partial f_r^c} \tag{B5}$$

By considering

$$\frac{\partial F}{\partial \delta_i^{cp}} = \frac{\partial F}{\partial \delta_r^{cp}}\frac{\partial \delta_r^{cp}}{\partial \delta_i^{cp}}, \quad \frac{\partial G}{\partial f_i^c} = \frac{\partial G}{\partial f_r^c}\frac{\partial f_r^c}{\partial f_i^c} \tag{B6}$$

the left-hand side of Eq.(B5) can be expressed as

$$\frac{\partial F}{\partial \delta_i^{cp}}\frac{\partial G}{\partial f_i^c}=\frac{\partial F}{\partial \delta_r^{cp}}\frac{\partial G}{\partial f_r^c}\left(\frac{\partial \delta_r^{cp}}{\partial \delta_i^{cp}}\frac{\partial f_r^c}{\partial f_i^c}\right) \tag{B7}$$

In Eq.(B7), the following equality can be proved

$$\frac{\partial \delta_r^{cp}}{\partial \delta_i^{cp}}\frac{\partial f_r^c}{\partial f_i^c}=1 \tag{B8}$$

since

$$\begin{cases}\dfrac{\partial \delta_r^{cp}}{\partial \delta_i^{cp}}=\left\{0,\dfrac{\delta_s^{cp}}{\sqrt{(\delta_s^{cp})^2+(\delta_t^{cp})^2}},\dfrac{\delta_t^{cp}}{\sqrt{(\delta_s^{cp})^2+(\delta_t^{cp})^2}}\right\}\\ \dfrac{\partial f_r^c}{\partial f_i^c}=\left\{0,\dfrac{f_s^c}{\sqrt{(f_s^c)^2+(f_t^c)^2}},\dfrac{f_t^c}{\sqrt{(f_s^c)^2+(f_t^c)^2}}\right\}\end{cases} \tag{B9}$$

Accordingly, Eq.(B8) can be rewritten as

$$\frac{\partial \delta_r^{cp}}{\partial \delta_i^{cp}}\frac{\partial f_r^c}{\partial f_i^c}=\frac{f_s^c\delta_s^{cp}+f_t^c\delta_t^{cp}}{\sqrt{(f_s^c)^2+(f_t^c)^2}\sqrt{(\delta_s^{cp})^2+(\delta_t^{cp})^2}}=\frac{W_r^p}{W_r^p}=1 \tag{B10}$$

in which W_r^p is the plastic work in the tangential direction. Therefore, Eq.(B4) can be established, which is useful for calculating the evolution of the plastic displacements. On the right-hand side of Eq.(B3), the partial derivatives can be expressed as

$$\frac{\partial F}{\partial \delta_r^{cp}}=-\frac{\left(f_n^c\right)^2 k_p^c\left(\tan\phi_p^c\right)^2}{\left(f_n^c\tan\phi_p^c+k_p^c\delta_r^{cp}\right)^2} \tag{B11}$$

$$\frac{\partial G}{\partial f_r^c}=\sqrt{\left(\frac{\partial G}{\partial f_s^c}\right)^2+\left(\frac{\partial G}{\partial f_t^c}\right)^2}=1 \tag{B12}$$

By inserting Eqs.(B11) and (B12) into Eq.(B3), the hardening part can be calculated as

$$\frac{\partial F}{\partial \kappa}\frac{\partial \kappa}{\partial \delta_i^{cp}}\frac{\partial G}{\partial f_i^c}=-\frac{\left(f_n^c\right)^2 k_p^c\left(\tan\phi_p^c\right)^2}{\left(f_n^c\tan\phi_p^c+k_p^c\delta_r^{cp}\right)^2} \tag{B13}$$

REFERENCES

Alawaji, H., Runesson, K., Sture, S., & Axelsson, K. (1992). Implicit integration in soil plasticity under mixed control for drained and undrained response. *International Journal for Numerical and Analytical Methods in Geomechanics*, *16*(10), 737-756.

Alonso, E. E., Gens, A., & Josa, A. (1990). A constitutive model for partially saturated soils. *Géotechnique*, *40*(3), 405-430.

Alonso, E. E., Pereira, J. M., Vaunat, J., & Olivella, S. (2010). A microstructurally based effective stress for unsaturated soils. *Géotechnique*, *60*(12), 913-925.

American Petroleum Institute (API). (2014). ANSI/API recommended practice 2GEO, 1st Ed., RP2GEO, Washington, DC.

Ando, E., Hall, S. A., Viggiani, G., Desrues, J., & Bésuelle, P. (2012). Grain-scale experimental investigation of localised deformation in sand: a discrete particle tracking approach. *Acta Geotechnica*, *7*(1), 1-13.

Andrade, J. E., & Borja, R. I. (2006). Capturing strain localization in dense sands with random density. *International Journal for Numerical Methods in Engineering*, *67*(11), 1531-1564.

Andrade, J. E., Baker, J. W., & Ellison, K. C. (2008). Random porosity fields and their influence on the stability of granular media. *International Journal for Numerical and Analytical Methods in Geomechanics*, *32*(10), 1147-1172.

Ardeljan, M., Knezevic, M., Nizolek, T., Beyerlein, I. J., Mara, N. A., & Pollock, T. M. (2015). A study of microstructure-driven strain localizations in two-phase polycrystalline HCP/BCC composites using a multi-scale model. *International Journal of Plasticity*, *74*(11), 35-57.

Bagi, K. (1993). On the definition of stress and strain in granular assemblies through the relation between micro-and macro-level characteristics. *Powders & Grains*, *93*, 117-121.

Bagi, K. (1996). Stress and strain in granular assemblies. *Mechanics of Materials*, *22*(3), 165-177.

Bagi, K. (2006). Analysis of microstructural strain tensors for granular assemblies. *International Journal of Solids and Structures*, *43*(10), 3166-3184.

Bardet, J. P., & Choucair, W. (1991). A linearized integration technique for incremental constitutive equations. *International Journal for Numerical and Analytical Methods in Geomechanics*, *15*(1), 1-19.

Barreto, D., & O'Sullivan, C. (2012). The influence of inter-particle friction and the intermediate stress ratio on soil response under generalised stress conditions. *Granular Matter*, *14*(4), 1-17.

Bažant, P., & Oh, B. H. (1986). Efficient numerical integration on the surface of a sphere. *ZAMM-Journal of Applied Mathematics and Mechanics/Zeitschrift für Angewandte Mathematik und Mechanik*, *66*(1), 37-49.

Been, K., & Jefferies, M. G. (1985). A state parameter for sands. *Géotechnique*, *35*(2), 99-112.

Belheine, N., Plassiard, J. P., Donzé, F. V., Darve, F., & Seridi, A. (2009). Numerical simulation of drained triaxial test using 3D discrete element modeling. *Computers and Geotechnics*, *36*(1), 320-331.

Biarez, J., & Hicher, P. Y. (1994). Elementary mechanics of soil behaviour: saturated remoulded soils. *AA Balkema*.

Bishop, A. W., & Blight, G. E. (1963). Some aspects of effective stress in saturated and partly saturated soils. *Géotechnique*, *13*(3), 177-197.

Borja, R. I. (2006). On the mechanical energy and effective stress in saturated and unsaturated porous continua. *International Journal of Solids and Structures*, *43*(6), 1764-1786.

Borja, R. I., & Lee, S. R. (1990). Cam-clay plasticity, part 1: implicit integration of elasto-plastic constitutive relations. *Computer Methods in Applied Mechanics and Engineering*, *78*(1), 49-72.

Borja, R. I., Sama, K. M., & Sanz, P. F. (2003). On the numerical integration of three-invariant elastoplastic constitutive models. *Computer Methods in Applied Mechanics and Engineering*, *192*(9), 1227-1258.

Brinkgreve, R. B. (2005). Selection of soil models and parameters for geotechnical engineering application. *In Soil Constitutive Models: Evaluation, Selection, and Calibration*, 69-98.

Brooks, R. H., & Corey, A. T. (1964). Hydraulic properties of porous media and their relation to drainage design. *Transactions of the ASAE*, *7*(1), 26-28.

Bui, H. H., Fukagawa, R., Sako, K., & Ohno, S. (2008). Lagrangian meshfree particles method (SPH) for large deformation and failure flows of geomaterial using elastic–plastic soil constitutive model. *International Journal for Numerical and Analytical Methods in Geomechanics*, *32*(12), 1537-1570.

Bui, H. H., Fukagawa, R., Sako, K., & Wells, J. C. (2011). Slope stability analysis and discontinuous slope failure simulation by elasto-plastic smoothed particle hydrodynamics (SPH). *Géotechnique*, *61*(7), 565-574.

Buscarnera, G., & Einav, I. (2012). The yielding of brittle unsaturated granular soils. *Géotechnique*, *62*(2), 147.

Buscarnera, G., & Mihalache, C. (2014). Instability of unsaturated soils: A review of theoretical methods. *Journal of Geo-Engineering Sciences*, *2*(1-2), 39-65.

Cai, M., Kaiser, P. K., Morioka, H., Minami, M., Maejima, T., Tasaka, Y., & Kurose, H. (2007). FLAC/PFC coupled numerical simulation of AE in large-scale underground excavations. *International Journal of Rock Mechanics and Mining Sciences*, *44*(4), 550-564.

Cambou, B., & Jean, M. (2009). Micromechanics of granular materials. John Wiley & Sons.

Cecílio, D. L., Devloo, P. R., Gomes, S. M., dos Santos, E. R., & Shauer, N. (2015). An improved numerical integration algorithm for elastoplastic constitutive equations. *Computers and Geotechnics*, *64*(3), 1-9.

Chalak, C., Chareyre, B., Nikooee, E., & Darve, F. (2017). Partially saturated media: from DEM simulation to thermodynamic interpretation. *European Journal of Environmental and Civil Engineering*, *21*(7-8), 798-820.

Chambon, R., Caillerie, D., & Viggiani, G. (2004). Loss of uniqueness and bifurcation vs instability: some remarks. *Revue Française de Génie Civil*, *8*(5-6), 517-535.

Chang, C. S., & Hicher, P. Y. (2005). An elasto-plastic model for granular materials with microstructural consideration. *International Journal of Solids and Structures*, *42*(14), 4258-4277.

Chang, C. S., & Hicher, P. Y. (2009). Model for granular materials with surface energy forces. *Journal of Aerospace Engineering*, *22*(1), 43-52.

Chang, C. S., Hicher, P. Y., & Daouadji, A. (2009). Investigating instability in granular materials by means of a microstructural model. *European Journal of Environmental and Civil Engineering*, *13*(2), 167-186.

Chang, C. S., Hicher, P. Y., Yin, Z. Y., & Kong, L. R. (2009). Elastoplastic model for clay with microstructural consideration. *Journal of Engineering Mechanics*, *135*(9), 917-931.

Chang, C. S., & Meidani, M. (2013). Dominant grains network and behavior of sand–silt mixtures: stress–strain modeling. *International Journal for Numerical and Analytical Methods in Geomechanics*, *37*(15), 2563-2589.

Chang, C. S., & Misra, A. (1990). Packing structure and mechanical properties of granulates. *Journal of Engineering Mechanics*, *116*(5), 1077-1093.

Chang, C. S., & Yin, Z. Y. (2009a). Modeling stress-dilatancy for sand under compression and extension loading conditions. *Journal of Engineering Mechanics*, *136*(6), 777-786.

Chang, C. S., & Yin, Z. Y. (2009b). Micromechanical modeling for inherent anisotropy in granular materials. *Journal of Engineering Mechanics*, *136*(7), 830-839.

Chang, C. S., & Yin, Z. Y. (2011). Micromechanical modeling for behavior of silty sand with influence of fine content. *International Journal of Solids and Structures*, *48*(19), 2655-2667.

Chang, C. S., Yin, Z. Y., & Hicher, P. Y. (2010). Micromechanical analysis for interparticle and assembly instability of sand. *Journal of Engineering Mechanics*, *137*(3), 155-168.

Chang, C. S., Yin, Z. Y., & Hicher, P. Y. (2011). Multi-scale analysis of instability in sand. In *Advances in Bifurcation and Degradation in Geomaterials*, 29-35. Springer, Dordrecht.

Cho, S. E., & Lee, S. R. (2001). Instability of unsaturated soil slopes due to infiltration. *Computers and Geotechnics*, *28*(3), 185-208.

Clausen, C. J. F., Aas, P. M., & Karlsrud, K. (2005, September). Bearing capacity of driven piles in sand, the NGI approach. In *Proceedings of Proceedings of International Symposium on Frontiers in Offshore Geotechnics, Perth*, 574-580.

Collins, I. F., Muhunthan, B., & Qu, B. (2010). Thermomechanical state parameter models for sands. *Géotechnique*, *60*(8), 611-622.

Collins, I. F., & Hilder, T. (2002). A theoretical framework for constructing elastic/plastic constitutive models of triaxial tests. *International Journal for Numerical and Analytical Methods in Geomechanics*, *26*(13), 1313-1347.

Collins, I. F., & Houlsby, G. T. (1997). Application of thermomechanical principles to the modelling of geotechnical materials. In *Proceedings of the royal society of London A: Mathematical, Physical and Engineering Sciences, 453*(1964), 1975-2001.

Coop, M. R. (1990). The mechanics of uncemented carbonate sands. *Géotechnique*, *40*(4), 607-626.

Coussy, O., Pereira, J. M., & Vaunat, J. (2010). Revisiting the thermodynamics of hardening plasticity for unsaturated soils. *Computers and Geotechnics*, *37*(1), 207-215.

Cui, Q. L., Wu, H. N., Shen, S. L., Yin, Z. Y., & Horpibulsuk, S. (2016). Protection of neighbour buildings due to construction of shield tunnel in mixed ground with sand over weathered granite. *Environmental Earth Sciences*, *75*(6), 458.

Cui, Y. J., & Delage, P. (1996). Yielding and plastic behaviour of an unsaturated compacted silt. *Géotechnique*, *46*(2), 291-311.

Cundall, P. A., & Strack, O. D. (1979). A discrete numerical model for granular assemblies. *Géotechnique*, *29*(1), 47-65.

Dang, H. K., & Meguid, M. A. (2008). Application of a multilaminate model to simulate the undrained response of structured clay to shield tunnelling. *Canadian Geotechnical Journal*, *45*(1), 14-28.

Dangla, P., & Pereira, J. M. (2014). A thermodynamic approach to effective stresses in unsaturated soils incorporating the concept of partial pore deformations. *Vadose Zone Journal*, *13*(5), 1-11.

Daouadji, A., Darve, F., Al Gali, H., Hicher, P. Y., Laouafa, F., Lignon, S., ... & Sibille, L. (2011). Diffuse failure in geomaterials: Experiments, theory and modelling. *International Journal for Numerical and Analytical Methods in Geomechanics*, *35*(16), 1731-1773.

Daouadji, A., Hicher, P. Y., Jrad, M., Sukumaran, B., & Belouettar, S. (2013). Experimental and numerical investigation of diffuse instability in granular materials using a microstructural model under various loading paths. *Géotechnique*, *63*(5), 368-381.

Darve, F., & Laouafa, F. (2000). Instabilities in granular materials and application to landslides. *Mechanics of Cohesive-frictional Materials*, *5*(8), 627-652.

Darve, F., Servant, G., Laouafa, F., & Khoa, H. D. V. (2004). Failure in geomaterials: continuous and discrete analyses. *Computer Methods in Applied Mechanics and Engineering*, *193*(27), 3057-3085.

Desrues, J., Chambon, R., Mokni, M., & Mazerolle, F. (1996). Void ratio evolution inside shear bands in triaxial sand specimens studied by computed tomography. *Géotechnique*, *46*(3), 529-546.

Desrues, J., & Viggiani, G. (2004). Strain localization in sand: an overview of the experimental results obtained in Grenoble using stereophotogrammetry. *International Journal for Numerical and Analytical Methods in Geomechanics*, *28*(4), 279-321.

Duriez, J., & Wan, R. (2016). Subtleties in discrete-element modelling of wet granular soils. *Géotechnique*, *67*(4), 365-370.

Elmekati, A., & El Shamy, U. (2010). A practical co-simulation approach for multiscale analysis of geotechnical systems. *Computers and Geotechnics*, *37*(4), 494-503.

Fang, Y. S., Lin, J. S., & Su, C. S. (1994). An estimation of ground settlement due to shield tunnelling by the Peck-Fujita method. *Canadian Geotechnical Journal*, *31*(3), 431-443.

Feia, S., Sulem, J., Canou, J., Ghabezloo, S., & Clain, X. (2016). Changes in permeability of sand during triaxial loading: effect of fine particles production. *Acta Geotechnica*, *11*(1), 1-19.

Fern, E. J., Robert, D. J., & Soga, K. (2016). Modeling the stress-dilatancy relationship of unsaturated silica sand in triaxial compression tests. *Journal of Geotechnical and Geoenvironmental Engineering*, *142*(11), 04016055.

Fu, P., & Dafalias, Y. F. (2011). Fabric evolution within shear bands of granular materials and its relation to critical state theory. *International Journal for Numerical and Analytical Methods in Geomechanics*, *35*(18), 1918-1948.

Fu, P., & Dafalias, Y. F. (2015). Relationship between void-and contact normal-based fabric tensors for 2D idealized granular materials. *International Journal of Solids and Structures*, *63*, 68-81.

Fredlund, D. G., & Xing, A. (1994). Equations for the soil-water characteristic curve. *Canadian Geotechnical Journal*, *31*(4), 521-532.

Fredlund, D. G., Rahardjo, H., & Fredlund, M. D. (2012). Unsaturated soil mechanics in engineering practice. *John Wiley & Sons*.

Gao, Z., & Zhao, J. (2013). Strain localization and fabric evolution in sand. *International Journal of Solids and Structures*, *50*(22), 3634-3648.

Gao, Z., & Zhao, J. (2017). A non-coaxial critical-state model for sand accounting for fabric anisotropy and fabric evolution. *International Journal of Solids and Structures*, *106*, 200-212.

Gao, Z., Zhao, J., Li, X. S., & Dafalias, Y. F. (2014). A critical state sand plasticity model accounting for fabric evolution. *International Journal for Numerical and Analytical Methods in Geomechanics*, *38*(4), 370-390.

Geers, M. G., Kouznetsova, V. G., & Brekelmans, W. A. M. (2010). Multi-scale computational homogenization: Trends and challenges. *Journal of Computational and Applied Mathematics*, *234*(7), 2175-2182.

Gens, A. (2010). Soil–environment interactions in geotechnical engineering. *Géotechnique*, *60*(1), 3-74.

Gens, A., Sánchez, M., & Sheng, D. (2006). On constitutive modelling of unsaturated soils. *Acta Geotechnica*, *1*(3), 137-147.

Gourvenec, S., Randolph, M., & Kingsnorth, O. (2006). Undrained bearing capacity of square and rectangular footings. *International Journal of Geomechanics*, *6*(3), 147-157.

Gudehus, G. (1979). A comparison of some constitutive laws for soils under radially symmetric loading and unloading. *Canadian Geotechnical Journal*, *20*, 502-516.

Gudehus, G., & Nübel, K. (2004). Evolution of shear bands in sand. *Géotechnique*, *54*(3), 187-201.

Guo, N., & Zhao, J. (2014). A coupled FEM/DEM approach for hierarchical multiscale modelling of granular media. *International Journal for Numerical Methods in Engineering*, *99*(11), 789-818.

Guo, N., & Zhao, J. (2016). Multiscale insights into classical geomechanics problems. *International Journal for Numerical and Analytical Methods in Geomechanics*, *40*(3), 367-390.

Hadda, N., Nicot, F., Bourrier, F., Sibille, L., Radjai, F., & Darve, F. (2013). Micromechanical analysis of second order work in granular media. *Granular matter*, *15*(2), 221-235.

Hadda, N., Nicot, F., Wan, R., & Darve, F. (2015). Microstructural self-organization in granular materials during failure. *Comptes Rendus Mécanique*, *343*(2), 143-154.

Hadda, N., Sibille, L., Nicot, F., Wan, R., & Darve, F. (2016). Failure in granular media from an energy viewpoint. *Granular Matter*, *18*(3), 1-17.

Hall, S. A., Bornert, M., Desrues, J., Pannier, Y., Lenoir, N., Viggiani, G., & Bésuelle, P. (2010). Discrete and continuum analysis of localised deformation in sand using X-ray μCT and volumetric digital image correlation. *Géotechnique*, *60*(5), 315-322.

Hassanizadeh, M., & Gray, W. G. (1980). General conservation equations for multi-phase systems: 3. Constitutive theory for porous media flow. *Advances in Water Resources*, *3*(1), 25-40.

He, X., Cai, G., Zhao, C., & Sheng, D. (2017). On the stress-force-fabric equation in triaxial compressions: Some insights into the triaxial strength. *Computers and Geotechnics*, *85*, 71-83.

Henke, S., Qiu, G., & Grabe, J. (2010). A coupled Eulerian Lagrangian approach to solve geotechnical problems involving large deformations. In *Proc. 7th Eur. Conf. Numer. Methods Geotech. Engng, Trondheim*, 233-238.

Hicher, P.Y., & Chang, C.S. (2005). Evaluation of two homogenization techniques for modeling the elastic behavior of granular materials. *Journal of Engineering Mechanics*, *131*(11), 1184-1194.

Hicher, P. Y., & Chang, C. S. (2006). Anisotropic nonlinear elastic model for particulate materials. *Journal of Geotechnical and Geoenvironmental Engineering*, *132*(8), 1052-1061.

Hicher, P. Y., & Chang, C. S. (2007). A microstructural elastoplastic model for unsaturated granular materials. *International Journal of Solids and Structures*, *44*(7), 2304-2323.

Hicher, P. Y., Chang, C. S., & Dano, C. (2008a). Multi-scale modeling of grouted sand behavior. *International Journal of Solids and Structures*, *45*(16), 4362-4374.

Hicher, P. Y., Dano, C., & Chang, C. (2008b). Multi-scale modelling of the mechanical behaviour of grouted sand. *Studia Geotechnica et Mechanica*, *30*(1-2), 83-94.

Hicks, M. A., Yap, T. Y., & Bakar, A. A. (2001). Adaptive and fixed mesh study of localisation in a strain-softening soil. *Bifurcation and Localisation Theory in Geomechanics, Balkema*, 147-155.

Hill, R. (1958). A general theory of uniqueness and stability in elastic-plastic solids. *Journal of the Mechanics and Physics of Solids*, *6*(3), 236-249.

Hill, R. (1963). Elastic properties of reinforced solids: some theoretical principles. *Journal of the Mechanics and Physics of Solids*, *11*(5), 357-372.

Houlsby, G. T. (1997). The work input to an unsaturated granular material. *Géotechnique*, 47(1), 193-196.

Houlsby, G. T., & Puzrin, A. M. (2007). Principles of hyperplasticity: an approach to plasticity theory based on thermodynamic principles. *Springer Science & Business Media*.

Hu, R., Chen, Y. F., Liu, H. H., & Zhou, C. B. (2015). A coupled stress-strain and hydraulic hysteresis model for unsaturated soils: thermodynamic analysis and model evaluation. *Computers and Geotechnics*, *63*, 159-170.

Hu, C., & Liu, H. (2014). Implicit and explicit integration schemes in the anisotropic bounding surface plasticity model for cyclic behaviours of saturated clay. *Computers and Geotechnics*, *55*, 27-41.

Huang, J., & Griffiths, D.V. (2009). Return mapping algorithms and stress predictors for failure analysis in geomechanics. *Journal of Engineering Mechanics*, *135*(4), 276-284.

Hutter, K., Laloui, L., & Vulliet, L. (1999). Thermodynamically based mixture models of saturated and unsaturated soils. *Mechanics of Cohesive Frictional Materials*, 4(4), 295-338.

Hyodo, M., Wu, Y., Aramaki, N., & Nakata, Y. (2017). Undrained monotonic and cyclic shear response and particle crushing of silica sand at low and high pressures. *Canadian Geotechnical Journal*, *54*(2), 207-218.

Jardine, R., Chow, F., Overy, R., & Standing, J. (2005). ICP design methods for driven piles in sands and clays (p. 112). London: Thomas Telford.

Jardine, R.J., Zhu, B.T., Foray, P., & Yang, Z.X. (2013a). Measurement of stresses around closed-ended displacement piles in sand. *Géotechnique*, 63(1), 1-17.

Jardine, R.J., Zhu, B.T., Foray, P., & Yang, Z.X. (2013b). Interpretation of stress measurements made around closed-ended displacement piles in sand. *Géotechnique,* 63(8), 613-627.

Jiang, Y., Einav, I., & Liu, M. (2017). A thermodynamic treatment of partially saturated soils revealing the structure of effective stress. *Journal of the Mechanics and Physics of Solids*, *100*, 131-146.

Jiang, M., Yu, H.S., & Leroueil, S. (2007). A simple and efficient approach to capturing bonding effect in naturally microstructured sands by discrete element method. *International Journal for Numerical Methods in Engineering*, *69*(6), 1158-1193.

Jiang, M., & Yin, Z. Y. (2012). Analysis of stress redistribution in soil and earth pressure on tunnel lining using the discrete element method. *Tunnelling and Underground Space Technology*, *32*, 251-259.

Jiang, M., & Yin, Z. Y. (2014). Influence of soil conditioning on ground deformation during longitudinal tunneling. *Comptes Rendus Mecanique*, *342*(3), 189-197.

Jiang, M. J., Yu, H. S., & Harris, D. (2006). Discrete element modelling of deep penetration in granular soils. *International Journal for Numerical and Analytical Methods in Geomechanics*, *30*(4), 335-361.

Jiang, M. J., Zhu, H. H., & Harris, D. (2008). Classical and non-classical kinematic fields of two-dimensional penetration tests on granular ground by discrete element method analyses. *Granular Matter*, *10*(6), 439-455.

Ken-Ichi, K. (1984). Distribution of directional data and fabric tensors. *International Journal of Engineering Science*, *22*(2), 149-164.

Kakogiannou, E., Sanavia, L., Nicot, F., Darve, F., & Schrefler, B. A. (2016). A porous media finite element approach for soil instability including the second-order work criterion. *Acta Geotechnica*, *11*(4), 805-825.

Khoei, A. R., & Jamali, N. (2005). On the implementation of a multi-surface kinematic hardening plasticity and its applications. *International Journal of Plasticity*, *21*(9), 1741-1770.

Kirsch, A. (2010). Experimental investigation of the face stability of shallow tunnels in sand. *Acta Geotechnica*, *5*(1), 43-62.

Klotz, E. U., & Coop, M. R. (2001). An investigation of the effect of soil state on the capacity of driven piles in sands. *Géotechnique*, *51*(9), 733-751.

Ko, J., Jeong, S., & Lee, J. K. (2016). Large deformation FE analysis of driven steel pipe piles with soil plugging. *Computers and Geotechnics*, *71*, 82-97.

Kolk, H.J., Baaijens, A.E., & Vergobi, P. (2005). Results of axial load tests on pipe piles in very dense sands: The EURIPIDES JIP. *Proc. Int. Symp. on Frontiers in Offshore Geomechanics, ISFOG*, *Taylor & Francis, London*, 661-667.

Kolymbas, D. (2012). Constitutive modelling of granular materials. *Springer Science & Business Media*.

Kolymbas, D., & Wu, W. (1990). Recent results of triaxial tests with granular materials. *Powder Technology*, *60*(2), 99-119.

Kuhn, M. R. (1997). Deformation measures for granular materials. In *Mechanics of Deformation and Flow of Particulate Materials*, 91-104. ASCE.

Kuhn, M.R. (1999). Structured deformation in granular materials. *Mechanics of Materials*, *31*(6), 407-429.

Kuganenthira, N., Zhao, D., & Anandarajah, A. (1996). Measurement of fabric anisotropy in triaxial shearing. *Géotechnique*, *46*(4), 657-670.

Krieg, R.D., & Krieg, D.B. (1977). Accuracies of numerical solution methods for the elastic-perfectly plastic model. *ASME, Transactions, Series J-Journal of Pressure Vessel Technology*, *99*, 510-515.

Kruyt, N.P. (2003). Statics and kinematics of discrete Cosserat-type granular materials. *International Journal of Solids and Structures*, *40*(3), 511-534.

Kruyt, N. P. (2012). Micromechanical study of fabric evolution in quasi-static deformation of granular materials. *Mechanics of Materials*, *44*, 120-129.

Kruyt, N.P. & Rothenburg, L. (1996). Micromechanical definition of the strain tensor for granular materials. *Journal of Applied Mechanics*, *118*, 706-711.

Kruyt, N. P., & Rothenburg, L. (2014). On micromechanical characteristics of the critical state of two-dimensional granular materials. *Acta Mechanica*, *225*(8), 2301-2318.

Kruyt, N. P., & Rothenburg, L. (2016). A micromechanical study of dilatancy of granular materials. *Journal of the Mechanics and Physics of Solids*, *95*, 411-427.

Kuwajima, K., Hyodo, M., & Hyde, A. F. (2009). Pile bearing capacity factors and soil crushabiity. *Journal of Geotechnical and Geoenvironmental Engineering*, ASCE, *135*(7), 901-913.

Lade, P.V. (2002). Instability, shear banding, and failure in granular materials. *International Journal of Solids and Structures*, *39*(13), 3337-3357.

Lade, P.V., & Liggio Jr, C.D. (2014). Stability and instability of granular materials under imposed volume changes: experiments and predictions. *International Journal of Geomechanics*, *14*(5), 04014020.

Lai, Y., Liao, M., & Hu, K. (2016). A constitutive model of frozen saline sandy soil based on energy dissipation theory. *International Journal of Plasticity*, *78*, 84-113.

Lehane, B.M., Schneider, J.A., & Xu, X. (2005). The UWA-05 method for prediction of axial capacity of driven piles in sand. In *Proc., 1st Int. Symp. on Frontiers in Offshore Geotechnics,* 683-689. Perth, Australia: Balkema.

Lewis, R. W., & Schrefler, B. A. (1987). The finite element method in the deformation and consolidation of porous media.

Lloret-Cabot, M., Sloan, S., Sheng, D., & Abbo, A. (2016). Error behaviour in explicit integration algorithms with automatic substepping. *International Journal for Numerical Methods in Engineering*, *108*(9), 1030-1053.

Li, J., Yin, Z. Y., Cui, Y. J., & Hicher, P. Y. (2017). Work input analysis for soils with double porosity and application to the hydro-mechanical modeling of unsaturated expansive clays. *Canadian Geotechnical Journal*, 54(2), 173-187.

Li, M., Yu, H., Wang, J., Xia, X., & Chen, J. (2015). A multiscale coupling approach between discrete element method and finite difference method for dynamic analysis. *International Journal for Numerical Methods in Engineering*, *102*(1), 1-21.

Li, P., Du, S. J., Ma, X. F., Yin, Z. Y., & Shen, S. L. (2014). Centrifuge investigation into the effect of new shield tunnelling on an existing underlying large-diameter tunnel. *Tunnelling and Underground Space Technology*, *42*, 59-66.

Li, X. (2016). Internal structure quantification for granular constitutive modeling. *Journal of Engineering Mechanics*, *143*(4), C4016001.

Li, X., & Li, X. S. (2009). Micro-macro quantification of the internal structure of granular materials. *Journal of Engineering Mechanics*, *135*(7), 641-656.

Li, X., Yu, H.S., & Li, X.S. (2009). Macro-micro relations in granular mechanics. *International Journal of Solids and Structures*, *46*(2009), 4331-4341.

Li, X., & Yu, H.S. (2011). Tensorial characterisation of directional data in micromechanics. *International Journal of Solids and Structures*, *48*(14), 2167-2176.

Li, X. & Yu, H.S. (2013). On the stress-force-fabric relationship for granular materials. *International Journal of Solids and Structures*, *50*(9), 1285-1302.

Li, X., Yu, H.S., & Li, X.S. (2013). A virtual experiment technique on the elementary behaviour of granular materials with discrete element method. *International Journal for Numerical and Analytical Methods in Geomechanics*, *37*(1), 75-96.

Li, X. S. (2003). Effective stress in unsaturated soil: a microstructural analysis. *Géotechnique*, *53*(2), 273-277.

Li, X.S. (2007). Thermodynamics-based constitutive framework for unsaturated soils. 1: Theory. *Géotechnique*, *57*(5), 411-422.

Li, X.S., & Dafalias, Y.F. (2011). Anisotropic critical state theory: role of fabric. *Journal of Engineering Mechanics*, *138*(3), 263-275.

Li, X. S., & Dafalias, Y. F. (2015). Dissipation consistent fabric tensor definition from DEM to continuum for granular media. *Journal of the Mechanics and Physics of Solids*, *78*, 141-153.

Liao, C.L., Chang, T.P., Young, D.H., & Chang, C.S. (1997). Stress-strain relationship for granular materials based on the hypothesis of best fit. *International Journal of Solids and Structures*, *34*(31-32), 4087-4100.

Liu, M. B., & Liu, G. R. (2010). Smoothed particle hydrodynamics (SPH): an overview and recent developments. *Archives of Computational Methods in Engineering*, *17*(1), 25-76.

Love, A.E.H. (1927). A treatise on the mathematical theory of elasticity. *Cambridge University Press*.

Lu, N. (2008). Is matric suction a stress variable? *Journal of Geotechnical and Geoenvironmental Engineering*, *134*(7), 899-905.

Lyamin, A.V., Salgado, R., Sloan, S.W., & Prezzi, M. (2007). Two-and three-dimensional bearing capacity of footings in sand. *Géotechnique*, *57*(8), 647-662.

Mair, R. J. (2008). Tunnelling and geotechnics: new horizons. *Géotechnique*, *58*(9), 695-736.

Mandel, J. (1971). Plasticité classique et viscoplasticité. *International Center for Mechanical Sciences (CISM). Springer, Udine*.

Marshall, A. M., & Mair, R. J. (2011). Tunneling beneath driven or jacked end-bearing piles in sand. *Canadian Geotechnical Journal*, *48*(12), 1757-1771.

McAuliffe, C., & Waisman, H. (2015). On the importance of nonlinear elastic effects in shear band modeling. *International Journal of Plasticity*, *71*, 10-31.

McDowell, G. R., Falagush, O., & Yu, H. S. (2012). A particle refinement method for simulating DEM of cone penetration testing in granular materials. *Géotechnique Letters*, *2*(3), 141-147.

Merritt, A. S., Schroeder, F. C., Jardine, R. J., Stuyts, B., Cathie, D., & Cleverly, W. (2012). Development of pile design methodology for an offshore wind farm in the North Sea. In *Offshore Site Investigation and Geotechnics: Integrated Technologies-Present and Future*. Society of Underwater Technology.

Mindlin, R. D. (1953). Elastic spheres in contact under varying oblique forces. *Trans. ASME, Journal of Applied Mechanics*, *20*, 327-344.

Mirone, G., & Corallo, D. (2010). A local viewpoint for evaluating the influence of stress triaxiality and Lode angle on ductile failure and hardening. *International Journal of Plasticity*, *26*(3), 348-371.

Misra, A., & Poorsolhjouy, P. (2015a). Granular micromechanics model for damage and plasticity of cementitious materials based upon thermomechanics. *Mathematics and Mechanics of Solids*, 1-26.

Misra, A., & Poorsolhjouy, P. (2015b). Micro-macro scale instability in 2D regular granular assemblies. *Continuum Mechanics and Thermodynamics*, *27*(1-2), 63-82.

Misra, A., & Singh, V. (2014). Nonlinear granular micromechanics model for multi-axial rate-dependent behavior. *International Journal of Solids and Structures*, *51*(13), 2272-2282.

Misra, A., & Singh, V. (2015). Thermomechanics-based nonlinear rate-dependent coupled damage-plasticity granular micromechanics model. *Continuum Mechanics and Thermodynamics*, *27*(4-5), 787.

Ng, C. W., & Chiu, A. C. (2003). Laboratory study of loose saturated and unsaturated decomposed granitic soil. *Journal of Geotechnical and Geoenvironmental Engineering*, *129*(6), 550-559.

Ng, C. W. W., & Shi, Q. (1998). A numerical investigation of the stability of unsaturated soil slopes subjected to transient seepage. *Computers and Geotechnics*, *22*(1), 1-28.

Nguyen, T. K., Claramunt, A. A., Caillerie, D., Combe, G., Dal Pont, S., Desrues, J., & Richefeu, V. (2017). FEM× DEM: a new efficient multi-scale approach for geotechnical problems with strain localization. In *EPJ Web of Conferences* 140, 11007. EDP Sciences.

Nguyen, H. N., Prunier, F., Djeran-Maigre, I., & Nicot, F. (2016). Kinetic energy and collapse of granular materials. *Granular Matter*, *18*(1), 5.

Nguyen, V. P., Stroeven, M., & Sluys, L. J. (2011). Multiscale continuous and discontinuous modeling of heterogeneous materials: a review on recent developments. *Journal of Multiscale Modelling*, *3*(04), 229-270.

Niedostatkiewicz, M., Lesniewska, D., & Tejchman, J. (2011). Experimental analysis of shear zone patterns in cohesionless for earth pressure problems using particle image velocimetry. *Strain*, *47*(s2), 218-231.

Nikooee, E., Habibagahi, G., Hassanizadeh, S. M., & Ghahramani, A. (2013). Effective stress in unsaturated soils: a thermodynamic approach based on the interfacial energy and hydromechanical coupling. *Transport in Porous Media*, *96*(2), 369-396.

Nicot, F., Daouadji, A., Laouafa, F., & Darve, F. (2011). Second-order work, kinetic energy and diffuse failure in granular materials. *Granular Matter*, *13*(1), 19-28.

Nicot, F., Darve, F., & Dat Vu Khoa, H. (2007). Bifurcation and second-order work in geomaterials. *International Journal for Numerical and Analytical Methods in Geomechanics*, *31*(8), 1007-1032.

Nicot, F., & Darve, F. (2005). A multi-scale approach to granular materials. *Mechanics of Materials*, *37*(9), 980-1006.

Nicot, F., & Darve, F. (2007). A micro-mechanical investigation of bifurcation in granular materials. *International Journal of Solids and Structures*, *44*(20), 6630-6652.

Nicot, F., & Darve, F. (2011). The H-microdirectional model: accounting for a mesoscopic scale. *Mechanics of Materials*, *43*(12), 918-929.

Nicot, F., & Darve, F. (2015). Describing failure in geomaterials using second-order work approach. *Water Science and Engineering*, *8*(2), 89-95.

Nicot, F., Hadda, N., & Darve, F. (2013). Second-order work analysis for granular materials using a multiscale approach. *International Journal for Numerical and Analytical Methods in Geomechanics*, *37*(17), 2987-3007.

Nicot, F., Lerbet, J., & Darve, F. (2017). Second-order work criterion: from material point to boundary value problems. *Acta Mechanica*, *228*(7), 2483-2498.

Nicot, F., Sibille, L., & Darve, F. (2009). Bifurcation in granular materials: an attempt for a unified framework. *International Journal of Solids and Structures*, *46*(22), 3938-3947.

Nicot, F., Sibille, L., & Darve, F. (2012). Failure in rate-independent granular materials as a bifurcation toward a dynamic regime. *International Journal of Plasticity*, *29*, 136-154.

Nitka, M., Combe, G., Dascalu, C., & Desrues, J. (2011). Two-scale modeling of granular materials: a DEM-FEM approach. *Granular Matter*, *13*(3), 277-281.

Nova, R. (1989). Liquefaction, stability, bifurcations of soil via strain-hardening plasticity. In *Proceedings of the International Workshop on Bifurcation and Localization in Soil and Rocks. Gdansk*, 117-131.

Nova, R. (1994). Controllability of the incremental response of soil specimens subjected to arbitrary loading programmes. *Journal of the Mechanical Behavior of Materials*, *5*(2), 193-201.

Oda, M., & Iwashita, K. (1999). Mechanics of granular materials: an introduction. *CRC Press*.

Oda, M., & Kazama, H. (1998). Microstructure of shear bands and its relation to the mechanisms of dilatancy and failure of dense granular soils. *Géotechnique*, *48*(4), 465-481.

Oda, M., Nemat-Nasser, S., & Konishi, J. (1985). Stress-induced anisotropy in granular masses. *Soils and Foundations*, *25*(3), 85-97.

Ortiz, M., & Simo, J.C. (1986). An analysis of a new class of integration algorithms for elastoplastic constitutive relations. *International Journal for Numerical Methods in Engineering*, *23*(3), 353-366.

O'Sullivan, C. (2011). Particulate discrete element modelling: a geomechanics perspective. *Taylor & Francis*.

Overy, R. (2007). The use of ICP design methods for the foundations of nine platforms installed in the U.K. North Sea. *Proc., 6th Int. Conf. on Offshore Site Investigations and Geotechnics, Society for Underwater Technology*, *London*.

Pan, Y.W., & Dong, J.J. (1999). A micromechanics-based methodology for evaluating the fabric of granular material. *Géotechnique, 49*(6), 761-775.

Peck, R. B. (1969). Deep excavations and tunneling in soft ground. *Proc. 7th Int. Con. SMFE, State of the Art*, 225-290.

Prunier, F., Chomette, B., Brun, M., & Darve, F. (2016). Designing geotechnical structures with a proper stability criterion as a safety factor. *Computers and Geotechnics*, *71*, 98-114.

Qiu, G., & Grabe, J. (2011). Explicit modeling of cone and strip footing penetration under drained and undrained conditions using a visco-hypoplastic model. *Geotechnik*, *34*(3), 205-217.

Radjai, F. (2008). Particle-scale origins of shear strength in granular media. In *Evolution, vol. 1. Van Nostrand Reinhold*, 2008, p. ix, 290.

Radjai, F., Roux, J. N., & Daouadji, A. (2017). Modeling granular materials: century-long research across scales. *Journal of Engineering Mechanics*, *143*(4), 04017002.

Rankine, W. M. (1857). On the stability of loose earth. *Philosophical Transactions of The Royal Society of London*, *147*, 9-27.

Rechenmacher, A.L. (2006). Grain-scale processes governing shear band initiation and evolution in sands. *Journal of the Mechanics and Physics of Solids*, *54*(1), 22-45.

Rechenmacher, A., Abedi, S., & Chupin, O. (2010). Evolution of force chains in shear bands in sands. *Géotechnique*, *60*(5), 343-351.

Rice, J.R. (1971). Inelastic constitutive relations for solids: an internal-variable theory and its application to metal plasticity. *Journal of the Mechanics and Physics of Solids*, *19*(6), 433-455.

Rothenburg, L., & Bathurst, R.J. (1989). Analytical study of induced anisotropy in idealized granular materials. *Géotechnique*, *39*(4), 601-614.

Rouainia, M., & Muir Wood, D. (2001). Implicit numerical integration for a kinematic hardening soil plasticity model. *International Journal for Numerical and Analytical Methods in Geomechanics*, *25*(13), 305-1325.

Rowe, P.W. (1962). The stress-dilatancy relation for static equilibrium of an assembly of particles in contact. In *Proceedings of the royal society of London a: mathematical, physical and engineering sciences*, *269*(1339), 500-527. The Royal Society.

Rudnicki, J.W., & Rice, J.R. (1975). Conditions for the localization of deformation in pressure-sensitive dilatant materials. *Journal of the Mechanics and Physics of Solids*, *23*(6), 371-394.

Santamarina, J. C., & Cascante, G. (1996). Stress anisotropy and wave propagation: a micromechanical view. *Canadian Geotechnical Journal*, *33*(5), 770-782.

Satake, M. (1982). Fabric tensor in granular materials. In *Proc., IUTAM Symp. on Deformation and Failure of Granular Materials, Delft, The Netherlands*.

Schofield, A., & Wroth, P. (1968). Critical state soil mechanics. *London: McGraw-Hill*.

Scholtès, L., Chareyre, B., Nicot, F., & Darve, F. (2009). Micromechanics of granular materials with capillary effects. *International Journal of Engineering Science*, *47*(1), 64-75.

Scholtès, L., Hicher, P. Y., Nicot, F., Chareyre, B., & Darve, F. (2009). On the capillary stress tensor in wet granular materials. *International Journal for Numerical and Analytical Methods in Geomechanics*, *33*(10), 1289-1313.

Schweiger, H. F. (2008). The role of advanced constitutive models in geotechnical engineering. *Geomechanics and Tunnelling*, *1*(5), 336-344.

Shen, S. L., Wu, H. N., Cui, Y. J., & Yin, Z. Y. (2014). Long-term settlement behaviour of metro tunnels in the soft deposits of Shanghai. *Tunnelling and Underground Space Technology*, *40*, 309-323.

Shen, W.Q., Shao, J.F., Kondo, D., & Gatmiri, B. (2012). A micro-macro model for clayey rocks with a plastic compressible porous matrix. *International Journal of Plasticity*, *36*, 64-85.

Sheng, D. (2011). Review of fundamental principles in modelling unsaturated soil behaviour. *Computers and Geotechnics*, *38*(6), 757-776.

Sheng, D., Sloan, S. W., & Gens, A. (2004). A constitutive model for unsaturated soils: thermomechanical and computational aspects. *Computational Mechanics*, 33(6), 453-465.

Sheng, D., Eigenbrod, K. D., & Wriggers, P. (2005). Finite element analysis of pile installation using large-slip frictional contact. *Computers and Geotechnics*, *32*(1), 17-26.

Sheng, D., Sloan, S.W., & Yu, H.S. (2000). Aspects of finite element implementation of critical state models. *Computational Mechanics*, *26*(2), 185-196.

Sibille, L., Nicot, F., Donze, F.V., & Darve, F. (2007). Material instability in granular assemblies from fundamentally different models. *International Journal for Numerical and Analytical Methods in Geomechanics*, *31*(3), 457-481.

Simo, J.C., & Hughes, T.J.R. (1987). General return mapping algorithms for rate-independent plasticity. *Constitutive Laws for Engineering Materials: Theory and Applications*, *1*, 221-232.

Simo, J.C., & Taylor, R.L. (1986). A return mapping algorithm for plane stress elastoplasticity. *International Journal for Numerical Methods in Engineering*, *22*(3), 649-670.

Sloan, S.W. (1987). Substepping schemes for the numerical integration of elastoplastic stress–strain relations. *International Journal for Numerical Methods in Engineering*, *24*(5), 893-911.

Sloan, S.W., Abbo, A.J., & Sheng, D. (2001). Refined explicit integration of elastoplastic models with automatic error control. *Engineering Computations*, *18*(1/2), 121-194.

Soga, K., Alonso, E., Yerro, A., Kumar, K., & Bandara, S. (2015). Trends in large-deformation analysis of landslide mass movements with particular emphasis on the material point method. *Géotechnique*, *66*(3), 248-273.

Staron, L., Radjai, F., & Vilotte, J.P. (2005). Multi-scale analysis of the stress state in a granular slope in transition to failure. *The European Physical Journal E: Soft Matter and Biological Physics*, *18*(3), 311-320.

Sun, D. A., Sheng, D., & Sloan, S. W. (2007). Elastoplastic modelling of hydraulic and stress–strain behaviour of unsaturated soils. *Mechanics of Materials*, *39*(3), 212-221.

Sze, H.Y., & Yang, J. (2013). Failure modes of sand in undrained cyclic loading: impact of sample preparation. *Journal of Geotechnical and Geoenvironmental Engineering*, *140*(1), 152-169.

Tamagnini, C., Castellanza, R., & Nova, R. (2002). A generalized backward Euler algorithm for the numerical integration of an isotropic hardening elastoplastic model for mechanical and chemical degradation of bonded geomaterials. *International Journal for Numerical and Analytical Methods in Geomechanics*, *26*(10), 963-1004.

Tejchman, J., & Wu, W. (1993). Numerical study on patterning of shear bands in a Cosserat continuum. *Acta Mechanica*, *99*(1), 61-74.

Tejchman, J., Bauer, E., & Tantono, S. F. (2007). Influence of initial density of cohesionless soil on evolution of passive earth pressure. *Acta Geotechnica*, *2*(1), 53.

Tejchman, J., Kozicki, J., & Leśniewska, D. (2011). Discrete simulations of shear zone patterning in sand in earth pressure problems of a retaining wall. *International Journal of Solids and Structures*, *48*(7), 1191-1209.

Tolooiyan, A., & Gavin, K. (2011). Modelling the cone penetration test in sand using cavity expansion and arbitrary Lagrangian Eulerian finite element methods. *Computers and Geotechnics*, *38*(4), 482-490.

Tordesillas, A., & Shi, J. (2009). Micromechanical analysis of failure propagation in frictional granular materials. *International Journal for Numerical and Analytical Methods in Geomechanics*, *33*(15), 1737-1768.

Tordesillas, A., Zhang, J., & Behringer, R. (2009). Buckling force chains in dense granular assemblies: physical and numerical experiments. *Geomechanics and Geoengineering: An International Journal*, *4*(1), 3-16.

van Genuchten, M. T. (1980). A closed-form equation for predicting the hydraulic conductivity of unsaturated soils. *Soil Science Society of America Journal*, 44(5), 892-898.

Vardoulakis, I. (1980). Shear band inclination and shear modulus of sand in biaxial tests. *International Journal for Numerical and Analytical Methods in Geomechanics*, *4*(2), 103-119.

Vardoulakis, I., Goldscheider, M., & Gudehus, G. (1978). Formation of shear bands in sand bodies as a bifurcation problem. *International Journal for Numerical and Analytical Methods in Geomechanics*, *2*(2), 99-128.

Vaunat, J., Cante, J.C., Ledesma, A., & Gens, A. (2000). A stress point algorithm for an elastoplastic model in unsaturated soils. *International Journal of Plasticity*, *16*(2), 121-141.

Veylon, G. (2017). Modélisation numérique du mécanisme de liquéfaction des sols-application aux ouvrages hydrauliques. *PhD thesis*.

Wan, R.G., & Guo, P.J. (2001). Effect of microstructure on undrained behaviour of sands. *Canadian Geotechnical Journal*, *38*(1), 16-28.

Wan, R.G., Pinheiro, M., Daouadji, A., Jrad, M., & Darve, F. (2013). Diffuse instability with transition to localization in loose granular materials. *International Journal for Numerical and Analytical Methods in Geomechanics*, *37(10*), 1292-1311.

Wan, R.G., Nicot, F., & Darve, F. (2017). Failure in Geomaterials: A Contemporary Treatise. *Elsevier*.

Wang, D., Bienen, B., Nazem, M., Tian, Y., Zheng, J., Pucker, T., & Randolph, M. F. (2015). Large deformation finite element analyses in geotechnical engineering. *Computers and Geotechnics*, *65*, 104-114.

Wang, J.P., Li, X., & Yu, H.S. (2017). Stress-force-fabric relationship for unsaturated granular materials in pendular states. *Journal of Engineering Mechanics*, *143*(9), 04017068.

Wang, J., & Zhao, B. (2014). Discrete-continuum analysis of monotonic pile penetration in crushable sands. *Canadian Geotechnical Journal, 51*(10), 1095-1110.

Wang, R., Fu, P., Zhang, J. M., & Dafalias, Y. F. (2017). Evolution of various fabric tensors for granular media toward the critical state. *Journal of Engineering Mechanics*, *143*(10), 04017117.

Wang, X., Wang, L.B., & Xu, L.M. (2004). Formulation of the return mapping algorithm for elastoplastic soil models. *Computers and Geotechnics*, *31*(4), 315-338.

Weber, J. (1966). Recherches concernant les contraintes intergranulaires dans les milieux pulvérulents. *Bulletin de Liaison des Ponts-et-chaussées*, *20*, 1-20.

Welker, P.R., & McNamara, S.C. (2009). What triggers failure in frictional granular assemblies? *Physical Review E*, *79*(6), 061305.

Wheeler, S. J., & Sivakumar, V. (1995). An elasto-plastic critical state framework for unsaturated soil. *Géotechnique*, 45(1), 35-53.

Widuliński, Ł., Kozicki, J., & Tejchman, J. (2009). Numerical simulations of triaxial test with sand using DEM. *Archives of Hydro-Engineering and Environmental Mechanics*, *56*(3-4), 149-172.

Wong, K. S., Ng, C. W. W., Chen, Y. M., & Bian, X. C. (2012). Centrifuge and numerical investigation of passive failure of tunnel face in sand. *Tunnelling and Underground Space Technology*, *28*, 297-303.

Wu, H. N., Shen, S. L., Liao, S. M., & Yin, Z. Y. (2015). Longitudinal structural modelling of shield tunnels considering shearing dislocation between segmental rings. *Tunnelling and Underground Space Technology*, *50*, 317-323.

Wu, S., Gray, D.H., & Richart Jr, F.E. (1984). Capillary effects on dynamic modulus of sands and silts. *Journal of Geotechnical Engineering*, *110*(9), 1188-1203.

Xie, Y. H., Yang, Z. X., Barreto, D., & Jiang, M. D. (2017). The influence of particle geometry and the intermediate stress ratio on the shear behavior of granular materials. *Granular Matter*, *19*(2), 35.

Xiong, H., Nicot, F., & Yin, Z.Y. (2017). A three-dimensional micromechanically based model. *International Journal for Numerical and Analytical Methods in Geomechanics*.

Xu, T.H., & Zhang, L.M. (2015). Numerical implementation of a bounding surface plasticity model for sand under high strain-rate loadings in LS-DYNA. *Computers and Geotechnics*, *66*, 203-218.

Yamakawa, Y., Hashiguchi, K., & Ikeda, K. (2010). Implicit stress-update algorithm for isotropic Cam-clay model based on the subloading surface concept at finite strains. *International Journal of Plasticity*, *26*(5), 634-658.

Yang, Y., & Misra, A. (2012). Micromechanics based second gradient continuum theory for shear band modeling in cohesive granular materials following damage elasticity. *International Journal of Solids and Structures*, *49*(18), 2500-2514.

Yang, Z.X., Li, X.S., & Yang, J. (2007). Undrained anisotropy and rotational shear in granular soil. *Géotechnique, 57*(4), 371-384.

Yang, Z.X., Li, X.S., & Yang, J. (2008). Quantifying and modelling fabric anisotropy of granular soils. *Géotechnique, 58*(4), 237-248.

Yang, Z.X., Yang, J., & Wang, L.Z. (2012). On the influence of inter-particle friction and dilatancy in granular materials: a numerical analysis. *Granular Matter*, *14*(3), 433-447.

Yang, Z.X., & Wu, Y. (2016). Critical state for anisotropic granular materials: a discrete element perspective. *International Journal of Geomechanics*, *17*(2), 04016054.

Yang, Z. X., Jardine, R. J., Zhu, B. T., Foray, P., & Tsuha, C. H. C. (2010). Sand grain crushing and interface shearing during displacement pile installation in sand. *Géotechnique*, *60*(6), 469-482.

Yang, Z. X., Jardine, R. J., Guo, W. B., & Chow, F. (2015a). A new and openly accessible database of tests on piles driven in sands. *Géotechnique Letters*, *5*(1), 12-20.

Yang, Z., Jardine, R., Guo, W., & Chow, F. (2015b). A comprehensive database of tests on axially loaded piles driven in sand. *Academic Press.*

Yin, Z.Y., & Chang, C.S. (2009a). Non-uniqueness of critical state line in compression and extension conditions. *International Journal for Numerical and Analytical Methods in Geomechanics*, *33*(10), 1315-1338.

Yin, Z.Y., & Chang, C.S. (2009b). Microstructural modelling of stress-dependent behaviour of clay. *International Journal of Solids and Structures*, *46*(6), 1373-1388.

Yin, Z.Y., & Chang, C.S. (2013). Stress-dilatancy behavior for sand under loading and unloading conditions. *International Journal for Numerical and Analytical Methods in Geomechanics*, *37*(8), 855-870.

Yin, Z.Y., Chang, C.S., & Hicher, P.Y. (2010). Micromechanical modelling for effect of inherent anisotropy on cyclic behaviour of sand. *International Journal of Solids and Structures*, *47*(14), 1933-1951.

Yin, Z.Y., Chang, C.S., Hicher, P.Y., & Karstunen, M. (2009). Micromechanical analysis of kinematic hardening in natural clay. *International Journal of Plasticity*, 25(8), 1413-1435.

Yin, Z.Y., Chang, C.S., Hicher, P.Y. & Wang, J.H. (2011). Micromechanical analysis of the behavior of stiff clay. *Acta Mechanica Sinica*, *27*(6), 1013-1022.

Yin, Z.Y., Chang, C.S., Karstunen, M., & Hicher, P.Y. (2010). An anisotropic elastic-viscoplastic model for soft clays. *International Journal of Solids and Structures*, *47*(5), 665-677.

Yin, Z.Y., Hattab, M., & Hicher, P.Y. (2011). Multiscale modeling of a sensitive marine clay. *International Journal for Numerical and Analytical Methods in Geomechanics*, 2011, *35*(15), 1682-1702.

Yin, Z.Y., Karstunen, M., Chang, C.S., Koskinen, M., & Lojander, M. (2011). Modeling time-dependent behavior of soft sensitive clay. *Journal of Geotechnical and Geoenvironmental Engineering*, *137*(11), 1103-1113.

Yin, Z.Y., Xu, Q. & Chang, C.S. (2013). Modeling cyclic behavior of clay by micromechanical approach. *ASCE Journal of Engineering Mechanics*, *139*(9), 1305-1309.

Yin, Z.Y., Zhao, J., & Hicher, P.Y. (2014). A micromechanics-based model for sand-silt mixtures. *International Journal of Solids and Structures*, *51*(6), 1350-1363.

Zhang, C., Nguyen, G. D., & Einav, I. (2013). The end-bearing capacity of piles penetrating into crushable soils. *Géotechnique*, *63*(5), 341-354.

Zhang, C., Yang, Z. X., Nguyen, G. D., Jardine, R. J., & Einav, I. (2014). Theoretical breakage mechanics and experimental assessment of stresses surrounding piles penetrating into dense silica sand. *Géotechnique Letters*, *4*(1), 11-16.

Zhang, X., Zhang, X., Shang, F., & Li, Q., 2016. Second-order work and strain burst in single-crystalline micropillar plasticity. *International Journal of Plasticity*, *77*, 192-213.

Zhang, Z. (2017). A thermodynamics-based theory for the thermo-poro-mechanical modeling of saturated clay. *International Journal of Plasticity*, *92*, 164-185.

Zhang, Y. D. (2016). Effect of water-particle interactions on the crushing of granular materials. *PhD thesis*.

Zhang, Y. D., & Buscarnera, G. (2014). Grainsize dependence of clastic yielding in unsaturated granular soils. *Granular Matter*, 16(4), 469-483.

Zhang, Y., & Buscarnera, G. (2016). Implicit integration under mixed controls of a breakage model for unsaturated crushable soils. *International Journal for Numerical and Analytical Methods in Geomechanics*, *40*(6), 887-918.

Zhang, Y.D., & Buscarnera, G. (2017). A rate-dependent breakage model based on the kinetics of crack growth at the grain scale. *Géotechnique*, 1-15.

Zhang, Y.D., Buscarnera, G., & Einav, I. (2016). Grain size dependence of yielding in granular soils interpreted using fracture mechanics, breakage mechanics and Weibull statistics. *Géotechnique*, *66*(2), 149-160.

Zhao, J., Jiang, M., Soga, K., & Luding, S. (2016). Micro origins for macro behavior in granular media. *Granular Matter*, *18*(3), 1-5.

Zhao, C. G., Liu, Y., & Gao, F. P. (2010). Work and energy equations and the principle of generalized effective stress for unsaturated soils. *International Journal for Numerical and Analytical Methods in Geomechanics*, *34*(9), 920-936.

Zhao, C., Salami, Y., Yin, Z.Y., & Hicher, P.Y. (2017) A micromechanical model for unsaturated soils based on thermodynamics. In *Poromechanics VI*, 594-601.

Zhao, J., & Guo, N. (2013). Unique critical state characteristics in granular media considering fabric anisotropy. *Géotechnique*, *63*(8), 695-704.

Zhao, J., & Guo, N. (2015). The interplay between anisotropy and strain localisation in granular soils: a multiscale insight. *Géotechnique*, *65*(8), 642-656.

Zhao, J., Sheng, D., Rouainia, M., & Sloan, S.W. (2005). Explicit stress integration of complex soil models. *International Journal for Numerical and Analytical Methods in Geomechanics*, *29*(12), 1209-1229.

Zhu, H., Nicot, F., & Darve, F. (2016). Meso-structure evolution in a 2D granular material during biaxial loading. *Granular Matter*, *18*(1), 3.

Zhu, Q., & Shao, J. (2016). Micromechanics of rock damage: advances in the quasi-brittle field. *Journal of Rock Mechanics and Geotechnical Engineering, 9*(1), 29-40.

Zhu, Q. Z., Shao, J. F., & Kondo, D. (2008). A discrete thermodynamic approach for modeling anisotropic coupled plasticity-damage behavior in geomaterials. *Comptes Rendus Mecanique*, *336*(4), 376-383.

Zhu, Q. Z., Zhou, C. B., Shao, J. F., & Kondo, D. (2010). A discrete thermodynamic approach for anisotropic plastic–damage modeling of cohesive-frictional geomaterials. *International Journal for Numerical and Analytical Methods in Geomechanics*, *34*(12), 1250-1270.

Ziegler, H., & Wehrli, C. (1987). The derivation of constitutive relations from the free energy and the dissipation function. *Advances in Applied Mechanics*, *25*, 183-238.

UNIVERSITE BRETAGNE LOIRE

CENTRALE NANTES

Thèse de Doctorat

Chaofa ZHAO

Modélisation multi-échelle des sols granulaires : de l'échelle des grains aux structures géotechniques

Multiscale modelling of granular soils: from the grain to the structure scale

Résumé

Le comportement mécanique des sols granulaires est un élément important à prendre en compte dans l'ingénierie géotechnique. Les approches de modélisation actuelles pour le comportement des sols granulaires utilisent des relations constitutives phénoménologiques basées sur la mécanique classique du continuum. Ce problème peut être contourné en utilisant des relations constitutives multi-échelles basées sur les principes thermodynamiques avec variables internes. En utilisant une approche multi-échelle, cette thèse tente de construire des relations constitutives multi-échelles qui tiennent compte de la microstructure des sols granulaires et les mettre en œuvre pour résoudre des problèmes géotechniques à la fois en petites et grandes déformations. La thèse vise à: 1) construire une relation constitutive multi-échelle pour les sols granulaires secs à partir d'un cadre thermodynamique qui nécessite moins d'hypothèses ad hoc; 2) étendre les formulations thermomécaniques multi-échelles aux sols granulaires partiellement saturés pour lesquels un modèle micromécanique est formulé; 3) implémenter le modèle en utilisant un algorithme d'intégration implicite dans un code aux éléments finis; 4) appliquer le modèle pour analyser l'instabilité des sols granulaires dans les cas de ruptures localisées et diffuses; et 5) démontrer la capacité de l'approche multi-échelle à résoudre certains problèmes géotechniques typiques en mettant en œuvre le modèle dans un code aux éléments finis explicite. L'approche multi-échelle proposée aboutit à un outil de simulation qui fournit des informations précieuses sur les problèmes d'ingénierie depuis l'échelle des grains jusqu'à l'échelle de la structure.

Mots clés

Sols granulaires, modélisation multi-échelle, principes thermodynamiques, algorithme d'intégration, instabilité, structures géotechniques

Abstract

The mechanical behaviour of granular soils is an important aspect in geotechnical engineering. Current modelling approaches for the behaviour of granular soils employ phenomenological constitutive relations based upon classical continuum mechanics. This problem can be circumvented by using multiscale constitutive relations based on thermodynamic principles with internal variables. Using a multiscale approach, this thesis attempts to construct multiscale constitutive relations that account for the microstructure of granular soils and to demonstrate their capabilities in solving geotechnical problems at both small and large deformations. The thesis aims to: 1) construct a multiscale constitutive relation for dry granular soils based on a thermodynamic framework which requires fewer *ad hoc* assumptions; 2) extend the multiscale thermomechanical formulations for partially saturated granular soils for which a micromechanical model is formulated; 3) implement the model using an implicit integration algorithm in a finite element code; 4) apply the model to analyse the instability of granular soils for both localised and diffuse failures; and 5) demonstrate the capability of the multiscale approach in solving some typical geotechnical problems by implementing the model in an explicit finite element code. The proposed multiscale approach offers a simulation tool that provides valuable insights into engineering problems from the grain to the structure scale.

Key words

Granular soils, multiscale modelling, thermodynamic principles, integration algorithm, instability, geotechnical structures